

Transmission Electron Microscopy Study of Deformation Processes in Metallic Glasses



TECHNISCHE
UNIVERSITÄT
DARMSTADT

Dissertation approved by the department of
Materials and Earth Sciences
in fulfillment of the requirements for the degree of
Doctor rerum naturalium
(Dr. rer. nat.)

by
Sangjun Kang

Referee: Prof. Dr. Christian Kübel
Co-referee: Prof. Dr. Karsten Durst
Date of submission: 25. 08. 2023
Date of oral exam: 09. 10. 2023

Darmstadt 2023

Sangjun Kang: Transmission Electron Microscopy Study of Deformation Processes in Metallic Glasses
Darmstadt, Technische Universität Darmstadt,
Year thesis published in TUprints 2024
Date of the viva voce 09. 10.2023

Published under CC BY-SA 4.0 International
<https://creativecommons.org/licenses>

Erklärung zur Dissertation

Hiermit versichere ich, dass ich meine Dissertation selbständig und nur mit den angegebenen Quellen und Hilfsmitteln angefertigt habe. Die Arbeit wurde bisher keiner anderen Prüfungsbehörde vorgelegt und noch nicht veröffentlicht.

Darmstadt, 30.08.2023

Sangjun Kang



Acknowledgments

First and foremost, I would like to express my sincerest gratitude to my supervisors, Prof. Christian Kübel and Dr. Xiaoke Mu, for their invaluable guidance and unwavering support throughout the scientific projects and for granting me the opportunity to pursue my doctorate at KIT and TUDa. Their mentorship has not only allowed me to develop my expertise but has also provided me with invaluable life experiences. Engaging in discussions with them has shaped me into a proficient electron microscopist and scientist. I would also like to extend my appreciation to my second supervisor, Prof. Karsten Durst, at TUDa, for his guidance, efforts, and the provision of samples through his student, Christian Minnert, which served as a valuable source of knowledge for scientific interpretation.

My colleagues and co-workers at the INT have been an immense source of inspiration and enlightenment. I am deeply grateful for their cooperation and the friendships we have cultivated over the years. From them, I have not only acquired scientific knowledge but also gained wisdom on how to be a good person. In particular, I would like to acknowledge Dr. Di Wang, Dr. Sabine Schlabach, and Dr. Vinga Szabo for their support and training, as well as the Karlsruhe Nano Micro Facility (KNMFi) for their assistance and access to FIB and TEM facilities. I would like to extend my special thanks to Dr. Vinga Szabo, who dedicated her time and efforts to reviewing my Ph.D. works and this thesis. Furthermore, I express my gratitude to all members of the electron microscopy & spectroscopy group (EMSG) for their friendly support in my research and their assistance in my daily life.

I am grateful to Dr. Sree Harsha Nandam and Dr. Julia Ivanisenko for their productive and insightful discussions, as well as their willingness to help me overcome challenging questions. I would also like to convey my sincere thanks to Prof. Arnaud Caron for his long-term support, guidance, and discussions spanning eight years, beginning with my Hiwi program at INM during my Bachelor's period. He has been my mentor, both in my scientific endeavors and personal life, and I will forever appreciate his friendship and kindness.

My deepest thanks are reserved for my partner, Bora, and my parents, whose infinite patience has been unwavering throughout my life. Bora's love and support have been immeasurable and have greatly contributed to my success. I would also like to express my profound gratitude to my family, teachers, and friends for their ongoing support and encouragement. Without their unwavering belief in me, none of this would have been possible.

Sangjun Kang

Darmstadt, 2023

Abstract

Amorphous metallic alloys known as metallic glasses exhibit remarkable mechanical strength, elasticity, and resistance to wear when compared to their crystalline counterparts. These intriguing attributes have generated considerable interest in utilizing them for engineering materials over the past decades. Nevertheless, a significant drawback of metallic glasses lies in their limited ductility, which causes them to undergo abrupt yielding when undergoing plastic deformation. This plastic deformation of metallic glasses primarily occurs through the creation of shear bands, brought by work-softening nature of glasses. As regions within the material experience plastic deformation, they become softer, promoting localized strain accumulation within a narrow band-like zone, so-called shear band. Unfortunately, the sudden emergence of shear bands contributes to the premature failure of metallic glasses and hinders their toughness. Hence, comprehending the mechanisms that give rise to shear band formation becomes pivotal in constructing the theory of glass deformation and enhancing the mechanical stability of metallic glasses. However, recent advancements in the deformation mechanisms of metallic glasses have predominantly leaned on simulations, as experimentally characterizing the amorphous phases and nanoscale volumes within shear bands comes with substantial challenges. The lack of experimental observations concerning the structures implicated in the deformation of metallic glasses has restricted research findings to a hypothetical level, stalling the progress in novel material development.

This thesis focuses on an experimental investigation of deformed structures of metallic glasses using transmission electron microscopy (TEM) techniques, particularly four-dimensional (4D) scanning-TEM (STEM). The study incorporates methodological advancements, such as developing correlative mapping of nanoscale strain fields and atomic packing structure of glasses using 4D-STEM and Lorentz 4D-STEM, enabling the correlation of atomic structure and magnetic information. Machine learning analysis is applied to extract principal and correlated information from the 4D-STEM dataset. This development allows for direct experimental observations and detailed examination of the deformed structures in metallic glasses. The research outcomes establish an experimental foundation for understanding the formation of an individual shear band and the multiplication of shear bands. This is achieved through direct observations of strain concentrations, shear bands, shear band-affected zones (SBAZs), and local heterogeneity within a deformed glass matrix. Structure-property correlations in metallic glasses are discussed based on these microscopic observations. This new methodology is expected to open up extensive research possibilities for addressing questions in amorphous materials.

Table of Contents

Acknowledgments	III
Abstract	IV
List of Figures	VII
List of Tables	XV
List of abbreviations	XVI
1. Introduction	1
2. Structure and deformation properties of metallic glass	5
2.1. Atomic-level structure description of metallic glasses	6
2.2. Elastic deformation	13
2.3. Initiation of plastic deformation: shear transformation zone	13
2.4. Formation of shear bands	16
2.5. Experimental observation of shear bands	20
2.6. Outline of the following chapters	28
3. Material preparation and characterization methods	30
3.1. Material preparation	31
3.2. Deformation methods: Scratch testing	34
3.3. Fundamentals of electron microscopy	36
3.4. Scanning electron microscope and focused ion beam	39
3.5. Scanning/transmission electron microscopy (S/TEM)	40
3.6. TEM sample preparation by FIB and SEM	45
3.7. Characterization of material structure from electron diffraction	46
4. 4D-STEM based characterization of metallic glasses	52
4.1. Data acquisition and processing	53
4.2. STEM-PDF analysis	55
4.3. Mapping of strain and atomic structure	57
4.4. Importance of TEM sample thickness for 4D-STEM observation	61
5. Mapping local atomic structure of metallic glasses using machine learning aided 4D-STEM PDF	65
5.1. Introduction	66
5.2. Experimental details	67
5.3. Phase decomposition and mapping for Fe-based metallic glasses	68
5.4. Summary	74
6. Direct observation of quadrupolar strain fields forming a shear band in metallic glasses	75
6.1. Introduction	76
6.2. Experimental details	76
6.3. Mapping strain and atomic density in shear bands	77
6.4. Quadrupolar strain field surrounding Eshelby inclusions	81
6.5. Alignment of Eshelby inclusion at a shear band	83
6.6. Evolution of shear bands with shear displacement	86

6.7. Summary	88
7. Effects of the annealing treatments on atomic structure and ductile deformation of metallic glasses	89
7.1. Introduction	90
7.2. Experimental details	91
7.3. Atomic structure of metallic glasses after annealing treatments	93
7.4. Tribological response of Zr-based metallic glasses	96
7.5. Shear band network formation after deformation of metallic glasses in different annealing states	98
7.6. Discussion of the correlation between structural features and deformation behavior of metallic glasses	106
7.7. Summary	107
8. Development of Lorentz 4D-STEM for correlative imaging of the magnetic/electric fields, strain fields, and atomic packing structure of metallic glasses	109
8.1. Background for the development	110
8.2. Microscopy setting, data acquisition, and processing	111
8.3. Direct measurement of magnetoelastic coupling in an amorphous soft ferromagnet	114
8.4. Summary	118
9. Conclusion and outlook	120
9.1. Conclusion	120
9.2. Outlook	124
Curriculum Vitae	127
List of publications/Patents/Conference papers	129
References	131

List of Figures

- Figure 2.1: The DRPHS model proposes five fundamental structures: (a) tetrahedron, (b) octahedron, (c) tetragonal dodecahedron, (d) trigonal prism capped with three half octahedra, and (e) Archimedean antiprism capped with two half octahedra. Reproduced from Ref. ^[25]6
- Figure 2.2: Clusters-indexed Voronoi cells consist of varying numbers of local Voronoi polyhedra. Reprinted from Ref. ^[25]7
- Figure 2.3: Distorted Z12 clusters due to topological restrictions. Voronoi tessellation allows for cluster distortion with deviations in atomic bond lengths by altering the coordination number. Examples include the Z12 cluster being distorted to $\langle 0,3,6,4 \rangle$, $\langle 0,4,6,3 \rangle$, $\langle 0,2,6,5 \rangle$, $\langle 0,2,5,3 \rangle$, as $\langle 0,1,5,2 \rangle$. Reprinted from Ref. ^[21]7
- Figure 2.4: (a) The process followed in NBED of an icosahedral cluster, utilizing a coherent electron beam with a diameter of 0.36 nm. (b) Simulated NBED patterns illustrating an ideal icosahedron. (c) Comparison between experimental and simulated NBED patterns for icosahedral clusters within a $Zr_{80}Pt_{20}$ metallic glass. Angular details between individual diffraction vectors are displayed on the right side of each segment for comparison. The distinctive diffraction spots representing icosahedral order are indicated by arrowheads. Reprinted from Ref. ^[34]9
- Figure 2.5: Schematic representation of relaxation processes in metallic glasses, depicting the potential energy landscape and atomic configurations. The many-body potential energy is illustrated as a function of atomic distances. Active atoms are represented by red color, and atoms surrounded by green dashed circles represent flow units. Modified from Ref. ^[84]11
- Figure 2.6: Tilted dark-field electron correlation microscopy. (a) Experimental setup: Tilted illumination displaces the transmitted beam from the microscope's optic axis. An on-axis objective aperture selects a specific speckle from the diffraction pattern, forming a real-space image. Intensity fluctuations in image speckles arise from structural rearrangements. A sequence of ~ 4000 dark-field images is captured and aligned to correct sample drift. (b) Computation of the time autocorrelation function $g_2(t)$: Intensity time series at each pixel yields $g_2(t)$, which is then fitted to the KWW equation for deriving the relaxation time τ and the stretching parameter β . Modified from Ref. ^[88]12
- Figure 2.7: STZ structure with the strain field around it (a) Calculated shear strain field at STZ subjected to a strain of 0.05. (b) Autocorrelation function of (a). (c) Experimentally measured self-correlation of the strains in a colloidal glass. Reprinted from Ref. ^[98]14
- Figure 2.8: STZ formation in a colloidal glass as a response to shear strain in a colloidal glass. (a) Strain distribution and shear transformation zones in the sheared glass. Particle color indicates the value of the local shear strain. (b) before shear load. (c) after shear load. The dashed zone indicates a circular zone with high positive shear strain. Dashed straight lines delineate four regions of negative shear strain that surround the high shear strain zone in the center. Reprinted from Ref. ^[109]15
- Figure 2.9: The synchronized sliding for the nucleation of shear bands in metallic glasses. (a) Displacement as a function of strain, showing the jumps in displacement (b) at the six points along the band. The figures are reprinted from Ref. ^[21]17
- Figure 2.10: Time-dependent progression of a shear band. Structural variations are depicted by Von Mises strain in the simulated metallic glass during the early stages of shear banding. The figures are reprinted from Ref. ^[120]18

Figure 2.11: Influence of nanoscale structural heterogeneity on shear banding in metallic glasses. Shear band generation in a metallic glass with different amounts of the STZ volume fractions (a) 0%, (b) 10%, (c) 20%, and (d) 30%. Reprinted from Ref. ^[127]	19
Figure 2.12: Heat generation during shear banding observed by infrared (IR) thermography. (a) The instantaneous appearance of the shear band, and (b) propagating heat front; Numbers indicate the frame number, whereby one frame is measured within 0.4 ms. Reprinted from Ref. ^[139]	20
Figure 2.13: TEM observation of shear bands: (a) a bright-field TEM image near a fracture surface of a Zr-based metallic glass and corresponding selected area electron diffraction pattern reprinted from Ref. ^[26] , (b) a high-resolution bright-field TEM image of a shear band in a deformed Fe-based metallic glass reprinted from Ref. ^[27] , (c)-(d) dark-field TEM images of deformed Cu-based metallic glasses reprinted from Ref. ^[28] , (e) HAADF-STEM image of a deformed Pd-based bulk metallic glass sample showing contrast reversals inside a shear band reprinted from Ref. ^[29] , and (f) HAADF-STEM images of shear bands of a Zr-based metallic glass reprinted from Ref. ^[30]	22
Figure 2.14: FEM analysis of a shear band in a deformed Zr-based metallic glass. (a) HAADF image showing a shear band that exhibits periodical fluctuation of scattering power along the propagation direction. The bright and dark regions on the shear band are numbered I-VIII (bottom). Normalized FEM variance profiles with different probe sizes, 0.8 nm ~ 3.2 nm for (b) as-cast sample, (c) the matrix beside the shear band indicated as a back box in (a), (d) the bright regions of the shear band (IV) and (e) the bright regions of the shear band (V). Reprinted from Ref. ^[149]	24
Figure 2.15: Analysis by APT of the deformed and undeformed regions of Vitreloy 105 ($Zr_{52.5}Cu_{17.9}Ni_{14.6}Al_{10}Ti_5$). (a) 3D reconstruction of the deformed sample featuring a shear band. The asymmetric distribution of Cu and Zr across the shear band is visible in the elemental map. (b) The 3D elemental map, along with individual elemental distributions, for the undeformed sample. (c) Composition profile perpendicular to the shear band, extracted from the cylinder in (a). (d) Depth-dependent concentration profile of all elements in the undeformed bulk. (e) Schematic illustrating the plane of the shear band. The figures are reprinted from Ref. ^[151]	25
Figure 2.16: Shear-band affected zone in a Fe-based metallic glass observed by AFM and MFM. (a) SEM image of shear bands after bending test. (b) AFM 3D topography of shear bands. (c) AFM topographic image of a shear band with a line scan along the black dashed line and (d) corresponding MFM phase image with a line scan along the red dashed line. (e) Schematic of the shear-band affected zone. The color regions represent the respective deformation zone after shear banding. The gray region illustrates a long-range elastic regime over the hundreds of micrometers (wave-like domain pattern in the MFM image). The blue region represents the extended strain gradient field spanning over tens of micrometers (extending domain pattern). The red region shows the severely deformed zone within tens of nanometers (zipper-like domain pattern). Reprinted from Ref. ^[157]	27
Figure 3.1: Schematic illustration of (a) a single-roller melt-spinning and (b) suction casting. Reprinted from Ref. ^[162] and Ref. ^[164]	32
Figure 3.2: SEM images of (a) tip and (b) scratched track with wear debris and shear offsets on the pile-up area. The scratches were imaged by (c) optical microscopy and (d) atomic force microscopy.....	35
Figure 3.3: Schematic description of how an electron beam interacts with an atom (nucleus and electron cloud) in a sample. The figure shows the elastic/inelastically scattered electrons as well as the transmitted ones. Secondary electrons are electrons generated as ionization products. They produce characteristic photons. Back-scattered electrons are electrons that are scattered backward due to the strong positive charge of the nucleus. The figure is reshaped from Ref. ^[167]	37

Figure 3.4: Schematic of a standard FIB/SEM. FIB/SEMs integrate both, a scanning electron microscope and a focused ion beam within a single system. These instruments are frequently equipped with diverse detectors, including Everhart–Thornley (ET), backscattered electron (BS), energy-dispersive spectroscopy (EDS), electron backscatter diffraction (EBSD) detectors, and in-lens detectors. FIB/SEMs commonly feature gas injection systems and manipulators as well. The figure is reprinted from Ref. ^[168]	39
Figure 3.5: Schematic view of the imaging and diffraction mode of TEM. Reprinted from Ref. ^[167]	42
Figure 3.6: Schematic view of conventional TEM and STEM modes.....	43
Figure 3.7: Cross-sectional TEM sample preparation by dual-beam SEM-FIB system. (a) milling trenches from the area of interest, (b) TEM lamella after lift-out before thinning, (c) after thinning for electron transparency, STEM-HAADF image, and (d) Thickness map of a typical TEM lamella for investigation obtained from energy-filtered transmission electron microscopy (EFTEM).....	45
Figure 3.8: Schematic illustration of typical atomic structures of solids, <i>e.g.</i> single crystal, polycrystal, amorphous, and corresponding electron diffraction patterns.	47
Figure 3.9: Sketch of the procedure to calculate the PDF from the electron diffraction pattern. An annular averaged diffraction profile obtained from a diffraction pattern of an amorphous sample. Structure factor deduced by background subtraction of single atomic form factor. Further background modeling with polynomial function to eliminate the low-frequency artifacts from multiple scattering. RDF can be calculated from the Fourier sine transform of the structure factor. Reprinted from Ref. ^[177]	49
Figure 3.10: Difference between the 2-D XRD pattern measured in two orientations P(0°)–P(90°) for a Fe-based metallic-glass sample annealed at 300°C (a) without stress (b) under stress. The sample annealed under stress undergoes creep and is expected to be similar to shear-band material; it shows anisotropy after unloading indicating the presence of residual stress within the material after deformation. Reprinted from Ref. ^[177]	51
Figure 4.1: Schematic illustration of 4D-STEM. A quasi-parallel electron probe is focused to the nm scale on an electron transparent sample. Electron diffraction patterns are acquired from the nanovolume at each scan position during stepwise scanning of the probe across the area of interest. The diffraction pattern of metallic glasses is characterized by a set of circular diffraction rings due to their isotropic atomic arrangement. Reprinted from Ref. ^[177]	53
Figure 4.2: Schematic illustration of STEM-PDF mapping. (a) Local diffraction patterns and corresponding PDFs acquired by microprobe 4D-STEM setup. (b) The diffraction patterns are individually processed into a PDF cube. Reprinted from Ref. ^[172]	55
Figure 4.3: STEM-PDF analysis for characterization of as-spun Fe _{85.2} Si _{10.5} B _{9.5} P ₄ Cu _{0.8} metallic glass ribbons. (a) a STEM-HAADF image. (b) Averaged structure factors and (c) averaged PDFs from the STEM-PDF data cube. (d) Maps for the first peak intensity of S(<i>q</i>)s and PDFs.	56
Figure 4.4: Schematic illustration of 4D-STEM-based strain and PDF mapping. (a) The quasi-parallel electron probe is focused on the TEM lamella. Spatially-resolved diffraction patterns are collected mapping a shear band region in a deformed metallic glass. (b) Data processing: principal strains (<i>P1</i> and <i>P2</i>) are calculated from the elliptic distortion of the diffraction ring. For better visualization, the diffraction pattern is elongated to the principal strain direction. The strain tensors are algebraically obtained by projecting the principal strains to the reference coordinates (<i>x</i> - and <i>y</i> -axis). For PDF analysis, the local diffraction patterns are azimuthally integrated into intensity profiles <i>I</i> (<i>q</i>). Structure	

factors, $S(q)$, are obtained by background subtraction of $I(q)$. The PDFs are obtained by Fourier sine transformation of $S(q)$	57
Figure 4.5: A typical diffraction pattern of $\text{Fe}_{85.2}\text{Si}_{10.5}\text{B}_{9.5}\text{P}_4\text{Cu}_{0.8}$ metallic glass (left) which was binarized using a threshold with $I(qx, qy) = 1$ for $0.95I_{\max} < I(qx, qy) < I_{\max}$ and 0 everywhere else (right).	58
Figure 4.6: Deformed $\text{Fe}_{85.2}\text{Si}_{10.5}\text{B}_{9.5}\text{P}_4\text{Cu}_{0.8}$ metallic glass ribbon. (a) first principal strain, $\mathbf{P1}$, (b) second principal strain, $\mathbf{P2}$, (c) volumetric strain, and (d) deviatoric strain.	60
Figure 4.7: Statistical analysis for the accuracy of the strain measurement. (a) Map of fitting error for strain measurement. (b) Map of the radius of the 1 st ring (q_{\max}). (c) Line profiles of the mismatch distance and the radius of the 1 st ring in the region indicated by white dash arrows in (a) and (b).	61
Figure 4.8: Influence of sample thickness on the volumetric strain of a deformed $\text{Fe}_{85.2}\text{Si}_{10.5}\text{B}_{9.5}\text{P}_4\text{Cu}_{0.8}$ metallic glass ribbon. (a) SEM image showing the area beside a scratch with shear offsets clearly visible. The shadowed rectangle indicates the location of the prepared TEM lamella. (b) STEM-HAADF image of the TEM lamella, where the expected locations of the shear bands are indicated by red dashed lines according to the shear offsets at the surface. A 4D-STEM map was acquired at the area indicated by the black rectangle, where the shear bands of interest are labeled SB1 and SB2. Volumetric strain map of the sample measured for different thicknesses of about (c) 300 nm, (d) 200 nm, (e) 130 nm, and (f) 70 nm.	62
Figure 4.9: Line profiles of the volumetric strain maps (a) along the SB1 and (b) perpendicular to SB2 in the directions indicated by dash arrows in Figure 4.8c-f for different thicknesses of about 300 nm, 200 nm, 130 nm, and 70 nm.	63
Figure 5.1: Conventional S/TEM investigation of as-spun and annealed $\text{Fe}_{85.2}\text{Si}_{10.5}\text{B}_{9.5}\text{P}_4\text{Cu}_{0.8}$ metallic glasses. (a) STEM-HAADF image and (b) SEAD pattern for the as-spun glass. (c) STEM-HAADF image and (d) SEAD pattern for the annealed glass. (e) PDFs calculated from the SEAD patterns of the as-spun and annealed glasses. The height of the PDFs is normalized by their first peak for easy presentation of peak shifts.	68
Figure 5.2: (a) Schematic illustration of NMF-aided STEM-PDF analysis. (b) Probabilistic blind source model underlying non-negative matrix factorization. The diagram model depicts a network in which experimental \mathbf{V}_n are in the bottom layer of nodes and the blind sources \mathbf{H}_i in the top layer of nodes (top). The experimental \mathbf{V} can be represented by a probability distribution with $\mathbf{Vn} = \mathbf{iWn}$, \mathbf{iHi} . According to the model, the significance of sources \mathbf{H}_i on \mathbf{V} is represented by a connection with the weighting matrix \mathbf{Wn} , \mathbf{i} . For the application to STEM-PDF cube, an experimental PDF is decomposed by PDFs from basis sources \mathbf{V}_1 , \mathbf{V}_2 , and \mathbf{V}_3 (basis PDFs) with weighting constants \mathbf{H}_1 , \mathbf{H}_2 , and \mathbf{H}_3	70
Figure 5.3: NMF results for a STEM-PDF dataset of the as-spun $\text{Fe}_{85.2}\text{Si}_{10.5}\text{B}_{9.5}\text{P}_4\text{Cu}_{0.8}$ metallic glass. (a) Obtained basis PDFs. The vertical dashed lines indicate the distances of the polyhedra connections with different numbers of shared atoms (ranging from 1 to 3) for structural type 1 (black) and structural type 2 (red). (b) Spatial distribution of the basic structural types indicated by different colors. The brightness indicates their population. All three maps are incorporated in the color mix map at the right.	71
Figure 5.4: Atomic structure mapping of the as-spun and annealed $\text{Fe}_{85.2}\text{Si}_{10.5}\text{B}_{9.5}\text{P}_4\text{Cu}_{0.8}$ metallic glasses using NMF-aided STEM-PDF analysis. Basis PDFs of (a) the liquid-like and (b) the solid-like structural bases separately obtained from both as-spun and annealed metallic glass samples. Maps of	

the liquid-like and solid-like structural bases for (c) as-spun and (d) annealed samples with the fraction of each structural type indicated.73

Figure 6.1: Deformed $\text{Fe}_{85.2}\text{Si}_{10.5}\text{B}_{9.5}\text{P}_4\text{Cu}_{0.8}$ metallic glass ribbon. (a) SEM image showing the area beside a scratch with shear offsets visible. The shadowed rectangle denotes the location of the prepared TEM lamella. (b) STEM-HAADF image of the TEM lamella, where the expected locations of the shear bands are indicated by red dashed lines according to shear offset at the surface. A 4D-STEM map was acquired of the area indicated by the black rectangle with the shear bands of interest labeled as SB1 and SB2. (c) Map of relative atomic packing density ($\Delta\rho$). (d) Map of maximum shear strain (τ_{max}). The color corresponds to the orientation and the brightness to the amplitude as indicated by the color wheel. For the strain tensor, the x-axis is defined to be parallel to SB1 and the y-axis perpendicular to SB1. (e) ϵ_{xx} , the strain component along the x-axis, (f) ϵ_{xy} , the shear component, and (g) ϵ_{yy} , the strain component along the y-axis. (h)-(j) show the correlation of the strain components and the atomic density, which are magnified images of the area indicated by the white rectangle in (d), (e), and (g) with the scale bar corresponding to 100 nm. The dashed ellipses indicate the quadrupole strain field. The yellow dashed arrows indicate the center of the quadrupoles. The figure is reprinted from Ref. ^[201]78

Figure 6.2: Deformed $\text{Zr}_{46}\text{Cu}_{38}\text{Al}_8\text{Ag}_8$ bulk metallic glass. (a) SEM image showing the area beside a scratch with shear offsets and microcracks. The shadowed rectangle denotes the location of the TEM lamella. (b) STEM-HAADF image of the TEM lamella, where the location of shear bands is indicated by red dash lines. A 4D-STEM map was acquired of the area indicated by the black rectangle, where the shear bands of interest are labeled SB1 and SB2. (c) Map of relative atomic density ($\Delta\rho$). (d) Map of maximum shear strain (τ_{max}). The color corresponds to the orientation of τ_{max} , the brightness to the amplitude, as indicated by the color wheel. For the strain tensors, the x-axis is defined to be parallel to SB1 and the y-axis perpendicular to SB1. (e) ϵ_{xx} , the strain tensor component along the x-axis, (f) ϵ_{xy} , the shear component, and (g) ϵ_{yy} , along the y-axis. (h)-(j) show the correlation of the strain components and the atomic density, which are magnified images of the area indicated by the white rectangle in (d), (e), and (g) with a scale bar corresponding to 100 nm. The dashed ellipses indicate the quadrupole strain field. The yellow dashed arrows indicate the centers of the quadrupole strain fields. The figure is reprinted from Ref. ^[201]80

Figure 6.3: Visualization of an Eshelby quadrupolar strain field. Experimental data of (a) shear strain ϵ_{xy} and (b) maximum shear strain τ_{max} in a $\text{Fe}_{85.2}\text{Si}_{10.5}\text{B}_{9.5}\text{P}_4\text{Cu}_{0.8}$ metallic glass ribbon obtained from 4D-STEM strain mapping and MD simulation of a STZ from Ref. ^[207] for (c) atomic strain and (d) rotation angle.....82

Figure 6.4: (a) Vector field visualization of the maximum shear strain overlaid on the map of ϵ_{Vol} for $\text{Fe}_{85.2}\text{Si}_{10.5}\text{B}_{9.5}\text{P}_4\text{Cu}_{0.8}$. (b) (top) Magnified region from the black rectangular area in (a) compared to maps of ϵ_{xy} and the nearest-neighbor distance from the same region. (c) Line profiles of the deviatoric strain, volumetric strain, nearest-neighbor distance, and curl of τ_{max} along the shear band in the region indicated by a red rectangle in (a). The positions of the Eshelby inclusions and their nano core are highlighted by red gradient windows. (d) PDFs averaged from typical inclusions and in-between inclusions marked by white and yellow dashed circles in (b-bottom) together with a PDF of the matrix taken from an area away from the quadrupoles. Each error bar (standard deviation) is obtained from 75 PDFs taken from 3 equivalent regions. The figure is reprinted from Ref. ^[201]83

Figure 6.5: (a) Vector field visualization of the maximum shear strain overlaid on the atomic density map for a $\text{Zr}_{46}\text{Cu}_{38}\text{Al}_8\text{Ag}_8$ bulk metallic glass. (b) Line profile of relative atomic density ($\Delta\rho$), deviatoric strain, volumetric strain, and curl of τ_{max} taken along the shear band in the region

indicated by a black dashed rectangle in (a). The red highlights indicate the position of the shear transformation inclusions.....	85
Figure 6.6: STEM-HAADF images showing secondary shear bands and their brunching points in $Zr_{46}Cu_{38}Al_8Ag_8$ bulk metallic glass. SB2 exhibits alternating fluctuation with a much shorter distance (< 100 nm).....	85
Figure 6.7: (a) Atomic density map of a $Fe_{85.2}Si_{10.5}B_{9.5}P_4Cu_{0.8}$ metallic glass ribbon where line profiles have been calculated along SB1 (left) and SB2 (right) showing periodic variations for SB1 and negligible variations along SB2. (b) Line profiles calculated across SB1(left) and SB2 (right) showing the antisymmetric atomic density distribution across both shear bands. The figure is reprinted from Ref. [199]	86
Figure 7.1: (a) Electron PDF calculated from SAED pattern of the as-cast, 20 h, and 240 h annealed $Zr_{46}Cu_{38}Al_8Ag_8$ metallic glasses. The first peaks of PDFs are enlarged in the inset. The heights of the PDFs are normalized by their first peak and displaced for easy presentation of peak shifts. The first peak positions of the first peak in the PDFs correspond to the nearest atomic neighbor distance, which is plotted in (b) together with mass density measured by Archimedes' principle.	94
Figure 7.2: (a) Synchrotron Synchrotron-based X-ray pair distribution function analysis of the as-cast, 20 h, and 240 h annealed $Zr_{46}Cu_{38}Al_8Ag_8$ metallic glasses obtained from synchrotron radiation X-ray diffraction. The first peaks of each PDF are enlarged in (b).....	94
Figure 7.3: (a) SEM images of a worn track, (b) a close view of the area indicated by the white box in a) showing the area for lamella preparation, and an arrow highlighting a lateral microcrack. (c) Friction curves as a function of sliding distance at the normal load 14 N, 17 N, and 20 N for the as-cast sample. (d) Friction curves as a function of sliding distance for as-cast, 20 h, and 240 h annealed samples at a normal load of 20 N. The black highlighted rectangle in the friction curves represents the static friction zone.	96
Figure 7.4: Tribological response of as-cast, 20 h, and 240 h annealed $Zr_{46}Cu_{38}Al_8Ag_8$ bulk metallic glasses. Load dependence of (a) friction force used to determine the friction coefficient as the slope and (b) of contact area used to determine the scratch hardness from the reciprocal slope; (c) friction coefficient and scratch hardness as a function of annealing time and (d) bar graph of specific wear rate.....	97
Figure 7.5: STEM-HAADF cross-sectional images of TEM lamellae from scratched the (a) as-cast, (c) 20 h, and (e) 240 h annealed $Zr_{46}Cu_{38}Al_8Ag_8$ metallic glasses at a normal load of 20 N. The piled-up area is highlighted in red, where microcracks are observed. The inset dash rectangles are magnified in (b, d, f) which show characteristic shear band networks.	99
Figure 7.6: Deformed $Zr_{46}Cu_{38}Al_8Ag_8$ bulk metallic glass. (a)-(c) STEM-HAADF images showing the areas for 4D-STEM mapping near the deformed surface (green rectangle). The pile-up areas are indicated in red. The coordinate system is defined with the x-axis parallel and the y-axis perpendicular to the major shear direction as indicated by the inserted axial bars. (d)-(g) are maps of the strain component ϵ_{xx} , (h)-(k) are maps of the strain component ϵ_{xy} , and (l)-(o) are maps of the strain component ϵ_{yy} of the as-cast, 20 h and 240 h annealed samples. (p)-(s) are relative atomic density maps of the as-spun and annealed samples	101
Figure 7.7: Secondary shear bands and their brunching points in the as-cast $Zr_{46}Cu_{38}Al_8Ag_8$ bulk metallic glass. (a) STEM-HAADF image showing the area for 4D-STEM mapping (green rectangle). (b) is a	

relative atomic density map. The coordinate system is defined as x-axis parallel and y-axis perpendicular to SB1 (c)-(e) are strain tensor ϵ_{xx} , ϵ_{xy} , and ϵ_{yy}102

Figure 7.8: Deformed $\text{Fe}_{85.2}\text{Si}_{10.5}\text{B}_{9.5}\text{P}_4\text{Cu}_{0.8}$ metallic glass ribbon. (a), (c), (e), (g), and (i) as-spun samples and (b), (d), (f), (h), and (j) annealed samples. (a)-(b) STEM-HAADF images showing areas for 4D-STEM mapping and the presence of shear offsets (green rectangles). The coordinate system is defined with the x-axis to be parallel to shear bands and the y-axis perpendicular to shear bands as shown in the inserted coordinate system. (c)-(d) display the strain component ϵ_{xx} , (e)-(f) the strain component ϵ_{xy} , and (g)-(h) the strain component ϵ_{yy} . (i)-(j) show the relative atomic density maps of as-spun and annealed samples.....104

Figure 8.1: Lens setting of Ltz-4D-STEM. The lenses in the image corrector are manipulated by tuning their direct current supply. The first lens in the image corrector, *i.e.* Lorentz lens, is used to converge the high scattering signal, and the double hexapole correctors are tuned to compensate for the distortion. Thereby, the recorded maximum scattering angle was corresponding to about 1 \AA^{-1} in reciprocal space without significant distortion.....111

Figure 8.2: Schematic illustration of Ltz-4D-STEM. (a) The electron probe is focused on the soft magnetic TEM sample under field-free conditions, *i.e.*, Lorentz condition. Spatially-resolved diffraction patterns are collected during scanning over an area of interest. (b) Data processing: the center position of the direct beam is a measure of the momentum transferred by the magnetic field (Lorentz forces) inside the sample. The first principal strain (ϵ_1) is calculated from the elliptic distortion of the 1st diffraction ring. The relative density ($\Delta\rho$) is measured by the relative variation of the area encircled by the 1st ring of each diffraction pattern.113

Figure 8.3: Ltz-4D-STEM observation of as-spun $\text{Fe}_{85.2}\text{Si}_{10.5}\text{B}_{9.5}\text{P}_4\text{Cu}_{0.8}$ metallic glass ribbon after plastic deformation. (a) STEM-HAADF image of the TEM lamella, where the expected locations of the shear bands are indicated by red dashed lines according to shear offset at the surface. A 4D-STEM map was acquired at the area indicated by the green rectangle, where the shear bands of interest are labeled as SB1 and SB2. (b) magnetic field (B), (c) first principal strain (ϵ_1). The color corresponds to the orientation, and the brightness corresponds to the amplitude of the fields, as indicated by the color wheel. For ϵ_1 , the strain orientation is presented by a two-fold symmetrical wheel following its nature. (c) relative density ($\Delta\rho$). Yellow color represents high density and dark blue color low density.115

Figure 8.4: Map of the strength of DPC signal from (a) unmagnetized (Ltz-condition), and fully magnetized (conventional STEM condition) $\text{Fe}_{85.2}\text{Si}_{10.5}\text{B}_{9.5}\text{P}_4\text{Cu}_{0.8}$ metallic glass ribbon. (c) Line profiles taken across the shear band from the measurements of (a) Ltz-condition indicated by a black dash arrow (Line scan 1) and (b) conventional STEM condition indicated by a red dash arrow (Line scan 2).116

Figure 8.5: As-spun $\text{Fe}_{85.2}\text{Si}_{10.5}\text{B}_{9.5}\text{P}_4\text{Cu}_{0.8}$ metallic glass ribbon after plastic deformation. (a) Vector field visualization of the magnetic moments (B_x , B_y) with white arrows and the first principal strain (ϵ_{1x} , ϵ_{1y}) with red sticks overlaid by the color map of B . (b) Angular mismatching between B and ϵ_1117

Figure 8.6: Deviatoric strain of as-spun $\text{Fe}_{85.2}\text{Si}_{10.5}\text{B}_{9.5}\text{P}_4\text{Cu}_{0.8}$ metallic glass ribbon after plastic deformation.117

Figure 8.7: Map of magnetoelastic energy of the as-spun $\text{Fe}_{85.2}\text{Si}_{10.5}\text{B}_{9.5}\text{P}_4\text{Cu}_{0.8}$ metallic glass ribbons after deformation.118



List of Tables

Table 3.1: Brief descriptions of samples used in the present work.

Table 7.1: Hardness and Young's modulus of the studied samples. The data for Fe-based metallic glass ribbon is reused from Ref. ^[1].

List of abbreviations

ADF	Annular dark field
AFM	Atomic force microscopy
APT	Atom probe tomography
BF	Bright field
BF-TEM	Bright field TEM
BSS	Blind source separation
CCD	Charged coupled device
CMOS	Complementary metal-oxide-semiconductor
CSRO	Chemical short-range order
CVD	Chemical vapor deposition
DF-TEM	Dark-field TEM
DSC	Differential scanning calorimetry
DTA	Differential thermal analysis
ECM	Electron correlation microscopy
EDX	Energy-dispersive X-ray spectroscopy
EELS	Electron energy-loss spectroscopy
EFTEM	Energy filtered TEM
EXAFS	Extended energy X-ray absorption fine structure
FEG	Field emission gun
FEM	Fluctuation electron microscopy
FFT	Fast Fourier transform
FIB	Focus ion beam
FTIR	Fourier transform Infrared (spectroscopy)
FWHM	Full width at half maximum
GFM	Geometrically favored motif
GUM	Geometrically unfavored motif
HAADF	High-angle annular dark-field
HDO	Hydrodeoxygenation
HRTEM	High-resolution transmission electron microscopy
ICP	Inductively coupled plasma
LMIS	Liquid metal ion sources
Ltz	Lorentz

PAS	Positron annihilation spectroscopy
PC	Principal component
PCA	Principal component analysis
PDF	Pair distribution function
PVD	Physical vapor deposition
MD	Molecular dynamics
ML	Machine learning
MLLS	Multi-linear least squares
MRO	Medium-range order
NBED	Nanobeam electron diffraction
NLLS	Non-linear least squares
NMR	Nuclear magnetic resonance
SAED	Selected area electron diffraction
SBAZ	Shear band-affected zone
SEM	Scanning electron microscopy
STEM	Scanning transmission electron microscopy
STZ	Shear transformation zone
SPD	Severe plastic deformation
SRO	Short-range order
SVD	Singular value decomposition
TEM	Transmission electron microscopy
TFMG	Thin-film metallic glass
T_g	Glass transition temperature
TSRO	Topological short-range order
WBP	Weighted back-projection
XPCS	X-ray photon correlation spectroscopy
XRD	X-ray diffraction
3D	Three-dimensional
4D	Four-dimensional

Chapter 1

1. Introduction

Metallic glasses are amorphous metallic alloys that exhibit significantly higher yield strength and elasticity compared to their crystalline counterparts.^[1-2] They were first discovered in 1960 by Duwez et al., who utilized melt quenching of Au-Si foils to create 10 μm -thick metallic glasses.^[3] These thin foils demonstrated exceptional ultimate strength, approaching the theoretical strength of solids in tension.^[4] This discovery, coupled with their excellent corrosion and wear resistance, has generated considerable interest in metallic glasses as potential engineering materials in bearing rollers, space machinery, and micro-electromechanical systems.^[1-2, 5]

However, metallic glasses generally suffer from limited ductility, leading to abrupt yielding under stress.^[1-2] Unlike crystalline materials, amorphous materials lack crystal-slip systems resulting in rigid interconnected units leading to high-energy barriers for plastic flow.^[6] Consequently, plastic deformation in metallic glasses is accompanied by work-softening, where plastically deformed regions become softer and more susceptible to subsequent plastic flow. This leads to an autocatalytic localization of strain in thin shear bands as opposed to the accommodation of crystallographic defects such as dislocations in polycrystalline materials.^[7] Shear bands are generally identified by narrow zones, where significant plastic deformation has occurred, and

which exhibit distinct structural characteristics such as reduced density compared to the undeformed glass matrix. The rapid formation of shear bands throughout the bulk is responsible for their limited ductility and catastrophic failure, significantly compromising their fracture toughness and impeding wide-range application.^[8]

To overcome the limitations of metallic glasses, understanding and controlling the formation of shear bands is crucial. Previous studies have revealed several characteristics of shear banding in metallic glasses, such as its asymmetric behavior under compression and tension,^[9] sensitivity to processing history,^[10-11] variable shear band velocity dependent on strain rate and temperature,^[12] and suppression of shear band formation in thin samples below a few micrometers.^[8] It has been also suggested that a heterogeneous microstructure of metallic glasses plays an important role in the formation of shear bands and shear band multiplication, and thus for constraining catastrophic propagation of shear bands.^[13] However, the behaviors of shear bands have not been fully understood and require further characterization efforts of the local glass structure and the structural variations inside shear bands.

Experimental approaches using synchrotron X-ray diffraction^[14], neutron diffraction^[15], and positron-annihilation spectroscopy^[16-17] have indicated an increase in free volume within severely deformed metallic glasses. Unfortunately, the amorphous nature of metallic glasses and the nanoscale size of shear bands pose challenges for experimental characterization techniques and direct imaging methods. The width of shear bands in the amorphous matrix is typically estimated to be around 10 nm, much smaller than the resolution of classical X-ray and neutron diffraction techniques.^[18] Atomistic simulations have provided insights into the atomic structure of metallic glasses and shear bands^[19-24], including volumetric dilation and reduced topological and chemical short-range order (SRO) at the core of shear bands.^[22-24] Nevertheless, the simulation results, while informative, have limitations in fully representing the deformation behavior of metallic glasses in real-world scenarios due to the constraints of temporal and spatial scales in the simulations. Therefore, it becomes imperative to complement these simulations with direct experimental investigations of the detailed structure of individual shear bands and their associated deformed zones to validate the theoretical studies and establish links to mechanical properties.^[25]

S/TEM techniques have been employed to understand shear bands in metallic glasses.^[26-31] These studies have uncovered that shear bands exhibit a linear morphology, and there are characteristic fluctuations in scattering power within the deformed glass matrix and along the shear bands. However, conventional S/TEM has limitations in providing precise information about the atomic structure of glasses, which is essential for understanding the shear band structure. This limitation

arises from a mixing of information on the disordered structure of metallic glasses, atomic density, and elemental composition projected through the sample thickness. One solution for probing nanoscale volumes has been the use of nanobeam electron diffraction (NBED) implemented in TEM.^[32] For instance, fluctuation electron microscopy (FEM) using a nanobeam has been instrumental in investigating the atomic structure of metallic glasses by measuring intensity fluctuations in local electron diffraction patterns at different probe positions.^[33] However, the NBED studies generally require very thin TEM specimens (ideally, < 10 nm) for minimal overlap of diffraction features; otherwise, the result suffers from nonlinear degradation.^[34] For these ultra-thin samples, the thinning process required raises concerns about structural variations introduced during sample thinning, particularly for highly strained metallic glasses with shear bands where residual stresses are crucial but easily relax during thinning. Moreover, NBED does not provide direct real-space information, and interpretation of atomic structure often necessitates sophisticated simulations, *e.g.* reverse Monte Carlo modeling, for interpreting the information stored in reciprocal space.^[35-38] As an alternative approach, Mu et al. recently developed STEM-pair distribution function (PDF) analysis, a technique based on 4D-STEM, to characterize the local atomic structure of amorphous materials and to provide directly interpretable structural information.^[39-41] Unlike FEM, STEM-PDF offers real-space information on atomic packing, which is intuitive to interpret and relatively robust against sample thickness variations. However, the obtained information is still subject to mixing due to projection overlap. Moreover, the finite collection angle of the electron diffraction patterns limits the resolution of the pair distribution peaks giving rise to difficulties in detecting subtle structural variations within shear bands.^[42]

The studies have enabled significant progress in understanding the relationship between the structure of metallic glasses and their mechanical response. However, several crucial aspects remain unclear when it comes to metallic glass deformation. Specifically, the atomic structure within shear bands remains poorly understood, as recent research indicates the existence of different kinds of shear bands, *e.g.*, shear bands only with a volumetric dilatation along the whole band and other shear bands with alternating density fluctuations. Therefore, it is essential to conduct a direct experimental investigation to confirm the theoretical studies and gain insights into the shear band structure, eventually linking them with the mechanical properties of metallic glasses.

To develop an improved experimental structural understanding of metallic glasses and their deformation features, this Ph.D. research aims to use and develop advanced TEM techniques to overcome the existing technical limitations for local nanoscale characterization to gain insights into the structure of shear bands and deformation processes in metallic glasses. To achieve this,

cutting-edge structural characterization was carried out, which enabled the mapping of strain and atomic packing density in metallic glasses using 4D-STEM. The analysis involves the STEM-PDF analysis, where the PDF provides crucial information about the local SRO and MRO in the glasses. This enables not only quantitative analysis of local density and strain variations with high precision but also allows for a direct pixel-level correlation of the structure components. This thesis also introduces new advanced analytic tools, *e.g.*, machine learning analysis for 4D-STEM data to solve part of the overlap problem and to extract subtle signal variations within STEM-PDF data sets. These innovative analytical tools successfully overcome major challenges in characterizing shear bands and provide direct experimental information on the atomic structure of shear bands in metallic glasses. This thesis specifically focuses on the TEM characterization of the deformation structure in metallic glasses. As a result, other aspects such as time/rate-dependent theory and unrelated bulk properties are only briefly discussed when necessary.

Chapter 2

2. Structure and deformation properties of metallic glass

This chapter serves as an introduction to the deformation mechanism of metallic glasses. It begins by describing the atomic-level structure of metallic glasses and establishes its connection with the deformation process, ranging from elastic to plastic deformation. The current theoretical understanding of shear band formation in metallic glasses is then presented, exploring various scenarios for their emergence.

Subsequently, this chapter delves into the internal aspects of shear bands, encompassing structural changes, temperature rise, potential stick-and-slip cycles, nanocrystallization induced by shearing, thickness evolution, and cavitation. Additionally, it evaluates the experimental observations of shear bands using a wide range of approaches, while also addressing the current limitations in experimental characterization.

2.1. Atomic-level structure description of metallic glasses

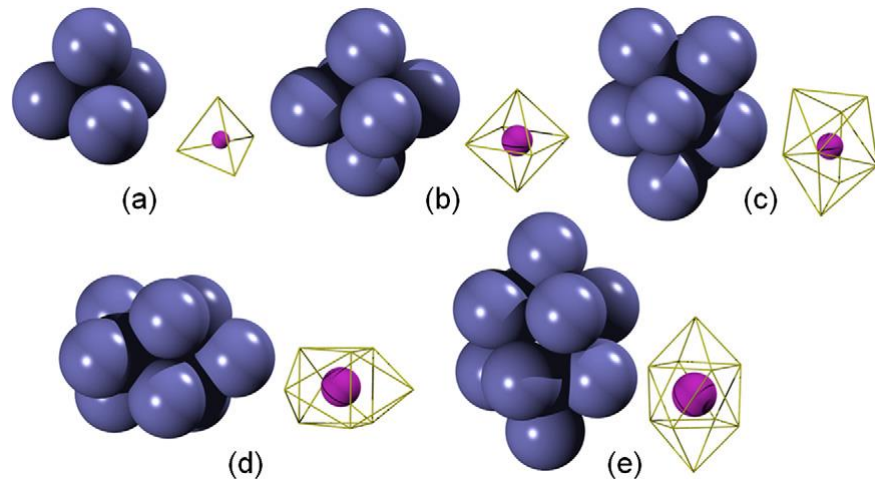


Figure 2.1: The DRPHS model proposes five fundamental structures: (a) tetrahedron, (b) octahedron, (c) tetragonal dodecahedron, (d) trigonal prism capped with three half octahedra, and (e) Archimedean antiprism capped with two half octahedra. Reproduced from Ref. [25].

The metallic glass structure emerges from its supercooled liquid state, which exhibits an intermediate atomic packing density, lying between that of the liquid and solid states. The atomic structure of the supercooled liquid can be represented using basis structural units resembling a dense arrangement of hard spheres. Figure 2.1 illustrates five types of cluster bases: (a) tetrahedron, (b) octahedron, (c) tetragonal dodecahedron, (d) trigonal prism capped with three half-octahedra, and (e) Archimedean antiprism capped with two half octahedra.^[43-44] Among these basic types, the tetrahedron offers the highest packing efficiency. However, tetrahedrons alone cannot completely fill a 3D space due to topological restrictions. It becomes necessary to employ a combination of different basic structures or introduce local distortions to achieve complete 3D filling. Local distortions can generate new possible structural bases, such as the polytetrahedron, which consists of 12 nearest-neighbor atoms surrounding a central atom. The excessive number of nearest neighbor atoms creates unfilled space in the atomic shell, *i.e.* free volumes, leading to a mismatch in atomic bonding lengths.^[45] The distortion of the short-range structure becomes an intrinsic characteristic of a supercooled liquid, particularly in a well-condensed state at room temperature. This distorted atomic structure can be energetically described by the so-called soft sphere model using simple pair potentials.^[46-47] In this model, the continuous potential energy of atomic pairs, which reaches a minimum at a specific interatomic distance, serves as a driving force for atomic packing.

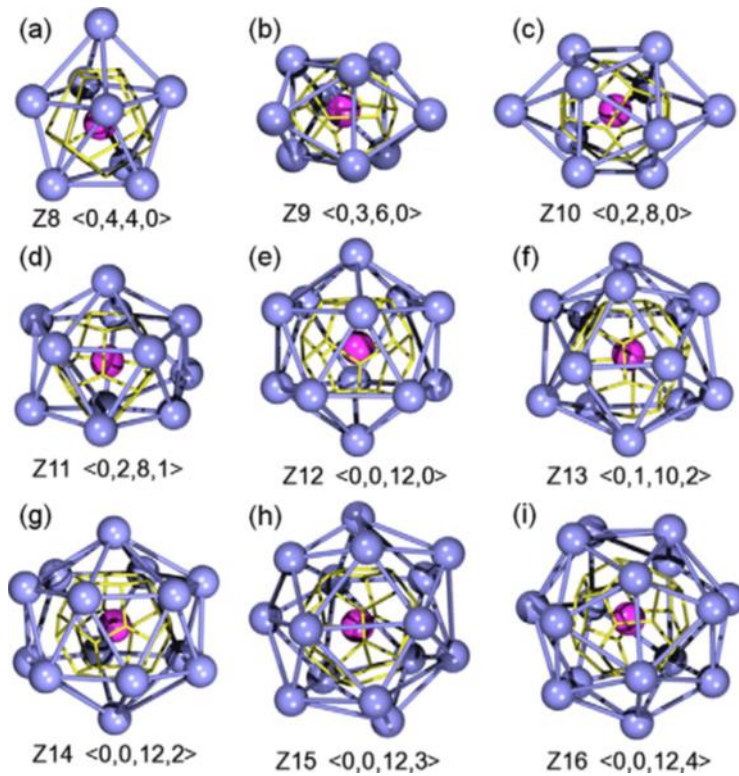


Figure 2.2: Clusters-indexed Voronoi cells consist of varying numbers of local Voronoi polyhedra. Reprinted from Ref. [25].

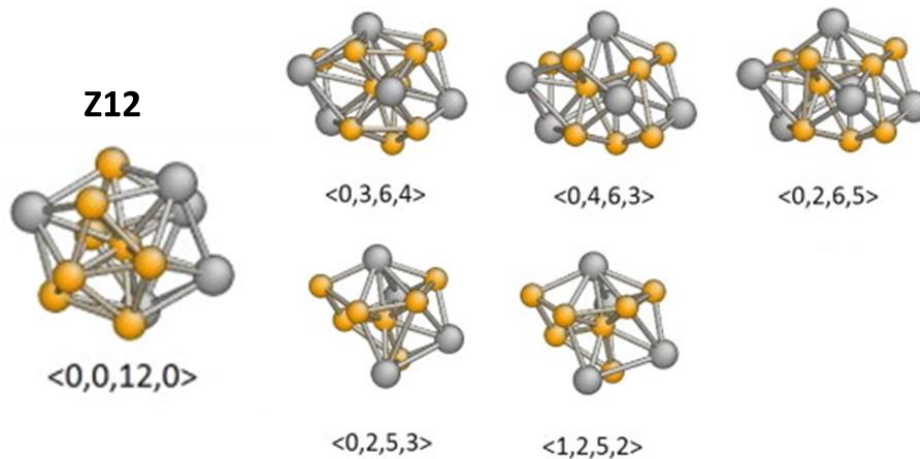


Figure 2.3: Distorted Z12 clusters due to topological restrictions. Voronoi tessellation allows for cluster distortion with deviations in atomic bond lengths by altering the coordination number. Examples include the Z12 cluster being distorted to $\langle 0,3,6,4 \rangle$, $\langle 0,4,6,3 \rangle$, $\langle 0,2,6,5 \rangle$, $\langle 0,2,5,3 \rangle$, as $\langle 0,1,5,2 \rangle$. Reprinted from Ref. [21].

The model does not restrict the atoms to be positioned at a certain interatomic distance and provides a realistic atomic structure of metallic glasses. The results indicate that metallic glasses exhibit not fully disordered atomic arrangements, but rather a certain degree of chemical and topological order, such as short-range order (SRO) and medium-range order (MRO).^[48-49] It is believed that SRO mainly arises from topological restrictions aimed at achieving high packing density, while MRO generally incorporates the chemical affinity between elements.^[50-52]

Experimental techniques, including X-ray absorption fine structure (EXAFS), nuclear magnetic resonance (NMR), and differential scanning calorimetry (DSC) analysis, have confirmed the presence of strong chemical order in various metallic glasses.^[53-57] In particular, Gaskell et al. conducted X-ray powder diffraction and observed a direct correlation between chemical bonding and MRO in metal-metalloid glasses.^[48] The local order of metallic glasses varies significantly depending on their elemental composition.^[25] While the soft sphere model, combined with experimental verifications, successfully describes the structure of some binary metallic glasses, it encounters difficulties in accurately representing multi-component metallic glasses due to the discrepancy in pair potentials among different elemental species.^[58]

Voronoi tessellation was proposed as a means to understand the topological basis of metallic glasses and has become a widely used method for quantifying the local atomic arrangement in various kinds of metallic glass systems.^[59] Voronoi tessellation mathematically standardizes the 3D atomic packing by dividing the space around each atom into regions using partitions. The resulting unit cell enclosed by these partitions is known as the Voronoi cell.

This method provides a clear determination of the number of involved atoms and polyhedra. By employing a vector with four numbers, $\langle i_3, i_4, i_5, i_6 \rangle$, the Voronoi cell describes the total number of triangles, quadrangles, pentagons, and hexagons in the Voronoi polyhedron. Thus, the sum of these numbers directly indicates the coordination number (CN), *i.e.*, the number of nearest neighboring atoms surrounding a central atom. Clusters with CN ranging from 8 to 16 can be represented by their corresponding Voronoi indices, as depicted in Figure 2.2. It has been observed that clusters with the maximum number of i_5 minimize disclinations due to their efficient packing, often referred to as Zwischenkristall (Z) clusters (Z8 to Z16), where the numbers represent the CN. The favored configuration for efficient packing can vary depending on the composition, energetic level, and topological efficiency of the metallic glass.^[60] Voronoi tessellation also allows for the distortion of clusters, exhibiting deviations in atomic bond lengths with a change of CN. For example, the Z12 cluster can be distorted to $\langle 0,3,6,4 \rangle$, $\langle 0,2,6,5 \rangle$, etc., as shown in Figure 2.3. ^{[61-}

^{63]} Each structural motif exhibits specific geometrical and chemical features, with various sharing and overlapping schemes resulting in different degrees of S/MRO.^[64-68]

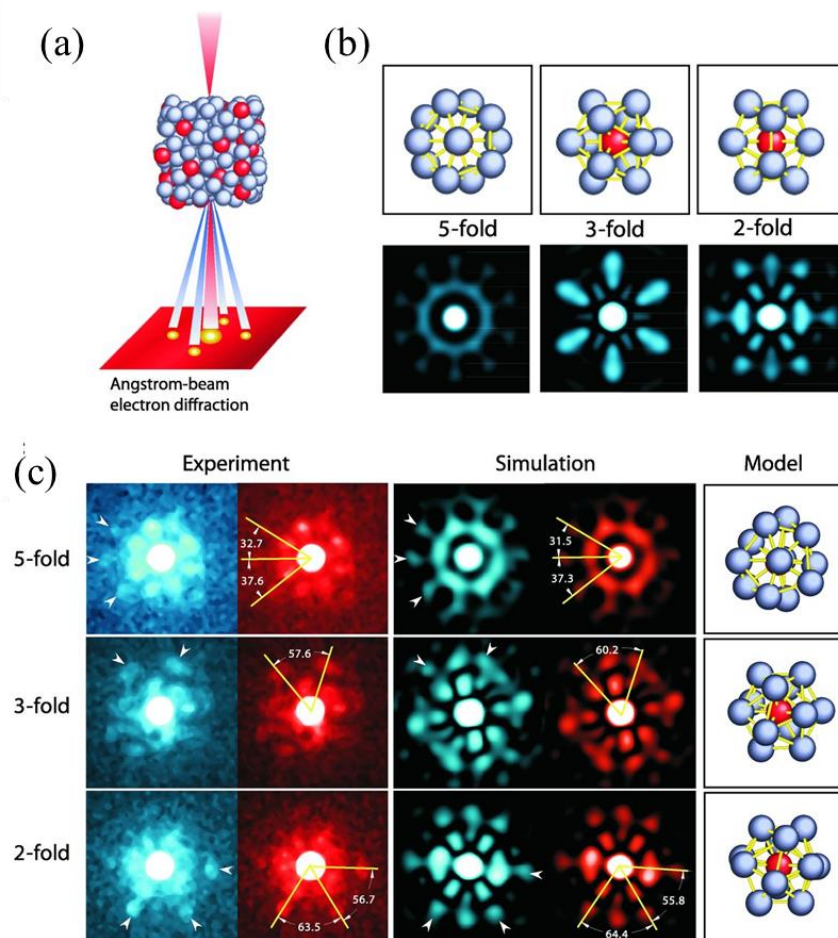


Figure 2.4: (a) The process followed in NBED of an icosahedral cluster, utilizing a coherent electron beam with a diameter of 0.36 nm. (b) Simulated NBED patterns illustrating an ideal icosahedron. (c) Comparison between experimental and simulated NBED patterns for icosahedral clusters within a $Zr_{80}Pt_{20}$ metallic glass. Angular details between individual diffraction vectors are displayed on the right side of each segment for comparison. The distinctive diffraction spots representing icosahedral order are indicated by arrowheads. Reprinted from Ref. ^[34].

An experimental determination of the atomic structure of such amorphous materials has posed a persistent challenge due to the absence of long-range translational and rotational symmetry, rendering conventional approaches unsuitable. To address this issue, Hirata et al. employed NBED to analyze the local icosahedral arrangement within a representative $Zr_{80}Pt_{20}$ metallic glass, as depicted in Figure 2.4.^[34] Multiple NBED patterns were captured from the edge of an ultra-thin TEM foil (~3 nm). They observed individual polyhedra in on-axis orientation and their investigation showed the existence of a substantial portion of projected structures with icosahedra symmetry as predicted by computational simulations. The authors proposed that similar polyhedral

structures aggregate within localized zones giving rise to structural heterogeneities within the glass matrix such as stable and less stable regions. However, despite these claims, none of the acquired NBED patterns precisely matched the simulated icosahedron patterns illustrated in Figure 2.4b. Instead, the obtained NBED patterns exhibited only partial resemblance to those of the five-, three-, and twofold orientations (Figure 2.4c). Hirata et al. attributed this discrepancy to distorted icosahedral structures, where the preservation of icosahedral order was only partial. Moreover, structural modifications due to surface relaxation and sample preparation artifacts in the ultra-thin films have not been considered.

The local atomic arrangement is not uniform throughout the material, owing to packing frustration caused by different size ratios, chemical affinities, or negative heat of mixing between atomic species.^[69] Studies indicated that metallic glasses exhibit heterogeneous packing at the nanoscale, with intermixing of more stable (solid-like) and less stable (liquid-like) regions within the overall glassy matrix. These regions are often referred to as geometrically favored motifs (GFM) and geometrically unfavored motifs (GUM).^[70] Typically, the stable region is characterized by efficient and dense polyhedral packing with minimal distortions, while the less stable region consists of unfavorable motifs with more free volume and distortions.^[71] Huang et al. demonstrated that GFMs centered at Pd atoms form a percolated chain, resulting in a high Young's modulus and yield strength in Pd-based metallic glasses.^[72] The spatial variation in local atomic structure has been identified as a key structural descriptor determining material properties.^[73-78]

Modification of the distribution of GFMs and GUMs can be achieved through various thermal processes, such as varying cooling rates and annealing temperature/times,^[79-81] which induce relaxation processes and tune the local atomic structure of metallic glasses. The potential energy landscape approach has been employed to gain insights into the relaxation dynamics of metallic glasses.^[82-83] This approach describes the many-body potential energy as a function of the configurational coordinate. Figure 2.5 illustrates a typical potential energy landscape of a metallic glass. The potential energy fluctuates along with the collective configurational coordinate, forming local minima, basins, and metabasins, each with corresponding energy barriers that represent the cost of atomic displacement.

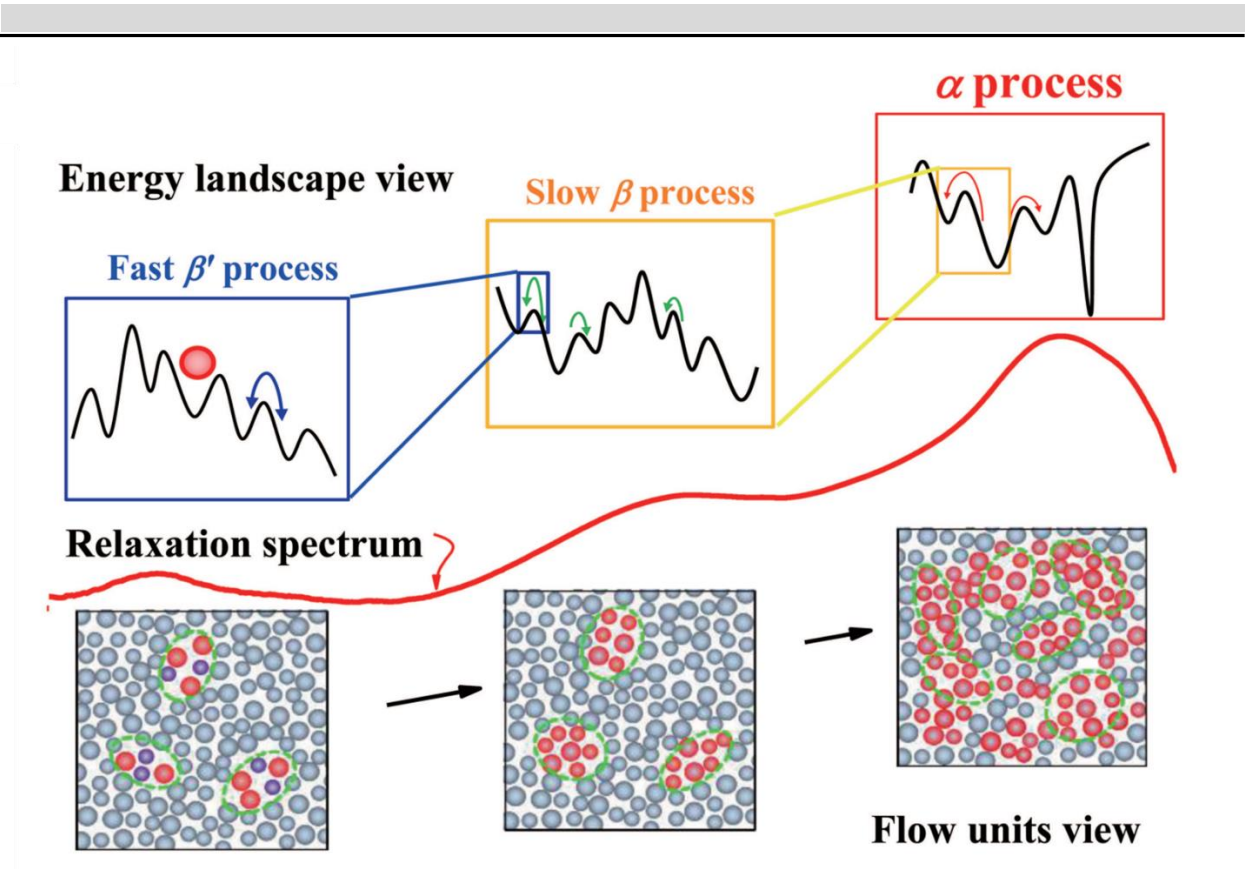


Figure 2.5: Schematic representation of relaxation processes in metallic glasses, depicting the potential energy landscape and atomic configurations. The many-body potential energy is illustrated as a function of atomic distances. Active atoms are represented by red color, and atoms surrounded by green dashed circles represent flow units. Modified from Ref.^[84].

The metabasins capture larger-scale topological fluctuations in the glass structure, while the basins correspond to local heterogeneity within the S/MRO. Under external stimuli such as thermal energy, atoms can statistically undergo displacements onto both unstable and stable coordinates, provided that the energy is sufficiently high to overcome adjacent barriers. The relaxation of metallic glass can be divided into primary (α) and secondary (β) relaxations near the glass transition temperature (T_g).^[85] The α relaxation involves diffusion-like atomic motion and is responsible for the vitrification of the glass-forming liquid, leading to the typical glass transition phenomenon. The β relaxation, occurring below T_g with vibrational atomic motions, is the primary source of local atomic rearrangement in the short range within the glassy state. Recent studies have revealed a splitting of the β relaxation into fast and slow components in metallic glasses.^[86] The slow β relaxation has an activation energy proportional to the glass transition temperature with $E_\beta \sim 25RT_g$, where E_β represents the activation energy and R is the gas constant. This corresponds to the well-known Johari–Goldstein (J-G) relaxation.^[87] The fast β' relaxation exhibits much faster dynamics and a lower magnitude of structural change. Unlike the J-G relaxation, the fast β

relaxation does not depend on T_g and appears as a distinct relaxation peak in dynamic mechanical analysis (DMA) responses.^[86] It is believed that the fast β' relaxation originates from a reversible elastic motion of atoms within the amorphous matrix.

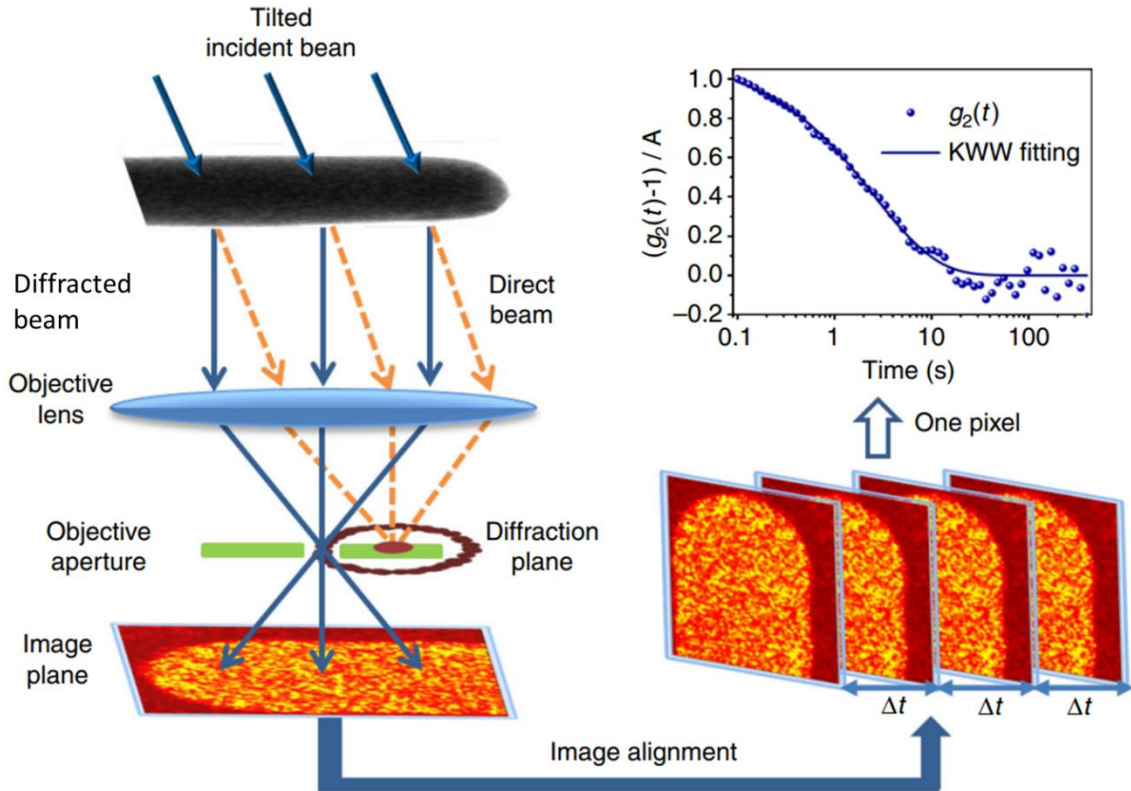


Figure 2.6: Tilted dark-field electron correlation microscopy. (a) Experimental setup: Tilted illumination displaces the transmitted beam from the microscope's optic axis. An on-axis objective aperture selects a specific speckle from the diffraction pattern, forming a real-space image. Intensity fluctuations in image speckles arise from structural rearrangements. A sequence of ~ 4000 dark-field images is captured and aligned to correct sample drift. (b) Computation of the time autocorrelation function $g_2(t)$: Intensity time series at each pixel yields $g_2(t)$, which is then fitted to the KWW equation for deriving the relaxation time τ and the stretching parameter β . Modified from Ref. ^[88].

The dynamics of atomic rearrangements within metallic glasses are spatially heterogeneous and encompass diffusion, viscous flow, nucleation, and growth of crystal phases at different time scales.^[89] Electron correlation microscopy (ECM) is an experimental method to investigate the dynamics with nanoscale spatial resolution.^[88] Employing time-resolved dark field imaging, ECM can investigate glass dynamics, similar to X-ray photon correlation spectroscopy (XPCS). For example, ECM analysis of a Pt-based metallic glass nanowire revealed relaxation dynamics with sub-nanometer spatial precision, as depicted in Figure 2.6.^[88] A sub-nanometer-thick near-surface layer was identified, which exhibits dynamics significantly faster than the bulk. The authors

emphasized the potential influence of this layer on wire crystallization. However, a complete understanding of this phenomenon remains elusive, and questions persist regarding the impact of the electron beam and sample thickness on these observations.

2.2. Elastic deformation

The primary response of a solid-state material to applied stress is elastic deformation. In the initial stages of deformation, typically at low strains, the material exhibits fully reversible behavior following Hooke's law, known as the elastic response.^[90] However, at larger strains beyond the elastic strain limit, the reversibility of the strain deviates, indicating the onset of non-linear and inelastic behavior in the material. Metallic glasses exhibit exceptional elastic limits of above 2%, which can be recovered during macroscopic loading and unloading experiments. This surpasses conventional crystalline alloys with limits below 0.2%.^[6, 91] The high elastic limit in metallic glasses is attributed to the absence of a crystal slip system, which results in the presence of rigid stereochemical units and high-energy barriers for plastic flow. Nevertheless, studies have shown that the elastic behavior of metallic glasses is not fully reversible at the atomic scale. Localized nonaffine atomic displacements occur during the elastic regime, which relieves long-range stresses that have built up in the material. Due to the disordered nature of metallic glasses, each atom possesses a unique atomic environment, and they exhibit inhomogeneous elastic/inelastic responses at different locations.^[92] The response of individual atoms can vary during the loading and unloading process, leading to a more complex elastic deformation.^[93] Consequently, the local atomic structure of metallic glasses significantly influences both their elastic behavior and subsequent plastic deformation.

2.3. Initiation of plastic deformation: shear transformation zone

The initiation of plastic deformation in metallic glasses occurs through deviatoric and shear strain, which leads to an anisotropic shape change and local distortion in the material. Unlike crystalline materials, amorphous materials like metallic glasses do not exhibit well-defined defects such as dislocations due to the absence of a crystallographic slip system. Different type of defect has been proposed to explain plastic deformation in metallic glasses.^[94-95] Argon introduced the concept of shear transformation as the primary plastic event in metallic glasses.^[94] Shear transformation refers

to a situation where a group of atoms surpasses the saddle point of the potential energy landscape in response to shear stress.^[96-97]

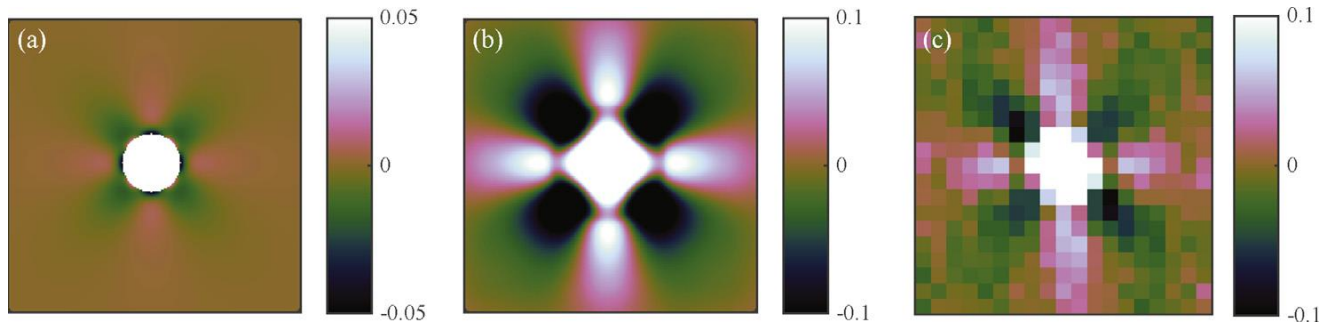


Figure 2.7: STZ structure with the strain field around it (a) Calculated shear strain field at STZ subjected to a strain of 0.05. (b) Autocorrelation function of (a). (c) Experimentally measured self-correlation of the strains in a colloidal glass. Reprinted from Ref. ^[98].

During loading, non-affine atomic motion defines a local zone known as the shear transformation zone (STZ).^[99] Simulations by Maloney et al. on a 2D glass under athermal quasistatic loading identified STZs as transient defects within the glassy matrix, causing stress concentration in their vicinity.^[99] Jensen et al. demonstrated the stress field surrounding a void in a colloidal glass and observed an inclusion with an Eshelby-like behavior, inducing an inhomogeneous strain field with a quadrupolar geometry as shown in Figure 2.7.^[98] The stress field is concentrated at the center of the inclusion and gradually diminishes, resulting in an unclear boundary.

Thermal energy can locally activate non-affine atomic displacement, contributing to a thermal background that smears out the spatial correlation of the authentic plastic event particularly for the atoms near the edges of the quadrupolar strain field. Argon et al. employed a model for the thermal background and estimated the size of STZs to be a few hundred atoms.^[100] Zink et al. determined the STZ size to be approximately 1.5 nm in diameter, corresponding to around 120 atoms, by measuring non-affine atomic displacement in a modeled Cu-Ti metallic glass. The authors claimed that each STZ appears with a quantized size and discrete activation energy.^[101] However, Delgu et al. disputed the idea by showing a wide size distribution of STZs involving a range of atoms (10-100) with an activation energy of 20-200 kJ mol⁻¹ in Ni-Zr metallic glass.^[102-103] Recent studies converge on the fact that the activation energy and size of STZs are not fixed values but can vary over a wide range and exhibit various morphologies in different metallic glasses, depending on the applied stress, strain rate, and energy state of the material.^[104-108]

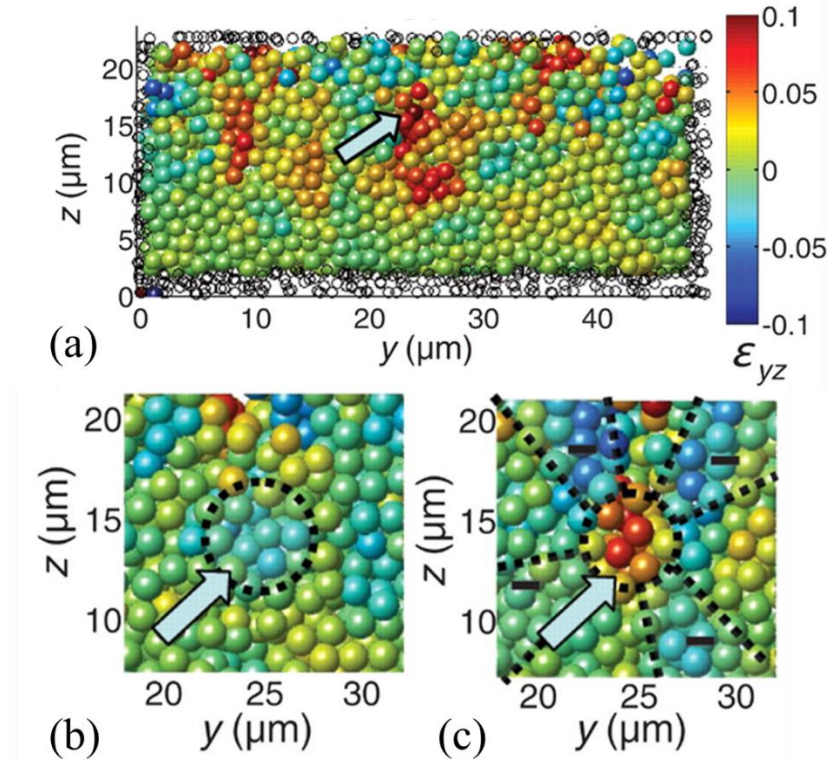


Figure 2.8: STZ formation in a colloidal glass as a response to shear strain in a colloidal glass. (a) Strain distribution and shear transformation zones in the sheared glass. Particle color indicates the value of the local shear strain. (b) before shear load. (c) after shear load. The dashed zone indicates a circular zone with high positive shear strain. Dashed straight lines delineate four regions of negative shear strain that surround the high shear strain zone in the center. Reprinted from Ref. [109].

Experimental efforts have been dedicated to providing direct evidence for the STZ theory in glasses.^[110-113] On average, these studies have revealed a reduced density of metallic glasses after plastic deformation, attributed to an increase in free volume, and attributed it to the activation of STZs. Schall et al. imaged STZs in a colloidal glass using confocal microscopy, where a highly concentrated strain field forming an inclusion was observed, matching the simulated STZ structure as shown in Figure 2.8.^[109]

In the colloidal glass experiment, a typical STZ consisted of approximately 20 colloidal particles, with the STZ size growing up to around 20 μm and an activation energy of approximately 20 kT. This experimental observation verified the STZ-based deformation theory of a colloidal glass derived from atomic modeling. However, The STZs found in metallic glasses are expected to exhibit differences compared to those in colloidal glasses, primarily because of the presence of interatomic interactions. These interactions play a critical role in the deformation behavior of atomic glasses.^[82] However, the limited spatial resolution of the microscopy hinders the structural characterization of individual STZs in metallic glasses. A comprehensive investigation of the

atomic structure at STZs in atomic/molecular glasses is currently lacking due to the difficulties in experimental characterization for the nanoscale volume within the amorphous matrix. This limitation hampers the current understanding of STZ-based deformation theory in the context of initiating metallic glass deformation.

2.4. Formation of shear bands

During the plastic deformation of metallic glasses at room temperature, large strains are accommodated through the formation of shear bands.^[8] The shear bands are thin zones that appear in materials experiencing catastrophic failure. They constitute the major mechanism of plastic deformation in metallic glasses attributed to their inherent work-softening behavior. Work-softening behavior is a common characteristic of glass during plastic deformation, wherein plastically deformed regions become softer and more prone to subsequent plastic flow. The work softening in metallic glasses is influenced by two distinct sources: thermal and geometrical origins. The thermal origin involves the local melting of the material due to heat generation during shear banding. This leads to the formation of a local molten zone that exhibits a low flow barrier, which in turn contributes to the softening phenomenon. The geometrical origin, on the other hand, is related to the excessive free volume induced by plastic strain, leading to mechanical softening.^[14] The softened zone readily accommodates further plastic deformation. This work-softening behavior leads to the autocatalytic localization of strain, causing it to concentrate within a thin band. Shear bands in metallic glasses operate rapidly because they lack a microscale structure to impede the propagation of shear bands. Consequently, their catastrophic formation results in limited ductility and abrupt failure of metallic glasses, particularly when subjected to tension.^[15]

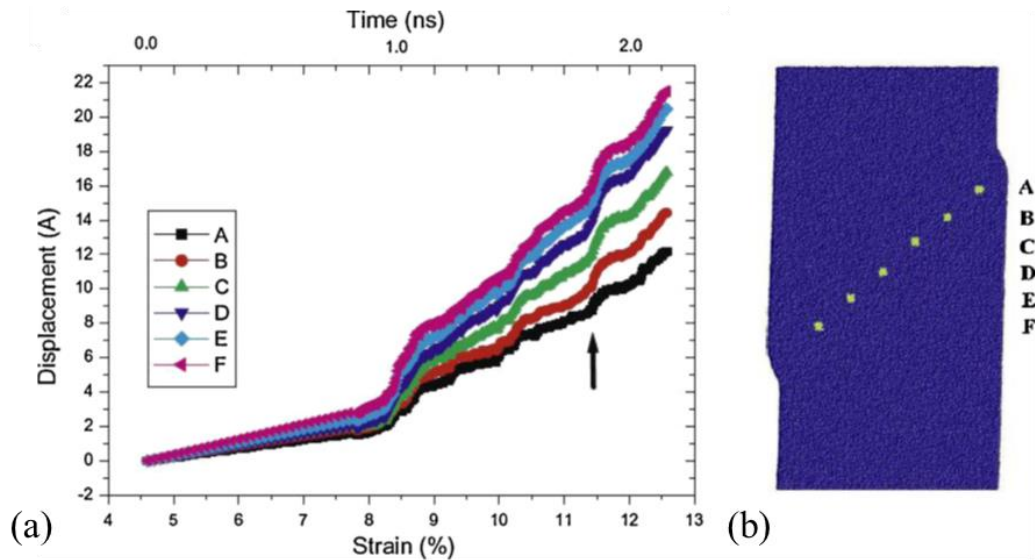


Figure 2.9: The synchronized sliding for the nucleation of shear bands in metallic glasses. (a) Displacement as a function of strain, showing the jumps in displacement (b) at the six points along the band. The figures are reprinted from Ref. [21].

Two mechanisms have been proposed for the nucleation of shear bands in metallic glasses at an atomic scale.^[8] The first mechanism involves the percolation of STZs, where a sufficiently large population of activated STZs percolates along a viable plane with maximum shear stress. This plane becomes softened due to the increase in free volume and preferentially accommodates subsequent strain, leading to the formation of a shear band.^[116] In this case, the planer plastic zones are believed to behave in a synchronized way and directly lead to the formation of a percolated shear band as shown in Figure 2.9.^[117] The nucleation of a shear band would be governed by the activation energy of all synchronized STZs on the shear plane and the capacity for accommodating STZs in the glassy matrix.^[117] This scenario illustrates the homogeneous nucleation of a shear band in a metallic glass, signifying that the shear band forms due to inherent structural fluctuations within the amorphous material itself. This phenomenon has been widely observed in various simulations, particularly those applying periodic boundary conditions.^[118]

The second mechanism describes a time-dependent progression of a shear band similar to stick-slip dynamics in crystalline materials.^[119] The stage involves the activation and localization of an STZ. The structural perturbation generated by stress concentration at the leading STZs triggers the activation of neighboring STZs via rotational shear fields, propagating as a shear wave as shown in Figure 2.10.^[120]

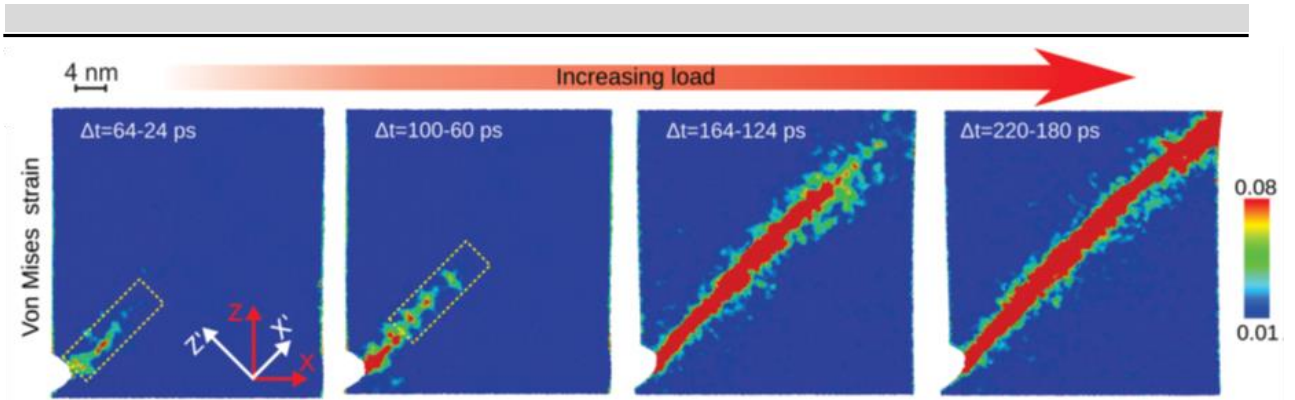


Figure 2.10: Time-dependent progression of a shear band. Structural variations are depicted by Von Mises strain in the simulated metallic glass during the early stages of shear banding. The figures are reprinted from Ref. ^[120].

In this scenario, the formation of a shear band is viewed as a two-stage process. The first stage involves the creation of a viable band with strain concentrations, while the second stage entails synchronized sliding and shearing along the band. It is important to note that the exact mechanism of shear band initiation in metallic glasses is a complex and active area of research. It is believed that factors such as the material composition, temperature, loading rate, and history change the initiation process.

Shimizu et al. associated the formation of shear band to thermodynamics, in which, the stage involves shear displacement of the rejuvenated planes, accompanied by significant heat generation.^[20] The authors proposed that the atoms on the rejuvenated plane become mobile and easily accommodate the plastic flow. The formation of a shear band is completed with the shear displacement of the rejuvenated planes. Shi et al. simulated the potential energy as a function of strain during shear banding and observed the structural rejuvenation along the shear band.^[121] The shear banding process turns the potential energy landscape to be in a higher energy state. Other simulation results also show that the shear banding is accompanied by a significant reduction in the number of icosahedral and an increase in the free volume along the band.^[10, 22-23, 122-124] Cao et al. observed significant heat generation during the shear displacement through friction.^[21] They proposed that the structure of a shear band during its formation is divided into four different zones: liquid-like zone, alienated glass zone, rejuvenated zone, and aged glass zone. The propagation of shear bands generates heat, which in turn influences the subsequent deformation, creating a liquid zone within the shear band. As a result, there is structural disordering and dilation at the front of the shear band. This change in the potential energy landscape leads to a higher energy state. The displacement of the shear planes continuously contributes to heat generation. This localized heat generation further facilitates the final stage of shear banding forming liquid zones along with the

shear band.^[114] Consequently, the formation of the liquid zone accelerates subsequent deformation.^[19, 125-126]

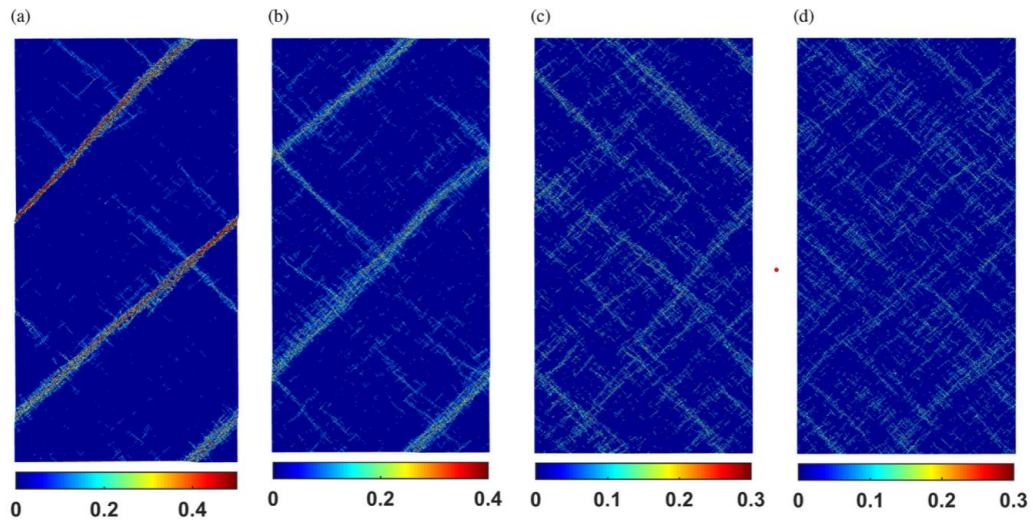


Figure 2.11: Influence of nanoscale structural heterogeneity on shear banding in metallic glasses. Shear band generation in a metallic glass with different amounts of the STZ volume fractions (a) 0%, (b) 10%, (c) 20%, and (d) 30%. Reprinted from Ref. ^[127].

Efforts have been made to enhance the deformability of metallic glasses through structural modifications, such as different cooling rates,^[127] ion implantation,^[128] and mechanical/thermal processing.^[15, 129-130] These modifications can promote multiple shear band formation, resulting in more delocalized plastic deformation and enhanced ductility in metallic glasses. In particular, Liu et al. observed superplasticity (~160 %) of a Zr-based bulk metallic glass at room temperature with the development of heterogeneity within the glass matrix after HPT processing.^[131] The induced heterogeneity provides initial sites for STZ nucleation and shear band formation, leading to the multiplication of shear bands during subsequent deformation.^[132-135] This suppresses the formation of a single dominant shear band traversing the entire glassy matrix and enhances ductility. Modeling studies have supported this concept, showing that heterogeneous metallic glasses exhibit higher ductility due to the enhanced deformability of the glass matrix.^[136-137] The influence of initial structural heterogeneity, characterized by STZ volume fractions, on the multiplication of shear bands in metallic glasses has been investigated as shown in Figure 2.11. The results show that denser shear band networks are formed under loading in metallic glasses with higher STZ volume fractions indicating more delocalized plastic deformation.

2.5. Experimental observation of shear bands

Experimental efforts have been undertaken to validate the proposed mechanisms of shear band formation through atomic modeling. Han et al. observed vein patterns on the fracture surfaces of deformed metallic glass using SEM.^[138] They attributed these irregular patterns to local melting caused by an increase in temperature during shear banding. Notably, these vein patterns were not observed in small samples where shear banding was confined to a small volume, preventing a significant temperature increase owing to surface relaxation. The presence of vein patterns was only observed in samples beyond a critical size.

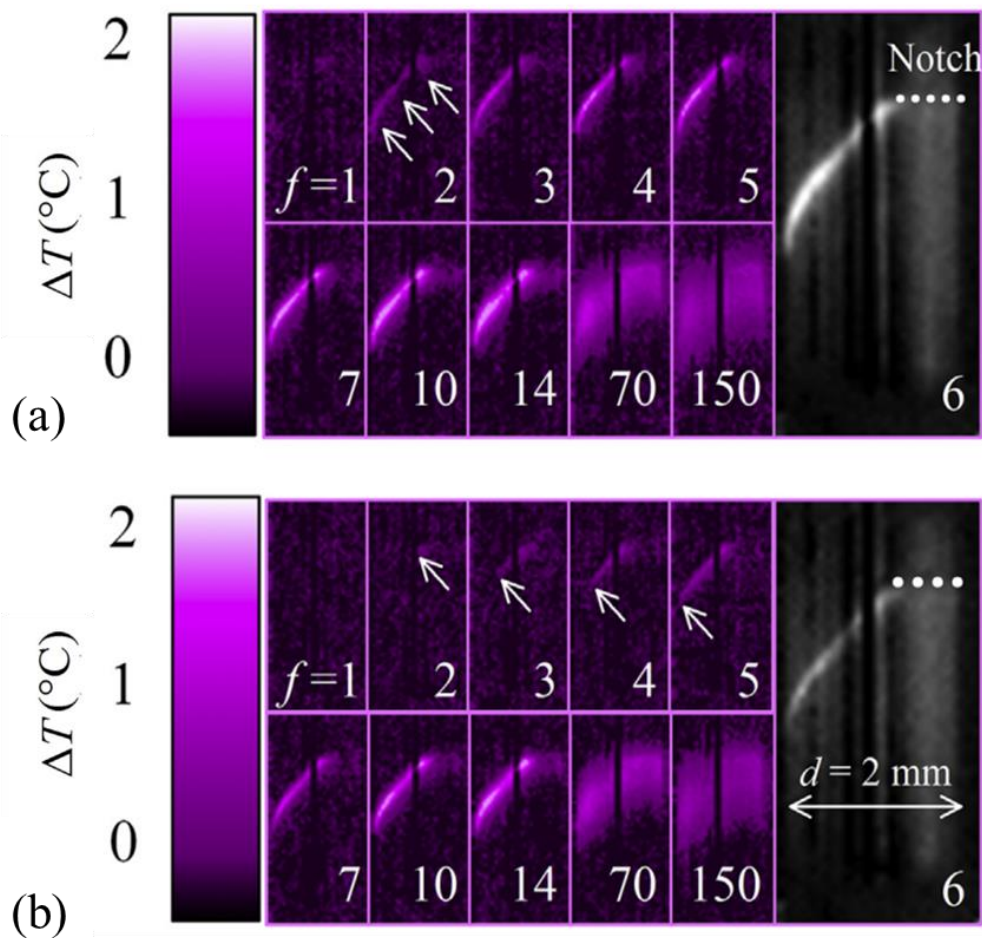


Figure 2.12: Heat generation during shear banding observed by infrared (IR) thermography. (a) The instantaneous appearance of the shear band, and (b) propagating heat front; Numbers indicate the frame number, whereby one frame is measured within 0.4 ms. Reprinted from Ref. ^[139].

Infra-red (IR) thermography has been employed to directly detect temperature changes during shear banding in metallic glasses. In these measurements, a temperature increase over a spatial range of approximately 0.1 mm was detected as shown in Figure 2.12.^[139-140] The limited temporal

resolution of the technique necessitates extrapolation to estimate the actual temperature increase, which was found to be in the range of 650 - 1200 K. Such temperatures are sufficiently high to induce local melting of the metallic glass.

Meanwhile, Spaepen et al. observed the formation of shear bands without generating heat, known as cold shear bands, which challenged the notion that temperature increase is the cause of work softening in metallic glasses.^[141] The authors attributed the different types of shear bands to two distinct formation mechanisms: stress-driven formation and diffusional annihilation formation processes. However, the understanding of these different observations is still under discussion. Shear bands have been investigated using differential thermal analysis (DTA)^[142] and positron annihilation spectroscopy (PAS).^[16-17] These studies revealed that severely deformed metallic glasses have a significantly higher amount of free volume compared to as-prepared samples.^[142] Experimental observations demonstrated the formation of nanovoids within shear bands, indicating large volumetric dilatation within the shear band.^[143] Diffraction techniques such as synchrotron X-ray diffraction^[14] and neutron diffraction^[15] also showed structural dilatation in severely deformed metallic glasses. Yuvari et al. quantified an increase in free volume of approximately 10% in a metallic glass foil using synchrotron X-ray diffraction, based on the shift of the first peak position of the structure factor.^[144] This observation suggests a volumetric dilatation within the metallic glass after plastic deformation. Additionally, Kanungo et al. conducted SEM observations on deformed metallic glasses and discovered nanometer-sized open volumes.^[16] They found that the size of these open volumes correlates with the energy state of the glass before plastic deformation. In metallic glasses with a high-energy state, small free volumes are present in high concentrations and are widely distributed throughout the material. In contrast, relaxed metallic glasses with a low-energy state exhibit larger free volumes that are sparsely distributed. SEM images of fracture surfaces of metallic glasses in a high-energy state display a more rough and uneven surface compared to relaxed glasses.^[145] This roughness indicates the presence of small voids or open volumes within the material. However, it is important to note that SEM-based techniques are primarily limited to providing information about surface morphology and cannot offer detailed structural information inside shear.

On the other hand, other studies have reported the densification of atomic packing after plastic deformation in metallic glasses. Dmowski et al., for example, found both closer and looser atomic packings using neutron scattering, indicating a simultaneous occurrence of densification and dilatation.^[15] This finding suggests that the changes in atomic structure during shear bands are more complex than simple pictures proposed by simulations. The discrepancy in the observations highlights the complexity of understanding the atomic-scale mechanisms governing plastic

deformation in metallic glasses. Factors such as deformation conditions, sample composition, and specific experimental techniques are believed to influence the observed changes in free volume and atomic packing. Further research is needed to reconcile these contrasting findings and obtain a comprehensive understanding of the deformation behavior of metallic glasses. However, conventional diffraction techniques, such as X-ray diffraction, have resolution limitations that prevent them from providing a detailed depiction of the local atomic arrangement inside shear bands.

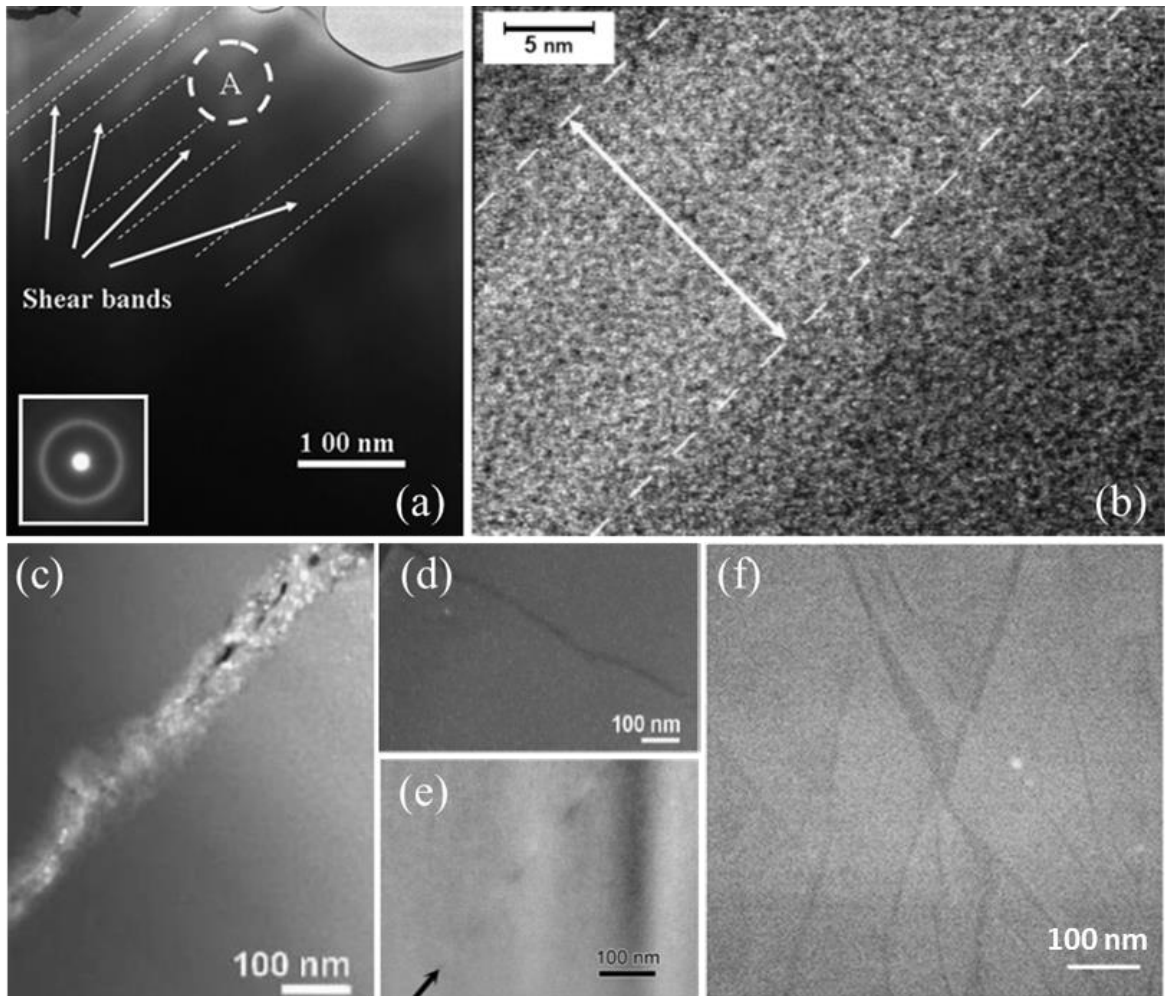


Figure 2.13: TEM observation of shear bands: (a) a bright-field TEM image near a fracture surface of a Zr-based metallic glass and corresponding selected area electron diffraction pattern reprinted from Ref. ^[26], (b) a high-resolution bright-field TEM image of a shear band in a deformed Fe-based metallic glass reprinted from Ref. ^[27], (c)-(d) dark-field TEM images of deformed Cu-based metallic glasses reprinted from Ref. ^[28], (e) HAADF-STEM image of a deformed Pd-based bulk metallic glass sample showing contrast reversals inside a shear band reprinted from Ref. ^[29], and (f) HAADF-STEM images of shear bands of a Zr-based metallic glass reprinted from Ref. ^[30].

TEM has been a powerful tool offering enough resolution to directly examine the core structure of shear bands. Some authors captured TEM images of a severely deformed region near a fracture surface as shown in Fig. 2.11.^[26-31] They use dashed lines to indicate shear bands, however, upon reviewing TEM images, it is evident that the features do not exhibit the characteristic linear band structure typically associated with shear bands in metallic glasses. Moreover, it turns out that the observed structure and geometry of the shear bands were not consistent among observations. It is crucial to consider the limitations of conventional TEM imaging when interpreting the shear band features. The amorphous nature of metallic glasses strongly limits the information gained from the direct imaging method and poses challenges in obtaining accurate structural information using conventional TEM techniques. The linear features observed in the images could potentially be artifacts caused by thickness fluctuations, residual aberrations, or other experimental factors rather than genuine shear bands.

Kumar et al. observed significant crystallization along a shear band in a Cu-based metallic glass, as shown in Figure 2.13c.^[28] The authors suggested that crystallization during shear banding enhances plasticity, considering the negligible crystallization observed in a relaxed metallic glass (Figure 2.13d). However, to validate their interpretation, it would be necessary to provide additional evidence supporting the presence of shear bands, such as complementary characterization techniques providing the local atomic structure within these features. Without such evidence, the claim that the observed features are shear bands in metallic glasses remains unsupported. Recently, Schmidt et al. used STEM and observed shear bands exhibiting sinusoidal fluctuations of scattering power along a shear band (Figure 2.13e). The authors related these fluctuations to local density variations and proposed a hypothesis involving the alignment of Eshelby quadrupoles during shear band formation.^[29] However, different types of shear bands have also been observed using STEM imaging.^[30] Some shear bands observed do not exhibit sinusoidal intensity fluctuations but instead, only show reduced scattering power along the shear bands suggesting spatially localized free volume (Figure 2.13f). These dark shear bands display a branching structure, where sub-branches (secondary shear bands) nucleate from the main stem (primary shear band) and form a network of shear bands. The authors noted that this degree of volumetric dilation is similar to the density increase observed during thermal annealing treatment and suggested a relaxation recovery occurring after the formation of shear bands. TEM observations generally agree on the typical thickness of shear bands, ranging from 10 nm to 50 nm. However, it should be noted that conventional S/TEM imaging techniques cannot provide concrete information on the atomic structure of amorphous materials due to the lack of direct information in real or reciprocal space, which poses challenges in directly validating the atomic structure within

a shear band. The existing studies have not conclusively explained why shear bands appear in different types and exhibit various internal structures.

One approach to directly investigate the atomic structure of shear bands in metallic glasses is through electron diffraction patterns acquired from a nano volume using a well-focused electron beam, such as NBED^[146-147] and FEM.^[33, 148] These techniques offer a sufficient resolution to study shear bands and are thus able to experimentally reveal information on the basic atomic configurations. glasses.^[149]

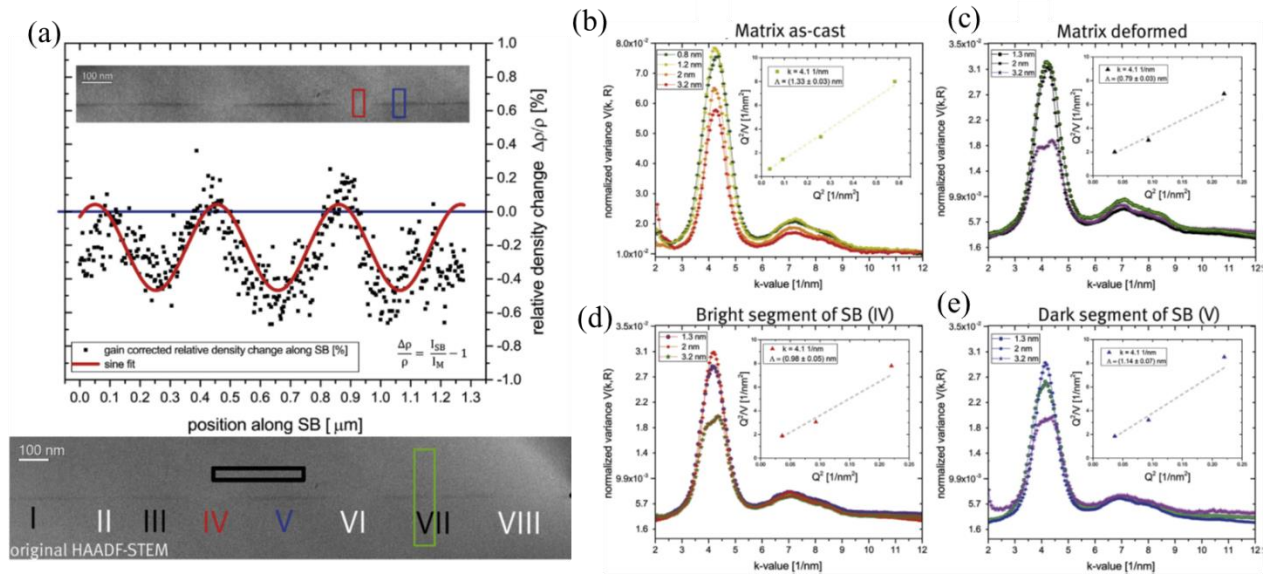


Figure 2.14: FEM analysis of a shear band in a deformed Zr-based metallic glass. (a) HAADF image showing a shear band that exhibits periodical fluctuation of scattering power along the propagation direction. The bright and dark regions on the shear band are numbered I-VIII (bottom). Normalized FEM variance profiles with different probe sizes, 0.8 nm ~ 3.2 nm for (b) as-cast sample, (c) the matrix beside the shear band indicated as a back box in (a), (d) the bright regions of the shear band (IV) and (e) the dark regions of the shear band (V). Reprinted from Ref. ^[149].

FEM measures intensity fluctuations in local electron diffraction patterns obtained from different sample volumes, revealing structural inhomogeneities in amorphous materials.^[33] The technique has been used to study shear bands and has provided evidence for structural variations within shear bands compared to the surrounding matrix. This information can contribute to understanding the short-range order and subtle structural changes in metallic glasses. FEM studies observed the structural changes inside a shear band of a deformed Zr-based metallic glass as shown in Figure 2.14. The results provide clear evidence for structural fluctuations within the shear bands and clear structural differences of the shear bands from the bulk glass matrix. However, it is important to consider the limitations of NBED-based techniques. The NBED studies generally require very thin

TEM specimens (ideally, < 10 nm) for minimal overlap of diffraction features; otherwise, the result suffers from nonlinear degradation. This raises a critical question regarding the extent of structural modification, such as strain relaxation, induced in thin samples due to the increased surface-to-volume ratio and the thinning process. Additionally, these techniques do not directly provide real-space information, and the interpretation of diffraction variations often requires complex simulations, such as reverse Monte Carlo modeling.^[150]

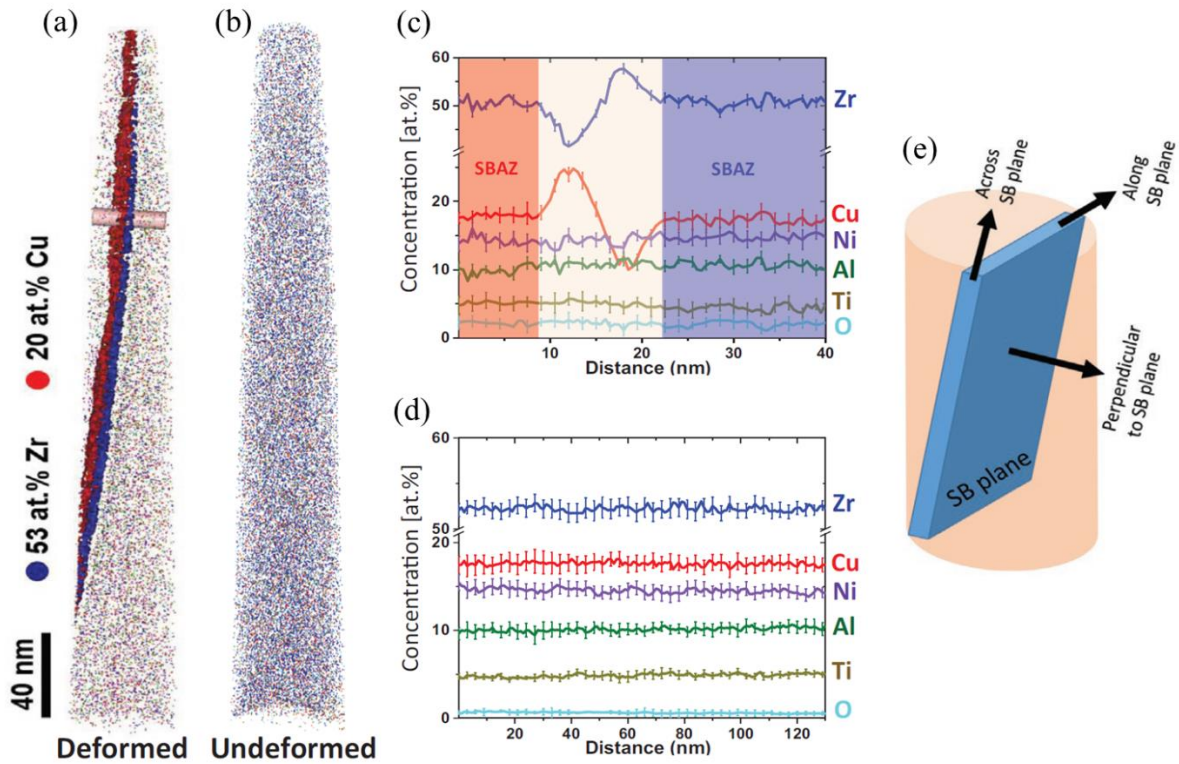


Figure 2.15: Analysis by APT of the deformed and undeformed regions of Vitreloy 105 ($Zr_{52.5}Cu_{17.9}Ni_{14.6}Al_{10}Ti_5$). (a) 3D reconstruction of the deformed sample featuring a shear band. The asymmetric distribution of Cu and Zr across the shear band is visible in the elemental map. (b) The 3D elemental map, along with individual elemental distributions, for the undeformed sample. (c) Composition profile perpendicular to the shear band, extracted from the cylinder in (a). (d) Depth-dependent concentration profile of all elements in the undeformed bulk. (e) Schematic illustrating the plane of the shear band. The figures are reprinted from Ref. ^[151].

Atom probe tomography (APT) enables three-dimensional imaging and chemical analysis at the (sub) nanometer level using tip-shaped specimens. A high voltage is applied to the tip, creating a strong electric field that nearly causes the surface atoms to evaporate. By adding a high-frequency voltage or utilizing a laser pulse, individual ions are evaporated and subsequently detected by a two-dimensional sensor. This sensor, capable of tracking both time and position, employs time-of-flight mass spectroscopy to determine the identity of the evaporated ions. Mu et al.

conducted a study involving APT on a specimen extracted from deformed Vitreloy 105 along a shear band.^[151] The three-dimensional APT reconstruction of the deformed area within Vitreloy 105 displays zones enriched in Cu and Zr along the shear band, whereas the unaffected bulk material demonstrates negligible chemical variation (refer to Figure 2.15a and b). The concentration profile reveals a notable asymmetry perpendicular to the shear band; one side of the shear band is enriched with Cu, while the other side is enriched with Zr. Mu et al. attribute this observation to the repositioning of Cu atoms and their selective segregation, providing greater adaptability for local chemical modifications within the shear band and lowering the energy barrier required to convert from GFMs to GUMs. However, the mechanism by which Cu atoms achieve this asymmetric rearrangement across the shear band was not fully answered and remains an open question.

To tackle the challenges and unresolved queries in characterizing shear bands, Mu et al. recently developed STEM-PDF, a method that uses 4D-STEM to map the local atomic packing of amorphous materials in real space.^[39-41] STEM-PDF offers direct information on atomic packing and is more intuitive for understanding short-range order. The experimental results provide compelling evidence that plastic deformation in metallic glasses leads to a decrease in geometrically favored polyhedral motifs. This deformation-induced structural change is not limited to the shear band itself but extends for several hundred nanometers, forming what is known as the shear band-affected zones (SBAZs). These zones exhibit localized variations in motifs and show antisymmetric segregation of bonds and chemical species. Furthermore, structural and chemical variations within the shear band were observed both perpendicular and parallel to the plane of the shear band by STEM-PDF analysis. Understanding these structural and chemical changes offers valuable insights into the plastic deformation of metallic glasses, particularly in the context of their functional applications and potential future advancements. However, challenges still exist, such as the overlap problem in projection and limitations in detecting subtle structural variations due to the finite collection angle of electron diffraction. Furthermore, recent investigations have raised questions about the energy dissipation and deformation mechanisms within shear bands.

Thermodynamic studies suggest that the energy dissipated within shear bands during the plastic deformation of metallic glasses may exceed their storage capacity. This has led to the suggestion of broad deformation zones surrounding shear bands, which are thought to play a crucial role in energy dissipation. Techniques, e.g., nanoindentation, and X-ray strain mapping have revealed SBAZs extending over micrometers from the shear bands.^[152-156]

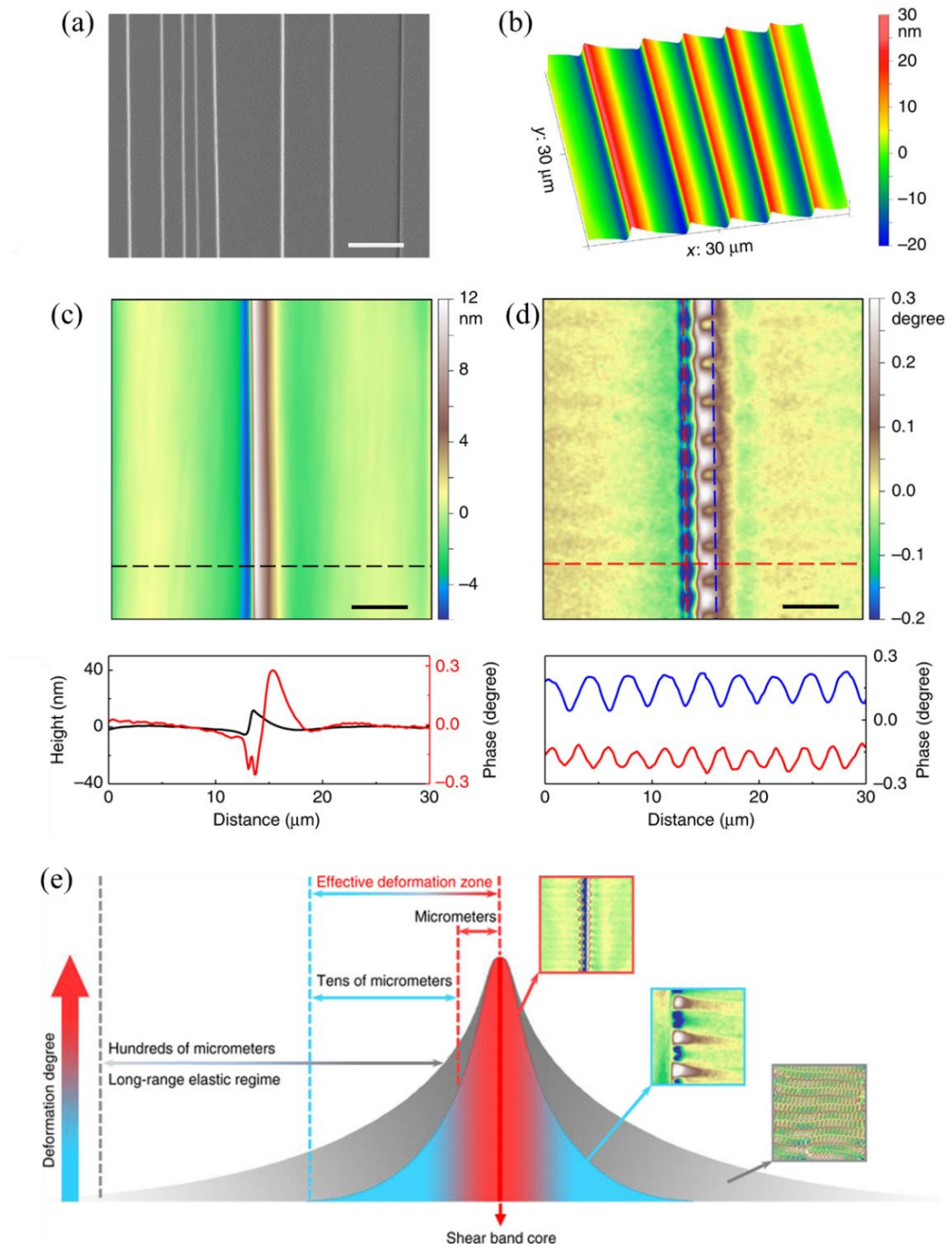


Figure 2.16: Shear-band affected zone in a Fe-based metallic glass observed by AFM and MFM. (a) SEM image of shear bands after bending test. (b) AFM 3D topography of shear bands. (c) AFM topographic image of a shear band with a line scan along the black dashed line and (d) corresponding MFM phase image with a line scan along the red dashed line. (e) Schematic of the shear-band affected zone. The color regions represent the respective deformation zone after shear banding. The gray region illustrates a long-range elastic regime over the hundreds of micrometers (wave-like domain pattern in the MFM image). The blue region represents the extended strain gradient field spanning over tens of micrometers (extending domain pattern). The red region shows the severely deformed zone within tens of nanometers (zipper-like domain pattern). Reprinted from Ref. [156].

Recently, Shen et al. used magnetic force microscopy (MFM) to measure the variation of magnetic domains due to shear banding-induced SBAZ (Figure 2.16).^[157] The SBAZ encompasses a nanoscale shear band, a micrometer-scale severely deformed zone adjacent to the shear band, and an extended strain gradient field spanning tens of micrometers. They concluded that the SBAZ of each band results in shear band interaction through the strain gradient field. However, the specific role and structure of SBAZs have not been sufficiently identified due to technical limitations, impeding a comprehensive understanding of plastic deformation in metallic glasses and the design of new materials.

2.6. Outline of the following chapters

This thesis aims to provide an experimental characterization of the microscopic structure of shear bands in metallic glasses to answer open questions and better understand their formation mechanism. This knowledge will serve as a basis to facilitate new material designs with higher ductility.

As discussed above, previous approaches to experimentally characterize deformation structures in metallic glasses have encountered two major challenges: (1) difficulty in imaging the amorphous structure and (2) dealing with the nanometer-level size of shear bands. To address these challenges, advanced 4D-TEM techniques, such as STEM-PDF and strain mapping, have been developed further and applied to two different metallic glasses: $\text{Fe}_{85.2}\text{Si}_{0.5}\text{B}_{9.5}\text{P}_4\text{Cu}_{0.8}$ and $\text{Zr}_{46}\text{Cu}_{38}\text{Al}_8\text{Ag}_8$, each with different thermal annealing states, before and after mechanical deformation.

Chapter 3 provides a comprehensive overview and basis of the material preparation and characterization methods. This includes an introduction to conventional TEM characterization approaches. Chapter 4 will introduce 4D-STEM techniques and their potential for structural analysis. This includes a range of emerging techniques based on 4D-STEM such as STEM-PDF, strain, and atomic density mapping, and will present the importance of sample thickness for TEM analysis of metallic glasses.

The initial experimental focus was on the characterization of the atomic packing in the undeformed metallic glasses in different annealing states, which is expected to have a substantial impact on their deformation behavior. Disentangling the information mixed for individual nanophases in amorphous materials has been a major problem in characterizing the local amorphous structure as discussed in chapter 2.1. As a new approach to deal with the projection problem, NMF-aided

STEM-PDF analysis has been developed and evaluated, which will be introduced in chapter 5 for phase mapping and to characterize the intrinsic heterogeneity in metallic glasses.

In chapters 6 and 7 the experimental analysis of deformed metallic glasses will be presented and the results are thoroughly discussed to illuminate the intricate relationship between structure and properties. Specifically, chapter 6 will meticulously investigate the structural attributes of individual shear bands as well as Eshelby inclusions within deformed metallic glasses. The results provide direct experimental visualization supporting a concrete scenario for the initiation of a shear band proposed by atomistic simulations. In chapter 7, the focus will be on the larger-scale deformability of metallic glasses by multiplication of shear bands. This chapter will delve into the details of shear band networks and SBAZs, establishing their connection to the overall deformability of metallic glasses. Furthermore, the wear mechanism is explored, bridging the gap between nanoscale observations and the macro-scale material properties.

In chapter 8, the development of a new innovative analytical approach termed Lorentz-4D-STEM will be introduced. This method enables a correlative mapping of magnetic and atomic structures at the nanoscale of soft magnetic glasses.

Finally, chapter 9 summarizes the primary discoveries of this thesis. This chapter will offer a conclusion and insights into potential pathways for future research and advancements within the realm of metallic glasses.

Overall, this thesis encompasses a diverse spectrum of EM techniques for the structural characterization of amorphous materials, the intricate interplay between the structure and properties of metallic glasses, the deformation theory of metallic glasses, and new method developments for characterizing amorphous materials.

Chapter 3

3. Material preparation and characterization methods

In this thesis, a range of experimental methods has been employed to investigate different types of metallic glasses. This chapter serves as an introduction to the methodology employed throughout the study. It provides background information on material and sample preparation techniques, as well as an overview of the characterization methods commonly used in the research. These methods are generally applied across the various subjects addressed in the subsequent chapters. Each chapter then focuses on specific subjects, delving into the experimental details and parameters relevant to those particular areas of investigation. By presenting the methodology in chapter 3 and subsequently providing detailed experimental descriptions in the respective chapters, the thesis ensures a thorough coverage of the experimental methods employed for the study of metallic glasses.

3.1. Material preparation

The primary challenge in manufacturing metallic glasses lies in rapidly cooling a molten alloy to a temperature below its T_g to preserve the glassy structure. During the 1960s, metallic glasses were initially developed in a limited range of shapes, typically with one dimension being extremely thin, to facilitate efficient heat dissipation.^[158] The composition of metallic glasses plays a crucial role in their formability. Compositions that include transition and noble metallic elements, such as Ti, Zr, Au, Pt, and Pd, have garnered attention due to their excellent ability to form metallic glasses. These compositions exhibit high glass-forming ability, meaning that even lower cooling rates can still result in the formation of a glassy structure.^[159] In 1995, Inoue et al. proposed three empirical rules for the fabrication of metallic glasses.^[160] Firstly, the system should be multicomponent, consisting of more than three elements. Secondly, the atomic numbers of the elements involved should exhibit significant differences. Lastly, the heat of mixing between the elemental species should be negative. These rules have significantly accelerated the development of new glass-forming systems, including alloys based on Ni, Fe, Co, and Cu.

Over time, various production methods for metallic glasses have been developed.^[161] These methods can be categorized based on the state of the source materials: liquid-state, vapor-state, and solid-state processes. Liquid state processes involve melt-quenching techniques, where a molten alloy is poured onto or into a cooling medium to enable rapid solidification. Melt-spinning and suction casting are common methods employed for liquid-state processing.^[161] Melt-spinning utilizes a rotating metallic wheel as the cooling medium onto which the molten alloy is jetted, facilitating rapid quenching and solidification of the molten alloy as shown in Figure 3.1a. This process results in the formation of thin ribbons, with cooling rates reaching up to 10^6 K/s due to the high rotation speed of the spinning wheel. However, it is important to note that the solidification process using spinning wheels imposes limitations on the shaping possibilities of the resulting material. Suction casting is a manufacturing method commonly used to produce bulk metallic glasses with favorable shaping possibilities. It involves a die-casting process combined with a suction step. In this method, a vacuum system is employed beneath the casting chamber to lower the pressure within the metallic mold. This reduced pressure facilitates the molten alloy being drawn into a cooled mold, as depicted in Figure 3.2b. Suction casting has been successfully utilized to produce large-diameter rods of Pd-based metallic glass exceeding 80 mm in size.^[162] However, it is important to note that suction casting is not suitable for metallic liquids with high viscosity, such as Ni-based metallic glass, which hinders the rapid flow of the liquid into the mold.

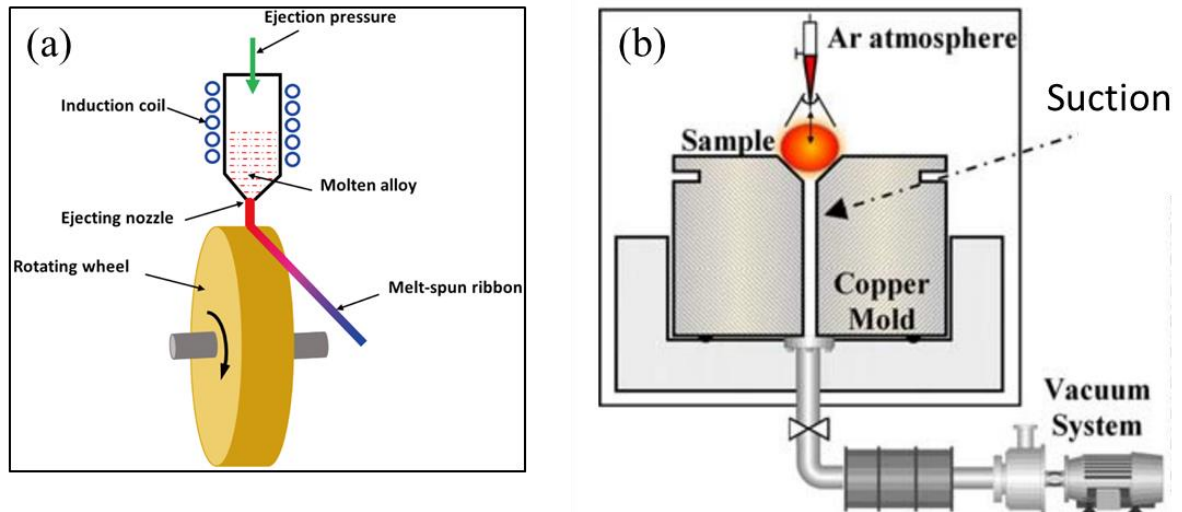


Figure 3.1: Schematic illustration of (a) a single-roller melt-spinning and (b) suction casting. Reprinted from Ref. ^[161] and Ref. ^[163].

As a result, alternative processing techniques need to be employed for such alloys. Another limitation of the suction casting method is the variation in cooling rates experienced by metallic glasses during solidification, leading to a significant difference in cooling rates between the surface and the core of the cast product. This discrepancy in cooling rates gives rise to substantial residual stress, which adds complexity to the amorphous structure of the material. This phenomenon must be considered when analyzing and characterizing the properties of suction-cast metallic glasses.

Vapor state processes are commonly employed for the fabrication of thin-film metallic glasses (TFMG). These processes involve vaporizing the target material and depositing it onto a substrate in the form of a thin film.^[164] By carefully adjusting environmental parameters such as substrate temperature, sputtering rate, and gas atmosphere, the amorphous phase can be achieved during the deposition process. Vapor state processes can be classified into three main categories: physical vapor deposition (PVD), chemical vapor deposition (CVD), and ion implantation. In PVD, the target material is vaporized through physical means, such as heating or bombardment, and then deposited onto a substrate. In CVD, the target materials are decomposed by exposure to a chemical reagent, and the resulting species are deposited onto a substrate by controlling the chemical environment. Ion implantation involves the ionization of atoms in the target material, and the ionized atoms are then directly deposited onto a substrate by applying an electric field, forming a thin film.

Solid-state processes, on the other hand, are based on mechanical alloying, similar to powder metallurgy techniques. In this approach, amorphous or nanocrystalline metallic powders are blended and compacted in a container, often with rotation, to achieve a high packing density. The

severe plastic deformation experienced during this process leads to the accumulation of defects and the introduction of structural disorder (amorphization). This, in turn, gives rise to various metastable phases, such as supersaturated solid solutions. By employing these different manufacturing methods, metallic glasses can be produced in various forms, including bulk shapes through suction casting, thin films through vapor-state processes, and metastable phases through solid-state processes. Each method offers unique advantages and limitations, making it crucial to select the appropriate technique based on the desired properties and applications of the metallic glass material.

Master alloys	Production methods	Sample dimensions	Sample provider
Fe_{85.2}Si_{0.5}B_{9.5}P₄Cu_{0.8} (at.%)	Melt spin quenching, Scratch testing	Ribbon (25 mm width and 20 μm thickness)	TU Darmstadt (Prof. Karsten Durst)
Zr₄₆Cu₃₈Al₈Ag₈ (at.%)	Water-cooled copper mold casting, Scratch testing	Bulk plate (1 cm × 1 cm and 1 mm thickness)	Koreatech (Prof. Arnaud Caron)
Zr_{52.5}Cu_{17.9}Ni_{14.6}Al₁₀Ti₅ (at.%)	Water-cooled copper mold casting, High-pressure torsion	Bulk plate (2 cm × 1 cm and 1 mm thickness)	Institute of Nanotechnology (Dr. Julia Ivanisenko)

Table 3.1: Brief descriptions of samples used in the present work.

In this Ph.D. work, metallic glass samples from various research groups were utilized, and they were prepared mainly using melt spinning and suction casting techniques. The focus was on investigating three specific metallic glass systems: Fe_{85.2}Si_{0.5}B_{9.5}P₄Cu_{0.8} (at.%), Zr₄₆Cu₃₈Al₈Ag₈ (at.%), and Zr_{52.5}Cu_{17.9}Ni_{14.6}Al₁₀Ti₅ (at.%), were intensively studied as outlined in Table 3.1. Note, in this thesis, the subscript numbers for the glass composition always reflect the nominal composition in atomic percent.

For the Fe-based sample, Fe_{85.2}Si_{0.5}B_{9.5}P₄Cu_{0.8} master alloy ingots were first prepared through arc melting in a Ti-gettered argon atmosphere. The melting process was repeated five times to ensure the homogeneity of the chemical composition. Subsequently, Fe_{85.2}Si_{0.5}B_{9.5}P₄Cu_{0.8} ribbons with a width of approximately 25 mm and a thickness of about 20 μm were produced by rapidly solidifying the melt on rotating copper wheels. To induce structural relaxation, the as-spun Fe_{85.2}Si_{0.5}B_{9.5}P₄Cu_{0.8} metallic glass ribbon underwent a flash annealing treatment at a temperature of T_a = 633 K (~ 1.1 T_g) for 10 minutes.

For the Zr-based metallic glass, a master alloy ingot of $Zr_{46}Cu_{38}Al_8Ag_8$ was prepared by arc melting a mixture of pure Zr, Cu, Al, and Ag in an argon atmosphere with Ti gettering. The melting process was repeated five times to ensure the chemical homogeneity of the alloy. Following this, plate samples measuring $1\text{ cm} \times 1\text{ cm}$ with a thickness of 1 mm were fabricated through suction-casting into a water-cooled copper mold. The as-prepared metallic glass samples were annealed under high vacuum conditions ($1.5 \times 10^{-5}\text{ Pa}$) at $T_a = 639\text{ K}$ ($\sim 0.9 T_g$) for different durations of time, specifically 20 hours and 240 hours, to induce structural relaxation. $Zr_{52.5}Cu_{17.9}Ni_{14.6}Al_{10}Ti_5$ also known as Vit105, was produced by LIQUIDMETAL Ltd., USA using a water-cooled copper mold. All samples underwent polishing to achieve a mirror-like finish with a surface roughness of less than 30 nm, minimizing the influence of surface topography and oxidation layer.

3.2. Deformation methods: Scratch testing

Scratch testing is a widely used tribological deformation method employed to investigate the wear characteristics of materials. It involves subjecting a material surface to controlled scratching forces, replicating the conditions encountered during wear. The wear process is complex and influenced by various factors, including mechanical, physical, and chemical conditions present on the surfaces in contact. Different methods can be utilized for conducting wear tests, such as pin-on-disk scratching, roller-on-plate wear, and single asperity scratching. Each method offers unique advantages and is suitable for specific research objectives. In this study, the focus was on single asperity scratching, which involves applying a controlled load to a single asperity on the material surface.

Friction, a key aspect of wear, is governed by two primary mechanisms: shearing and plowing. According to the research by Bowden and Tabor,^[165] The friction force (F_f) can be mathematically expressed as the sum of shearing (τA_c) and plowing ($\mu_p F_N$) contributions as $F_f = \tau A_c + \mu_p F_N$. Here, τ represents the shear strength of the material, A_c is the real contact area between the scratch front and the submerged part of the indenter, μ_p denotes the plowing friction coefficient, and F_N is the normal load applied to the material. To decouple the shearing term from the plowing term and gain further insights into the friction behavior, the friction force can be alternatively expressed as $F_f = \tau A_c + HA_f = (\mu_s + \mu_p)F_N$, where H is the hardness of the material, A_f is the projected area between the scratch front and the indenter's submerged portion, and μ_s is the shear friction coefficient.

To analyze the wear and tribological response of materials, it is crucial to determine the total friction coefficient. In the wear regime, the linear slope of the friction force corresponds to the superposed effects of shearing and plowing, therefore, the situation can be mathematically written as $\frac{dF_f}{dF_N} = (\mu_s + \mu_p) = \mu_{total}$, where μ_{total} is the total friction coefficient. As contact area A_c , hardness H , and total friction coefficient μ_{total} can be easily determined experimentally by a single asperity scratching condition, specific wear, and tribological response can be studied accordingly.

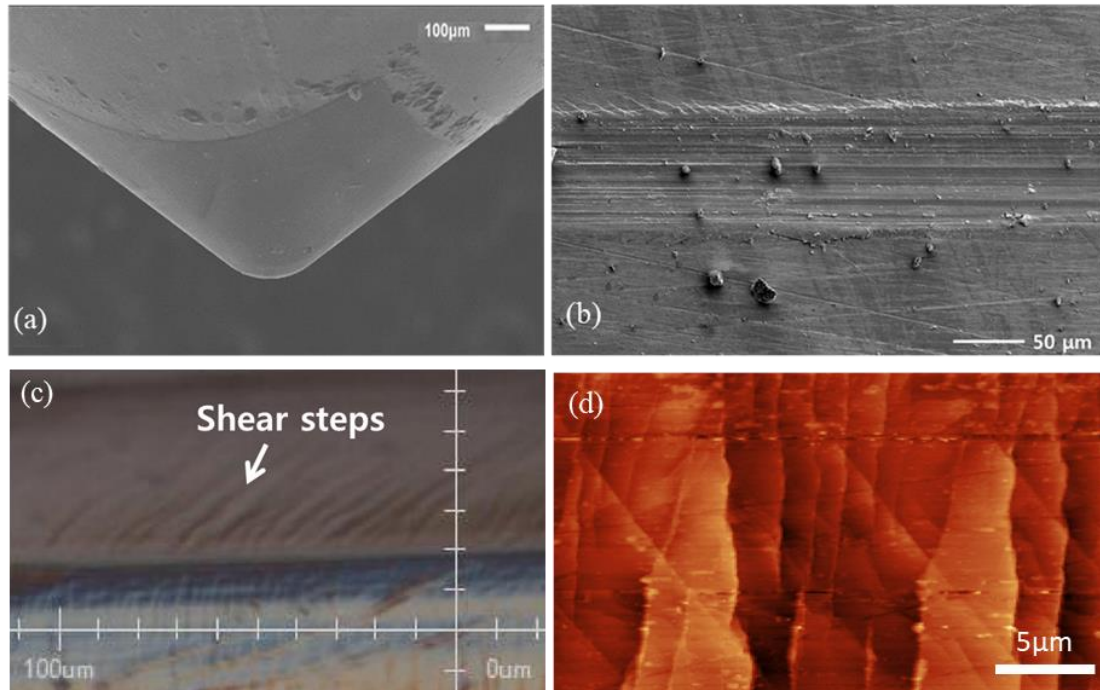


Figure 3.2: SEM images of (a) tip and (b) scratched track with wear debris and shear offsets on the pile-up area. The scratches were imaged by (c) optical microscopy and (d) atomic force microscopy.

Scratch testing often results in the development of a shear band network as shown in Figure 3.2. The test can be performed to obtain an optimal density of shear bands, sufficiently high for analysis, but avoiding excessive overlap, thus facilitating a clear examination of the deformation behavior. This is advantageous for TEM sample preparation due to its ability to create localized defects and selectively focus on areas of interest with a sufficient shear band density.

In the scope of this Ph.D. work, single asperity scratching experiments were conducted at Koreatech. The scratching process involved sliding a spherical diamond tip, provided by J&L Tech, with a radius of 210 μm, over the material surface for a distance of 1 mm. The normal load (F_n) was varied within the range of 14 N to 20 N, and a sliding velocity of 0.1 mm per second was

maintained under ambient conditions. The lateral forces (F_L) were measured by monitoring the lateral tilting angle of the tip during the sliding process. The contact area between the indenter and the material was determined based on the width of the scratched tracks W_s following $A_c = \frac{\pi W_s^2}{4}$. This allowed accurate calculation of the contact area, enabling the normalization of wear response for comparative studies. The metallic glass surfaces exhibited distinct localized shear steps and bands, as observed in Figure 3.2c, which indicated the presence of material deformation and tribological interactions. To evaluate the hardness and friction coefficient of the material, the load dependence of the contact area and the friction force were analyzed. The reciprocal of the slope of the contact area as a function of the normal load, expressed as $\frac{1}{H} = \frac{dA_c}{dF_N}$ or $H = \frac{dF_N}{dA_c}$, provided an estimation of the material's scratch hardness. Conversely, the friction coefficient was determined by examining the slope of the friction force as a function of the normal load, given by $\mu = \frac{dF_f}{dF_N}$. To ensure the validity of the results, the tip used for scratching was imaged using SEM before and after the scratch tests. This step was essential to verify that any observed changes in the wear response were not influenced by alterations in the geometry of the diamond tip.

3.3. Fundamentals of electron microscopy

Electron microscopy (EM) has emerged as a powerful tool for investigating the nanostructure of materials, offering superior spatial resolution compared to other optical microscopy techniques. The resolution of an EM can be understood through various concepts, depending on the specific functions of the instrument. One common approach to describe the spatial resolution of a microscope is the Rayleigh criterion, which relates to the minimum resolvable distance between two independent object points. It can be expressed as $\delta = \frac{0.61 \lambda}{N \sin \beta}$, where λ represents the wavelength of the radiation used for imaging, N is the refractive index of the medium between the lens and the sample, and β is the semi-collection angle. This shows that the resolution in microscopy is mainly limited by the wavelength λ . In EM, the wavelength of an electron is directly associated with the acceleration voltage, as described by de Broglie's relation between momentum and wavelength. The typical acceleration voltages used range from 5 to 300 keV, resulting in electron wavelengths in the range of 2 to 10 pm. This provides the potential for high-resolution imaging with a wavelength well below characteristic interatomic distances. Unlike optical microscopy, however, the resolution in EM is not only constrained by wavelength (diffraction limit), but rather by imperfections of the lens system, e.g. aberrations, and the energy spread of the

electron source. Advances in aberration correction and energy filtering have significantly enhanced the resolution to observe and characterize materials at the atomic scale, leading to profound advancements in nanoscience and nanotechnology.

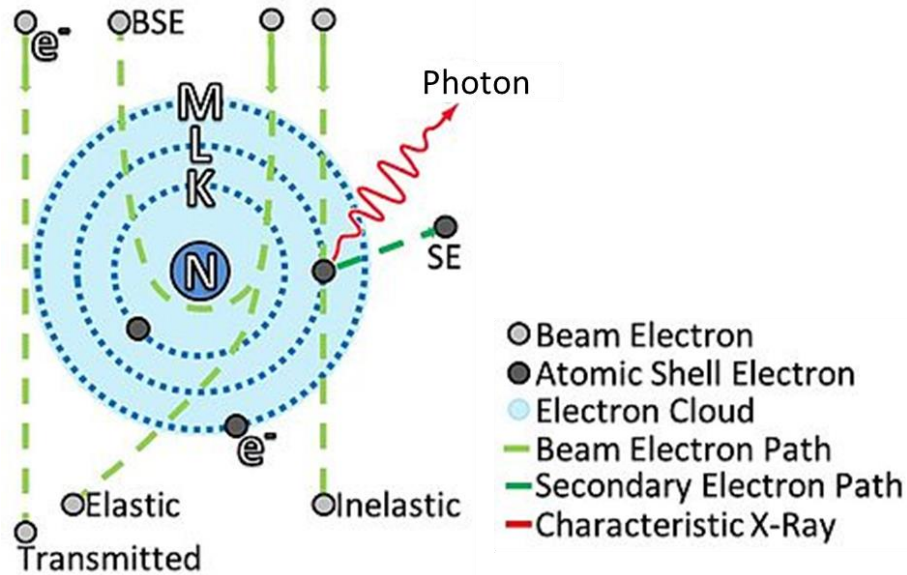


Figure 3.3: Schematic description of how an electron beam interacts with an atom (nucleus and electron cloud) in a sample. The figure shows the elastic/inelastically scattered electrons as well as the transmitted ones. Secondary electrons are electrons generated as ionization products. They produce characteristic photons. Back-scattered electrons are electrons that are scattered backward due to the strong positive charge of the nucleus. The figure is reshaped from Ref. ^[166].

The electron beam undergoes strong interactions with matter, resulting in scattering phenomena that carry structural information and form the basis for EM imaging. Scattering can occur elastically and inelastically, as depicted in Figure 3.3. Elastic scattering arises from the interaction of incident electrons with the electron cloud or the positive nucleus of an atom. Electron-electron scattering leads to a slight deviation in the scattering angle, while electron-nucleus scattering results in a higher angular deviation, varying in strength depending on the nature of the interaction. High-angle scattering is dominated by Rutherford and thermally diffuse scattering, with the scattering strength heavily influenced by the atomic number (Z) of the element species within the sample.

Coherent elastic scattering by the lattice of the material is referred to as Bragg diffraction, a process widely employed for investigating the crystallographic structure of materials. The position and intensity of the diffraction peaks provide valuable information about the crystal structure. By measuring the angles and intensities of the diffracted waves, one can determine the spacing

between adjacent crystal planes and the arrangement of atoms within the unit cell. This information can be used to identify the crystal structure, determine the crystal symmetry, and analyze the presence of defects or impurities in the crystal.

Inelastic interactions involve a transfer of energy from an incident electron to the sample due to electronic or vibronic transitions. Electronic transitions occur when an electron within the sample interacts with the incident electrons. In this process, energy is transferred from the incident electron to the sample material, causing an excited electron to transition from a ground state to an unoccupied orbital in an outer shell (or to be emitted as a secondary electron). Subsequently, the excited electrons relax and emit photons (as X-rays or cathodoluminescence) or Auger electrons. These can be detected using appropriate detectors and utilized for chemical characterization, e.g. in energy-dispersive X-ray spectroscopy (EDX) analysis. Similarly, electrons that have undergone energy loss during interactions can be employed for chemical characterization, for example, in electron energy loss spectroscopy (EELS).

The various operation modes relevant to this work will be explained in detail in the subsequent sections. The application of EM enables a comprehensive understanding of the atomic structure of the sample, its chemical composition, and its electronic structure.

3.4. Scanning electron microscope and focused ion beam

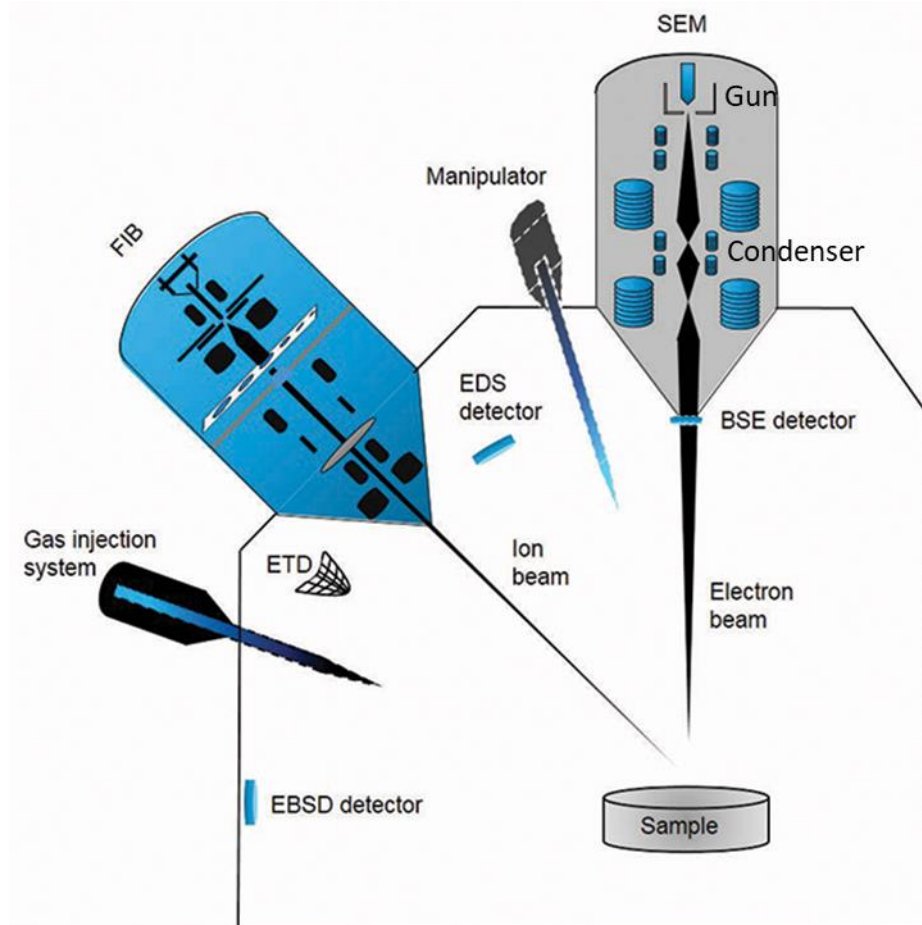


Figure 3.4: Schematic of a standard FIB/SEM. FIB/SEMs integrate both, a scanning electron microscope and a focused ion beam within a single system. These instruments are frequently equipped with diverse detectors, including Everhart–Thornley (ET), backscattered electron (BS), energy-dispersive spectroscopy (EDS), electron backscatter diffraction (EBSD) detectors, and in-lens detectors. FIB/SEMs commonly feature gas injection systems and manipulators as well. The figure is reprinted from Ref. ^[167].

An SEM is a type of electron microscope as shown in the top, Figure 3.4. SEM is often employed to study a bulk sample where the focused beam of electrons scans the sample surface and collects signals emitted from the surface. The interaction between the electrons and the sample generates an array of signals during scanning, housing vital data for constructing images. Central to the SEM is an electron gun that emits an electron beam from its apex. Multiple electron gun types, such as thermionic gun (TG) and field emission gun (FEG), are available. The electron beam emitted from the gun, typically carrying energy spanning 5 keV to 40 keV, is focused onto a nanometer-scale focal point using one or two condenser lenses. As it passes through the column, culminating in the final lens, the beam navigates pairs of scanning coils or deflector plates. These components

collaborate to steer the beam along the x and y axes, executing a scan in a configuration across a rectangular segment of the sample surface. The outcome of the primary electron beam encountering the sample encompasses a series of events as introduced in the previous chapter. Electron energy disperses through recurrent, stochastic scattering and absorption, transpiring within a unique teardrop-shaped area called the interaction volume. This volume extends from nanometer-level depths to roughly micrometer-level beneath the surface. The authentic size of the interaction volume hinges on variables such as the initial energy of the electron beam, and the density of samples. The interplay of the electron beam and the sample materializes in the form of multiple outcomes. For SEM, high-energy electrons undergo reflection due to elastic scattering, secondary and back-scattered electrons are emitted due to elastic and inelastic scattering, and electromagnetic radiation can be also released. These signals are amenable to detection by specialized devices, e.g. electron and EDX detectors, which in turn allows for comprehensive analysis and imaging.

A FIB system is closely related to a SEM but employs an ion beam for imaging and structuring. The most commonly used ion sources in FIB instruments are liquid metal ion sources (LMIS)^[168], especially those based on gallium. For a gallium LMIS, a tungsten needle comes into contact with gallium metal. When the gallium is heated, it wets the tungsten and flows to the needle tip. The opposing forces of surface tension at the tip and electric field shape the gallium into a cusp-like tip called a Taylor cone. The intense electric field at the tip causes ionization and field emission of the gallium atoms. The produced ions are typically accelerated to energies ranging from 1 to 50 keV and focused onto the sample using electrostatic lenses similar to the SEM system. In modern FIB setups, tens of nano amperes of current can be delivered to a sample, and the sample can be imaged with a spot size on the order of a few nanometers. More recently, instruments utilizing plasma beams of noble gas ions, such as xenon, have become more widely available.^[169] Specialized detectors, e.g. secondary ion detectors, can count the ions scattered/escaped by/from the materials and produce an image.

3.5. Scanning/transmission electron microscopy (S/TEM)

3.4.1. Design and Principles

TEM employs electrons that traverse the sample, referred to as transmitted electrons, to generate an image.^[170] Typically, the specimen is an ultrathin section less than 100 nm thick or a suspension on a grid for electron transparency. The image is created through the interaction of the primary

electrons with the sample, akin to the ray optics in conventional light microscopy. Subsequently, the image on an intermediate image plane is magnified and directed onto an imaging system such as a fluorescent screen, a layer of photographic film, or a sensor such as a scintillator coupled to a charge-coupled device (CCD).

A TEM consists of several key components similar to a SEM, including a gun and electromagnetic lenses. As in the SEM, the gun is responsible for generating electrons in TEMs. Modern TEMs often utilize a FEG due to its ability to generate a coherent and monochromatic electron beam.

The condenser system, composed of two or three sets of lenses and apertures, shapes the electron beam. In modern TEMs, multiple condenser lenses allow independent optimization of spot size, diameter, and convergence angle. By adjusting the crossover between the condenser lenses, the spot size and convergence angle can be controlled, thus modifying the portion of the beam passing through the condenser apertures. The apertures are positioned below the lenses to filter the beam and improve the coherency of the electron beam.

The objective system is located below the condenser system, positioned around the sample, consisting of an upper and lower part of the objective lens. The electron beam passes through the region of interest in the sample, interacting with the matter, thereby acquiring information on the structure, morphology, and chemical state. An intermediate image is formed in the image plane, while a diffraction pattern is produced at the back focal plane of the objective lens. To enhance the image contrast, an aperture known as the objective aperture can be inserted at the back focal plane to selectively block a selected angular range of the diffracted signal. Additionally, an aperture can be inserted in the imaging plane of the objective lens to obtain a diffraction pattern from a specific area of interest within the image.

The intermediate image or diffraction pattern is then projected and magnified by the projection system to create the final magnified image or pattern. This image or pattern is displayed on a phosphor screen or captured by a camera attached at the bottom of the column. Different types of cameras and detectors can be incorporated into the TEM to meet the specific requirements of various experiments. The complex lens system enables various operating modes, such as bright-field TEM, dark-field TEM, and selected area electron diffraction (SAED), offering versatility in imaging and diffraction techniques.^[170]

3.4.2. Operating modes in TEM

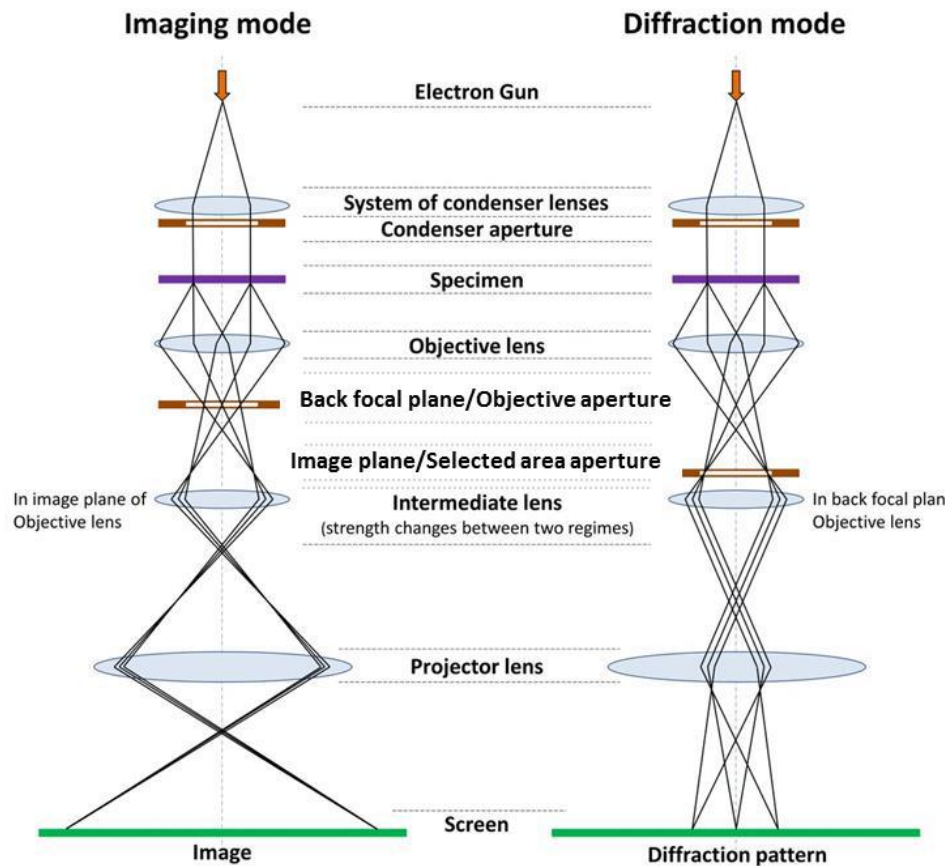


Figure 3.5: Schematic view of the imaging and diffraction mode of TEM. Reprinted from Ref. ^[166].

TEM can operate in imaging or diffraction modes as shown in Figure 3.5, each providing distinct information about the sample being analyzed. Bright-field TEM imaging is a fundamental mode of operation in TEM. In this imaging mode, the objective lens of the TEM forms a magnified image using the electrons that are transmitted through the sample and scattered in a forward direction. The objective aperture in the back focal plane blocks parts of the diffracted electrons and the objective lens forms a bright-field image with the remaining electrons in the intermediate image plane, which is further magnified by the projection system. Bright-field TEM imaging utilizes two contrast mechanisms: mass-thickness contrast and diffraction contrast. Mass-thickness contrast arises from electrons scattered to high angles due to their strong interaction with the atomic nucleus. The scattering intensity depends on the average atomic number and the thickness or atomic density of the sample. Regions with higher mass-thickness exhibit stronger scattering, resulting in a dark contrast in the bright-field image. Diffraction contrast, on the other hand, is caused by coherent scattering events where high-angle diffracted beams are blocked by the

objective aperture. Regions that exhibit strong diffraction appear dark in a bright-field image. Alternatively, TEM can also be operated in a dark-field mode for imaging. In this mode, only the diffracted beams are selected for imaging, while the direct beam is blocked. Achieving dark-field imaging involves tilting the beam to select a specific diffracted beam in the objective aperture and blocking the direct and all other diffracted beams. In contrast to bright-field imaging, dark-field image highlights regions with strong diffraction by displaying them more brightly. The size of the aperture used determines whether one or multiple diffracted beams are selected for imaging.

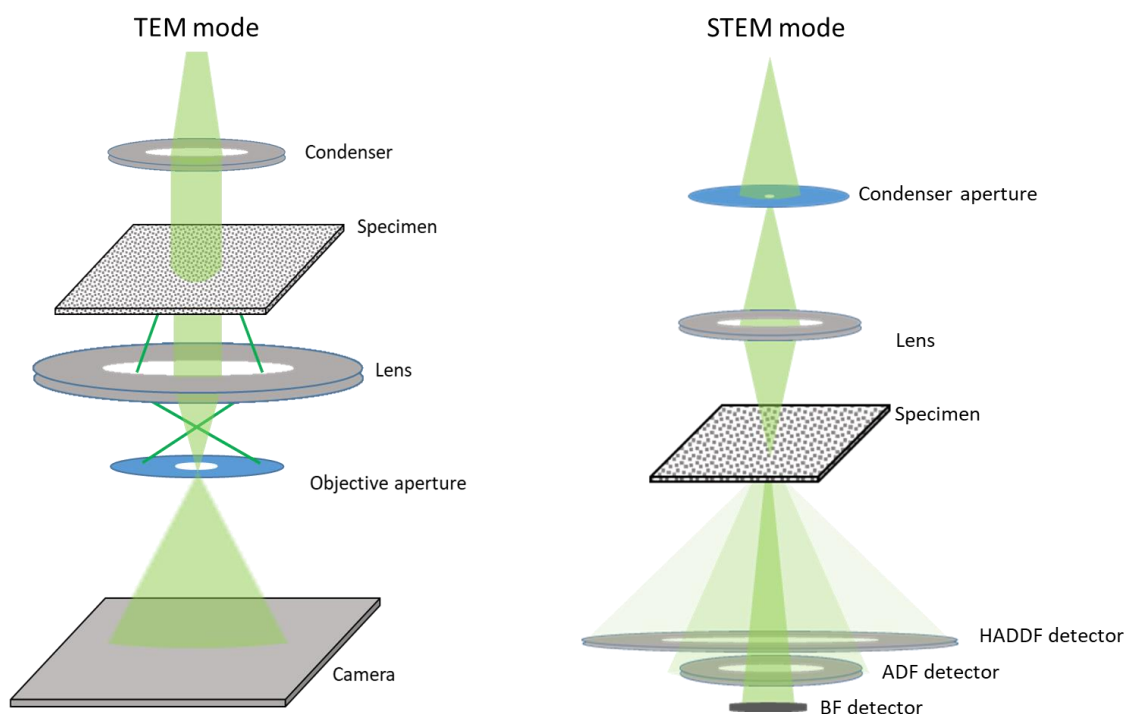


Figure 3.6: Schematic view of conventional TEM and STEM modes.

The diffraction mode involves specific imaging techniques to capture electron diffraction patterns, where the diffraction lens is configured to position the diffraction pattern on an image plane. Electron diffraction emerges when an electron beam interacts with a sample, leading to electrons scattering in distinct patterns due to the periodic arrangement of atoms. This scattering generates a diffraction pattern, serving as a distinctive identifier of the atomic structure. These patterns thereby provide information about the structure, orientation, and size of atomic neighbors within the material. Crystalline materials adhere to Bragg's condition, which states that $2d \sin \theta = n\lambda$, where d is the distance between planes, θ is the semi-scattering angle, n is an integer, and λ is the wavelength of electrons. According to Bragg's condition, diffraction occurs when the path length difference traveled by the electron wave between parallel lattice planes is an integer multiple of

the wavelength. Consequently, diffraction spots reflecting these planes can be observed in the diffraction pattern from crystalline materials.

TEM can typically also be used in STEM mode, where the electron beam is focused and scanned over the sample as shown in Figure 3.6. STEM allows image formation by measuring the scattered electron intensity detected within a specific angular range. Different imaging conditions, such as bright-field (BF), annular dark field (ADF), and high-angle annular dark field (HAADF), can be achieved by positioning the detectors accordingly. The resolution in STEM is limited by the size of the electron probe. To achieve higher resolution, the condenser system strongly demagnifies the electron source with appropriate convergent angles. However, a higher convergent angle can introduce lens aberration issues that degrade the probe size and resolution. To mitigate aberrations, an additional condenser aperture can be inserted to block the beam edge at the condenser lens crossover. Modern STEMs employ probe correctors, which computationally adjust and compensate for aberrations, resulting in electron probes smaller than 50 pm. Techniques like Ronchigram and probe correctors play crucial roles in achieving high-resolution STEM imaging. Further details can be found in specialized textbooks.^[166, 171]

3.6. TEM sample preparation by FIB and SEM

When high-energy ions impact the sample surface, they transfer sufficient energy to sputter atoms from it. FIB is commonly utilized for preparing TEM samples, especially when dealing with materials that require analysis of small defined regions of interest. For this purpose, FIB works in conjunction with SEM as shown in Figure 3.4, where SEM facilitates precise imaging to select an area of interest, and the sample is milled using a finely focused ion beam. The drawbacks of FIB sample preparation are surface damage and chemical changes induced by ion implantation. Therefore, it is crucial to consider the potential damage to the specimen when using FIB, as it can lead to noticeable effects for TEM observation, especially for high-resolution imaging and spectroscopy investigations. A comprehensive examination of how the remaining TEM sample thickness impacts the atomic structure and strain in metallic glasses will be provided in chapter 4.4.

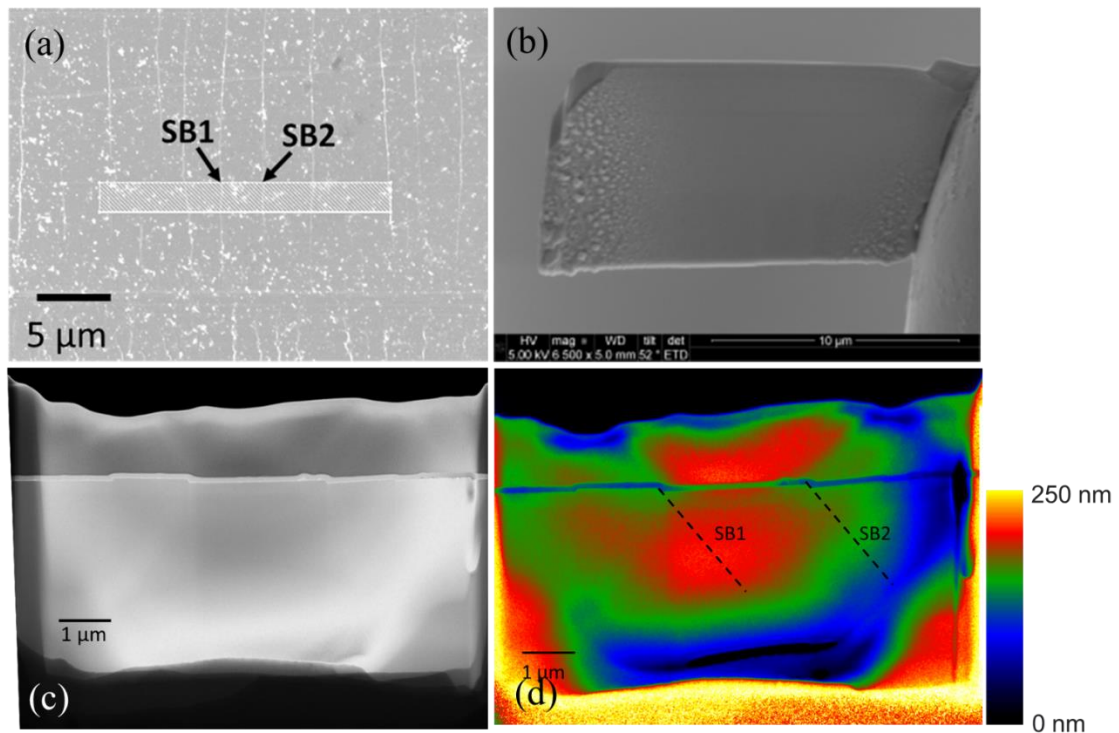


Figure 3.7: Cross-sectional TEM sample preparation by dual-beam SEM-FIB system. (a) milling trenches from the area of interest, (b) TEM lamella after lift-out before thinning, (c) after thinning for electron transparency, STEM-HAADF image, and (d) Thickness map of a typical TEM lamella for investigation obtained from energy-filtered transmission electron microscopy (EFTEM).

The FIB technique entails a series of crucial steps to guarantee precise and controlled sample preparation. These steps generally involve the following: (1) The material of interest is first

mounted onto a suitable substrate, such as a TEM grid or specialized holder, to ensure stability during the subsequent processes, (2) the sample is imaged using SEM to identify the specific area for analysis, (3) to protect the region of interest during milling, a thin layer of protective material, such as platinum or carbon, is deposited onto the sample surface using the FIB system (Figure 3.7a), (4) the FIB system is then used to selectively mill away material from the targeted area, (5) the trenched sample is lift-out and attached to TEM grid (Figure 3.7b), and the sample is gradually thinned to the desired thickness for TEM examination (Figure 3.7c), (6) after thinning and polishing, a low-energy ion beam is used to clean the sample, removing any residual amorphous carbon or redeposited material, and (7) the lamella is then transferred to a TEM for further examination.

In this Ph.D. work, TEM lamellae were prepared by Strata 400S Dual Beam System (FEI / ThermoFisher). The FIB-based sample preparation enables sampling from a precisely selected target area. TEM lamellae were trenched and lifted out from the vicinity of the scratches with a typical size of $15 \times 10 \times 1 \mu\text{m}$. Thinning was performed in the FIB at a range of acceleration voltage of 5kV - 30 kV with gradually decreasing beam currents from 2 nA to 8 pA to reduce temperature increase (thermal damage). A final lamella thickness of ~ 200 nm was obtained to balance electron transparency and prevent strain relaxation due to an enlarged surface-to-volume ratio (Figure 3.7d).

3.7. Characterization of material structure from electron diffraction

3.6.1. Diffraction pattern

In classical physics, the diffraction phenomenon can be explained using wave propagation theory. When a wave encounters an obstacle or passes through an aperture, each point on the wavefront becomes a source of secondary waves. These secondary waves propagate in various directions, and their superposition results in the formation of a new wavefront. The interference of wavefronts produces a diffraction pattern that provides information about the structure of the object. For instance, when an electromagnetic wave encounters atomic species that are arranged periodically, a diffraction pattern emerges. This pattern is formed by the superposition of diffracted waves from each atomic plane within the illuminated volume. The diffraction intensity, which describes the distribution of the intensity of the diffracted waves, can be mathematically characterized using the Debye formula as

$$I(k) = \sum_m^N f_m(q)^2 + \sum_m^N \sum_n^N \delta(r - r_{mn}) f_m(q) f_n(q) \frac{\sin(2\pi q r_{mn})}{2\pi q r_{mn}}, \quad (3-1)$$

where q is the reciprocal vector, the δ is the delta function, r_{mn} is the pair distance between the atom n and atom m .

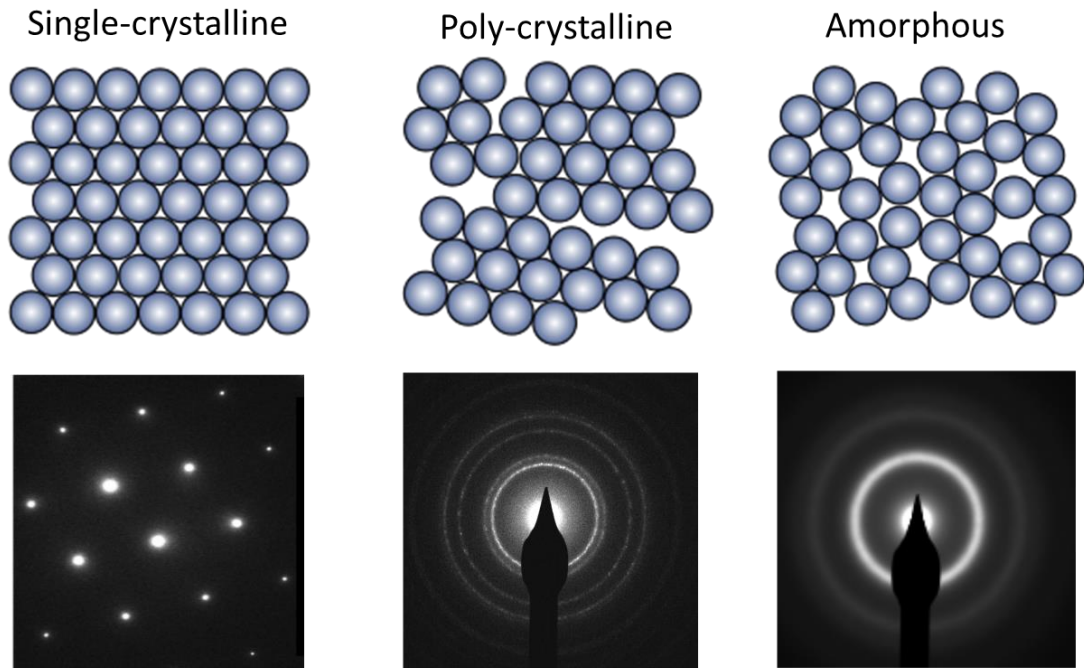


Figure 3.8: Schematic illustration of typical atomic structures of solids, *e.g.* single crystal, polycrystal, amorphous, and corresponding electron diffraction patterns.

The diffraction intensity consists of two mathematical terms reflecting two different scattering conditions. The first term, denoted as $f_m(q)$, represents the single atomic scattering factor of specific elements m . The second term, known as the structure factor, captures the diffracted information arising from the reciprocal periodicity of each scattering point. Figure 3.8 provides schematic illustrations of the typical atomic structure of solids and their diffraction patterns. In a single crystal, the diffraction pattern manifests as periodically arranged spots, representing the crystallographic lattices. For polycrystals with a sufficient number of illuminated grains, the diffraction pattern exhibits sharp rings due to the superposition of diffraction points from various crystallographic orientations. This type of diffraction pattern enables the determination of unit cell structure, and lattice parameters in the materials. Conversely, an amorphous system produces a diffuse ring in its diffraction pattern, owing to its isotropic atomic arrangement and lack of structural order.

3.6.2. Structure factor

The structure factor serves as a mathematical representation of how a material scatters incident radiation, making it a crucial descriptor for the material's structure. Various mathematical expressions exist to describe the structure factor, but in this thesis, only the simplified mathematical treatment pertaining to the processing aspect is discussed. More comprehensive explanations can be found in textbooks.^[172] The structure factor, denoted as $S(q)$, can be derived through background modeling for $I(k)$. Mathematically, it is expressed as follows:

$$S(q) = \frac{I(q) - N \langle f(k)^2 \rangle}{N \langle f(k) \rangle^2} , \quad (3-2)$$

where N is the number of atoms in the illuminated volume, and $\langle f(k) \rangle = \sum_i C_i f_i(k)$ denotes the total atomic form factor over all elements i with the individual atomic form factor $f_i(k)$ weighted by the elemental fraction C_i . $f_i(k)$ of electron scattering can be calculated from the dataset of atomic form factors from traditional scattering experiments, *e.g.*, X-ray, using the Mott-Bethe formula.^[172] In practice, the estimated $f_i(k)$ often does not perfectly match the experimental $I(q)$ at both small and large angles simultaneously. This discrepancy is primarily due to the presence of multiple elastic and inelastic scattering events due to the strong electron-matter interaction in TEM. However, unlike crystalline materials that have well-defined atomic columns, amorphous materials lack such structural regularity. As a result, the scattering in an amorphous sample does not exhibit channeling effects but instead manifests as multiple self-convolutions of the two-dimensional kinetic diffraction pattern.^[173] Therefore, multiple scattering in amorphous materials does not introduce any additional peaks or peak shifts but gives rise to a smooth background to the diffraction pattern.^[174-175] A recent development by Mu et al. introduces a method to mitigate this artifact by employing a smooth polynomial background modeling approach for amorphous materials.^[176] In this study, a smooth 4th-order polynomial function is subtracted from the structure factor to reduce the effects caused by plural scattering and the contribution from inelastic scattering as demonstrated in Ref. ^[176].

3.6.3. Pair distribution function

X-ray and neutron sources have traditionally been used for Pair distribution function (PDF) analysis to investigate various types of amorphous materials, including organic solids, liquids, and metallic glasses. The PDF describes the distribution of atomic pairs as a function of their distance, providing insights into the SRO or MRO of disordered materials. The PDF can be obtained by frequency decomposition of the structure factor, $S(k)$, using Fourier sine transform.

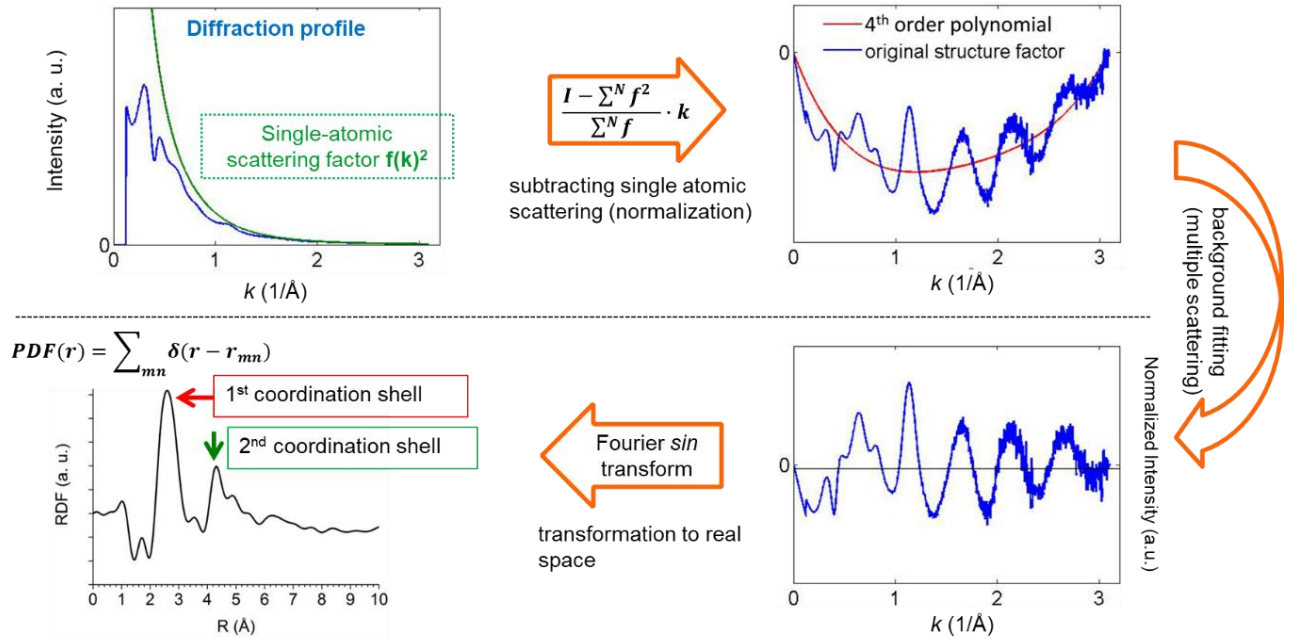


Figure 3.9: Sketch of the procedure to calculate the PDF from the electron diffraction pattern. An annular averaged diffraction profile obtained from a diffraction pattern of an amorphous sample. Structure factor deduced by background subtraction of single atomic form factor. Further background modeling with polynomial function to eliminate the low-frequency artifacts from multiple scattering. RDF can be calculated from the Fourier sine transform of the structure factor. Reprinted from Ref. [176].

In recent years, electron diffraction in Transmission Electron Microscopy (TEM) has emerged as a technique capable of producing high-quality PDFs, thanks to advancements in sample preparation and energy filtering systems. The probability of finding an atom at a specific radius, r , from a central atom can be mathematically expressed as $P(r) = \sum_m^N \sum_{n \neq m}^N \delta(r - r_{mn})$, where δ represents a delta function indicating atomic positions, and r_{mn} denotes the pair distance between atoms n and m in an isotropic model containing a total of N atoms. By utilizing the information on pair distances, the atomic density function, $\rho(r)$, can be determined as $\rho(r) = \frac{N!}{(N-n)!} P(r)$. The

PDF, $g(r)$, can then be written as $g(r) = 4\pi r^2 \rho(r)$, with the weighting factor $4\pi r^2$ accounting for the spherical nature of the atomic shell.

Experimentally, PDFs are obtained by performing a sine Fourier transformation of the structure factors, following the equation $\text{PDF}(r) = \int_0^{k_{max}} S(k) \sin(2\pi kr) dk$. The only adjustable parameter in the PDF calculation is N , which is determined for each PDF by minimizing $S(q)$ to approach zero at large k . Figure 3.9 illustrates the procedure for calculating the PDF from an electron diffraction pattern of an amorphous sample. The first peak in the PDF corresponds to the average distance between central atoms and their nearest neighbors, while the second peak represents the distance to the second-nearest neighbor atom. One significant advantage of TEM-based PDF analysis is its ability to provide local information about samples with higher spatial resolution compared to X-ray and neutron-based methods. This accessibility to fine-scale details enhances the understanding of the atomic structure and arrangements within amorphous materials.

3.6.4. Strain measurement

The presence of stress in a material leads to a distortion of its atomic structure and introduces anisotropy, which manifests as an azimuthally elliptic distortion of the diffraction ring as shown in Figure 3.10. Different from high-resolution (HR)TEM-based strain mapping methods such as geometric phase analysis (GPA), which analyzes real space atomic lattice displacements,^[177] the strain measurement used here analyzes the diffraction ring in the diffraction image. It thus enables the capability to measure strain for amorphous materials and a large field of view (up to micrometers).

From the fitted ellipse, the principal strains can be determined as $\vec{P}_1 = \frac{k_0 - k_{max}}{k_0} \begin{pmatrix} \cos(\theta) \\ \sin(\theta) \end{pmatrix}$ and $\vec{P}_2 = \frac{k_0 - k_{min}}{k_0} \begin{pmatrix} \cos(\theta + 90^\circ) \\ \sin(\theta + 90^\circ) \end{pmatrix}$, where k_0 is the reciprocal radii of the 1st ring for the unstrained case (averaged from an area far away from the deformed region), q_{max} , and q_{min} are the lengths of the maximum and minimum elliptical axis of the 1st ring. θ is the corresponding azimuthal angle of q_{max} to the x-axis. Additionally, the radius of the diffraction ring reflects the distance between atoms and provides information on the atomic density. Using the hard sphere model, the local atomic density can be determined by quantifying the area encircled by the 1st ring as $\Delta\rho = \frac{k_{max}k_{min} - k_0^2}{k_{max}k_{min}}$. This approach considers the elliptical deviation of the diffraction rings due to strain

and separates the atomic density information. The deviatoric strain can be calculated as $\varepsilon_{dev} = \frac{|\vec{P}_1| - |\vec{P}_2|}{2}$. The volumetric strain was calculated as $\varepsilon_{vol} = \frac{|\vec{P}_1| + |\vec{P}_2|}{2}$.

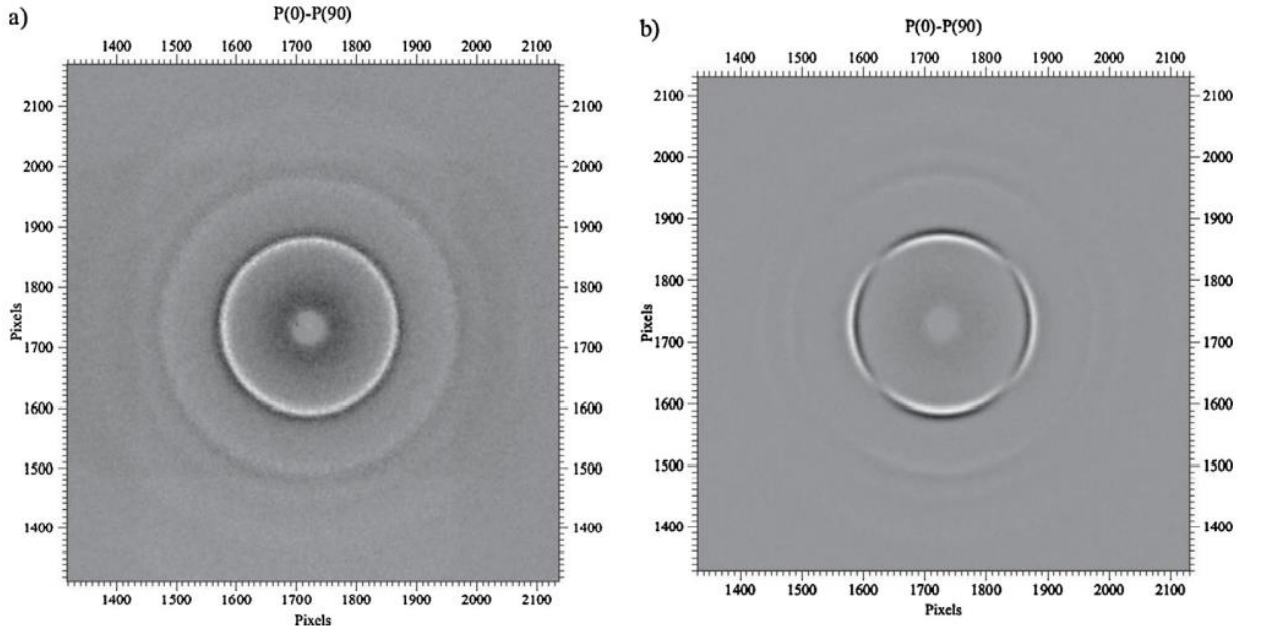


Figure 3.10: Difference between the 2-D XRD pattern measured in two orientations P(0°)–P(90°) for a Fe-based metallic-glass sample annealed at 300°C (a) without stress (b) under stress. The sample annealed under stress undergoes creep and is expected to be similar to shear-band material; it shows anisotropy after unloading indicating the presence of residual stress within the material after deformation. Reprinted from Ref. [176].

The maximum strain energy can be calculated as $E = \frac{1}{2} (|\vec{P}_1| + |\vec{P}_2|)^2$, taking into account that the elastic strain follows Hook's law. Strain tensors can be calculated by setting the coordinate system with the x-axis parallel to a shear band of interest and the y-axis perpendicular to the shear band as $\begin{pmatrix} \varepsilon_{xx} & \varepsilon_{xy} \\ \varepsilon_{yx} & \varepsilon_{yy} \end{pmatrix} = R \begin{pmatrix} |\vec{P}_1| & 0 \\ 0 & |\vec{P}_2| \end{pmatrix} R^T$, where $R = \begin{pmatrix} \cos(\theta) & -\sin(\theta) \\ \sin(\theta) & \cos(\theta) \end{pmatrix}$ is a rotation matrix. ε_{xx} and ε_{yy} represent the strain along the x-axis and y-axis. A positive value indicates tensile strain, meaning that the atoms are pulled away from each other, while a negative value indicates compressive strain, corresponding to atoms being squeezed closer along the axial direction. ε_{xy} represents the shear component of the strain tensor, where a positive value indicates clockwise shear and a negative value indicates anticlockwise shear. The maximum shear strain can be determined as $\tau_{max} = \frac{|\vec{P}_1| - |\vec{P}_2|}{2} \begin{pmatrix} \cos(\theta) \\ \sin(\theta) \end{pmatrix}$. The amplitude is defined as deviatoric strain and the orientation indicates the maximum tensile direction.

Chapter 4

4. 4D-STEM-based characterization of metallic glasses

Probing the local atomic structure within the amorphous phase has posed a significant challenge in materials research. Traditional diffraction techniques, such as X-ray diffraction, neutron diffraction, and selected area electron diffraction (SAED), provide averaged structural information due to their limited spatial resolution. As a result, they are unable to resolve the fine details of the local atomic structure of metallic glasses. To overcome this limitation, one approach is to focus the electron probe on a nanometer-sized area and acquire a diffraction pattern from this nano-volume in a scanning transmission electron microscopy (STEM) setup. By performing stepwise scanning of every probe position, an array of diffraction patterns can be obtained. This technique is referred to as 4D-STEM, named after the typical 4D dataset that records 2D diffraction images over a 2D grid of probe positions. The concept of 4D-STEM is reviewed in this chapter, highlighting its potential for characterizing amorphous materials at the nanoscale. Furthermore, the chapter introduces the specific application of 4D-STEM characterization in the context of the Ph.D. work being discussed.

4.1. Data acquisition and processing

The advancement of high-speed detectors plays a crucial role in enabling 4D-STEM techniques. While charge-coupled devices (CCDs) are commonly used detectors for recording full images in TEM, they have limitations in terms of frame rate and dynamic range, despite offering high electron sensitivity. These limitations have posed challenges for the application of 4D-STEM, which requires fast acquisition speeds comparable to STEM imaging and the ability to capture both direct (bright) and high-angle diffracted (weak) electrons in full diffraction images. To address these challenges, two main directions have been pursued in detector development for 4D-STEM: monolithic active pixel sensors (APS) and complementary metal-oxide-semiconductor (CMOS) detectors. APS and CMOS detectors have been commercialized and provide improved capabilities for 4D-STEM applications. More detailed information on these detectors can be found in a review paper by Ophus et al.^[178]

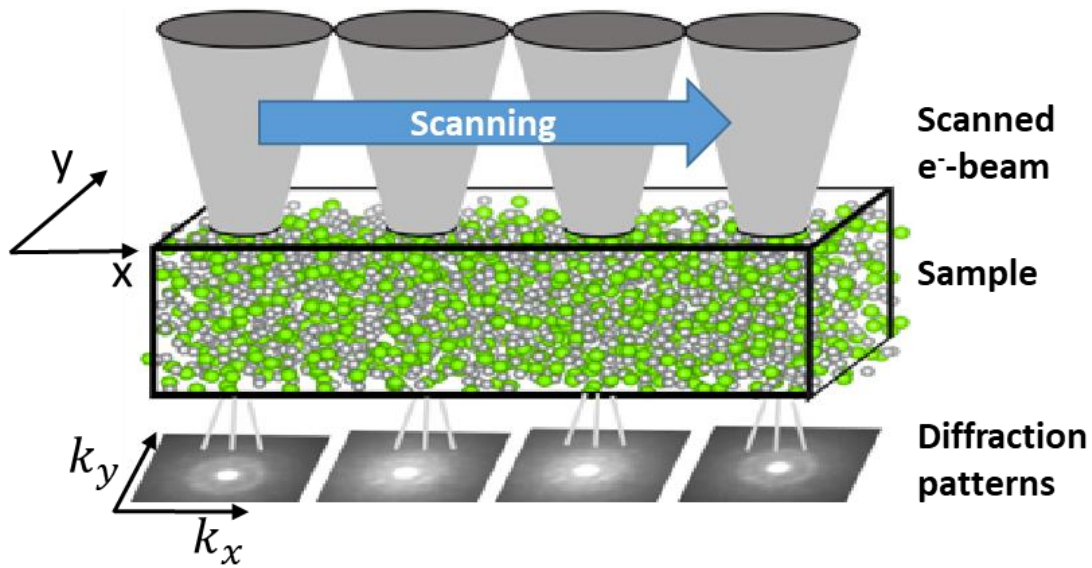


Figure 4.1: Schematic illustration of 4D-STEM. A quasi-parallel electron probe is focused to the nm scale on an electron transparent sample. Electron diffraction patterns are acquired from the nano-volume at each scan position during stepwise scanning of the probe across the area of interest. The diffraction pattern of metallic glasses is characterized by a set of circular diffraction rings due to their isotropic atomic arrangement. Reprinted from Ref. ^[176].

During the stepwise scanning, a series of diffraction patterns is captured at each scan position, providing reciprocal space information of the sample as shown in Figure 4.1. This results in a 4D dataset that encompasses the 2D scanning dimensions (x , y) and 2D reciprocal dimensions (k_x , k_y), hence the name 4D-STEM. To extract meaningful insights from the 4D dataset, suitable

processing is essential. One approach for 4D-STEM data processing is virtual imaging making use of virtual detectors to collect intensity data from specific scattering angles. This allows for the reconstruction of traditional STEM imaging modes, such as bright-field (BF) and annular dark-field (ADF) imaging.^[178] By analyzing the intensity variations within the diffraction patterns, one can generate images with diverse contrasts, enabling the characterization of the sample morphology, composition, and crystallographic structure. Another valuable technique enabled by 4D-STEM is orientation mapping, which involves determining the crystallographic orientation of different regions within the sample.^[179] By analyzing the diffraction patterns, it is possible to map the spatial distribution of phases, providing insights into grain boundaries, defects, and texture in polycrystalline materials.

Strain mapping is another powerful technique that can be employed within the framework of 4D-STEM to analyze the local distribution of strain fields within a sample.^[180] When a material undergoes deformation, such as at an interface between two different materials or due to external stresses, it can result in local distortions. This distortion manifests as strain, which can be either deviatoric or volumetric. By analyzing the distortions in diffraction patterns as described in chapter 3.5, 4D-STEM can determine the local strain at each pixel of the scanned area.

FEM utilizes the principles of statistical physics and analyzes the fluctuations of diffraction intensity observed in the electron diffraction patterns obtained from glassy samples.^[181] By collecting a series of diffraction patterns at different scan positions within the sample, FEM captures the local variations in atomic arrangement and density. It provides valuable insights into the atomic arrangements and disorder in glassy materials.

When the electron probe becomes sufficiently small, reaching a comparable size to the length scale of the gradient of the electrostatic potential, it will experience partial deflection with a momentum change. This gives rise to differential phase information. Differential phase-contrast (DPC) imaging is an advanced technique that can be combined with 4D-STEM to visualize differential phase information by local variations in the sample.^[182] DPC imaging provides improved contrast, especially for specimens with weak phase contrast, allowing to visualization of subtle structural details and variations. Conventionally, segmented detectors are used for DPC analysis that rely on intensity contrast.^[183] This reduces the information transfer efficiency. Unlike the conventional method, 4D-STEM-based DPC directly measures the phase shift of the electron waves passing through the sample using a center position measurement over all pixels. By doing so, it surpasses the limitations of the intensity-based method, making it particularly effective for imaging lightweight or low-contrast materials. The ability of differential phase-contrast imaging to enhance

the visibility of such materials enables a detailed examination of their structures and features. It also provides improved contrast and fidelity compared to traditional methods, allowing to gain deeper insights into the internal structure of these samples. DPC imaging offers distinct advantages for imaging magnetic/electric materials and performing their internal field imaging.

4.2. STEM-PDF analysis

As mentioned earlier in chapter 3.5, PDF analysis is a powerful technique for characterizing the atomic structure of amorphous materials. In combination with 4D-STEM, Mu et al. introduced a method called STEM-PDF analysis, enabling local phase mapping and analysis of heterogeneous amorphous structures at the nanoscale.^[176] Figure 4.2 illustrates the procedure for computing PDFs from experimental diffraction patterns. For the STEM-PDF analysis, a STEM setup with a small convergence angle, typically less than 1 mrad, is used to provide a quasi-parallel probe that illuminates a nanosized volume.

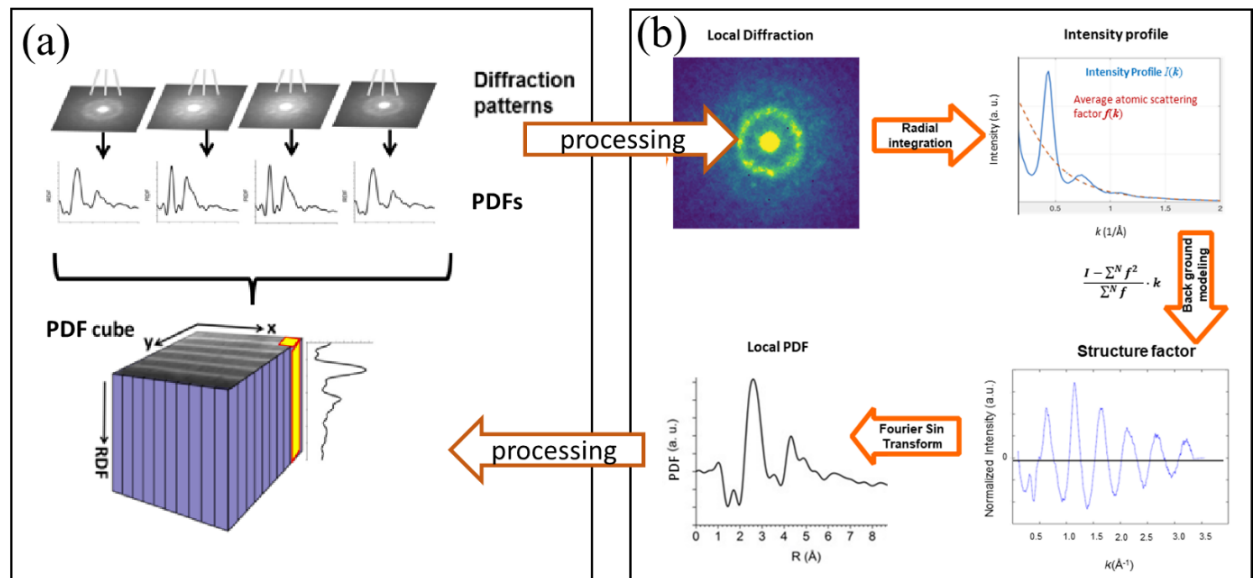


Figure 4.2: Schematic illustration of STEM-PDF mapping. (a) Local diffraction patterns and corresponding PDFs acquired by microprobe 4D-STEM setup. (b) The diffraction patterns are individually processed into a PDF cube. Reprinted from Ref. ^[172].

The local diffraction patterns are azimuthally integrated to obtain intensity profiles $I(q)$ s. If the materials exhibit structural anisotropy and directionality, the PDF can be analyzed at each azimuthal angle of each diffraction pattern. However, in this work, the diffraction pattern is azimuthally averaged to achieve the required signal quality for the PDF analysis. The obtained

intensity profiles $I(q)$ s provide averaged information within the probed nano volume. Each diffraction pattern obtained from 4D-STEM is individually processed to obtain structure factors by subtracting and normalizing with atomic form factors as described in chapter 3.5. ePDFs can be directly computed from the structure factors $S(q)$ without deconvolution with the probe spread function owing to the small convergence angle of the beam. Consequently, the diffraction patterns in the experimental 4D-STEM data can be processed to construct a 3D STEM-PDF data cube as shown in Figure 4.2a.

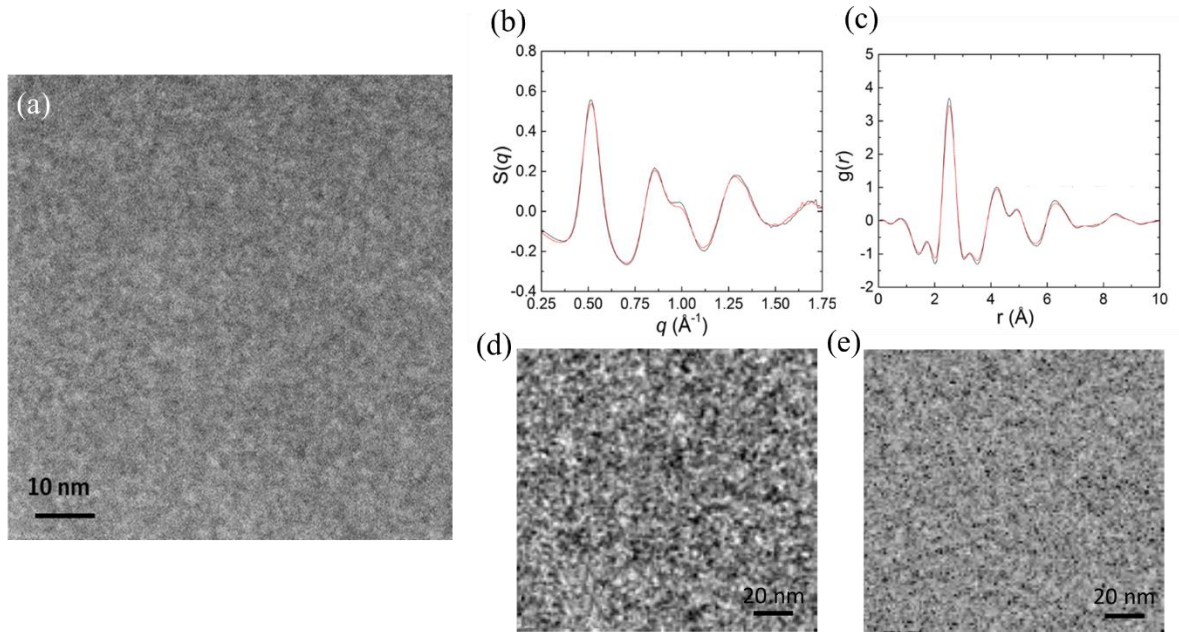


Figure 4.3: STEM-PDF analysis for characterization of as-spun $\text{Fe}_{85.2}\text{Si}_{0.5}\text{B}_{9.5}\text{P}_4\text{Cu}_{0.8}$ metallic glass ribbons. (a) a STEM-HAADF image. (b) Averaged structure factors and (c) averaged PDFs from the STEM-PDF data cube. (d) Maps for the first peak intensity of $S(q)$ s and PDFs.

Figure 4.3 illustrates the typical STEM-PDF analysis employed to characterize as-spun $\text{Fe}_{85.2}\text{Si}_{0.5}\text{B}_{9.5}\text{P}_4\text{Cu}_{0.8}$ metallic glass ribbons. STEM-HAADF image shows inhomogeneous intensity fluctuations represented by dark and bright intensity contrasts (Figure 4.3a). The intensity fluctuations are related to local structural variations of the materials, where dark and bright contrast in STEM-HAADF indicate lower and higher local density, respectively. Figure 4.3b and c display the averaged structure factors and PDFs in the 3D data cube, where one can analyze the overall atomic structure of the sample. Virtual images can be produced directly from the $S(q)$ and PDF cube by integrating the range of interest in q -space and r -space. Figure 4.3d and e depict virtual images generated using the first peak intensity, providing direct visualization of specific bonding information within the sample. Additionally, this approach offers phase mapping, allowing for the capture of structural heterogeneity revealed by SRO and MRO among different probe positions.

Hyperspectral analysis techniques, such as non-linear least squares (NLLS) or multi-linear least squares (MLLS), offer valuable tools for analyzing the $S(q)$ and PDF data cubes. NLLS involves fitting the data cube into a model with non-linear parameters, often utilizing Gaussian fitting for peak analysis. MLLS, on the other hand, fits the cube using linear combinations of reference spectra. Both methods reduce the dimensionality of the cube, resulting in 2D images of the fitting coefficients, commonly referred to as feature extraction analysis.

4.3. Mapping of strain and atomic structure

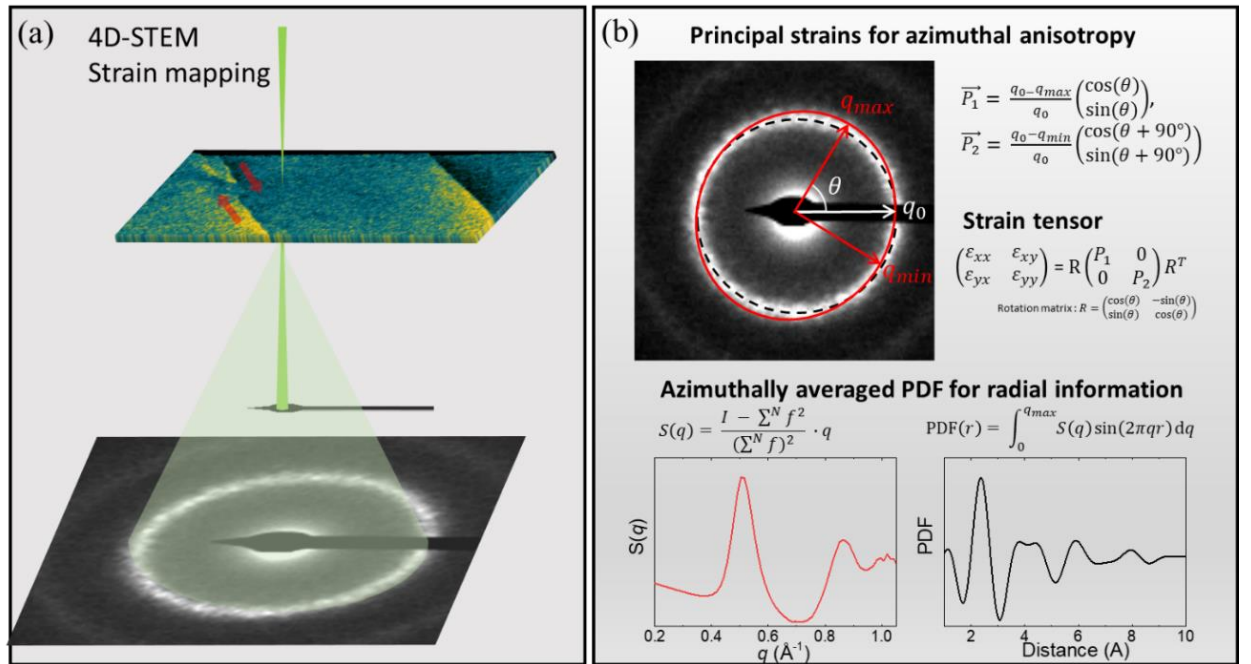


Figure 4.4: Schematic illustration of 4D-STEM-based strain and PDF mapping. (a) The quasi-parallel electron probe is focused on the TEM lamella. Spatially-resolved diffraction patterns are collected mapping a shear band region in a deformed metallic glass. (b) Data processing: principal strains (\vec{P}_1 and \vec{P}_2) are calculated from the elliptic distortion of the diffraction ring. For better visualization, the diffraction pattern is elongated to the principal strain direction. The strain tensors are algebraically obtained by projecting the principal strains to the reference coordinates (x- and y-axis). For PDF analysis, the local diffraction patterns are azimuthally integrated into intensity profiles $I(q)$. Structure factors, $S(q)$, are obtained by background subtraction of $I(q)$. The PDFs are obtained by Fourier sine transformation of $S(q)$.

Figure 4.4a provides a schematic representation of the 4D-STEM setup utilized for correlative strain and PDF mapping. In this setup, a quasi-parallel electron probe is focused to approximately 5 nm in diameter on an electron-transparent sample. The diffraction patterns contain azimuthal and radial information. The presence of stress induces distortions in the atomic structure,

introducing an anisotropy that manifests as an azimuthally elliptical distortion of the diffraction ring. By measuring the elliptical deviation of the local diffraction patterns, strain mapping can be achieved, as demonstrated by Poulsen et al.^[184] Figure 4.4b shows how the principal strains, represented by q_{max} and q_{min} , can be obtained from the long and short axes of the ellipse. Different from the previous studies^[180], an algebraic method was adopted for this thesis work using singular value decomposition (SVD) proposed by A. Fitzgibbon et al.^[185] to fit an ellipse to the diffraction ring. This provides an unbiased approach and reduces the demand for computational power orders of magnitudes compared to non-linear and iterative fitting methods.

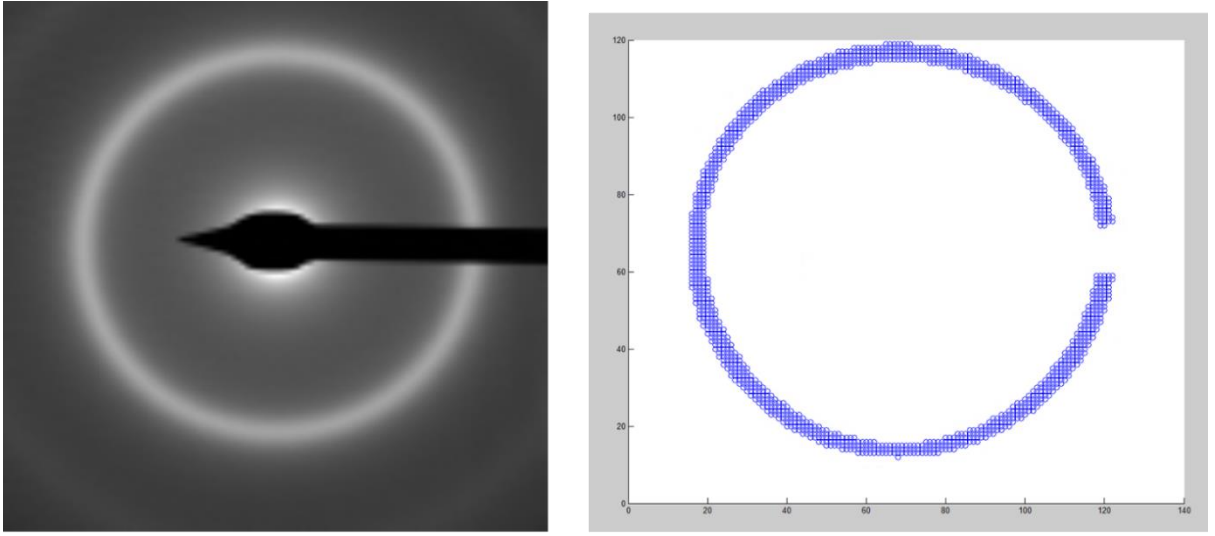


Figure 4.5: A typical diffraction pattern of $\text{Fe}_{85.2}\text{Si}_{0.5}\text{B}_{9.5}\text{P}_4\text{Cu}_{0.8}$ metallic glass (left) which was binarized using a threshold with $I(q_x, q_y) = 1$ for $0.95I_{\max} < I(q_x, q_y) < I_{\max}$ and 0 everywhere else (right).

The diffraction patterns are binarized using intensity = 1 when $0.95 I_{\max} < I(q_x, q_y) < I_{\max}$ and intensity = 0 everywhere else, where I_{\max} is the maximum intensity in the diffraction pattern and q_x and q_y are the coordinates of the pixels in reciprocal space (Figure 4.5).

An ellipse in the reciprocal space can be represented by an implicit second-order polynomial equation:

$$\mathbf{F}(\mathbf{C}, \mathbf{Q}) = \mathbf{C} \cdot \mathbf{Q} = aq_x^2 + bq_xq_y + cq_y^2 + dq_x + eq_y + f,$$

where $\mathbf{C} = [a \ b \ c \ d \ e \ f]$ and $\mathbf{Q} = [q_x^2 \ q_xq_y \ q_y^2 \ q_x \ q_y \ 1]^T$. $\mathbf{F}(\mathbf{C}, \mathbf{Q})$ is the mismatch distance of a data point (q_x, q_y) to the ellipse $\mathbf{F}(\mathbf{C}, \mathbf{Q}) = 0$. Thus, the best fit of an ellipse to the diffraction ring is equivalent to finding \mathbf{C} to minimize the sum of squared mismatch distances $\mathbf{D}(\mathbf{C}) = \min \sum_{i=1}^N \mathbf{F}(\mathbf{C}_i, \mathbf{Q}_i)^2$, where N is the total number of selected pixels by the thresholding and i is

the pixel sequence number. This least square problem can be solved by singular value decomposition (SVD) considering a rank-deficient generalized eigenvalue system, as $\mathbf{Q}\mathbf{Q}^T\mathbf{C}^T = \lambda\mathbf{P}\mathbf{C}^T$, where \mathbf{P} is a constrain matrix to avoid trivial solutions, e. g. $\mathbf{C} = 0$, as defined by

$$\mathbf{P} = \begin{bmatrix} 0 & 0 & -2 & 0 & 0 & 0 \\ 0 & 1 & 0 & 0 & 0 & 0 \\ -2 & 0 & 0 & 0 & 0 & 0 \\ 0 & 0 & 0 & 0 & 0 & 0 \\ 0 & 0 & 0 & 0 & 0 & 0 \\ 0 & 0 & 0 & 0 & 0 & 0 \end{bmatrix}$$

Solving the eigenproblem produces six eigenvalues and eigenvectors. The eigenvector associated with the smallest eigenvalue is the \mathbf{C} component minimizing the sum of squared mismatch distances, which is equivalent to the linear least square fitting method. Note that the center position of the diffraction patterns can shift when scanning a large field of view due to the distortion of the beam-focusing lens. The fitting algorithm simultaneously tracks the centers of the individual diffraction patterns for accurate fitting. From the fitted ellipse, the principal strains were determined as $\vec{\mathbf{P}}_1 = \frac{q_0 - q_{max}}{q_0} \begin{pmatrix} \cos(\theta) \\ \sin(\theta) \end{pmatrix}$ and $\vec{\mathbf{P}}_2 = \frac{q_0 - q_{min}}{q_0} \begin{pmatrix} \cos(\theta + 90^\circ) \\ \sin(\theta + 90^\circ) \end{pmatrix}$, where q_0 is the radius of the 1st ring for the unstrained case (averaged from an area far away from the deformed region), q_{max} , and q_{min} are the lengths of the maximum and minimum elliptical axis of the 1st ring. θ is the corresponding azimuthal angle of q_{max} to the x-axis. The deviatoric strain was calculated as $\varepsilon_{dev} = \frac{|\vec{\mathbf{P}}_1| - |\vec{\mathbf{P}}_2|}{2}$. The volumetric strain was calculated as $\varepsilon_{vol} = \vec{\mathbf{P}}_1 + \vec{\mathbf{P}}_2$. As shown in the equation, the measurement provides only in-plan strain ($\vec{\mathbf{P}}_1$ and $\vec{\mathbf{P}}_2$) and can only assess the z-axis averaged volumetric strain, assuming a homogeneous distribution of $\vec{\mathbf{P}}_3$ throughout the sample. Under an approximation, e.g. without consideration of chemical variation, relative density can be calculated by quantifying the area encircled by the 1st ring of each diffraction pattern in the 4D-STEM data. and compare them to an undeformed case.^[186] This approach considers the elliptical deviation of the diffraction rings due to strain and disentangles the density information from sample thickness.

Figure 4.6 shows an example of the processed strain fields, *i.e.* principal strain (\mathbf{P}_1 and \mathbf{P}_2), deviatoric (ε_{dev}), and volumetric (ε_{vol}) strains for a deformed $\text{Fe}_{85.2}\text{Si}_{0.5}\text{B}_{9.5}\text{P}_4\text{Cu}_{0.8}$ metallic glass ribbon. The amplitude of the principal strain representation (brightness) is defined by the strength of \mathbf{P}_1 and \mathbf{P}_2 . The orientation of \mathbf{P}_1 and \mathbf{P}_2 is represented by the colors. The color code for the deviatoric strain and the volumetric strain indicate strain amplitude.

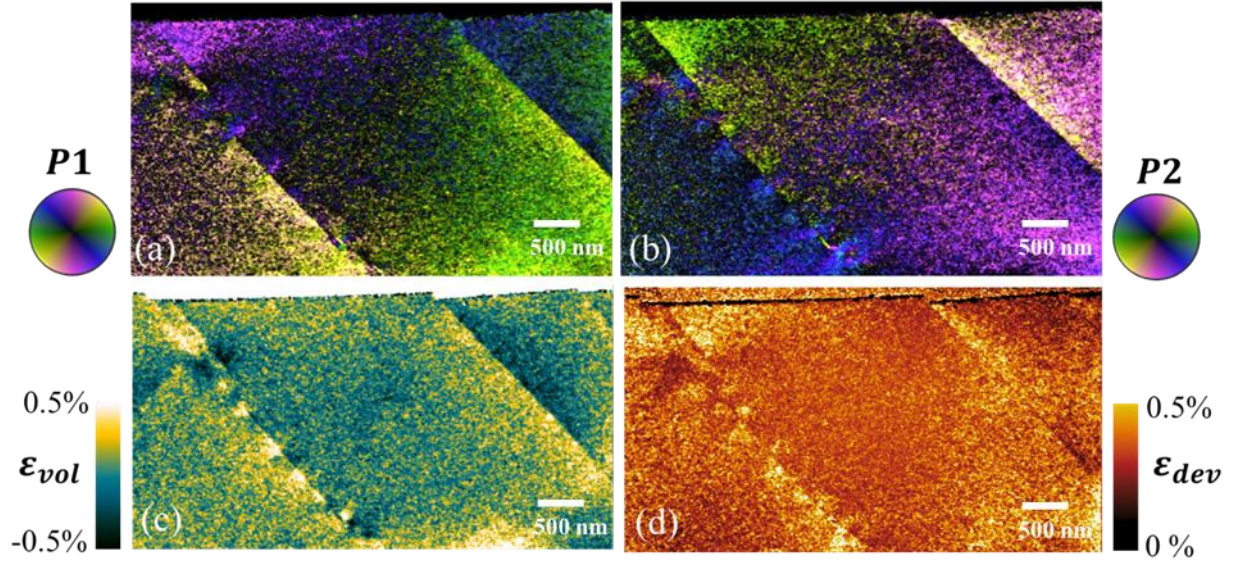


Figure 4.6: Deformed $\text{Fe}_{85.2}\text{Si}_{10.5}\text{B}_{9.5}\text{P}_4\text{Cu}_{0.8}$ metallic glass ribbon. (a) first principal strain, \mathbf{P}_1 , (b) second principal strain, \mathbf{P}_2 , (c) volumetric strain, and (d) deviatoric strain.

It is important to note that the strain signals are inherently averaged over the thickness of the sample due to the nature of the projected information in TEM. This averaging may lead to a loss of information regarding the full 3D strain field. Despite this limitation, analyzing the projected 2D strain provides a qualitative fingerprint and an easier way to visualize and interpret the behavior of strain states in materials.

Strain tensors can be calculated by setting the coordinate system with the x-axis parallel to the shear band of interest and the y-axis perpendicular to the shear band as $\begin{pmatrix} \varepsilon_{xx} & \varepsilon_{xy} \\ \varepsilon_{yx} & \varepsilon_{yy} \end{pmatrix} = \mathbf{R} \begin{pmatrix} |\vec{\mathbf{P}}_1| & 0 \\ 0 & |\vec{\mathbf{P}}_2| \end{pmatrix} \mathbf{R}^T$, where $\mathbf{R} = \begin{pmatrix} \cos(\theta) & -\sin(\theta) \\ \sin(\theta) & \cos(\theta) \end{pmatrix}$ is a rotation matrix. ε_{xx} and ε_{yy} represent the strain along the x-axis and y-axis. A positive value means tensile strain indicating the atoms are pulled away from each other and a negative value indicates compressive strain corresponding to atoms squeezed closer along the axial direction. ε_{xy} represents the shear component of the strain tensor. A positive value indicates the clockwise and a negative value anticlockwise shearing. The maximum shear strain was determined as $\tau_{max} = \frac{|\vec{\mathbf{P}}_1| - |\vec{\mathbf{P}}_2|}{2} \begin{pmatrix} \cos(\theta) \\ \sin(\theta) \end{pmatrix}$. The amplitude is defined as deviatoric strain and the orientation indicates the maximum tensile direction.

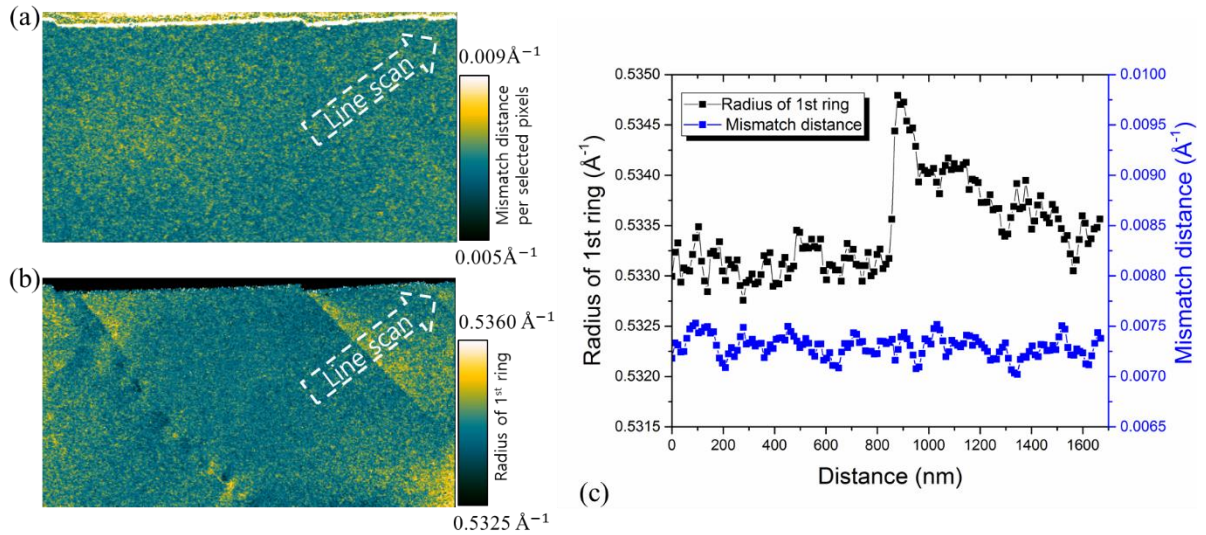


Figure 4.7: Statistical analysis for the accuracy of the strain measurement. (a) Map of fitting error for strain measurement. (b) Map of the radius of the 1st ring (q_{max}). (c) Line profiles of the mismatch distance and the radius of the 1st ring in the region indicated by white dash arrows in (a) and (b).

For statistical analysis of the accuracy of the strain measurement, the standard deviation of volumetric strain (Figure 4.6c) is calculated using the data acquired far away from any shear band. The standard deviation of the volumetric strain is 0.08%. However, this standard deviation is also affected by the true local structural variations in the material as discussed in chapter 2.1, and is, therefore, an upper limit for the uncertainty of the strain measurement. Nevertheless, the standard deviation is well below the typical shear band features (> 0.2-0.5 %), thus explaining the clear detectability of the strain distribution. Furthermore, the average squared mismatch distance for the ellipse fitting is calculated for a statistical understanding of fitting error and compared to the variation of the 1st ring radius in Figure 4.7a. Only random noise can be observed in the fitting error map. This value gives rise to an accuracy of about 0.1 % of the fitting method, which also exceeds the typical shear band features observed in this work. As a comparison, the map of the radius of the 1st diffraction ring shows clear shear band features, *e.g.*, asymmetric distribution across shear bands and alternating fluctuations along the shear band (Figure 4.7b). This confirms that the observed strain features in 4.7b are from the authentic material structure.

4.4. Importance of TEM sample thickness for 4D-STEM observation

As discussed, TEM studies typically require thin electron-transparent specimens to minimize projection artifacts and reduce the contributions of multiple scattering. The FIB technique is

commonly utilized for preparing TEM samples. However, an important consideration arises regarding the extent of structural modifications, such as strain relaxation, induced in thin samples due to the increased surface-to-volume ratio and the thinning process itself. To investigate the influence of TEM sample thickness on the measurement of strain fields, 4D-STEM has been employed as a pre-study. A model system involving a deformed $\text{Fe}_{85.2}\text{Si}_{10.5}\text{B}_{9.5}\text{P}_4\text{Cu}_{0.8}$ metallic glass ribbon was utilized.^[187]

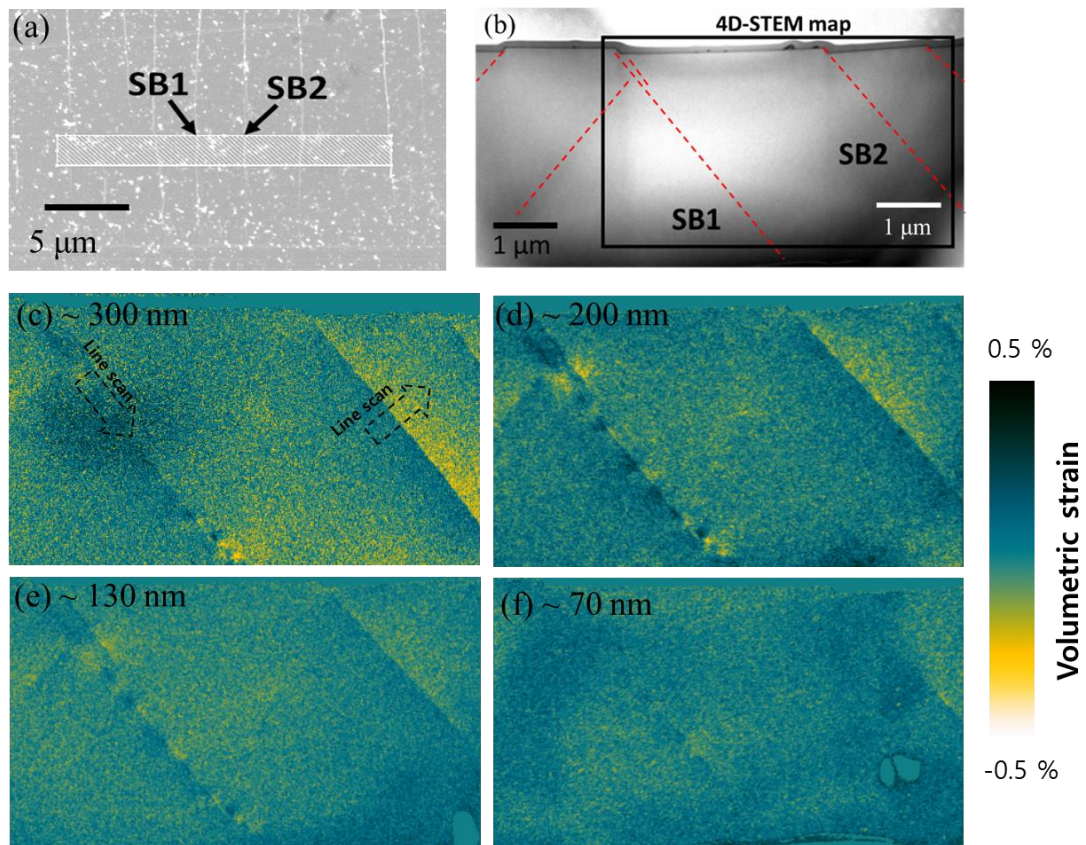


Figure 4.8: Influence of sample thickness on the volumetric strain of a deformed $\text{Fe}_{85.2}\text{Si}_{10.5}\text{B}_{9.5}\text{P}_4\text{Cu}_{0.8}$ metallic glass ribbon. (a) SEM image showing the area beside a scratch with shear offsets clearly visible. The shadowed rectangle indicates the location of the prepared TEM lamella. (b) STEM-HAADF image of the TEM lamella, where the expected locations of the shear bands are indicated by red dashed lines according to the shear offsets at the surface. A 4D-STEM map was acquired at the area indicated by the black rectangle, where the shear bands of interest are labeled SB1 and SB2. Volumetric strain map of the sample measured for different thicknesses of about (c) 300 nm, (d) 200 nm, (e) 130 nm, and (f) 70 nm.

The local strain field near a shear band in the deformed metallic glass was measured, and the ribbon was subsequently thinned in several steps. The strain distribution at the same location was then analyzed to assess any potential variations caused by the sample thinning process. Figure 4.8c-f displays maps visualizing the measured volumetric strain (ϵ_{Vol}) of the 300 nm to 70 nm

thick TEM sample. This measurement directly indicates the contribution of residual hydrostatic stress, disregarding differences in coordination. The color scheme represents strain amplitude, with dark blue indicating tension (positive sign) and bright yellow indicating compression (negative sign), reflecting a decrease in atomic distance. The strain maps reveal an asymmetric distribution of strain across the shear bands, with a distinct transition occurring at the shear plane. Taking into account the probe and scan step size, the width of the shear band can be estimated to be below 20 nm. Notably, a particular type of shear band was observed, exhibiting alternating tension and compression features along the shear direction. Further details about this shear band feature will be discussed in subsequent chapters, providing a more in-depth analysis and understanding. Here, only considering the observed stress distribution, it becomes clear that the 200 nm thick sample exhibits better-defined alternating stress features and the sharp transition at the shear plane, as well as the local structural heterogeneity at the nanometer scale within the overall glass matrix (Figure 4.8d). Further thinning does not enhance the contrast of these features but reduces them. Particularly, the asymmetric strain level across the shear band is reduced for the 130 nm thick sample (Figure 4.8e). Eventually, the 70 nm thick sample exhibits minimal asymmetric strain and alternating features, indicating a significant reduction in residual stresses (Figure 4.8f).

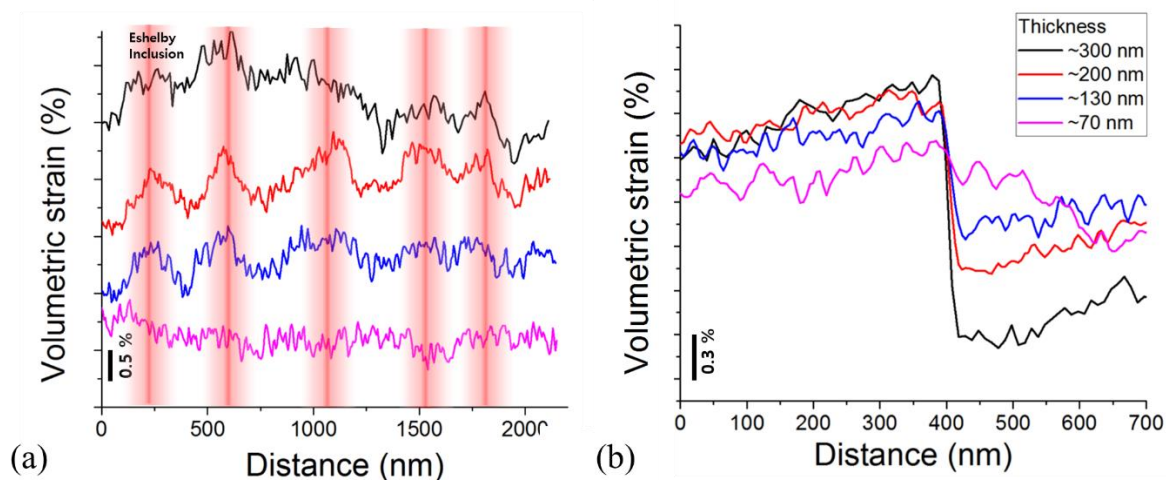


Figure 4.9: Line profiles of the volumetric strain maps (a) along the SB1 and (b) perpendicular to SB2 in the directions indicated by dash arrows in Figure 4.8c-f for different thicknesses of about 300 nm, 200 nm, 130 nm, and 70 nm.

Figure 4.9a depicts the changes in the signal-to-noise ratio (SNR) using line profiles along the alternating features of a shear band in the same area of a sample thinned to different thicknesses. In the case of the 300 nm thick sample, the strong background obscures the contrast of the alternating features, resulting in blurred peaks. This is primarily attributed to the low SNR caused by significant plural scattering of the electron beam. This plural scattering leads to a significant

background in the diffraction patterns, which masks the anisotropy of the first diffraction ring and introduces errors in the strain measurement. Hence, the thickness of the sample affects the signal and the information obtained from it. In the 200 nm thick sample, the alternating features along the shear band are much more clearly visible due to the increased SNR with the reduced plural scattering. When the sample is thinned further, the contrast of the features is gradually reduced until it (almost) disappears at a thickness of 70 nm. This indicates that the deformed structure relaxes during excessive thinning. Looking at the absolute variation of the volumetric strain across the shear band (Figure 4.9b), the 300 nm thick sample has a difference of approximately 1.2% across the shear band. Subsequent thinning, already starting at 200 nm sample thickness, leads to a gradual reduction in the strain difference across the shear band. This can be attributed to two main factors. During thinning, the surfaces of the sample are damaged, causing the projected information from the damaged layers to contribute stronger when the sample becomes thin. Additionally, the thin sample is more susceptible to strain relaxation at the surface due to the increased surface-to-volume ratio. This highlights the critical importance of maintaining an adequate sample thickness to preserve the native deformation and the fundamental atomic configuration of metallic glasses. As the strain measurement is inherently averaged along the thickness direction, the out-plane strain cannot be easily analyzed. However, it is reasonable to expect that the distribution of the out-plane strain state will become non-trivial when the stored residual strain starts to relax during sample thinning. This can lead to an incorrect determination of the precise strain values when using the S/TEM to examine thin lamella. Nevertheless, to minimize the influence of sample thinning, samples with about 200 nm thickness, balancing data quality (SNR), and the preservation of the strain distribution, are used for this work.

Chapter 5

5. Mapping local atomic structure of metallic glasses using machine learning aided 4D-STEM PDF

The spatial distribution of local phases is of significant importance in metallic glasses that consist of mixed-type nano-phases or structural variants. However, characterizing the atomic arrangement of the amorphous structure, including nanoscale structural variations, poses a significant experimental challenge, which has hindered the exploration of new material designs. In this study, a novel approach called, machine learning aided 4D-STEM PDF, is introduced to map the distribution of structural variants and to characterize the local atomic structure in metallic glasses.

This chapter has been adapted from a manuscript currently under review for publication in *Acta Materialia*. The presented results have been reproduced in this chapter. Sentences and paragraphs which have been reused with only minor modifications from the original manuscript are indicated by quotation marks.

5.1. Introduction

In chapter 4, STEM-PDF was introduced as a method to characterize the local atomic packing structure of amorphous materials. By utilizing a nanometer-scale electron probe and employing 4D-STEM acquisition, STEM-PDF enables the analysis of the atomic structure and phase mapping at the nanoscale. However, the information obtained from STEM-PDF is subject to averaging over the (anisotropic) column in the projection direction, leading to an overlap problem. Additionally, the limited collection angle of the electron diffraction patterns poses challenges in resolving the peaks of the pair distribution function, making it difficult to detect subtle variations in the probed atomic structure.^[42]

In recent efforts, multivariate statistical analysis (MSA), such as principal component analysis (PCA) and independent component analysis (ICA), have been applied to overcome the projection problem and extract subtle signal variations from STEM-PDF datasets.^[174] The results have demonstrated the effectiveness of combining STEM-PDF and MSA techniques to reveal the atomic structure of amorphous materials at the nanoscale. However, PCA calculation is only based on progressive approximations of the entire dataset and yields only representations for phases present in significant amounts^[188], while ICA assumes statistically independent and non-Gaussian distributed base functions to make up the PCA results.^[189-190] These approximations limit the identification of complex dependencies between hidden variables, especially when different atomic short- and medium-range orders (S/MROs) exhibit similar partial features. Furthermore, PCA, which is based on linear combinations involving both negative and positive numbers, often entails complex cancellations, making it challenging to intuitively interpret resulting pair distribution functions in many cases. Due to these reasons, the utilization of matrix factorization, which permits only additive combinations with non-negativity constraints, can be beneficial in analyzing STEM-PDF datasets and determining the atomic configuration of distinct structural types.^[190]

To address these limitations, a novel analytical approach is proposed to study the local atomic structure of metallic glasses using nonnegative matrix factorization (NMF) applied to STEM-PDF. A $\text{Fe}_{85.2}\text{Si}_{10.5}\text{B}_{9.5}\text{P}_4\text{Cu}_{0.8}$ metallic glass ribbon has been employed as a model system due to its soft ferromagnetism.^[187] This approach identifies the structural bases of the glass phase without relying on prior knowledge from atomic simulations. The resulting pair distribution functions provide interpretable packing information for individual structural bases, forming the heterogeneous amorphous matrix. With this analysis, the presence of two distinct structural types was uncovered, which exhibit characteristics resembling a more liquid-like and a more solid-like state, distributed

at a length scale of a few nanometers. Interestingly, even after thermal annealing, the average atomic configuration of these two structural types remains unaltered, indicating the persistence of local structures during relaxation without the emergence of new structural phases. However, the relative population and spatial distribution of these two structural types underwent significant changes during annealing.

5.2. Experimental details

The as-spun $\text{Fe}_{85.2}\text{Si}_{0.5}\text{B}_{9.5}\text{P}_4\text{Cu}_{0.8}$ glassy ribbon was rapidly annealed for approximately 10 seconds at a temperature $T_a = 633 \text{ K}$ ($\sim 1.1 T_g$). TEM lamellae from both as-spun and annealed ribbons were prepared by FIB (FEI Strata 400S). Thinning was performed to a sample thickness of about 50 nm for electron transparency with gradually decreasing acceleration voltage from 30 kV to 5 kV and beam currents from 8 nA to 2 pA to reduce the ion beam damage. The thicknesses of the FIB-prepared lamellae were measured by energy-filtered transmission electron microscopy (EFTEM) and confirmed to be about 50 nm for both samples using an estimated inelastic mean free path of 75 nm for electrons at an operation voltage of 300 kV and a mass density of 7.3 g/cm^3 .^[191]

Conventional high-angle annular dark-field (HAADF)-STEM measurements were performed using an aberration-corrected Titan 80-300 (FEI Company) operated at a voltage of 300 kV with a 50 μm condenser C2 aperture, a camera length of 90 mm, and collection angle 70-200 mrad. Selected area electron diffraction (SAED) measurements were performed in TEM mode with parallel illumination using a camera length of 245 mm to determine the average PDFs of the as-spun and annealed metallic glasses.

4D-STEM experiments were performed using microprobe STEM mode with spot size 7, and a 30 μm C2 aperture resulting in a semi-convergence angle of 0.6 mrad. These settings result in a probe diameter of approximately 2 nm. A Merlin pixelated direct electron detector (Quantum Detector Ltd.) was used to record the diffraction patterns with a camera length of 195 mm. 4D-STEM maps were acquired by capturing the diffraction patterns (256 \times 256 pixels) with 4 ms exposure time for each pattern while scanning the electron probe over the 2D sample plane with a step size of 1.2 nm and a scan range of 128 \times 128 pixels. As described in chapter 4.2, the diffraction patterns were integrated azimuthally to obtain radial profiles $I(q)$, where $q = 2\theta/\lambda$, θ is half of the scattering angle, and λ is the wavelength of the incident electrons. The structure factor was

calculated by subtracting and normalizing with atomic scattering factors. The PDFs are obtained by a Fourier sine transformation of the structure factors according to the following equation.

5.3. Phase decomposition and mapping for Fe-based metallic glasses

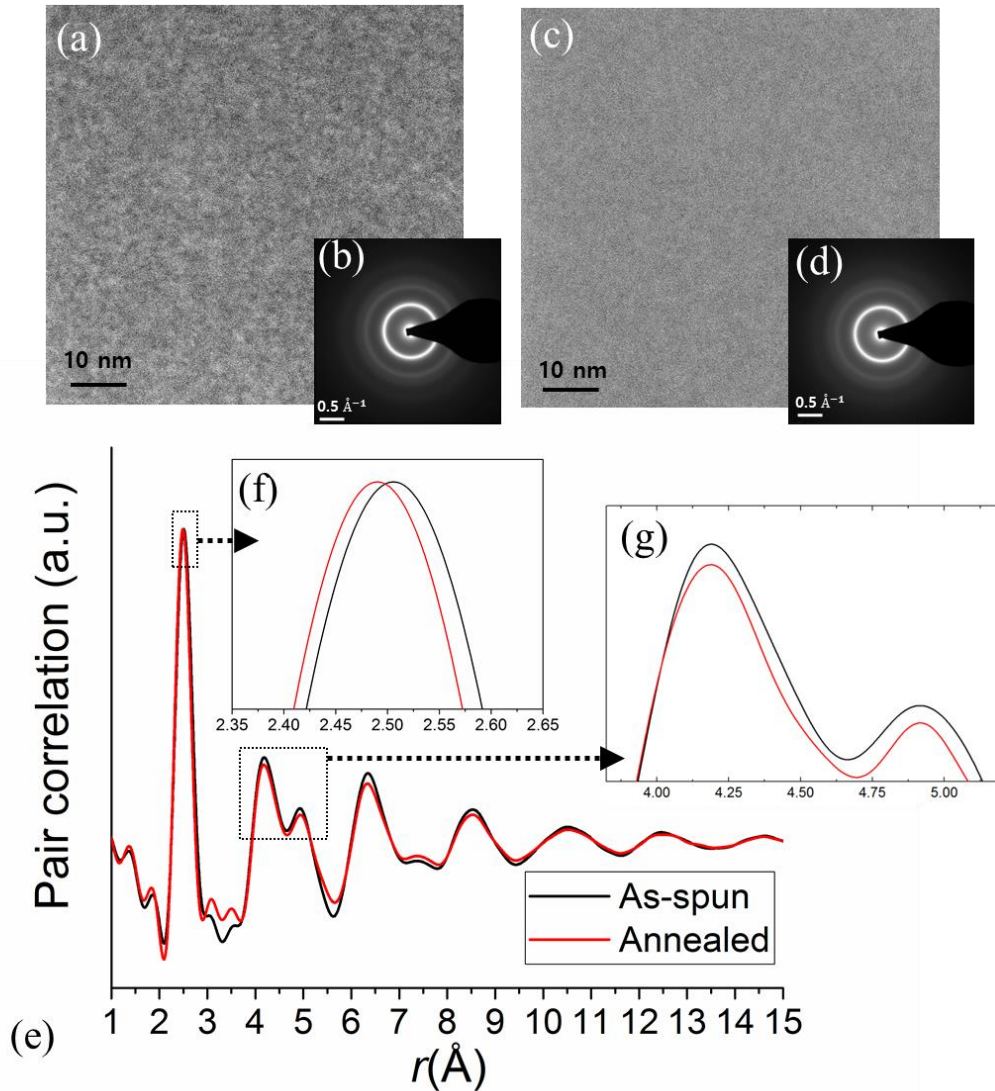


Figure 5.1: Conventional S/TEM investigation of as-spun and annealed $\text{Fe}_{85.2}\text{Si}_{0.5}\text{B}_{9.5}\text{P}_4\text{Cu}_{0.8}$ metallic glasses. (a) STEM-HAADF image and (b) SEAD pattern for the as-spun glass. (c) STEM-HAADF image and (d) SEAD pattern for the annealed glass. (e) PDFs calculated from the SEAD patterns of the as-spun and annealed glasses. The height of the PDFs is normalized by their first peak for easy presentation of peak shifts.

The as-spun and annealed $\text{Fe}_{85.2}\text{Si}_{0.5}\text{B}_{9.5}\text{P}_4\text{Cu}_{0.8}$ metallic glasses are investigated by conventional S/TEM analysis as shown in Figure 5.1. STEM-HAADF images reveal inhomogeneous intensity fluctuations showing darker and brighter regions. The intensity fluctuation can be related to local

structural variations in the metallic glasses, where dark regions indicate lower density and bright regions represent higher density. The length scale of the fluctuation is about 3 - 5 nm and is evenly distributed in the as-spun sample (Figure 5.1a). “The length scale matches the previous TEM study on metallic glasses.”^[147] It can be seen that the intensity fluctuation is substantially reduced after annealing treatment (Figure 5.1c). The difference between the samples, which have a similar thickness, indicates different degrees of structural heterogeneity within the samples.

The SAED diffraction patterns show the amorphous nature of both samples (Figure 5.1b and d). PDFs are calculated from the SAED patterns to compare the average atomic configuration in the as-spun and annealed samples (Figure 5.1e). Although quantitative analysis of the electron pair correlation values is not possible due to different multiple scattering contributions from the samples, the shift of PDF peak positions can still be reliably determined. It can be seen that the first peak of the PDF (2.51 Å for as-spun and 2.49 Å for annealed samples) is shifted to a shorter atomic distance, indicating expected structural densification after the annealing treatment. This corresponds to an approximate decrease of the free volume of about 2.5 % ignoring differences in medium-range coordination.^[192] No significant differences in the peaks at high r are observed between samples, revealing that major structural change only happened in the short/medium range during the annealing.

For local analysis, the 4D-STEM datasets are transformed into PDF cubes and analyzed using an NMF algorithm, as depicted in Figure 5.2. To model the signal mixing, the STEM-PDF data cube is represented by a 2D matrix V , where the rows are PDFs at different locations and the columns correspond to the atomic pair distance. Ideally, the experimental PDFs can be seen as a linear combination of basis PDFs. In other words, the PDFs are from basis motifs. The mixed signal can therefore be modeled by a matrix factorization $V = WH$, where the rows of the matrix H represent the basis PDFs and W is a weighting matrix describing the contributions of basis PDFs mixed in V . The NMF calculation can deconvolute the basis PDFs and their relative contributions by finding W and H . The NMF is distinguished from other statistics-based learning methods by its non-negativity constraints for the matrix factors.^[190] To satisfy these constraints, V is shifted to be positive by adding the global minimum before applying the algorithm. The exact height of V is not crucial for the success of NMF in identifying the basis PDFs because the information in the PDFs lies in the oscillations of the signals, not the background. The non-negativity constraint only allows additions during matrix factorization, which aligns with the idea of a neural network where neuron connectivity and synaptic strength cannot be negative. These characteristics enable the recovery of the individual structure of basis motifs, providing a part-based representation (Figure 5.2b, top).

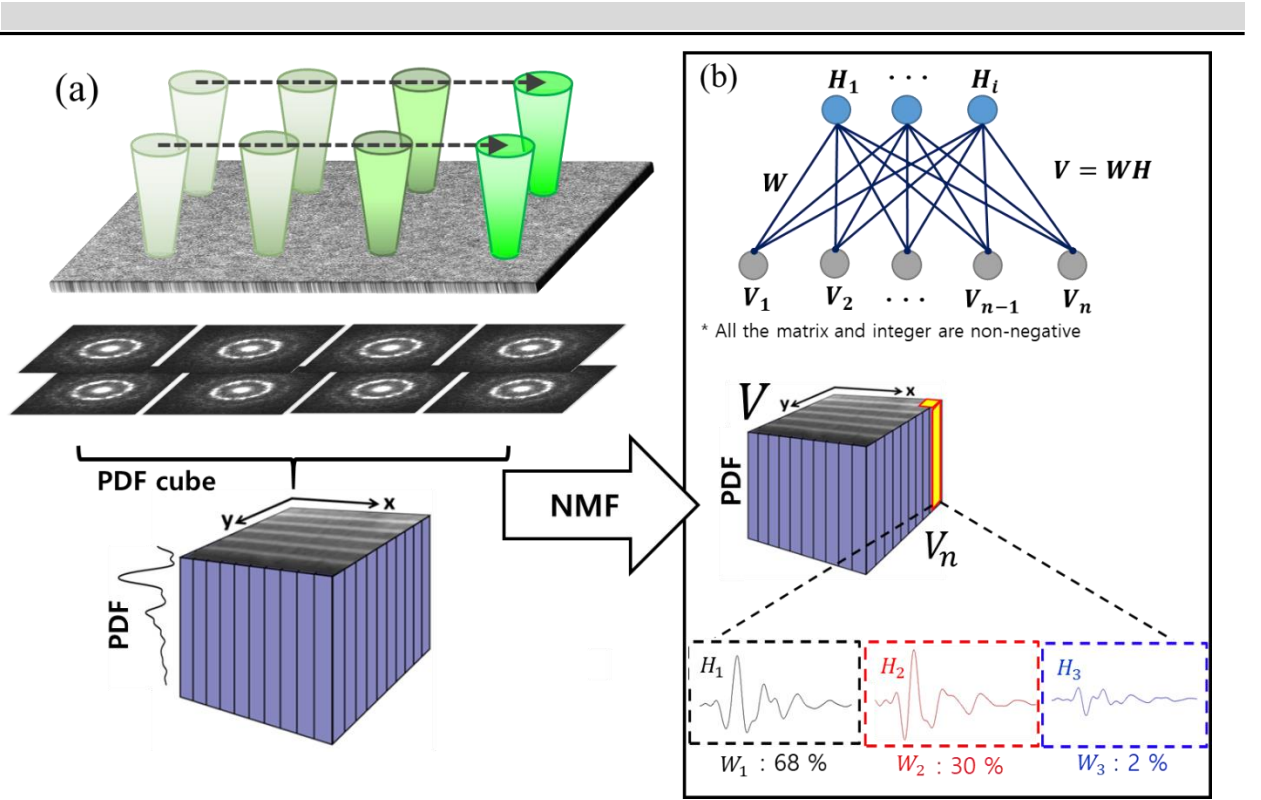


Figure 5.2: (a) Schematic illustration of NMF-aided STEM-PDF analysis. (b) Probabilistic blind source model underlying non-negative matrix factorization. The diagram model depicts a network in which experimental V_n are in the bottom layer of nodes and the blind sources H_i in the top layer of nodes (top). The experimental V can be represented by a probability distribution with $V_n = \sum_1^i W_{n,i} H_i$. According to the model, the significance of sources H_i on V is represented by a connection with the weighting matrix $W_{n,i}$. For the application to STEM-PDF cube, an experimental PDF is decomposed by PDFs from basis sources V_1, V_2 , and V_3 (basis PDFs) with weighting constants H_1, H_2 , and H_3 .

In this work, the low-rank approximate NMF algorithm was used, which is implemented in Matlab.^[193] The algorithm finds an approximate factorization WH using iterative update rules for nonnegative V . A 2-step NMF calculation is applied to the STEM-PDF dataset to ensure a unique and accurate solution targeting 3 principal factors (with the expectation of 2 different glassy configurations and a residual noise signal, which has been confirmed as discussed below). The first NMF calculation roughly searches for the global minimum as a unique solution with low termination tolerance for the residual signal, using a maximum of 5 iterations to find good starting points W_0 and H_0 for the next calculation. In the second step, NMF starts from the initial W_0 and H_0 and calculates an accurate solution with 0.00001% termination tolerance for the residual signal and up to 1000 iterations.

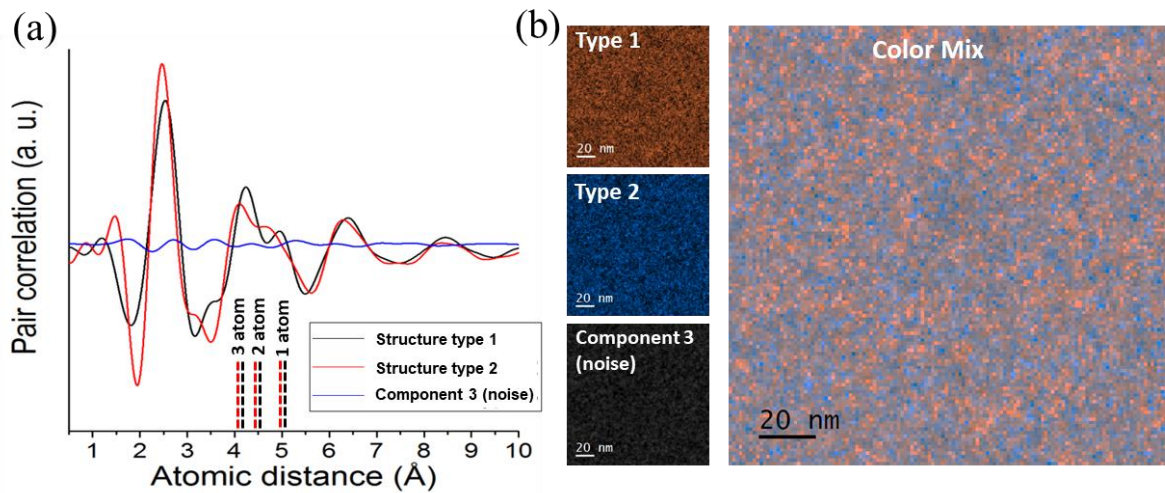


Figure 5.3: NMF results for a STEM-PDF dataset of the as-spun $\text{Fe}_{85.2}\text{Si}_{10.5}\text{B}_{9.5}\text{P}_4\text{Cu}_{0.8}$ metallic glass. (a) Obtained basis PDFs. The vertical dashed lines indicate the distances of the polyhedra connections with different numbers of shared atoms (ranging from 1 to 3) for structural type 1 (black) and structural type 2 (red). (b) Spatial distribution of the basic structural types indicated by different colors. The brightness indicates their population. All three maps are incorporated in the color mix map at the right.

Figure 5.3 shows the NMF results for a STEM-PDF dataset. The basis PDFs represent the average atomic configuration for each structural type, which may consist of various atomic motifs and different connection schemes. Structural types 1 and 2 show typical PDF patterns of the S/MRO structure of an amorphous material. Note that Structural type 3 only shows wave-like fluctuations with a significantly reduced correlation amplitude compared to other PDFs. Such simple fluctuations are also observed in PCA analysis for low-ranked information which can be considered to be background noise.^[194] Structural types 1 and 2 can be clearly distinguished by their first and second peaks. The first peak position of structural type 1 corresponds to larger atomic distances of 2.53 Å compared to structural type 2 at 2.46 Å. The first peak of structural type 2 is substantially higher and shaper than that of structural type 1, *e.g.*, their full width at half maximum (FWHM) are 0.65 Å (structural type 1) and 0.48 Å (structural type 2). This observation indicates that Structural type 2 possesses denser (with higher coordination number) and more well-defined nearest neighbors than structural type 1. In line with the first peak information, the second peak of structural type 2 (4.10 Å) is located at a shorter atomic distance compared to that of structural type 1 (4.24 Å), indicating that structural type 2 exhibits a denser structure even in the second nearest neighbor arrangement. Notably, the second peaks of both types appear with a shoulder peak at a higher atomic distance. Since the polyhedral clusters used to describe the structure in metallic glasses share different numbers of atoms to overcome packing frustration, the position of the shoulder peak can be related to the number of shared atoms, which can offer insights into cluster

connectivity and the resulting MRO.^[195-196] For polyhedra connections corresponding to 1 atom, 2 atoms, and 3 atoms, the most probable distance for the 2nd peak can be estimated to be $2R_1$ (5.05 Å for type 1 and 4.92 Å for type 2), $\sqrt{3}R_1$ (4.38 Å for type 1 and 4.26 Å for type 2), and $\sqrt{\frac{8}{3}}R_1$ (4.13 Å for type 1 and 4.02 Å for type 2), where R_1 is the first peak position of each motif. The estimated distances for the polyhedra connections with the number of shared atoms are marked by dashed lines for both structural types in Figure 5.3a. The position of the second peak maximum occurs at $\sqrt{\frac{8}{3}}R_1$ for both structural types, indicating that the structural types are dominated by polyhedra connected by sharing three atoms. Interestingly, only their side peaks appearing at larger pair distances show a meaningful difference between the two types. The side peak of type 1 is located at a relatively large atomic distance (4.95 Å), which corresponds to vertex connections (single atom shared between clusters). In contrast, the position of the shoulder of structural type 2 (4.66 Å) indicates that edge connections (two atoms shared between clusters) dominate here. Since the number of shared atoms in the polyhedral connections increases when the medium-range packing efficiency of the system becomes higher,^[64, 197] this means that structural type 2 exhibits a higher packing efficiency in the SRO and MRO consisting of more energetically stable motifs, *i.e.*, geometrically favored motif (GFM), compared to structural type 1 possessing more geometrically unfavored motifs (GUM).^[70] Following the commonly used description in simulations, structural type 1 is referred to as “liquid-like” and structural type 2 as “solid-like”.^[198] “The spatial distribution of each structural type is shown in Fig. 5.3b. Note that structural type 3 is regarded as noise and excluded from further analysis. The correlation length of each structural type is measured by an autocorrelation analysis of the maps. The size of the local zones is 5.43 nm for the liquid-like region and 5.66 nm for the solid-like region, which is in good agreement with previous observations obtained from nanobeam diffraction and simulations.^[147]”

Figure 5.4 compares the PDFs for the liquid-like and solid-like structural basis of the as-spun and annealed $\text{Fe}_{85.2}\text{Si}_{10.5}\text{B}_{9.5}\text{P}_4\text{Cu}_{0.8}$ metallic glasses and their spatial distribution. The PDFs for the liquid-like and solid-like structural basis, which have been obtained fully independently for the two different samples, are in excellent agreement with each other except for slight peak height deviations due to sample thickness differences (Figure 5.4a and b).

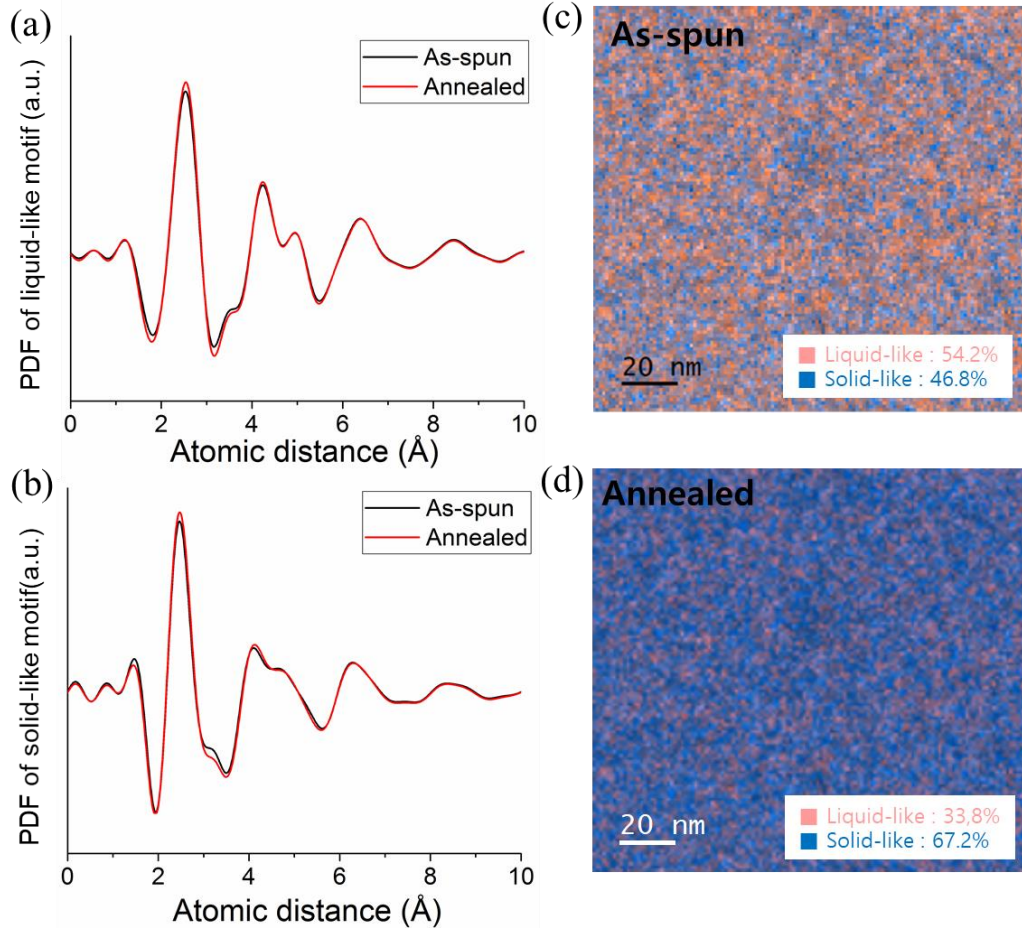


Figure 5.4: Atomic structure mapping of the as-spun and annealed $\text{Fe}_{85.2}\text{Si}_{10.5}\text{B}_{9.5}\text{P}_4\text{Cu}_{0.8}$ metallic glasses using NMF-aided STEM-PDF analysis. Basis PDFs of (a) the liquid-like and (b) the solid-like structural bases separately obtained from both as-spun and annealed metallic glass samples. Maps of the liquid-like and solid-like structural bases for (c) as-spun and (d) annealed samples with the fraction of each structural type indicated.

This agreement confirms the reliability and validity of the method. More importantly, the results reveal that both as-spun and annealed samples possess the same basic structural types with nearly identical atomic configurations. This indicates that the basic configuration of each structural type persists during relaxation. The observation of the two types of structural motives matches MD simulations, which characterized the glass motifs into two groups of basis motifs, *i.e.* GFMs and GUMs.^[75, 199] Their relative contribution and the spatial distribution was further quantified in both the as-spun and annealed sample using MLLS. It was found that the annealing treatment effectively changes the concentration and spatial distribution of the structural bases. The difference can be seen in Figure 5.4c and d, where the concentration of the solid-like regions significantly increases from 46.8 % (as-spun sample) to 67.2 % (annealed sample). This experimental observation supports the theoretical hypothesis that the relaxation process near the glass transition temperature leads to a larger fraction of the stable structural type with the annihilation of excessive free volume.

5.4. Summary

A new approach has been proposed for characterizing the local atomic packing and mapping their distribution in metallic glasses using machine learning-assisted analysis for the 4D-STEM PDF dataset. NMF is utilized for blind source separation of STEM-PDF datasets, offering a part-based representation that facilitates intuitive interpretation of the structural bases of metallic glasses. The study focuses on experimentally investigating the local atomic configuration and distribution in metallic glasses. The results reveal the existence of two fundamental glassy structures, representing more liquid-like and more solid-like states. These structures are found to be distributed at the nanoscale in both as-spun and annealed $\text{Fe}_{85.2}\text{Si}_{0.5}\text{B}_{9.5}\text{P}_4\text{Cu}_{0.8}$ metallic glasses. Notably, the atomic configuration of these two structures remains essentially unchanged between the as-spun and annealed glass, indicating structural persistence during relaxation. However, the relative population and distribution of these structures undergo significant changes during annealing, without the emergence of additional structural types. These findings contribute to a deeper understanding of the relaxation phenomena in metallic glasses and provide insights into the structural evolution of these materials.

Chapter 6

6. Direct observation of quadrupolar strain fields forming a shear band in metallic glasses

For decades, S/TEM techniques have been employed to understand shear bands in metallic glasses and their formation to improve their mechanical properties. However, conventional S/TEM cannot provide information on the local strain and atomic structure, which is the key to describing the structure of shear bands, due to intermixing sample thickness, atomic density, and elemental species in the regular image information. For this work, 4D-STEM has been applied to map and directly correlate the local strain and the atomic structure at the nanometer scale in deformed metallic glasses.

This chapter is based on a modified version of the publication entitled “Direct observation of quadrupolar strain fields forming a shear band in metallic glasses” published in *Advanced materials* 2023.^[200] The results presented in this chapter have been reproduced from that publication.

6.1. Introduction

Considerable efforts have been dedicated to experimentally demonstrating the existence of STZs, which are theoretically defined as Eshelby inclusions in a plastically deformed glassy matrix, using techniques such as DSC^[201], DMA^[111, 202], and XRD^[203]. These studies have statistically shown a decrease in density in metallic glasses after plastic deformation and attributed an increase in free volume to the activation of STZs. However, the limited spatial resolution of these methods hampers the ability to obtain structural information about individual STZs.

Recently, Maaß et al. observed a reduction in scattering intensity at the core of shear bands, indicating localized dilation in a deformed metallic glass^[30], while Rösner et al.^[204] observed alternating scattering intensity along a shear band associated with local density fluctuations. These observations provided detailed insights into the morphology of shear bands.

However, conventional STEM-ADF imaging averages information related to sample thickness, atomic density, and elemental composition, thereby hindering direct imaging of Eshelby inclusions. To date, neither Eshelby inclusions nor surrounding stress fields have been visualized experimentally and thus an experimental verification of the STZ-based deformation theory is missing. This lack of experimental information has impeded further development of deformation theories and new material designs. Therefore, 4D-STEM is employed to correlate atomic density and strain fields at the nanoscale in deformed metallic glasses, enabling the visualization of quadrupolar strain fields forming a shear band. To confirm the universality of the phenomenon, two distinct metallic glasses, $\text{Zr}_{46}\text{Cu}_{38}\text{Al}_8\text{Ag}_8$ and $\text{Fe}_{85.2}\text{Si}_{0.5}\text{B}_{9.5}\text{P}_4\text{Cu}_{0.8}$ were studied with an identical 4D-STEM setup.

6.2. Experimental details

$\text{Fe}_{85.2}\text{Si}_{0.5}\text{B}_{9.5}\text{P}_4\text{Cu}_{0.8}$ (at.%) and $\text{Zr}_{46}\text{Cu}_{38}\text{Al}_8\text{Ag}_8$ (at.%) master alloy ingots were prepared by arc melting in a Ti-gettered argon atmosphere. The $\text{Fe}_{85.2}\text{Si}_{0.5}\text{B}_{9.5}\text{P}_4\text{Cu}_{0.8}$ (at.%) ribbons, width ~ 25 mm and thickness ~ 20 μm , were prepared from the melt by rapid solidification onto rotating Cu wheels. The $\text{Zr}_{46}\text{Cu}_{38}\text{Al}_8\text{Ag}_8$ bulk metallic glass (1 cm \times 1 cm \times 1 mm plate) was fabricated by suction-casting into a water-cooled copper mold. The amorphous nature of samples was confirmed by X-ray diffraction (XRD), electron diffraction as well as differential scanning calorimetry (DSC). Scratch tests were performed with a scratch length $l_s = 1$ mm with normal loads $F_n = 10$ N for the Fe-based metallic glass ribbon and $F_n = 15$ N for the Cu-Zr-based bulk metallic

glass with a sliding velocity $v_s = 0.1$ mm/s under ambient conditions using a diamond tip with a radius of $210 \mu\text{m}$. For the STEM analysis, electron transparent TEM lamellae were prepared by focused ion beam (FIB), FEI Strata 400S, lifting out a specimen from the vicinity of the scratches. Thinning was performed in the FIB at an acceleration voltage of 30 kV with gradually decreasing beam currents from 2 nA to 8 pA to reduce the ion beam damage. A lamella thickness of ~ 200 nm was obtained to balance electron transparency and prevent strain relaxation due to an enlarged surface-to-volume ratio.

For the STEM analysis, electron transparent TEM lamellae were prepared by FIB lift-out in the vicinity of the scratches. Thinning using the FIB was performed to obtain a lamella thickness of ~ 200 nm, balancing electron transparency and preventing strain relaxation due to an enlarged surface-to-volume ratio. 4D-STEM measurements were conducted using a ThermoFisher Scientific Themis Z TEM operated at 300 kV in microprobe STEM mode with spot size 6 and a semi-convergence angle of 0.26 mrad giving rise to a probe size of ~ 5 nm. A Gatan OneView Camera with a camera length of 115 mm was used to capture the diffraction patterns. This camera length was chosen to capture the first ring with a diameter as large as possible to enhance the sensitivity of measuring the distortion and area of the diffraction ring. The 4D-STEM map was acquired by scanning the electron probe over a 2D sample plane with a step size of 5.8 nm and frame size of 900×500 for the $\text{Fe}_{85.2}\text{Si}_{10.5}\text{B}_{9.5}\text{P}_4\text{Cu}_{0.8}$ metallic glass ribbon and with a step size of 9.7 nm and frame size of 350×270 for the $\text{Zr}_{46}\text{Cu}_{38}\text{Al}_8\text{Ag}_8$ metallic glass with an exposure time 3.3 ms per frame (frame rate of ~ 300 f/s). For the fitting of the diffraction patterns, the SVD method, which is introduced in chapter 4.3, is used

6.3. Mapping strain and atomic density in shear bands

6.3.1. Fe-based metallic glass ribbons

Figure 6.1b shows a STEM-HAADF image of a TEM lamella, where the location of shear bands can be expected based on the shear offset at the surface (red dashed lines). A 4D-STEM map was obtained for the area outlined by the black rectangle, using a step size of 5.8 nm. This map encompasses the shear bands of interest, denoted as SB1 and SB2. Figure 6.1c shows a map of the relative atomic density ($\Delta\rho$). Figure 6.1d visualizes the maximum shear strain (τ_{max}). The amplitude of the field (brightness) is determined by the strength of the deviatoric strain, while the colors in the field correspond to the orientation of the maximum tensile strain. Maximum shear

strain τ_{max} provides information on local distortions without contributions from volumetric changes.

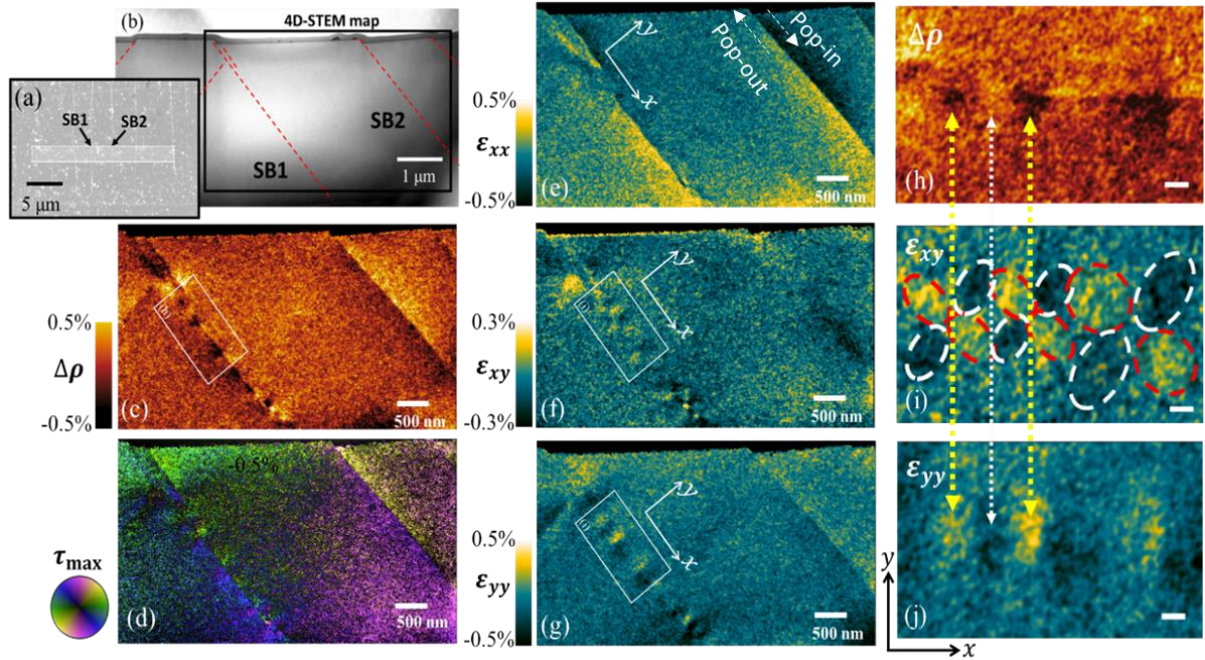


Figure 6.1: Deformed $\text{Fe}_{85.2}\text{Si}_{0.5}\text{B}_{9.5}\text{P}_4\text{Cu}_{0.8}$ metallic glass ribbon. (a) SEM image showing the area beside a scratch with shear offsets visible. The shadowed rectangle denotes the location of the prepared TEM lamella. (b) STEM-HAADF image of the TEM lamella, where the expected locations of the shear bands are indicated by red dashed lines according to shear offset at the surface. A 4D-STEM map was acquired of the area indicated by the black rectangle with the shear bands of interest labeled as SB1 and SB2. (c) Map of relative atomic packing density ($\Delta\rho$). (d) Map of maximum shear strain (τ_{max}). The color corresponds to the orientation and the brightness to the amplitude as indicated by the color wheel. For the strain tensor, the x-axis is defined to be parallel to SB1 and the y-axis perpendicular to SB1. (e) ϵ_{xx} , the strain component along the x-axis, (f) ϵ_{xy} , the shear component, and (g) ϵ_{yy} , the strain component along the y-axis. (h)-(j) show the correlation of the strain components and the atomic density, which are magnified images of the area indicated by the white rectangle in (d), (e), and (g) with the scale bar corresponding to 100 nm. The dashed ellipses indicate the quadrupole strain field. The yellow dashed arrows indicate the center of the quadrupoles. The figure is reprinted from Ref. [200].

The strain tensors are shown in Figure 6.1e-g, where the x-axis is defined to be parallel to SB1 and the y-axis perpendicular to SB1 to visualize shear band-related features. The color code in ϵ_{xx} and ϵ_{yy} indicates the strain amplitude: dark blue (negative sign) represents compression corresponding to atoms squeezed closer along the axial direction, whereas bright yellow (positive sign) represents tension indicating an increased distance between atoms. The color code in ϵ_{xy} indicates shearing: positive values for clockwise shearing and negative ones for anticlockwise.

ε_{xx} (Figure 6.1e) reveals an antisymmetric strain distribution across both SB1 and SB2 with a sharp transition occurring at the shear plane. Based on the shear offset, it can be confirmed that the pop-in side of the shear band is compressed and the opposite side is in tension as indicated by white arrows. This matches with the observations of shear band-affected zones (SBAZs) made by Scudino et al.^[205] and Shahabi et al.^[206] using X-ray diffraction. However, in contrast to the micrometer resolution of the X-ray-based technique, the nanometer resolution in 4D-STEM reveals new details of the strain variation around the shear bands. ε_{xy} (Figure 6.1f) shows zigzag-arranged shear fields on SB1. ε_{yy} (Figure 6.1g) alternately varies from tension to compression along SB1. The features can be understood better by the τ_{max} map, where the orientation of the strain field exhibits circular rotation along SB1. In the atomic density map, alternating fluctuations are observed along SB1, directly correlated with the strain field. An enlarged area is indicated by the white rectangles in the ε_{xy} , ε_{yy} , and $\Delta\rho$ is shown in Figure 6.1h-j. Eshelby-like inclusions are observed, which are aligned along SB1. The ε_{xy} map shows that the inclusions produce quadrupolar shear fields. Each of the quadrupoles possesses a positive pair (red dashed ellipse) and a negative pair (white dashed ellipse). They are perpendicular to each other and oriented $\sim 45^\circ$ to the shear band plane. The core of each quadrupolar inclusion exhibits low atomic density and highly tensile ε_{yy} as indicated by yellow-dashed arrows. Between the inclusions, compressive ε_{yy} and high atomic density are observed, as indicated by a white-dashed arrow.

The strain maps reveal local strain variations at a scale of approximately 5-10 nm. These variations in strain could be linked to local structures exhibiting liquid- and solid-like structural types as discussed in chapter 4, which, in turn, may correspond to localized brittle and ductile properties of metallic glasses. Establishing this connection would lead to a more profound comprehension of the deformation mechanism. To gain insight into this relationship, NBED patterns from thin samples with a thickness of a few nanometers, comparable to the local structural heterogeneity, can be employed. However, performing such correlation in the experimental setup poses challenges. As explained in Section 4.4, the thinning process during sample preparation eliminates the residual strain, making it difficult to accurately correlate the structural information obtained from a thin sample to the strain resulting from deformation measured under thick sample conditions. To address this issue, new experimental considerations, particularly regarding sample preparation, need to be taken into account.

6.3.2. Zr-based bulk metallic glasses

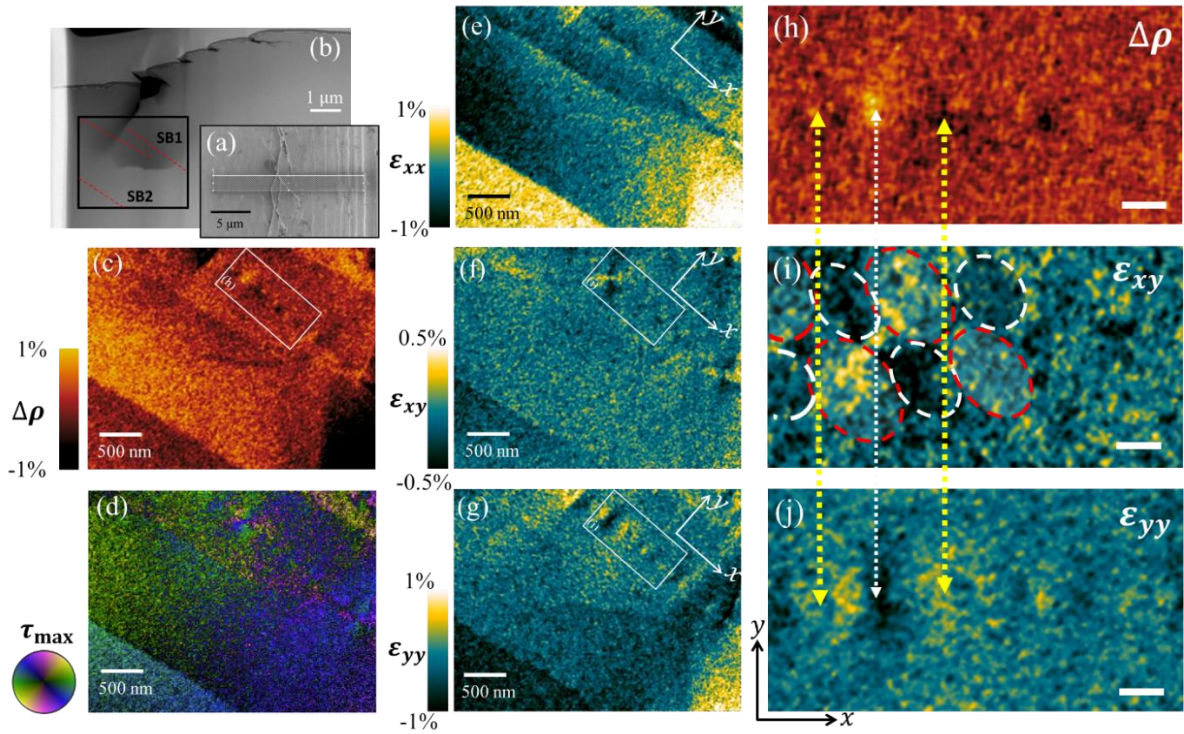


Figure 6.2: Deformed $Zr_{46}Cu_{38}Al_8Ag_8$ bulk metallic glass. (a) SEM image showing the area beside a scratch with shear offsets and microcracks. The shadowed rectangle denotes the location of the TEM lamella. (b) STEM-HAADF image of the TEM lamella, where the location of shear bands is indicated by red dash lines. A 4D-STEM map was acquired of the area indicated by the black rectangle, where the shear bands of interest are labeled SB1 and SB2. (c) Map of relative atomic density ($\Delta\rho$). (d) Map of maximum shear strain (τ_{max}). The color corresponds to the orientation of τ_{max} , the brightness to the amplitude, as indicated by the color wheel. For the strain tensors, the x-axis is defined to be parallel to SB1 and the y-axis perpendicular to SB1. (e) ϵ_{xx} , the strain tensor component along the x-axis, (f) ϵ_{xy} , the shear component, and (g) ϵ_{yy} , along the y-axis. (h)-(j) show the correlation of the strain components and the atomic density, which are magnified images of the area indicated by the white rectangle in (d), (e), and (g) with a scale bar corresponding to 100 nm. The dashed ellipses indicate the quadrupole strain field. The yellow dashed arrows indicate the centers of the quadrupole strain fields. The figure is reprinted from Ref. [200].

To confirm the universality of the observation, a $Zr_{46}Cu_{38}Al_8Ag_8$ bulk metallic glass, which possesses mechanical properties very distinct from the Fe-based metallic glass, was investigated using identical deformation and imaging conditions as used for the Fe-based metallic glass. Figure 6.2a shows a scratched surface of the metallic glass. A TEM sample including the pile-up area has been prepared from the area indicated by the shadowed rectangle. A 4D-STEM map was acquired below the deformed surface in the area indicated by the black rectangle in Figure 6.2b, where the shear bands of interest are labeled SB1 and SB2. The amplitude of the principal strain fields

(brightness) is defined by the strength of P1 and P2. The orientation of the fields (colors) follows the orientation of P1 and P2. The color code for ε_{dev} and ε_{vol} indicates the strain amplitude. Figure 6.2c and d are maps of $\Delta\rho$ and τ_{max} . The strain tensors obtained from the principal strains are shown in Figure 6.2e-g, where the x-axis is parallel to SB1 and the y-axis is perpendicular to SB1. The results show qualitatively similar phenomena as observed in the Fe-based metallic glass.

Figure 6.2d (τ_{max}) visualizes strain vortexes located at SB1, whereas SB2 only exhibits an asymmetric rotation of τ_{max} across to the shear band. ε_{xx} reveals an asymmetric distribution across the shear bands with a sharp interface at the shear band. Two types of shear bands are observed similar to the Fe-based example before. For SB1, the quadrupolar strain fields are concentrated at the dilated inclusions. SB2 displays minimal variation along the shear band, yet it clearly shows an antisymmetric distribution of strain and density across the band. Figure 6.2f visualizes strongly localized ε_{xy} at SB1 and whereas SB2 exhibits negligible structural features only showing a weak asymmetric variance of ε_{xy} across the shear band.

Figure 6.2g reveals alternating fluctuations of varying tensile and compressive ε_{yy} along SB1. In contrast, ε_{yy} near SB2 exhibits an asymmetric strain distribution across the shear band. The atomic density again correlates with the strain distribution similarly. The area with the higher compressive strain (ε_{xx}) correlates with the higher density and the area with the higher tensile strain (ε_{xx}) matches with the lower density. In Figure 6.2h-j, the Eshelby quadrupoles are concentrated at the inclusions. Figure 6.2h (ε_{xy}) shows the STZ inclusions centered at the regions with high tensile ε_{yy} as indicated by the yellow-dashed arrows (Figure 6.2i) and are again matching with the lower density regions (Figure 6.2j). A higher compressive strain is observed in between inclusions and corresponds to higher-density regions as indicated by the white-dashed arrows. The Eshelby quadrupoles are orientated $\sim 45^\circ$ to the shear propagation direction.

6.4. Quadrupolar strain field surrounding Eshelby inclusions

Each of the quadrupolar strain fields observed consists of a positive pair and a negative pair perpendicular to each other and oriented $\sim 45^\circ$ to the shear plane, where the orientation of the shear field circularly rotates along SB1 in between the quadrupoles as shown in Figure 6.3a. Upon examination, it is evident that the features, particularly the quadrupolar shear fields surrounding the inclusions, share similarities with the characteristics of the simulated STZ (Figure 6.3), except for the size difference compared to the present experimental observations. This discrepancy may

be attributed to the fact that most simulation studies focus on the initiation stage of STZs at the nano- and pico-second levels. Consequently, their size is usually estimated based on their volume at the initiation stage. Recent simulation results, such as from Şopu et al.^[207] and Wen et al.^[208], have shown the growth of STZs during further shearing, but the evolution of the STZ morphology exceeds the spatial and temporal scale that MD can handle.

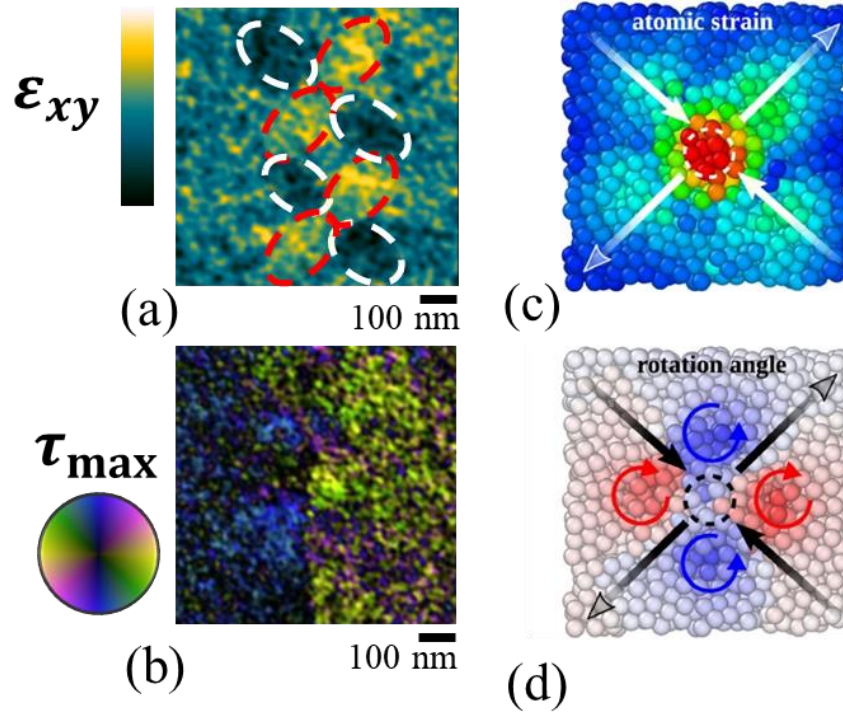


Figure 6.3: Visualization of an Eshelby quadrupolar strain field. Experimental data of (a) shear strain ε_{xy} and (b) maximum shear strain τ_{\max} in a $\text{Fe}_{85.2}\text{Si}_{10.5}\text{B}_{9.5}\text{P}_4\text{Cu}_{0.8}$ metallic glass ribbon obtained from 4D-STEM strain mapping and MD simulation of a STZ from Ref. ^[207] for (c) atomic strain and (d) rotation angle.

The observed quadrupolar strain fields, which have been preserved after plastic deformation, concentrate around the core of the inclusions. These strain fields influence the surrounding material and diminish only gradually. This poses a challenge in experimentally determining the true size of the inclusion core. Nevertheless, the deviatoric strain, which isolates the genuine material distortion from the volumetric change, displays a remarkably sharp maximum (2-3 pixels, corresponding to ~ 15 nm), which is an upper boundary for the observed feature size and approaches the STZ size observed in simulations. However, as the distance between STZs in simulation is much smaller than the distances between quadrupolar strain fields, the observed inclusions likely result from the agglomeration of STZs. In this case, an open question remains what determines the size and distance between these inclusions?

6.5. Alignment of Eshelby inclusion at a shear band

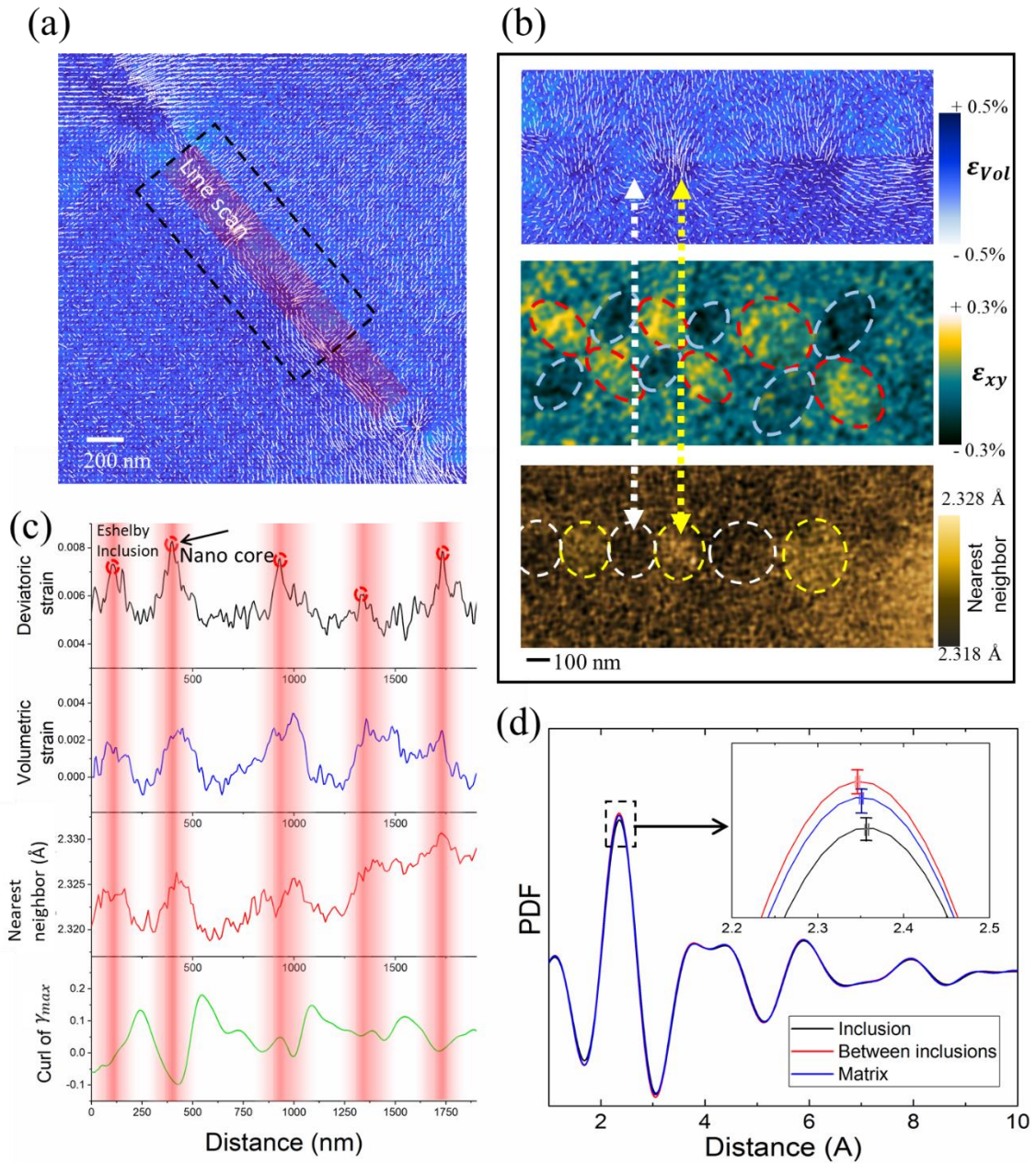


Figure 6.4: (a) Vector field visualization of the maximum shear strain overlaid on the map of ϵ_{Vol} for $\text{Fe}_{85.2}\text{Si}_{0.5}\text{B}_{9.5}\text{P}_4\text{Cu}_{0.8}$. (b) (top) Magnified region from the black rectangular area in (a) compared to maps of ϵ_{xy} and the nearest-neighbor distance from the same region. (c) Line profiles of the deviatoric strain, volumetric strain, nearest-neighbor distance, and curl of τ_{max} along the shear band in the region indicated by a red rectangle in (a). The positions of the Eshelby inclusions and their nano core are highlighted by red gradient windows. (d) PDFs averaged from typical inclusions and in-between inclusions marked by white and yellow dashed circles in (b-bottom) together with a PDF of the matrix taken from an area away from the quadrupoles. Each error bar (standard deviation) is obtained from 75 PDFs taken from 3 equivalent regions. The figure is reprinted from Ref. [200].

To examine the details of the strain field at SB1, τ_{max} is plotted as arrow-less vectors overlaid on the map of ε_{Vol} in Figure 6.4. The length of the lines represents the strength of τ_{max} and the orientation indicates the maximum tensile direction. The black dashed rectangular area is magnified at the top of Figure 6.4b. The oscillatory feature is compared with the quadrupolar features from the same area of the shear strain map (middle) and with the map of the nearest-neighbor distance obtained from STEM-PDF. Observations indicate that the strain concentrates at the core of inclusions positioned in the center of the quadrupoles, where larger nearest-neighbor atomic distances exist. The strain fields radiate outward from the core in a circular manner, creating a vortex-like rotation field in the space between adjacent inclusions. In Figure 6.4c, the maps of the deviatoric, volumetric strain, and atomic nearest-neighbor distance are quantified as well as the curvature (curl) of the rotational τ_{max} field by line profiles along SB1. The maxima of the deviatoric strain, where the materials suffer the strongest shear transformation, coincide with the maxima of the volumetric strain and the increased nearest-neighbor distance. The inclusions are separated by regions with a high curl of τ_{max} , weak deviatoric, and volumetric strain, where atoms are arranged with a smaller 1st coordination shell. The stress field, concentrated around the inclusion, exerts an influence on the surrounding material and diminishes gradually, posing challenges in experimentally determining the actual size of the core of the inclusions. Nevertheless, it is worth noting that the deviatoric strain (Figure 6.4c, black line), which disentangles the true material distortion from the volumetric change, exhibits remarkably sharp maxima with a size of < 20 nm (~ 3 scan steps).

Figure 6.4d shows PDFs averaged from dashed circular areas marked in Figure 6.4b (bottom) for a typical inclusion, in between inclusions and the matrix away from the quadrupoles. No significant differences among the PDFs can be observed, except a statistically meaningful shift towards a larger distance of the 1st peak and a reduced height of the peak from the inclusions compared to the compressed area in-between inclusions and the matrix away from the shear band. Considering the volumetric strain along with this observation, this finding reinforces the conclusion that the hydrostatic stress encompassing the inclusions leads to an increase in the average atomic distance and causes dilation of the material at these inclusions.

The features observed in the Cu-Zr based metallic glass are weaker compared to the Fe-based sample. This may be due to the softer nature of the Cu-Zr-based metallic glass^[2]: on one hand, the soft Cu-Zr-based glass possesses more intrinsic structural inhomogeneity compared to the rigid Fe-based glass, giving rise to a higher background in the maps. On the other hand, the stress built up during deformation relaxes more easily in a soft glass, which may lead to the weaker deformed

features observed. Nevertheless, the quadrupolar features and the low-density inclusions can be confirmed as shown in Figure 6.5.

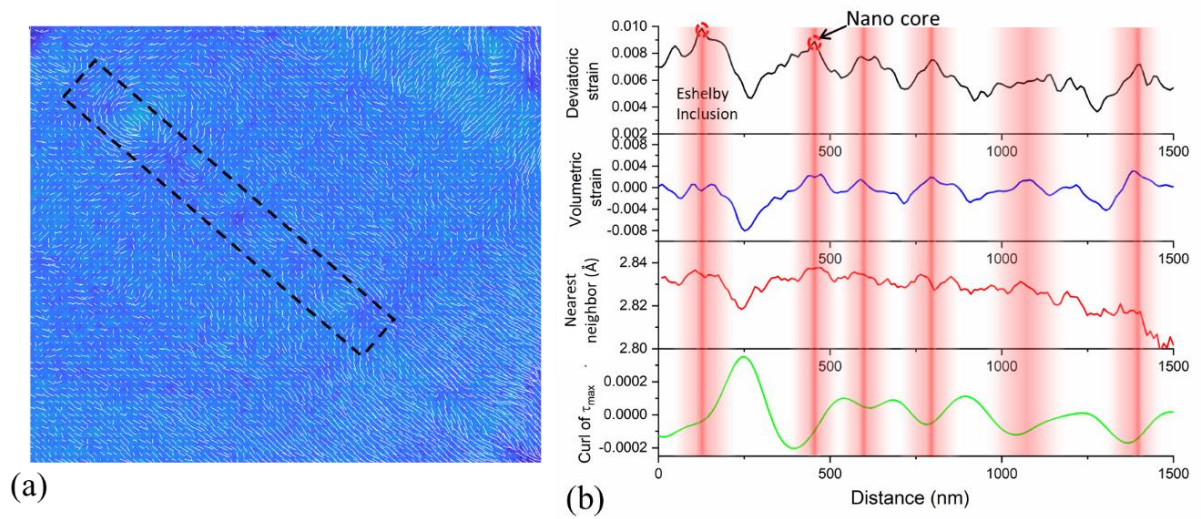


Figure 6.5: (a) Vector field visualization of the maximum shear strain overlaid on the atomic density map for a $Zr_{46}Cu_{38}Al_8Ag_8$ bulk metallic glass. (b) Line profile of relative atomic density ($\Delta\rho$), deviatoric strain, volumetric strain, and curl of τ_{max} taken along the shear band in the region indicated by a black dashed rectangle in (a). The red highlights indicate the position of the shear transformation inclusions.

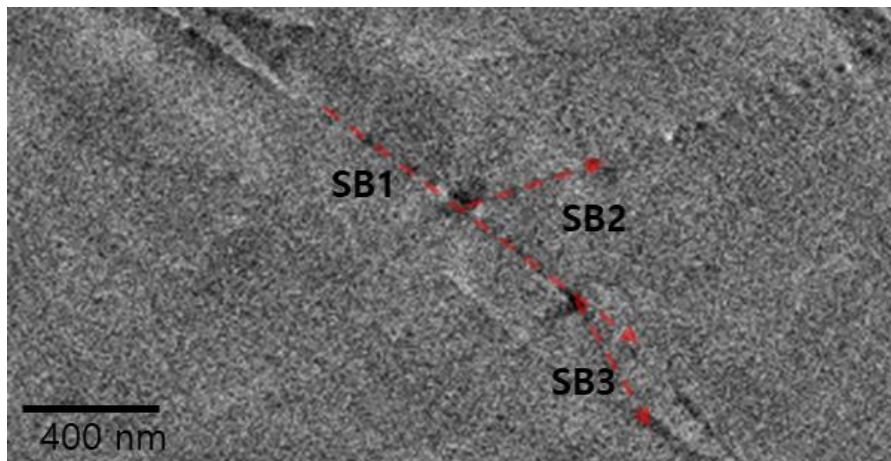


Figure 6.6: STEM-HAADF images showing secondary shear bands and their brunching points in $Zr_{46}Cu_{38}Al_8Ag_8$ bulk metallic glass. SB2 exhibits alternating fluctuation with a much shorter distance (< 100 nm).

Density fluctuations at a similar length scale as our 4D-STEM analysis have also been observed by H. Rösner et al.^[204, 209-210], who systematically discuss the length scale of experimentally observed alternating contrast in $Al_{88}Y_7Fe_5$, $Pd_{40}Ni_{40}P_{20}$, and also $Zr_{52.5}Cu_{17.9}Ni_{14.6}Al_{10}Ti_5$. They

observed qualitatively similar features with a periodic fluctuation length of about 150 ± 20 nm for three different types of metallic glasses. As these three glasses cover the full range of characteristic (mechanical) properties of metallic glasses, they concluded that the length scale of the density fluctuations within shear bands is generic for all metallic glasses. However, in the current work, the length scale of the periodic fluctuations is not constant even in a single sample. For example, Figure 6.4c and Figure 6.5b show length scales of the periodic fluctuation larger than 270 nm, and one period can even extend to about 500 nm, whereas the SB2 in Figure 6.1. exhibits a length scale of only ~ 70 nm. Very recently, Sheng. et al. also observed the two types of shear bands with drastically different periodic lengths, where one shear band exhibits several hundred nm lengths and another one exhibits a much smaller length scale.^[186] This may infer that the fluctuations and their length scale can change during the shear banding process, *e.g.* from the initial shear banding state to the formation of a mature shear band, as well as depending on material properties.

6.6. Evolution of shear bands with shear displacement

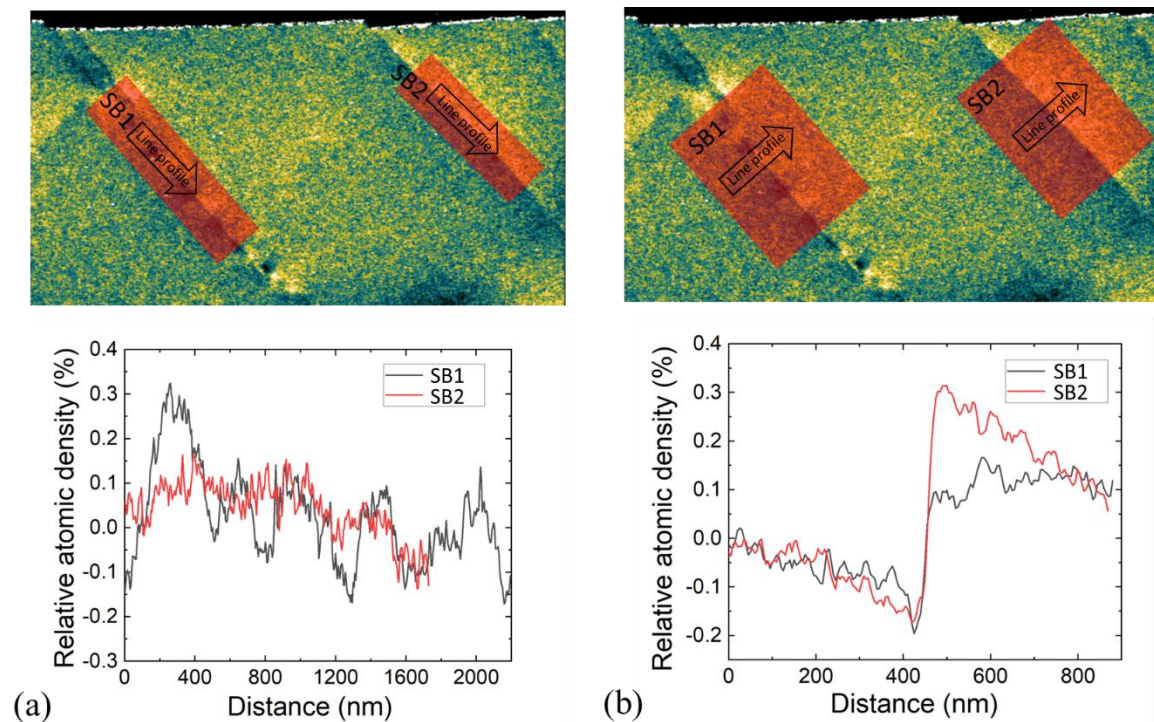


Figure 6.7: (a) Atomic density map of a $\text{Fe}_{85.2}\text{Si}_{0.5}\text{B}_{9.5}\text{P}_4\text{Cu}_{0.8}$ metallic glass ribbon where line profiles have been calculated along SB1 (left) and SB2 (right) showing periodic variations for SB1 and negligible variations along SB2. (b) Line profiles calculated across SB1(left) and SB2 (right) showing the antisymmetric atomic density distribution across both shear bands. The figure is reprinted from Ref. ^[199].

Due to the limitations of any postmortem characterization and the rapid propagation of shear bands, direct observation of the time-dependent progression of shear bands has not been possible. Nevertheless, the observation of the two different types of shear bands fits the hypothesis derived from atomistic simulations that quadrupolar stress features, formed during the initiation of a shear band (SB1-like), are later on smeared out during further shear displacement, giving rise to a more homogeneous, more mature shear band (SB2-like).^[120, 211] The weak but detectable fluctuations still observed along SB2 shown in the red line profile in Figure 6.7a, could be residuals from the early stages of shear band formation. However, it is unclear why shear bands in the same local region, where a similar level of strain was induced, exhibit such different features. Nevertheless, this indicates that the fluctuations and their length scale can change significantly during shear banding.

An alternative explanation for the distinct shear bands can arise from the relationship between the 3D strain state of the material and the measured 2D projection of the strain through the sample thickness. In the thickness study in chapter 4.4, the core of each Eshelby inclusion remains at nearly identical locations on the shear band when the sample thickness is reduced (Figure 4.8 and Figure 4.9). This suggests that a similar deformation state is preserved at least for a couple of 100 nanometers in the thickness direction. Moreover, one can notice that there are large strain variations, *e.g.* deviatoric strain up to 0.5 % and volumetric strain up to 1 %, observed at the projected core of inclusions with a diameter of a few tens of nanometers. Considering that the projected information is an average across the sample thickness, the required strain would not be physically reasonable for a 200 nm thick sample if the inclusion core is a point-like 0D structure. This suggests that the inclusion has a 3D structure extending out of the imaging page. In this case, the quadrupolar features with density fluctuation in shear bands can appear differently depending on the misorientation of the strain fields from the projection axis.

Nevertheless, both interpretations for the adjacent shear bands with different structures would fit the observation of different shear band structures. They also explain the distinct differences among STEM observations of shear bands, *e.g.* Rösner et al. observed shear bands showing alternating STEM-ADF contrast,^[204, 210] whereas Maaß et al. showed shear bands simply exhibiting a reduced intensity^[30] as well as the previous observation of an asymmetric variation of the interatomic distances across shear bands.^[212]

6.7. Summary

The correlative analysis of strain field and PDF mapping using 4D-STEM presents a novel approach to obtaining essential information for studying deformation mechanisms in metallic glasses. It offers, for the first time, an experimental visualization of Eshelby inclusions encompassed by quadrupolar strain fields that are aligned along a shear band in deformed metallic glasses. By examining two distinct metallic glasses, the findings suggest the universality of this observation. The results provide direct experimental visualization supporting a concrete scenario for the initiation of a shear band: the dilatated Eshelby inclusions result from localized plastic atomic displacements within the glassy matrix, which concentrate a stress field exhibiting quadrupolar symmetry. This quadrupolar stress field disrupts the surrounding material in a vortex-like manner and spreads to neighboring inclusions, ultimately leading to shear band formation as has been suggested by Sopy et al.^[207] This observation provides possible explanations for the differences in previous TEM observations of shear bands, suggesting that the fluctuation and its length scale can change during the shear banding process and also depending on material properties. This method is anticipated to open up broad research possibilities for addressing questions in amorphous materials.

Chapter 7

7. Effects of the annealing treatments on atomic structure and ductile deformation of metallic glasses

This chapter presents a comprehensive investigation into the atomic structure of two distinct metallic glasses in various annealing states, as well as its connection to subsequent deformation using scratch testing. To characterize the undeformed glass structure, conventional STEM and SAED-PDF analysis are utilized. Subsequently, localized defects were induced in the metallic glasses through scratch testing, allowing us to closely examine multiple shear bands and their affected regions beneath the scratches. To analyze the nanoscale strain fields and atomic density mappings of the deformed metallic glasses, advanced 4D-STEM techniques were employed. Based on the 4D-STEM results, the stored elastic energy of the deformed glass matrix is also calculated to study the residual features at shear bands and their respective deformed. The observation discovers the structural effects on shear band multiplication and ductile deformation of metallic glasses, providing insights into the wear deformation.

7.1. Introduction

The mechanical properties of metallic glasses are highly sensitive to their frozen-in configurational state.^[75] In chapter 5, it was discussed that the local configuration of metallic glasses is not uniform throughout the glass matrix due to packing frustration. As a result, metallic glasses exhibit a heterogeneous packing at the nanoscale, with regions of more stable (solid-like) and less stable (liquid-like) structures intermixed within the overall glassy matrix.^[146] The connections and relative distribution of these regions play a crucial role in determining the shear banding process and mechanical properties of metallic glasses.^[75]

Sopu et al. conducted MD simulations to investigate the process of shear band multiplication in a heterogeneous metallic glass with interfaces between soft and hard glassy regions.^[13] The results showed that the interfaces act as easy nucleation sites for shear bands and promote the formation of multiple shear bands. Notably, at the intersecting points between the primary shear band and the intrinsic interfaces, secondary shear bands emerge as branches from the primary shear band. This shear band multiplication suppresses the formation of a dominant shear band that would traverse through the entire glassy matrix, thus enhancing the deformability of the glass matrix.^[131, 213] The formation of shear band networks through branching and intersection effectively dissipates the stored elastic energy and enhances deformability.^[214]

As shown in chapter 5.3, the local structure of metallic glasses can be effectively tuned through thermomechanical treatments,^[15, 129, 215] leading to relaxation/rejuvenation phenomena that eliminate/increase excessive free volumes and residual stresses present in the as-quenched/relaxed state.^[216-217] Different methods, such as varying cooling rates^[218], annealing treatments^[214], ion implantation^[218], and mechanical/thermal rejuvenation^[15, 129, 215], have been used to tailor the material for desirable properties. Such structural modification of metallic glasses can change the local structure and influence their subsequent deformation behavior. In general, higher-energy states exhibit more interfaces and soft spots, resulting in increased plasticity,^[219] while slower cooling rates or annealing treatments lead to a more brittle behavior due to limited shear band formation.

Experimentally, some rejuvenated metallic glasses exhibit very large plasticity at room temperature, *e.g.*, superplasticity.^[220] As a result of ductile deformation, a dense shear band network is observed in the rejuvenated metallic glasses after a compression test.^[221] Conversely, slower cooling rates or annealing treatments relax the amorphous structure and homogenize local structural fluctuations, consisting of more of a solid-like phase. They exhibit higher flow barriers and atomic structures with a higher degree of order. This leads to more brittle characteristics of

the metallic glass under deformation, *i.e.* thermal embrittlement, due to the limited formation of shear bands.^[222]

Recent findings suggest the existence of broad SBAZs in the deformed matrix,^[157, 223] which can store significant deformation energy and likely influence subsequent plastic deformation.^[152] Some microscopic studies have provided evidence of SBAZs in deformed glass matrices^[154-155, 157, 212, 223-224] and suggested their importance in the deformation behavior and functional properties of metallic glasses.^[212] However, a detailed depiction of the structure of multiple shear bands and the atomic arrangement in the SBAZs is still missing. This has eventually led to a limited understanding of the plastic deformation of metallic glasses

Alloy	Fe _{85.2} Si _{0.5} B _{9.5} P ₄ Cu _{0.8}			Zr ₄₆ Cu ₃₈ Al ₈ Ag ₈	
	As-cast	20 h	240 h	As-spun	Annealed
Young's modulus (GPa)	108.5±0.8	109.0±0.6	109.6±0.5	140.1±0.9	144.8 ±0.3
Hardness(GPa)	4.3±0.1	4.53±0.1	4.60±0.1	9.8±0.1	9.9±0.1

Table 7. 2: Hardness and Young's modulus of the studied samples. The data for Fe-based metallic glass ribbon is reused from Ref. ^[225].

This chapter involves a structural investigation of deformed metallic glasses on different annealing states using a 4D-STEM approach, including PDF analysis for characterizing the original structure, and strain and density mapping. To confirm the universality of the phenomenon, two metallic glasses with distinct mechanical properties (Table 7. 2) were studied with an identical 4D-STEM setup. Plastic deformation was induced by micro-scratching glass samples before and after various thermal relaxation treatments. This methodology enables a comprehensive examination of multiple shear bands and their affected regions beneath the scratches in metallic glasses. The subsequent section delves into the understanding of the influence of the annealing treatments on atomic structure and plastic deformation of metallic glasses.

7.2. Experimental details

Zr₄₆Cu₃₈Al₈Ag₈ (at.%) and Fe_{85.2}Si_{0.5}B_{9.5}P₄Cu_{0.8} (at.%) master alloy ingots were prepared by arc-melting in a Ti-gettered argon atmosphere. The Zr₄₆Cu₃₈Al₈Ag₈ bulk metallic glass

(1 cm × 1 cm × 1 mm plate) was fabricated by suction-casting into a water-cooled copper mold. Fe_{85.2}Si_{0.5}B_{9.5}P₄Cu_{0.8} (at.%) metallic glass, width ~ 25 mm and thickness ~ 20 μm, was prepared by melt spinning on a Cu wheel. As-cast Zr₄₆Cu₃₈Al₈Ag₈ metallic glass samples were annealed at 639 K (~ 0.9T_g) for 20 h and 240 h, while an as-spun Fe_{85.2}Si_{0.5}B_{9.5}P₄Cu_{0.8} metallic glass was flash-annealed at 633 K (~ 1.1T_g) for 10 seconds. All samples were polished to a mirror finish with roughness below 30 nm to reduce the effects of surface topography and oxidation layer. Scratch tests were performed in ambient conditions using a conical diamond indenter with an apex radius of 210 μm. Thereby, the samples were scratched with a sliding velocity $v_s = 0.1$ mm/s over a length $l_s = 1$ mm at normal loads $F_n = 15$ N for Zr-based metallic glass and $F_n = 10$ N for Fe-based metallic glass ribbon.

For the STEM study, electron transparent TEM lamellae were prepared by FIB lifting out from scratched regions. The sampling location was carefully selected from pile-up regions at 0.3 mm away from scratch ends to ensure that the prepared TEM samples underwent a similar degree of plastic deformation. Thinning was performed by FIB at an acceleration voltage of 30 kV with gradually decreasing beam currents from 2 nA to 8 pA to reduce the ion beam damage. TEM lamellae with a thickness of ~200 nm were obtained to balance electron transparency and prevent strain relaxation.

SAED was performed in TEM mode with parallel illumination to determine the average glass structure and elemental distribution. The recorded maximum scattering angle corresponded to 2.5 Å⁻¹ in reciprocal space. The SAED patterns are integrated azimuthally to obtain radial profiles $I(q)$, where $q = 2\theta/\lambda$, θ is half of the scattering angle, and λ is the incident wavelength. The azimuthal integration provides a high signal-to-noise ratio at large scattering angles of the diffraction pattern to reach the necessary signal quality for the PDF analysis.

To clarify the observation of electron PDF, synchrotron radiation X-ray diffraction (SR-XRD) was performed at 1-ID of Advanced Photon Source (APS), Argonne National Laboratory, USA with a wavelength of 0.117 Å and a beam size of 0.3 × 0.3 mm². The diffraction patterns were recorded by a flat-panel Si detector (Perkin-Elmer 1621) with a size of 200 × 200 mm² and a pixel size of 2048 × 2048 pixels. The acquisition time was 1 s for each diffraction pattern and every 100 patterns were summed to output a statistical data set. Scattering intensities $I(q)$ s were integrated under the software package FIT2D^[226] and the experimental structure factors $S(q)$ s were derived from $I(q)$ by subtracting the appropriate background and correcting for oblique incidence, absorption, sample geometry, multiple scattering, fluorescence, Compton scattering and secondary

container-scattering contributions through the program PDFgetX2. SR-XRD PDFs are obtained by a Fourier sine transformation of the structure factors.^[227]

4D-STEM measurements were conducted using a Themis Z double-corrected TEM operated at 300 kV in microprobe STEM mode with spot size 6 and 20 μm C2 aperture. The setup results in a semi-convergence angle of 0.26 mrad giving rise to a diffraction-limited probe size of ~ 5 nm. OneView camera (Gatan Inc.) with a camera length of 1.15 m is used to record the diffraction patterns. This camera length was chosen to capture the first diffuse diffraction ring with a sufficient diameter on the camera to enhance the sensitivity for measuring distortions. A beam stopper was inserted to prevent damage to the camera from the direct beam. 4D-STEM records local 2D diffraction patterns over a 2D array of probe positions by stepwise scanning of the probe with a step size of ~ 10 nm at an exposure time of 3.3 ms per frame (frame rate of ~ 300 f/s). The local strain is determined by the ellipticity of the diffraction ring in each diffraction pattern of the 4D-STEM dataset. The relative density was calculated by quantifying the area encircled by the 1st ring of each diffraction pattern in the 4D-STEM data. This calculation is under an approximation, *e.g.* without consideration of chemical variation, and compares them to an undeformed case. For the fitting of the diffraction patterns, the SVD method, which is introduced in chapter 4.3, is used

7.3. Atomic structure of metallic glasses after annealing treatments

The amorphous structure of the samples is initially examined using SAED. Figure 7.1a displays the PDF calculated from the SAED patterns. To facilitate the comparison of peak positions, the PDFs are normalized based on their first peaks. After the annealing treatment, there is a noticeable shift towards shorter atomic neighbor distances in the first peak of the PDF, as shown in Figure 7.1b (2.774 \AA for as-cast, 2.765 \AA for 20 h, and 2.7575 \AA for 240 h samples). This decrease corresponds to a density increase of about 1.8 % ignoring differences in medium-range coordination and chemical order.

In Figure 7.1c, the nearest interatomic distance is plotted together with the mass density of the samples, which is measured following Archimedes' principle, showing their inverse correlation. The 1 % density increase after 240 h annealing treatment from the mass-density measurement shows a similar order of magnitude as the density increase estimated from the PDF analysis. This indicates that the structure of the metallic glasses is densified after the annealing treatment.

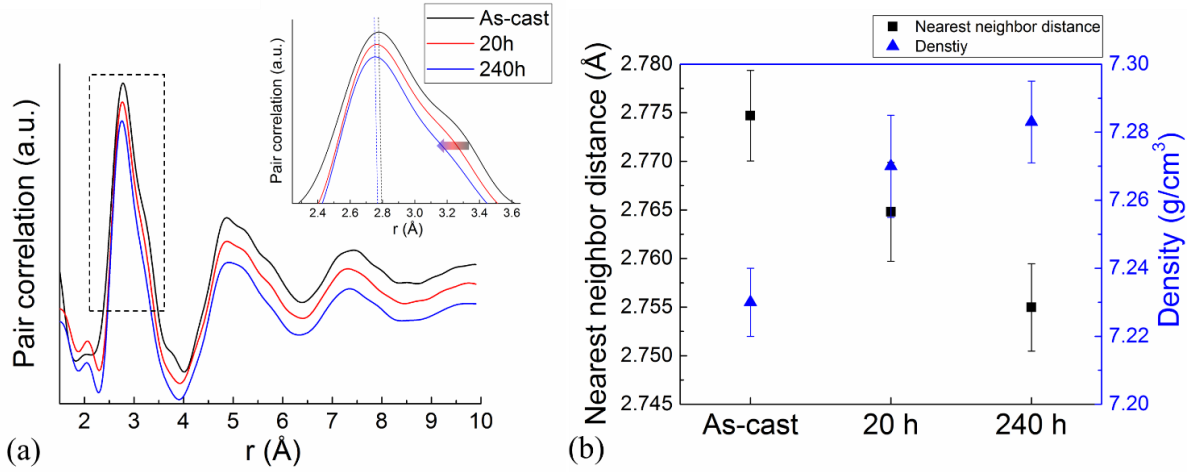


Figure 7.1: (a) Electron PDF calculated from SAED pattern of the as-cast, 20 h, and 240 h annealed $Zr_{46}Cu_{38}Al_8Ag_8$ metallic glasses. The first peaks of PDFs are enlarged in the inset. The heights of the PDFs are normalized by their first peak and displaced for easy presentation of peak shifts. The first peak positions of the first peak in the PDFs correspond to the nearest atomic neighbor distance, which is plotted in (b) together with mass density measured by Archimedes' principle.

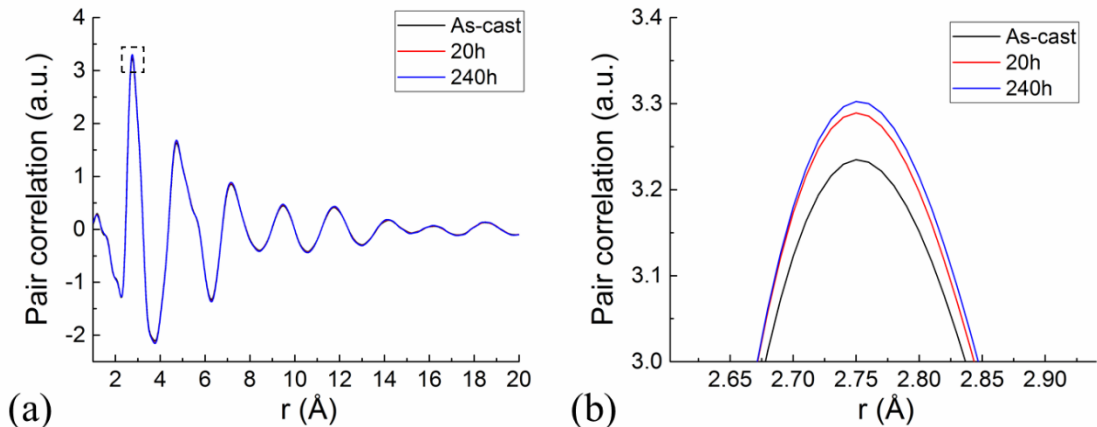


Figure 7.2: (a) Synchrotron X-ray pair distribution function analysis of the as-cast, 20 h, and 240 h annealed $Zr_{46}Cu_{38}Al_8Ag_8$ metallic glasses obtained from synchrotron radiation X-ray diffraction. The first peaks of each PDF are enlarged in (b).

In addition, the first peak exhibits a shoulder at larger interatomic distances of about 3.3 Å. This peak separation can be associated with the distinct interatomic bonding types coexisting in the system. The peak separation is reduced after the annealing treatment as indicated by an arrow in Figure 7.1b, suggesting a homogenization of the distinct nearest atomic bonding during relaxation. The second peak of the PDFs is also a convolution of several separated sub-peaks that can be associated with different types of connectivity between polyhedral clusters.^[194-195] Clusters can share different numbers of atoms to overcome packing frustration, resulting in different degrees of MRO. The separation of distinct features of the second peak also reduces during annealing

treatment. $\text{Fe}_{85.2}\text{Si}_{10.5}\text{B}_{9.5}\text{P}_4\text{Cu}_{0.8}$ samples show similar structural densification, *i.e.* the first peak shift towards a shorter atomic distance (2.51 Å for as-spun and 2.49 Å for annealed samples), after the annealing treatment, as discussed in chapter 5.3.

To clarify the observations derived from electron PDFs, a comparison is undertaken with an X-ray PDF determined from synchrotron X-ray diffraction data (Figure 7.2). While the electron PDF analysis cannot ensure precise peak height determination due to varying multiple scattering contributions among different samples, X-ray PDF offers high precision in peak height information. The initial peak intensity of the X-ray PDF progressively increases with longer annealing times, signifying an increased coordination number and enhanced short-range order. This suggests a denser atomic packing resulting from the annealing treatment delivering a similar finding to the electron PDF analysis. However, there is no noticeable shift in peak position within the X-ray PDF, and no changes in the MRO peaks are visible in the X-ray PDFs. This discrepancy needs to be investigated further, with the different wavelengths of the X-rays of 117 pm and the electrons in the TEM of 2.24 pm being a possible explanation.

7.4. Tribological response of Zr-based metallic glasses

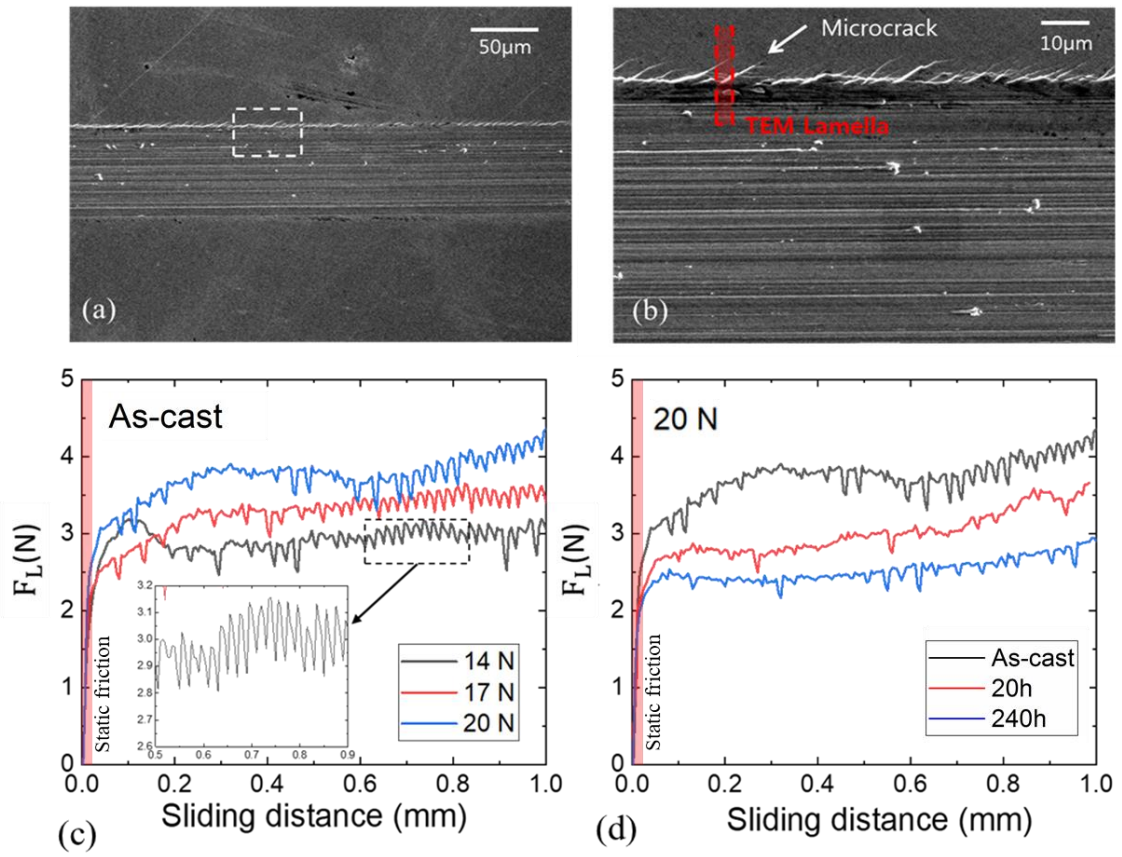


Figure 7.3: (a) SEM images of a worn track, (b) a close view of the area indicated by the white box in a) showing the area for lamella preparation, and an arrow highlighting a lateral microcrack. (c) Friction curves as a function of sliding distance at the normal load 14 N, 17 N, and 20 N for the as-cast sample. (d) Friction curves as a function of sliding distance for as-cast, 20 h, and 240 h annealed samples at a normal load of 20 N. The black highlighted rectangle in the friction curves represents the static friction zone.

Figure 7.3a shows an SEM image of a typical scratch produced at a normal load $F_n = 20$ N. The area marked with a dashed white line is magnified in Figure 7.3b. The scratch exhibits clear pileups at its sides that further extend to 10 mm long microcracks that form angles of 30° - 45° with the length axis of the scratch (See arrow in Figure 7.3b). The highlighted red area in Figure 7.3b shows the location where the TEM lamella was cut to include the pileup region and lateral cracks. Figure 7.3c shows typical friction curves for the lateral force F_L as a function of the sliding distance for the as-cast sample at normal loads $F_n = 14$ N, 17 N, and 20 N. The static friction region is highlighted by the red rectangle.

The lateral force sharply increases in the static friction region and shows unstable fluctuations (stick-slip) in the kinetic friction regime during sliding (magnified inset of Figure 7.3c).

In tribology, such stick-slip motion of an asperity over a surface corresponds to the storage of elastic energy within the contact until it reaches a threshold value to initiate the shearing of a contact junction. In analogy, serrated plastic flow has been observed in various metallic glass under different deformation scenarios^[119, 228], *e.g.*, indentation, bending, and compression. In these cases, serration is associated with an avalanche process leading to the creation of isolated defects. The correlation length of the observed stick-slip motion is in the range of 10 to 20 μm . Noteworthy this range of values matches the intervals of the lateral microcracks. Figure 7.3d shows the friction curves for the as-cast, 20 h, and 240 h annealed samples at a normal load $F_n = 20$ N. The as-cast sample shows a higher level of lateral force during sliding compared to the annealed samples. The longer-term annealing treatment further decreases the lateral force during sliding. Meanwhile, the serration and unstable fluctuation of lateral force are reduced in the annealed samples.

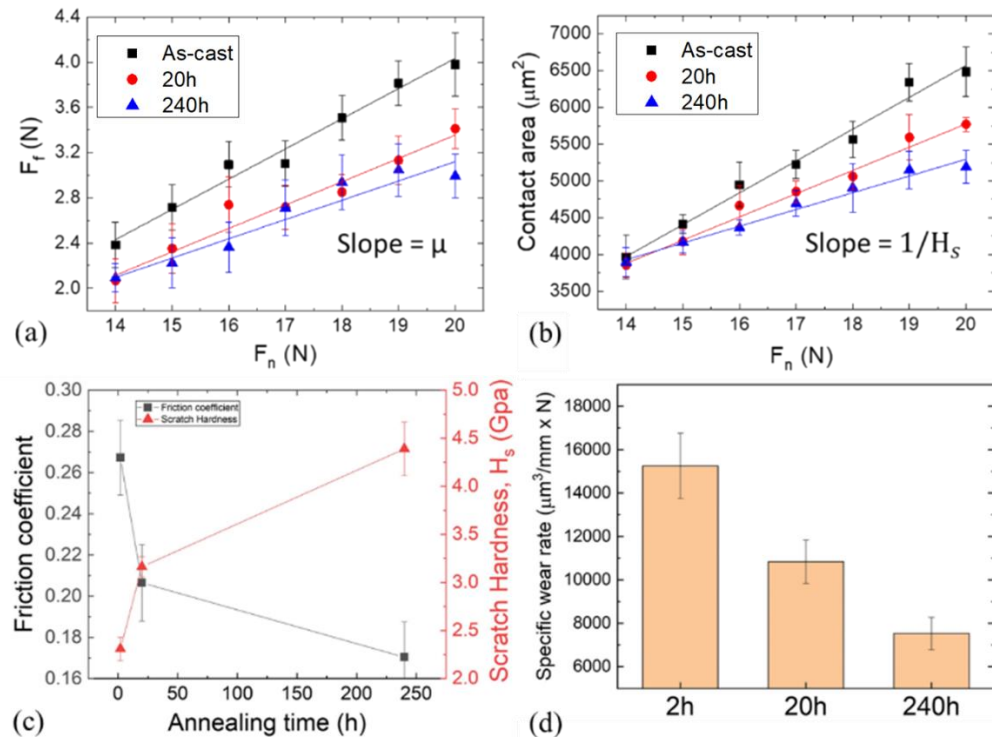


Figure 7.4: Tribological response of as-cast, 20 h, and 240 h annealed $\text{Zr}_{46}\text{Cu}_{38}\text{Al}_8\text{Ag}_8$ bulk metallic glasses. Load dependence of (a) friction force used to determine the friction coefficient as the slope and (b) of contact area used to determine the scratch hardness from the reciprocal slope; (c) friction coefficient and scratch hardness as a function of annealing time and (d) bar graph of specific wear rate.

The statistical friction force F_f is determined by averaging F_1 in the stable kinetic friction region from sliding distance $l_s = 0.5$ mm to $l_s = 1$ mm. Figure 7.4a and b show the load dependence of friction force F_f and contact area A_c for the as-cast, 20 h, and 240 h annealed samples. Linear increases of F_f and A_c are observed with increasing F_n , which follows the shearing of asperity

junctions.^[229] The linear dependences are fitted to calculate friction coefficient $\mu = \frac{dF_f}{dF_n}$, and scratch hardness $\frac{1}{H_s} = \frac{dA_c}{dF_n}$. Figure 7.4c shows that the friction coefficient decreases from 0.26 (as-cast) to 0.21 (20 h) and 0.19 (240 h), while H_s increases from 2.4 GPa (as-cast) to 3.3 GPa (20 h) and 3.8 GPa (240 h). The specific wear is calculated to $W_s = \frac{1}{L} \frac{dV_s}{dF_n}$, where V_s is the specific volume loss. Figure 7.4d shows that the specific wear decreases from 15000 $\mu\text{m}^3/\text{N mm}$ (as-cast) to 11000 $\mu\text{m}^3/\text{N mm}$ (20 h), and 7500 $\mu\text{m}^3/\text{N mm}$ (240 h).

7.5. Shear band network formation after deformation of metallic glasses in different annealing states

7.5.1. Zr-based bulk metallic glass

Figure 7.5 presents cross-sectional STEM-HAADF images of the worn surfaces of the samples. Scratching results in uneven surfaces with material piling up aside from the scratched track (Figure 7.5a, c, and e). The height of the piled-up area decreases from 2.33 μm (as-cast) to 1.7 μm (20 h) and 0.76 μm (240 h). The piled-up area entails microcracks that laterally propagate inward from the pile-up surfaces with low angles. The microcracks are spaced between adjacent microcracks forming step-like features in the pile-up regions. The size of the microcracks is significantly larger in the as-cast sample compared to the annealed samples. Additionally, shear bands are observed near the worn surfaces as well as in the glassy bulk matrix below the surface (Figure 7.5b, d, and f). These shear bands mainly appear with a darker contrast than the adjacent undeformed amorphous matrix, indicating structural dilatation within the shear band core. The dilatation phenomenon has been widely observed in previous TEM investigations of deformed metallic glasses.^[8, 30] Interestingly, alternating scattering contrast consisting of brighter and darker regions near the shear bands within the deformed matrix is observed indicating both volumetric contraction and dilatation. Furthermore, the shear bands branch out from primary shear bands or intersect one another, forming a network. The density of the shear band network differs among the samples, with the as-cast sample exhibiting a denser formation of the shear band network compared to the 20h annealed sample. This trend continues for the 240 h annealed samples, where only a limited number of shear bands are observed (Figure 7.5f).

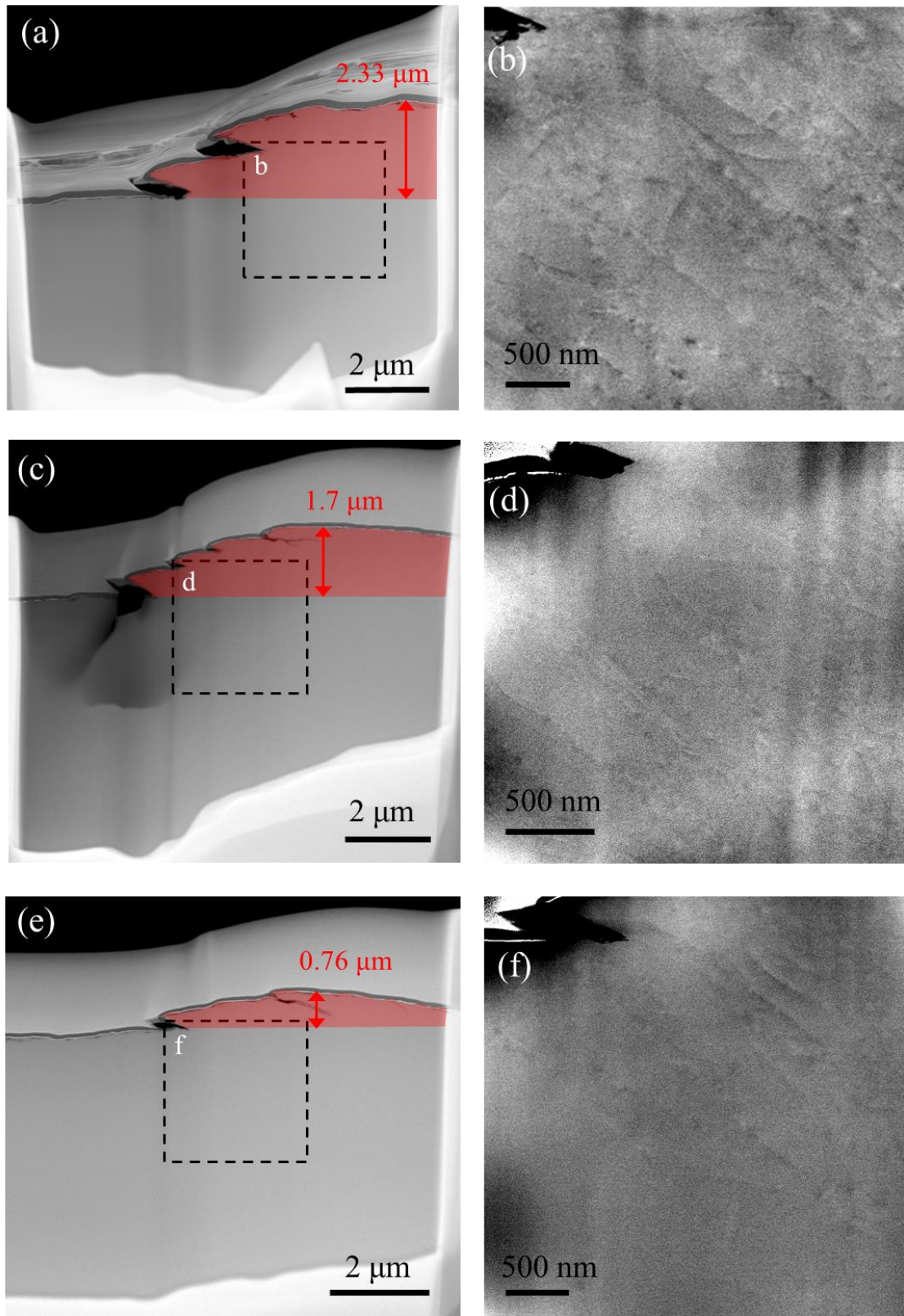


Figure 7.5: STEM-HAADF cross-sectional images of TEM lamellae from scratched the (a) as-cast, (c) 20 h, and (e) 240 h annealed $Zr_{46}Cu_{38}Al_8Ag_8$ metallic glasses at a normal load of 20 N. The piled-up area is highlighted in red, where microcracks are observed. The inset dash rectangles are magnified in (b, d, f) which show characteristic shear band networks.

4D-STEM maps spanning the area including the shear bands were acquired at the area indicated by the green-lined rectangles (Figure 7.6a, b, and c). The local strain is calculated by determining the ellipticity of the diffraction ring in each diffraction pattern of the 4D-STEM dataset as introduced in chapter 4.3. For strain tensor calculation, the X-axis is set to be parallel and the Y-axis is to be perpendicular to the major shear direction as indicated by the inserted axial bars. Moreover, the radius of the diffraction ring reflects the distance between atoms oriented along the radius in the nano-volume, giving rise to information on atomic density. Thereby, the relative density is calculated by quantifying the area encircled by the 1st ring of each diffraction pattern in the 4D-STEM data as demonstrated by Gammer et al.^[186]. This approach considers the elliptical deviation of the diffraction rings due to strain and disentangles the atomic density information from sample thickness and elemental species.

The strain component maps ε_{xx} (Figure 7.6c-g), ε_{xy} (Figure 7.6h-k), ε_{yy} (Figure 7.6l-o) and relative density maps (Figure 7.6p-s) are shown for the as-cast, 20 h, and 240 h annealed samples. The color code in ε_{xx} and ε_{yy} indicates the strain amplitude: dark blue (negative sign) represents compression corresponding to atoms squeezed closer along the axial direction, whereas bright yellow (positive sign) represents tension indicating an increased interatomic distance relative to the least deformed region between shear bands. The color code in ε_{xy} indicates shearing: positive values for clockwise shearing and negative ones for counterclockwise.

The strain tensor maps visualize dominant shear bands and SBAZs. The dominant shear bands are observed with an asymmetric strain distribution with sharp interfaces tilted 30~45 degrees from the scratched surface. The shear bands form a network and introduce a superposition of their respective deformed zones. In heavily deformed regions, *e.g.*, the pile-up region and near the tip of the lateral crack of the as-cast sample, the strain component ε_{xx} exhibits a wave-like pattern, tilted to ~45 degrees over the entire mapping area (Figure 7.6e). In these areas, individual shear bands and SBAZs are no longer differentiable. This indicates that the scratching introduced a dense shear band network with a superposition of shear bands and their respective deformed zone. Notably, the complex ε_{xx} features are reduced in the annealed samples (Figure 7.6f and g) and the individual shear bands are more clearly identified in the 20 h and 240 h annealed samples. This indicates a significantly reduced shear band formation and interaction in the annealed samples.

Inhomogeneous local fluctuations in the deformed matrix are visualized in the ε_{xy} maps (Figure 7.6h-k). The shear fields concentrate on some particular zones, *e.g.*, branching points of shear bands, revealing that strong shear transformation occurred at these specific zones. For the as-spun sample, ε_{xy} is distributed forming strain concentrators spread over regions extending micrometers

below the scratched surface and the piled-up region (Figure 7.6h and i). In contrast, the annealed samples possess a limited number of strain concentrators which are mainly localized near the scratched surfaces ϵ_{xy} (Figure 7.6j-k).

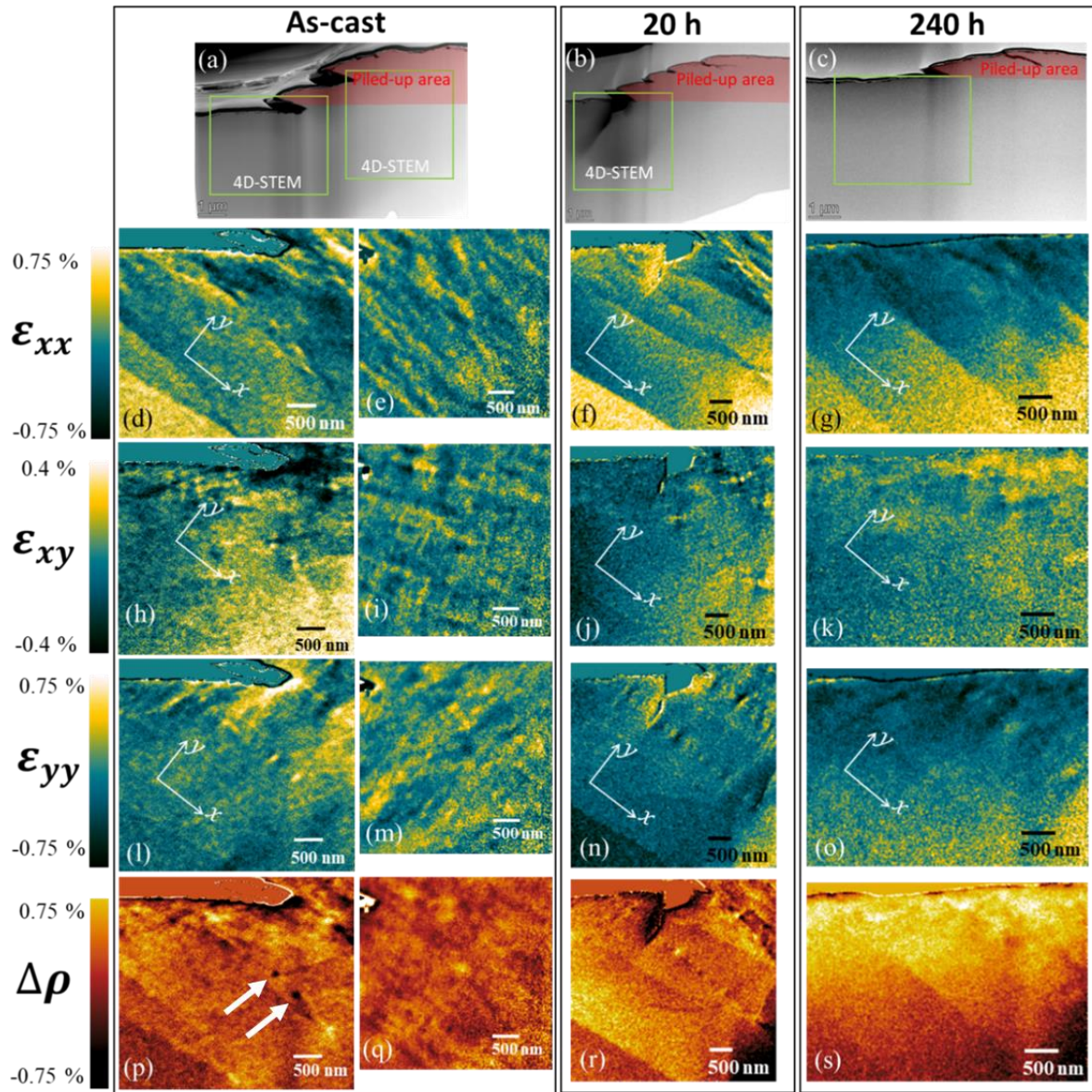


Figure 7.6: Deformed $Zr_{46}Cu_{38}Al_8Ag_8$ bulk metallic glass. (a)-(c) STEM-HAADF images showing the areas for 4D-STEM mapping near the deformed surface (green rectangle). The pile-up areas are indicated in red. The coordinate system is defined with the x-axis parallel and the y-axis perpendicular to the major shear direction as indicated by the inserted axial bars. (d)-(g) are maps of the strain component ϵ_{xx} , (h)-(k) are maps of the strain component ϵ_{xy} , and (l)-(o) are maps of the strain component ϵ_{yy} of the as-cast, 20 h and 240 h annealed samples. (p)-(s) are relative atomic density maps of the as-spun and annealed samples

Figure 7.6l-o (ϵ_{yy}) visualize periodic strain fluctuation along the shear bands forming zones of elliptic tension and contraction. The fluctuation of the strain component ϵ_{yy} indicates that the interatomic distances are stretched/squeezed along the orthogonal direction of shear bands.

Otherwise, the strain component ε_{yy} shows a similar trend with the strain component ε_{xx} : the as-cast sample exhibits a wider distribution of inhomogeneities while localized/limited fluctuations are observed for both annealed samples. Note that distinct shear bands are also observed within the samples, *e.g.* simple asymmetric (*e.g.*, bottom left, Figure 7.6d, f, and g) and alternating features (*e.g.*, middle, Figure 7.6n) along the shear bands. As discussed in chapter 6.5, the different morphologies of the shear bands, *e.g.* simple homogeneous dilatation and alternating features along the shear bands, may be related either to their time-dependent progression or to the orientation of the 2D projection of the 3D strain state of the material.

The relative atomic density $\Delta\rho$ (Figure 7.6p-s) is closely correlated with the overall strain tensor maps. It visualizes the dominant shear bands and their SBAZs in three different samples. Inhomogeneous density fluctuations are observed near shear bands matching with the strain inhomogeneity. The density fluctuation in the as-cast sample is also reduced after annealing treatment. Some dark points, as indicated by white arrows in Figure 7.6p, are located at shear band branching points revealing a strong structural dilatation occurred at the locations.

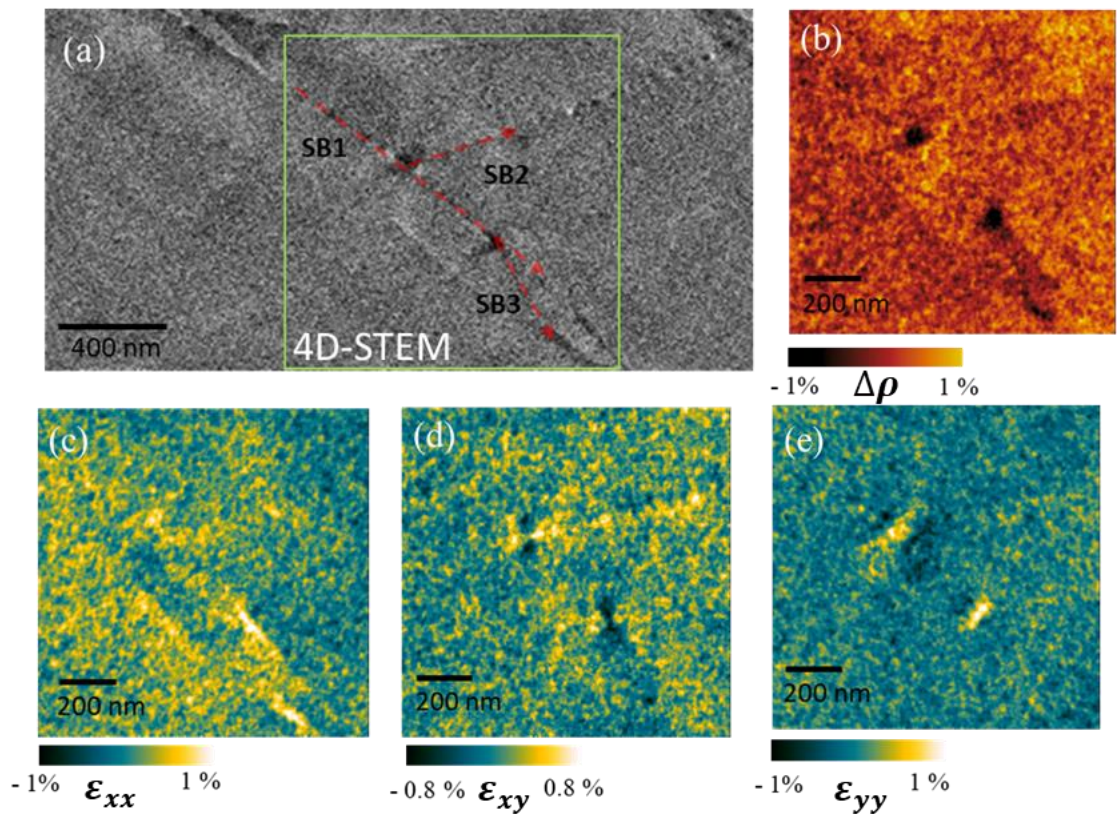


Figure 7.7: Secondary shear bands and their brunching points in the as-cast $\text{Zr}_{46}\text{Cu}_{38}\text{Al}_8\text{Ag}_8$ bulk metallic glass. (a) STEM-HAADF image showing the area for 4D-STEM mapping (green rectangle). (b) is a relative atomic density map. The coordinate system is defined as x-axis parallel and y-axis perpendicular to SB1 (c)-(e) are strain tensor ε_{xx} , ε_{xy} , and ε_{yy} .

For a detailed examination of the structure of the branching points, the higher magnification is shown in Figure 7.7. The STEM-HAADF image at the branching point displays the shear bands based on the darker scattering intensity, indicating localized volumetric dilatation (SB2 and SB3 are branched out from SB1). A 4D-STEM map was acquired for the area indicated by the green rectangle. The strain tensor has been calculated from the principal strains by setting the coordinate system with the x-axis parallel and the y-axis perpendicular to SB1 to visualize the strain distribution along with the primary shear band. Figure 7.7c (ϵ_{xx}) shows shear bands with asymmetric strain distribution across the shear bands. Two quadrupole shear strain fields were observed at the two branching points (Figure 7.7d). Each of the quadrupoles consists of a positive pair (red dashed ellipse) and a negative pair (white dashed ellipse) perpendicular to each other and oriented $\sim 45^\circ$ to the shear band plane. Interestingly, the positive pair of the quadrupoles is aligned to the secondary shear band, *e.g.*, SB2. Meanwhile, ϵ_{yy} demonstrates strong out-of-plane tension with elongated features perpendicular to SB1 at the branching point (Figure 7.7e). The orientation of these features represents the direction of maximum residual stress in an established shear band SB1. It indicates that the material is elastically stretched orthogonal to SB1.

7.5.2. Fe-based metallic glass ribbon

To verify the universality of the phenomenon, the same 4D-STEM approach was applied to the as-spun and annealed $\text{Fe}_{85.2}\text{Si}_{0.5}\text{B}_{9.5}\text{P}_4\text{Cu}_{0.8}$ metallic glass ribbons after scratch deformation, which possesses mechanical properties distinct from the Zr-based metallic glass (Table 7.1) investigated previously. Figure 7.8a and b show HAADF-STEM images of the scratched surfaces of the as-spun and annealed $\text{Fe}_{85.2}\text{Si}_{0.5}\text{B}_{9.5}\text{P}_4\text{Cu}_{0.8}$ metallic glasses, where the location of shear bands can be estimated based on the shear offset at the surface. 4D-STEM maps were acquired below the deformed surface in the area indicated by the green rectangles with a step size of 5 nm. The strain tensor maps visualize dominant shear bands and their affected zones. The shear bands are tilted ~ 45 degrees from the scratched surface and spaced several micrometers. In this reference coordinate system, the x-axis is defined to be parallel to the shear bands, while the y-axis is perpendicular to the shear bands.

The shear band results in an asymmetric ϵ_{xx} distribution with sharp interfaces across the shear plane (Figure 7.8c and d) similar to the observations of the Zr-based sample. The pop-in shear side suffers in-plane compression, and the opposite shear side is in tension as indicated by the white dash arrows in Figure 7.8c and d. The gradient strain fields span up to several micrometers perpendicular to the shear band forming broad SBAZs centered at a shear band. The nanometer

resolution in 4D-STEM reveals unprecedented details of the strain variation within the SBAZs as ϵ_{xy} exhibits inhomogeneous strain fluctuations in the SBAZs (Figure 7.8e and f).

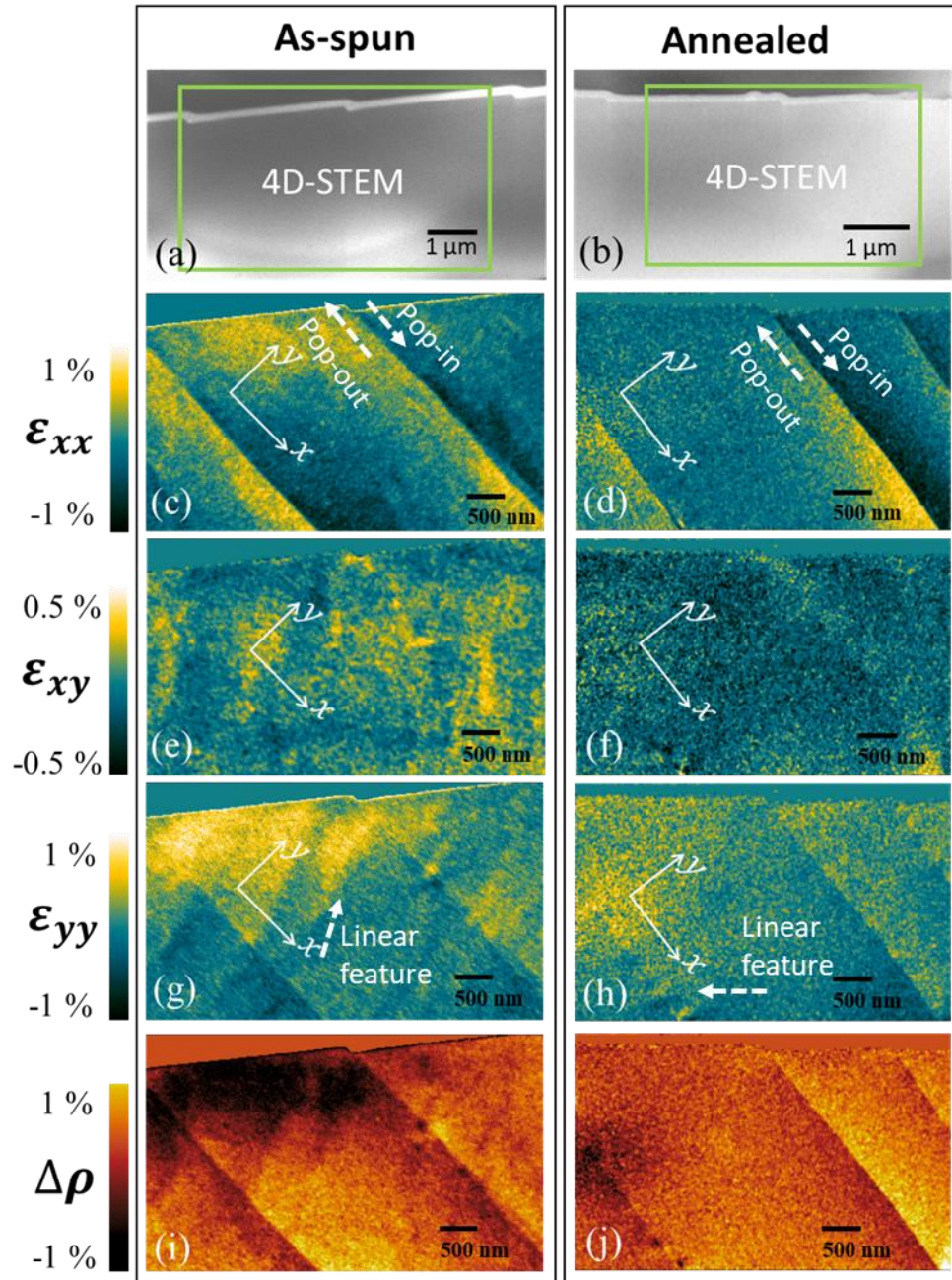


Figure 7.8: Deformed $\text{Fe}_{85.2}\text{Si}_{0.5}\text{B}_{9.5}\text{P}_4\text{Cu}_{0.8}$ metallic glass ribbon. (a), (c), (e), (g), and (i) as-spun samples and (b), (d), (f), (h), and (j) annealed samples. (a)-(b) STEM-HAADF images showing areas for 4D-STEM mapping and the presence of shear offsets (green rectangles). The coordinate system is defined with the x-axis to be parallel to shear bands and the y-axis perpendicular to shear bands as shown in the inserted coordinate system. (c)-(d) display the strain component ϵ_{xx} , (e)-(f) the strain component ϵ_{xy} , and (g)-(h) the strain component ϵ_{yy} . (i)-(j) show the relative atomic density maps of as-spun and annealed samples.

For the as-spun sample, the local inhomogeneity of the strain component ϵ_{xy} in SBAZs is distributed over the entire area without an obvious connection to the shear bands. In the annealed

sample, the strain component ε_{xy} is homogeneous with a fine background (noise-like) with a slight localization at one of the shear bands. As discussed in chapter 6.3, these fine strain variations are likely linked to the intrinsic structure of the glass, with characteristics of both liquid- and solid-like structural types, rather than being deformation-induced features. Consequently, the local inhomogeneity in the SBAZs is significantly higher in the as-spun sample compared to the annealed samples.

The strain component ε_{yy} (Figure 7.8d and j) again reveals an asymmetric structure with strain gradients across the SBs in both as-spun and annealed samples. In contrast to the strain component ε_{xx} , the pop-in shear side experiences out-of-plane tension (positive ε_{yy}), while the pop-out side has experienced out-of-plane compression (negative ε_{yy}). The reversed strain levels of ε_{xx} and ε_{yy} are expected due to the Poisson effect. However, the ε_{yy} gradient field is confined to a considerably shorter length scale than ε_{xx} . In addition to the asymmetrical strain gradient field, a strong tensile ε_{yy} is present near the surfaces. The tensile ε_{yy} fields exhibits features roughly perpendicular to the shear bands as indicated by white dash arrows in Figure 7.8g and h, giving rise to inhomogeneous fluctuations along the y-axis in the SBAZs. The perpendicular features in ε_{yy} are considerably more extended in the as-spun sample than those in the annealed sample. Notably, the perpendicular features in ε_{yy} connect the adjacent shear band in as-spun sample. In contrast, the perpendicular features in ε_{yy} are barely visible in the annealed sample, but only with the elliptical elongation of the fields perpendicular to the shear band.

The $\Delta\rho$ (Figure 7.8e-k) are correlated with the strain distribution. The compressed area of the strain component ε_{xx} exhibits the higher density and tensile area of the strain component ε_{xx} matches with the lower-density area. This can be simply understood with a scenario in which the compressive field squeezes atoms closer to each other resulting in densification. The traction on the opposite side leads to tension giving rise to the volumetric expansion. Considering the Poisson effect observed in the strain components ε_{xx} and ε_{yy} , the atomic density confirms that the major loading axis is the X-axis which follows the orientation of shear bands. Localized expansions are observed near the surface in the as-spun sample where the strong tensile ε_{yy} fields are present. Moreover, the inhomogeneous density fluctuations in SBAZs confidently match the strain tensor maps. The as-spun sample demonstrates stronger inhomogeneous density fluctuations in the SBAZs compared to the annealed sample. Additionally, the density inhomogeneity in the as-spun sample extends over the entire area investigated, while the annealed sample shows inhomogeneities only in the vicinity of the shear bands.

7.6. Discussion of the correlation between structural features and deformation behavior of metallic glasses

The local structure of metallic glasses was effectively tuned by annealing that induces structural densification and eliminates structural heterogeneity present in the as-quenched state, which eventually gives rise to the increased hardness and reduced specific wear, as shown explicitly for the CuZr-based glass in chapter 7.4. Shear band networks were formed as a result of the intersecting and branching of shear bands during plastic deformation. Different morphologies of the shear band network at different annealed states indicate substantial differences in their primary deformation. The as-cast sample possesses a denser shear band network, indicating more delocalized plastic deformation occurred during deformation compared to the annealed samples. Such formation of a dense shear band network can be considered to be the origin of a ductile deformation in metallic glasses, which suppresses the formation of a dominant shear band traversing through the entire glassy matrix.^[230-231]

The initiation of a shear band is believed to occur through the activation of Eshelby inclusions as discussed in chapter 2, which is believed to preferentially take place at intrinsic soft spots in the glass matrix.^[197, 233] Atomistic modeling estimated that the typical size of the primary inclusions is around tens of cubic nanometers.^[21, 118] However, in chapter 6, larger Eshelby inclusions were observed with a typical core radius of about 15 nm encompassed by surrounding strain fields. The present work also identified large shear transformation regions at shear band branching points. The core of the shear band branching points exhibits dilatation and a strong concentration of tensile ε_{yy} , which may naturally occur at such branching points of shear bands in metallic glasses.

In addition, the 4D-STEM approach provides a detailed view of the shear band networks. Asymmetric interfaces are observed across shear bands forming broad SBAZs with measurable structural changes on a larger length scale. There the residual strain fields give rise to variations in the local atomic density: the compressive strain field results in densification and tension in dilatation. These SBAZs alter the local material properties and may influence subsequent deformation processes.

The features in the strain component ε_{yy} perpendicular to the shear bands visible in Figure 7.8g and h show the direction of maximum residual stress near the shear bands and in the SBAZs, whereas no comparable features are present in the strain component ε_{xx} . This indicates that the stress component along the shear band ε_{xx} relaxes during the propagation of shear bands, but noticeable residual stresses are maintained in the perpendicular direction. These features could be

the nucleation points for shear band multiplication leading to secondary shear bands when the out-of-plane stress components overcome the activation barrier for the secondary shear band generation. This would explain the observation of secondary shear bands generated at high angles to the primary shear band in uniaxial compression tests by Antonaglia et al.^[235].

The strain/density inhomogeneity observed away from individual shear bands points to large-scale shear transformations occurring not only within the shear plane but also in distant regions of the matrix. These spread-out shear transformations likely arise from the ubiquitous formation of STZ at intrinsic soft spots within the glass matrix and their subsequent agglomeration, which nevertheless do not lead to full shear band formation. As the as-prepared samples have more intrinsic heterogeneity with corresponding soft spots, they exhibit a more heterogeneous strain concentration compared to the annealed samples after deformation. Shear bands may interact with those local strain concentrations and form secondary shear bands through the overlap of their respective deformation zones, thus reducing strain localization in metallic glasses. This suggests that the appearance of locally heterogeneous features in the as-prepared samples during deformation, as seen in Figure 7.8e, allows for a globally more homogeneous plastic deformation during subsequent deformation processes. This would also explain how less-relaxed glasses can accommodate substantially higher material flow during their plastic deformation. In contrast, in well-relaxed samples, the heterogeneous features are much weaker, resulting in a limited formation of fertile STZs and locally heterogeneous features. This results in a reduced formation of shear bands and their limited interactions, eventually leading to stronger strain localization in the matrix and restricting the deformability of metallic glasses.

7.7. Summary

The use of 4D-STEM-based PDF and strain analysis has been demonstrated as a new approach to obtaining crucial information for studying deformation mechanisms in metallic glasses. The results provide detailed structural information of shear band networks and SBAZs including long-range strain gradient and strain inhomogeneity. The observations suggest that deformation energy is stored in a wider region rather than the nanoscale core of shear bands after plastic deformation.

The annealing induces short-range ordering and densification leading to an increased hardness and an increased flow barrier in metallic glasses. Thereby, the wear resistance of the metallic glasses is significantly improved after annealing. In contrast, the as-prepared samples promote a more ubiquitous shear transformation compared to the annealed samples after deformation. Shear bands

interact with those local shear transformation regions and may form secondary shear bands through the overlap of their respective deformation zones, thus reducing strain localization in metallic glasses. The development of ubiquitous shear transformation regions during deformation allows for a globally more homogeneous plastic deformation during subsequent deformation processes. Moreover, the present work further identifies strong shear transformation regions with cooperative shear fields at shear band branching points. This indicates that Eshelby inclusions can be naturally formed in metallic glasses on a larger scale than the typical size of STZ-like inclusions. This direct experimental observation provides a crucial understanding of how the original atomic structure affects the formation of the shear band network and, eventually, the deformation process of metallic glasses. Examination of the two distinct different metallic glasses in different annealing states suggests the universality of the observation.

Chapter 8

8. Development of Lorentz 4D-STEM for correlative imaging of the magnetic/electric fields, strain fields, and atomic packing structure of metallic glasses

In this thesis work, a new microscopy technique “Lorentz (Ltz)-4D-STEM” is developed for correlative mapping of the magnetic/electronic structure, strain fields, and relative packing density. The correlative measurement of these properties allows not only for a precise quantitative analysis of local density and strain variations in amorphous materials but also enables the direct correlation, at the pixel level, between the magnetic/electric field and the atomic structure. Consequently, the magnetoelastic energy of magnetic/electric materials can be experimentally mapped. This chapter dedicatedly focuses on the method development, as a result, the description for material understanding is only briefly discussed.

8.1. Background for the development

Soft ferromagnetic materials, such as silicon ferrites and Fe-based amorphous alloys, play a significant role in energy conversion due to their high energy efficiency and power density.^[232] Specifically, soft magnetic amorphous alloys, like Fe- and Co-based metallic glasses, have recently received attention in power electronics and electrical machines, such as motors and generators, because of their small coercivity (H_c) and high mechanical strength.^[233] Their dense and isotropic atomic structure results in a very small coercivity and a competitively high saturation magnetization (M_s), leading to reduced hysteresis loss and increased power density.^[234-235]

The magnetic structure of ferromagnets is composed of domains, where magnetic dipoles are grouped together and aligned to minimize magnetostatic energy.^[236] In soft ferromagnetic materials, domain walls are easily movable, and the motion and structure of domains govern their soft magnetic properties. The domain structure is closely related to the local atomic arrangements and the development of structural anisotropy, such as magnetocrystalline anisotropy (K_c) and stress anisotropy (K_σ).^[237-238] Anisotropy gives rise to a preferred direction (easy axis) for magnetization, which can be described by magnetoelastic energy.^[236] The magnetic moments of the domains are influenced by the elastic stress field within the material, resulting in the development of a stress anisotropy also known as inverse magnetostriction.^[237, 239-240] Consequently, the deviatoric strain within a magnet can reorient magnetic moments and alter the domain arrangement to minimize the total magnetic energy. Generally, anisotropy contributions increase H_c , which should be kept small (< 100 A/m) for efficient soft magnetic applications, by limiting domain motion.

For soft magnetic amorphous alloys, which lack magnetocrystalline anisotropy, the magnetic structure is primarily influenced by stress anisotropy. Consequently, residual strain fields resulting from plastic deformation can reorganize magnetic domains and magnetic moments within domains. Previous studies have shown that the magnetic domain structure of Fe-based metallic glasses becomes complex after plastic deformation.^[157] In general, plastic deformation negatively affects the performance of soft ferromagnets.^[232] This is particularly crucial for magneto-mechanical applications, such as stators in induction motors, where the magnetic components are often subjected to rotational forces. Therefore, there is a need for highly correlated measurements of magnetic and strain fields, as well as atomic structure, in soft ferromagnetic materials to fundamentally understand the magnetic properties and develop new materials.

In this Ph.D. work, a new analytical method called Ltz 4D-STEM has been developed for correlative mapping of the magnetic and atomic structure at the nanoscale. This approach takes into account the momentum transfer of the electrons caused by the local magnetic field, the elliptic distortion of the amorphous diffraction ring under strain, and the area enclosed by the ring to quantify the relative density and reveal their spatial-correlative variance. This method enables the visualization of magnetic and atomic structures with pixel-level correlation, allowing to experimentally map the magnetoelastic energy of soft ferromagnets.

8.2. Microscopy setting, data acquisition, and processing

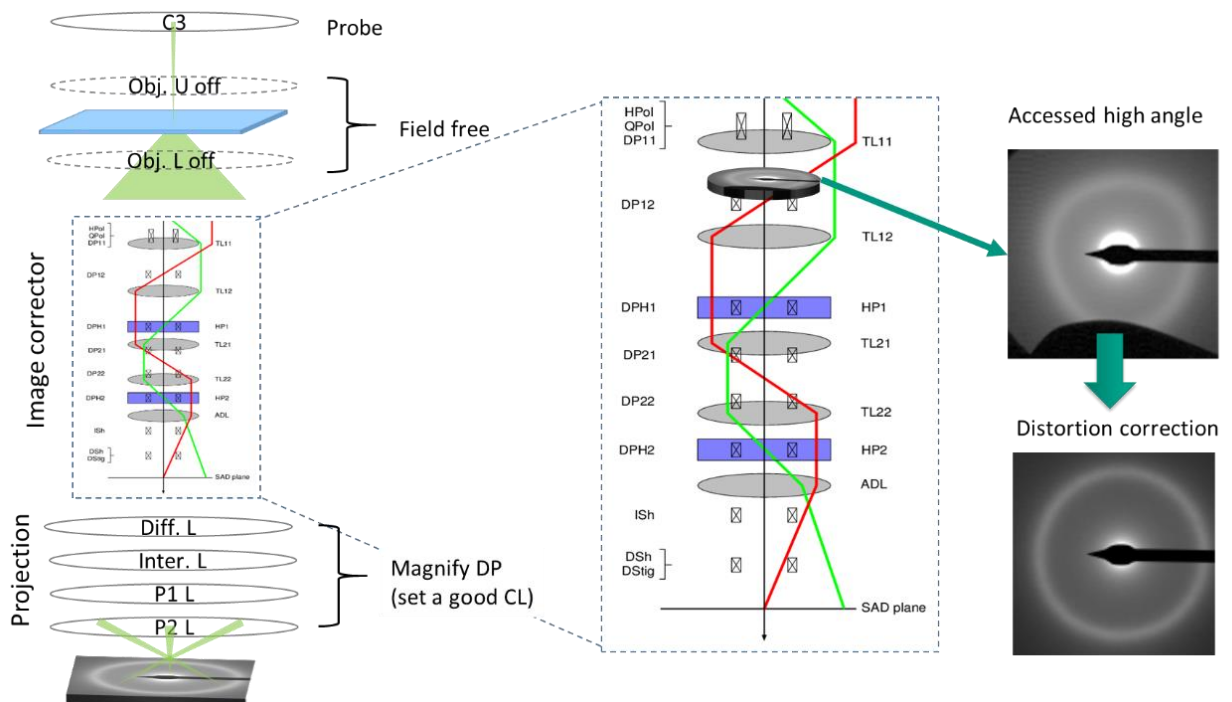


Figure 8.1: Lens setting of Ltz-4D-STEM. The lenses in the image corrector are manipulated by tuning their direct current supply. The first lens in the image corrector, *i.e.* Lorentz lens, is used to converge the high scattering signal, and the double hexapole correctors are tuned to compensate for the distortion. Thereby, the recorded maximum scattering angle was corresponding to about 1 \AA^{-1} in reciprocal space without significant distortion.

The development of Ltz-4D-STEM has been conducted using a Themis Z double-corrected TEM (Thermofisher Scientific). The microscope has been operated at 300 kV with a semi-convergence angle of 0.26 mrad in microprobe STEM mode giving rise to a diffraction-limited probe size of about 5 nm. Figure 8.1 shows the lens setting for the Ltz-4D-STEM configuration. To achieve field-free conditions, the objective lens is turned off in microprobe STEM mode. As not only the

upper part of the objective lens is turned off, but also the lower pole piece of the objective lens, it is difficult to collect electrons scattered to high angles. Thereby, the lowest nominal camera length in this mode is limited to 6.1 m. Furthermore, the diffraction pattern suffers from a triangular distortion by the image corrector aligned for the standard objective lens settings in STEM mode. To get access to the high-angle scattered electrons and correct the diffraction distortions, it is necessary to realign the image corrector. The lenses of the image corrector were adjusted by directly modifying the lens currents through the CEOS control software. Specifically, the initial lens in the image corrector was utilized to bring together the highly scattered signal. The double hexapole correctors were fine-tuned to counteract the triangular distortion. To achieve this, manual adjustments were made to the triangular lens and the hexapoles (TL-11, TL-12, HP-1, and HP-2 as indicated in CEOS control software) of the image corrector until optimal conditions (homogeneous ring pattern) were reached. As a result, the lowest nominal camera length is reduced to about 1.15 m without introducing significant distortions. Thereby, the attainable maximum scattering angle was enhanced from approximately about 0.4 \AA^{-1} (before tuning) to around 2 \AA^{-1} (after tuning). With these settings, an array of diffraction patterns can be captured using 4D-STEM, a technique referred to as Ltz-4D-STEM. However, the central position of each diffraction pattern tends to shift due to misalignment of the scan pivot point during scanning. To mitigate this effect, the Descan function was employed, which involves adjusting a paired set of coils to compensate for the shifting. Furthermore, any remaining shift was corrected with post-background processing by capturing a reference map without the sample.

Figure 8.2a illustrates the setup of the Ltz-4D-STEM system. A nearly parallel electron probe is focused to approximately 5 nm in diameter on an electron-transparent sample. Electron diffraction patterns are obtained from the nano-volume at each scan position while incrementally moving the probe over the desired area. The magnetic fields within the sample deflect the electron beam due to Lorentz force, expressed as $F = q(E + v \times \vec{B})$, where q is the electric charge, E is the external electric field, v is the velocity, \vec{B} is the magnetic field. The position of the direct beam provides information about the direction and intensity of the magnetic fields analogous to DPC imaging.^[182] 4D-STEM based DPC directly measures the phase shift of the electron waves passing through the sample using a center position measurement over all pixels. Mathematically, the magnetic field can be expressed as $\vec{B} = \frac{-\Delta\vec{P}}{q \cdot \Delta z}$, where \vec{B} is the magnetic field, $\Delta\vec{P}$ is the momentum transfer of fast electrons, q is the electric charge, and Δz is the sample thickness.^[241]

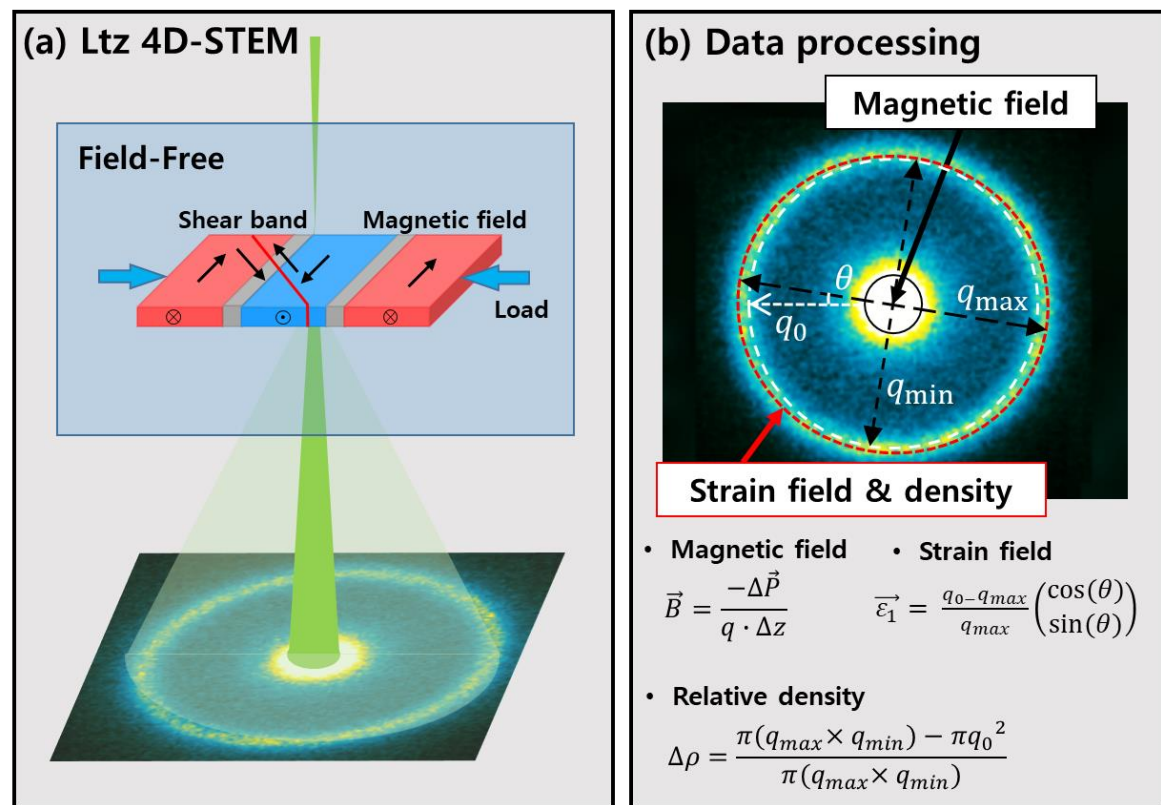


Figure 8.2: Schematic illustration of Ltz-4D-STEM. (a) The electron probe is focused on the soft magnetic TEM sample under field-free conditions, *i.e.*, Lorentz condition. Spatially-resolved diffraction patterns are collected during scanning over an area of interest. (b) Data processing: the center position of the direct beam is a measure of the momentum transferred by the magnetic field (Lorentz forces) inside the sample. The first principal strain ($\vec{\varepsilon}_1$) is calculated from the elliptic distortion of the 1st diffraction ring. The relative density ($\Delta\rho$) is measured by the relative variation of the area encircled by the 1st ring of each diffraction pattern.

The strain and atomic density were computed using the methods described in chapter 4.4. In order to simultaneously record structural information, the camera length was set to 1.15 m. This configuration has been designed to capture the first diffraction ring on the camera with the largest possible diameter, enhancing the sensitivity for measuring the distortion and area of the diffraction ring. The SVD-based fitting algorithm simultaneously tracks the centers of the individual diffraction patterns for simultaneous measurement of the magnetic fields and atomic structure of a sample.

8.3. Direct measurement of magnetoelastic coupling in an amorphous soft ferromagnet

As an exemplary study, the magnetic $\text{Fe}_{85.2}\text{Si}_{10.5}\text{B}_{9.5}\text{P}_4\text{Cu}_{0.8}$ metallic glass has been used. 4D-STEM maps were acquired by scanning the electron probe over a 2D sample plane with an exposure time of 3.3 ms per frame with a step size of 15.8 nm and a frame size of 620×225 for the as-spun sample. A OneView camera (Gatan Inc.) is used for recording the diffraction patterns. The diffraction patterns capture the complete first diffraction ring of $\text{Fe}_{85.2}\text{Si}_{10.5}\text{B}_{9.5}\text{P}_4\text{Cu}_{0.8}$ metallic glass as shown in Figure 8.2b. Typical results from the Ltz-4D-STEM are shown in Figure 8.3b-d, which depict the (pixel-wise correlated) magnetic field (\vec{B}), first principal strain ($\vec{\epsilon}_1$), and relative density ($\Delta\rho$) of the as-spun $\text{Fe}_{85.2}\text{Si}_{10.5}\text{B}_{9.5}\text{P}_4\text{Cu}_{0.8}$ metallic glass ribbon after plastic deformation. For the maps of \vec{B} and $\vec{\epsilon}_1$, the brightness represents the strength of the magnetic field and strain, while the color indicates the respective orientation based on the color wheel. The strain orientation is presented with two-fold symmetry. In the $\Delta\rho$ map, higher densities are represented by a yellow color, and lower densities are depicted by a dark blue color. The heavily deformed regions, such as the worn surface and vicinity of shear bands, exhibit a complex domain structure (Figure 8.3b). Furthermore, an asymmetric arrangement of the domains across shear bands can be observed. Based on the shear offset, it can be confirmed that the domain structure is non-uniform on the pop-in side of the shear band, where domain walls perpendicular to the shear bands extend several micrometers away from them. On the pop-out side, however, the domain structure appears relatively homogeneous.

The map of the first principal strain $\vec{\epsilon}_1$ (Figure 8.3c) also visualizes the asymmetric feature of strain distribution across shear bands with a sharp transition occurring at the shear plane. The orientation of the first principal strain $\vec{\epsilon}_1$ is aligned toward the shear propagation direction. This matches the previous strain observations in deformed metallic glasses using X-ray diffraction.^[154-155] The asymmetric feature can be understood by the opposite motion of the material on each side of the shear band during the deformation. Before plastic deformation, it is expected that a long-range elastic field builds up during the elastic regime in the overall glassy matrix. The plastic deformation initiates at a local zone, *e.g.* STZ, when local strain exceeds elastic limits. The plastic strain relaxes the long-range stress and forms well-defined defects, *e.g.*, shear bands. The shear bands can pin the imposed stress giving rise to a residue strain field surrounding them. Complementary to the micrometer resolution of the X-ray-based technique, the nanometer resolution in 4D-STEM detects further details of deformed structure, *e.g.*, the nanoscale core of shear bands and inhomogeneous strain fluctuations near shear bands. It can be seen that the strain

concentrates on localized zones giving rise to the development of local heterogeneity, where the first principal strain $\vec{\epsilon}_1$ forms with a rotational field at the heterogeneity (sharp color change in the map) in the deformed matrix. Meanwhile, the core of the shear bands does not preserve residual strain inferring that the stress is fully relaxed there during the shear banding. Inhomogeneous density variation is observed within the matrix even away from individual shear bands similar to the observation in chapter 7.5.

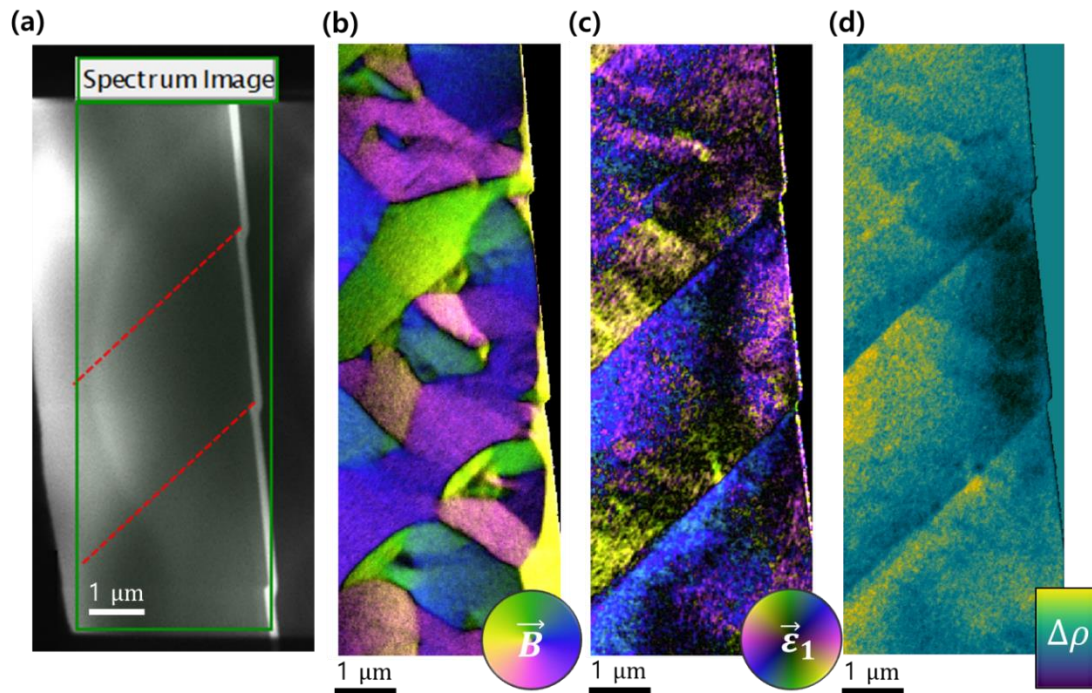


Figure 8.3: Ltz-4D-STEM observation of as-spun $\text{Fe}_{85.2}\text{Si}_{0.5}\text{B}_{9.5}\text{P}_4\text{Cu}_{0.8}$ metallic glass ribbon after plastic deformation. (a) STEM-HAADF image of the TEM lamella, where the expected locations of the shear bands are indicated by red dashed lines according to shear offset at the surface. A 4D-STEM map was acquired at the area indicated by the green rectangle, where the shear bands of interest are labeled as SB1 and SB2. (b) magnetic field (\vec{B}), (c) first principal strain ($\vec{\epsilon}_1$). The color corresponds to the orientation, and the brightness corresponds to the amplitude of the fields, as indicated by the color wheel. For $\vec{\epsilon}_1$, the strain orientation is presented by a two-fold symmetrical wheel following its nature. (d) relative density ($\Delta\rho$). Yellow color represents high density and dark blue color low density.

The $\Delta\rho$ map (Figure 8.3d) also visualizes asymmetric features across the shear bands. The $\Delta\rho$ measurement primarily relates to the local net volume change due to hydrostatic stress. The pop-in side of the shear bands exhibits relatively high density, while the opposite side shows lower density. This can be understood by considering the hydrostatic stress field, which compresses atoms on the pop-in side and induces tension on the opposite side. The density variation gradually fades out perpendicular to shear bands in both the compressed and tensile regions. To confirm that the DPC

signal originates from the magnetic structure, a conventional 4D-STEM measurement was conducted on the same sample under fully magnetized conditions (conventional STEM condition). The observed uniform image in Figure 8.4 confirms that the features observed in the non-magnetized sample are due to the magnetic fields of the sample.

The analysis confirms directly that plastic deformation affects the magnetic structure differently depending on the axial direction. It can be observed that the highly compressed area possesses a more complicated magnetic domain structure compared to the area under tension.

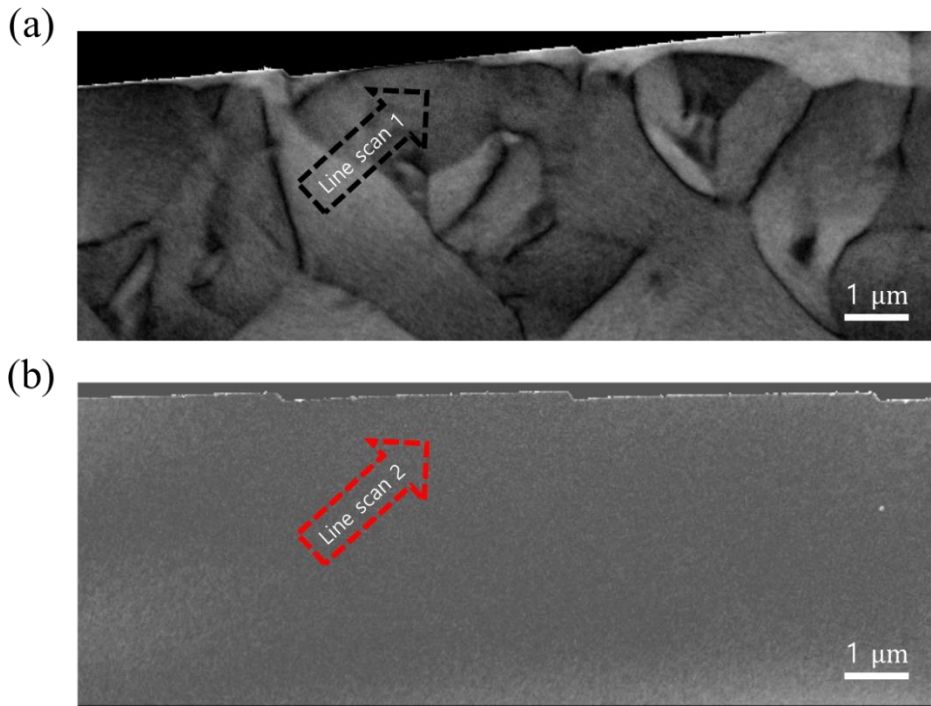


Figure 8.4: Map of the strength of DPC signal from (a) unmagnetized (Ltz-condition), and fully magnetized (conventional STEM condition) $\text{Fe}_{85.2}\text{Si}_{0.5}\text{B}_{9.5}\text{P}_4\text{Cu}_{0.8}$ metallic glass ribbon. (c) Line profiles taken across the shear band from the measurements of (a) Ltz-condition indicated by a black dash arrow (Line scan 1) and (b) conventional STEM condition indicated by a red dash arrow (Line scan 2).

According to the magnetoelastic coupling theory, magnetoelastic energy can be written as $E_{ME} = -\frac{3}{2}\lambda \sum_{i=1}^3 \sigma_i \gamma_i^2$,^[242] where λ is the magnetostriction constant, σ_i is the applied stress and γ_i is the cosine of angular mismatching between the magnetic field \vec{B} and first principal strain $\vec{\epsilon}_1$. Magnetic domains form in order to minimize the total magnetization energy in a magnetic material. The local strain induces a reorientation of the magnetic moments, stabilizing the magnetic energy and leading to the restructuring of magnetic domains.^[238, 243] Fe-based metallic glasses possess a positive magnetostriction constant (~ 25 ppm),^[244-245] causing a tendency for magnetic moments to align parallel to the tensile direction and perpendicular to the compressive direction. Due to

exchange interaction, the ferromagnetism with positive λ can deviate when the inter-dipole distance decreases. This is presumably responsible for the complicated domain structure observed in the highly compressed zones on the pop-in side of shear bands.

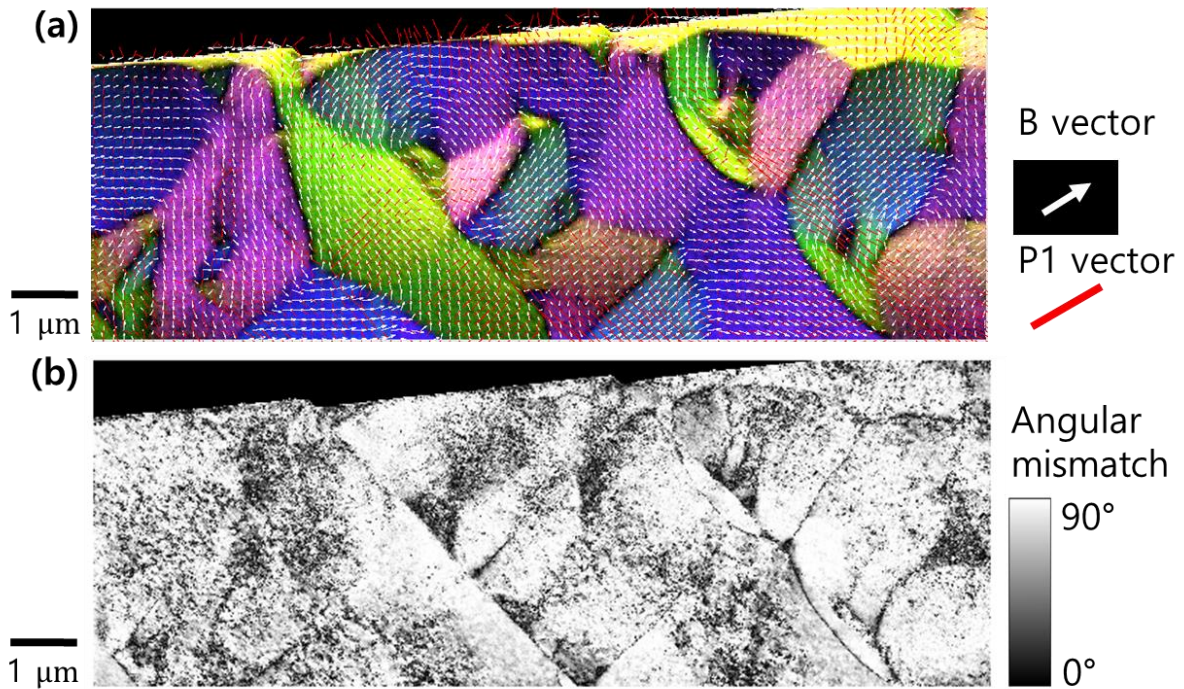


Figure 8.5: As-spun $\text{Fe}_{85.2}\text{Si}_{10.5}\text{B}_{9.5}\text{P}_4\text{Cu}_{0.8}$ metallic glass ribbon after plastic deformation. (a) Vector field visualization of the magnetic moments (B_x, B_y) with white arrows and the first principal strain ($\epsilon_{1x}, \epsilon_{1y}$) with red sticks overlaid by the color map of \vec{B} . (b) Angular mismatching between \vec{B} and $\vec{\epsilon}_1$.

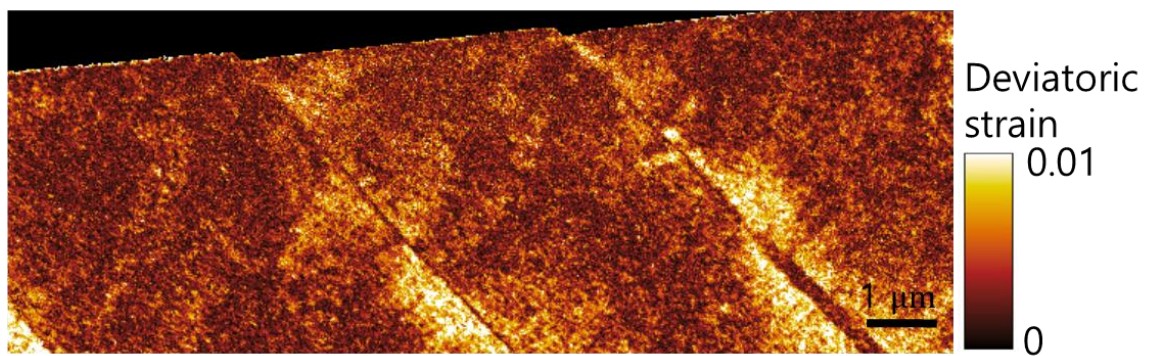


Figure 8.6: Deviatoric strain of as-spun $\text{Fe}_{85.2}\text{Si}_{10.5}\text{B}_{9.5}\text{P}_4\text{Cu}_{0.8}$ metallic glass ribbon after plastic deformation.

Figure 8.5a depicts a vector field visualization of the magnetic moments (black arrows) and first principal strains (red arrows) overlaid with the color map of the magnetic field \vec{B} . Figure 8.5b

illustrates the angular mismatch between magnetic moments and strain direction. It can be observed that the magnetic moments and first principal strains are orthogonally correlated in most areas of the map, except in the vicinity of shear bands and domain walls.

By quantifying the deviatoric strain (Figure 8.6) and angular difference of \vec{B} and \vec{P}_1 (Figure 8.5b), the magnetoelastic energy E_{ME} can be mapped as depicted in Figure 8.7. The formation of magnetic domains aims to minimize the total magnetization energy in a magnetic material. As a result of local atomic strain, magnetic moments undergo reorientation to stabilize the magnetic energy, leading to the restructuring of magnetic domains. Notably, the subnanometer scale strain effects substantially modulate the domain structure. Areas experiencing high levels of stress after plastic deformation exhibit unstable characteristics in terms of magnetoelastic energy.

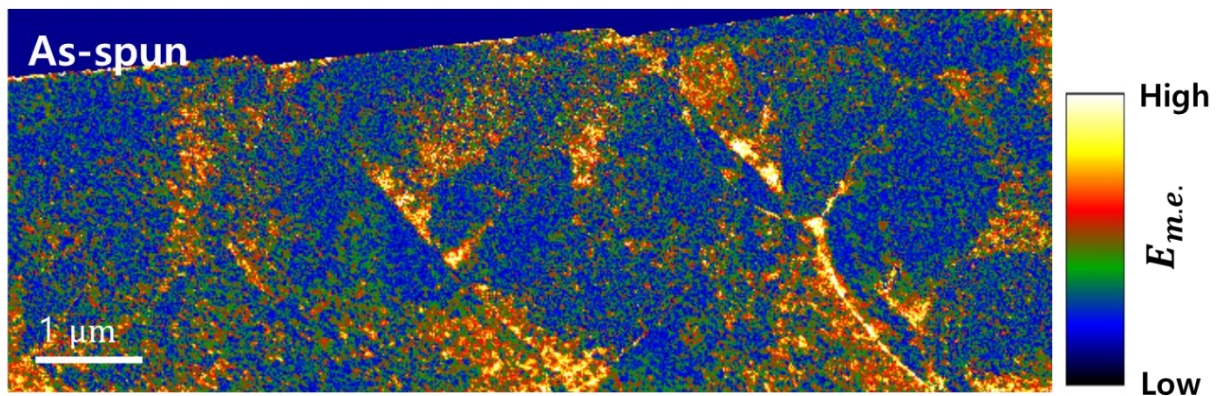


Figure 8.7: Map of magnetoelastic energy of the as-spun $\text{Fe}_{85.2}\text{Si}_{0.5}\text{B}_{9.5}\text{P}_4\text{Cu}_{0.8}$ metallic glass ribbons after deformation.

These unstable zones are distributed throughout the deformed regions of the sample. This observation can provide novel insights into the interplay between material properties and highlights the potential for improving magnetoelastic stability through thermal treatments of Fe-based metallic glasses. The method employed in this study is expected to pave the way for extensive research opportunities exploring the correlation between magnetic properties and atomic structure in magnetic materials.

8.4. Summary

A novel analytical setting called Ltz-4D-STEM has been developed to enable correlative mapping of magnetic and strain fields as well as relative density in ferromagnetic materials at the nanoscale. This method takes into account the momentum transfer of the electron beam caused by local

magnetic fields, the elliptic distortion of the amorphous diffraction ring due to strain, and the area covered by the ring to quantify the relative atomic density, enabling an analysis of their spatial-correlative variations. It allows for direct pixel-level correlation between the magnetic and atomic structures, enabling an experimental mapping of magnetoelastic energy in soft ferromagnets. Using this technique, the magnetoelastic energy of soft magnetic $\text{Fe}_{85.2}\text{Si}_{0.5}\text{B}_{9.5}\text{P}_4\text{Cu}_{0.8}$ metallic glass ribbons after plastic deformation has been visualized experimentally. The results demonstrate that plastic deformation leads to the emergence of residual strain fields and triggers the development of a complex magnetic structure to stabilize the magnetoelastic energy. This observation provides fresh insights into the interplay of material properties and highlights the importance of correlative analysis in understanding magnetoelastic phenomena.

Chapter 9

9. Conclusion and outlook

9.1. Conclusion

The application of metallic glasses is limited by their lack of ductility, attributed to shear banding-induced catastrophic failure during mechanical deformation. The work in this thesis aimed to experimentally characterize the microscopic structure of shear bands in metallic glasses as a basis to better understand the deformation mechanisms and further develop the deformation theory of metallic glasses with the ultimate aim of facilitating new material design with higher ductility.

In previous electron microscopic studies^[26-31], the characterization of deformed metallic glass structures has primarily relied on direct S/TEM imaging. While S/TEM imaging allows the observation of individual shear bands with sufficient resolution, it does not provide direct information about the atomic structure of amorphous materials. Alternatively, NBED^[33, 148, 181, 246-247] and FEM^[35-38] approaches have been used to investigate the local structure of metallic glasses. However, the NBED measurements require very thin specimens, preferably a few tens of atomic layers, to prevent significant overlap of features in the projected diffraction patterns.^[248] The results presented in chapter 4.4 underline the significant experimental challenge in preparing such

thin samples, where the structure and residual stresses are maintained, despite the damage during preparation and surface relaxation with the increased surface-to-volume ratio. To overcome these challenges, advanced 4D-TEM approaches, such as STEM-PDF and strain mapping, have been applied and further developed, where it is possible to work with noticeably thicker samples. Two different metallic glasses, $\text{Fe}_{85.2}\text{Si}_{0.5}\text{B}_{9.5}\text{P}_4\text{Cu}_{0.8}$ and $\text{Zr}_{46}\text{Cu}_{38}\text{Al}_8\text{Ag}_8$, each at different thermal annealing states, as well as before and after mechanical deformation have been used as examples for analyzing the structure and correlating this with mechanical properties.

STEM-PDF provides relatively easily interpretable structural information, facilitating straightforward structural analysis and phase mapping at the nanoscale. However, the information from STEM-PDF is inevitably averaged over the projection direction giving rise to an overlap problem. Moreover, the finite collection angle of the electron diffraction patterns limits the resolution of the pair distribution peaks giving rise to difficulties in detecting subtle variations of the probed atomic structure. For these reasons, the use of NMF, which only allows additive combinations with non-negativity constraints, was investigated for analyzing STEM-PDF datasets (chapter 5). The work showed that NMF-aided STEM-PDF can be used to identify the structural bases of the glass phase without any pre-knowledge from atomic simulations. The resulting PDFs showed directly interpretable packing information of individual structural basis motives forming the heterogeneous amorphous matrix. The approach was utilized to characterize the intrinsic heterogeneity in metallic glasses at different annealing states. The results revealed the existence of two fundamental glassy structures, representing more liquid-like and more solid-like phases distributed throughout the glass matrix. The relative population and distribution of these structures underwent significant changes during annealing, *i.e.* the solid-like regions significantly increased after annealing treatment. However, these changes occurred without the emergence of new additional structural types. The atomic configuration of these two phases remained essentially unchanged between the as-spun and annealed glass, indicating the structural persistence during thermal annealing, suggesting that these two phases are the dominant structures in the thermally accessible states. This presents an improved understanding of the glass structures and the evolution induced during annealing.

Chapter 6 focused on the analysis of individual shear bands formed during plastic deformation by scratch testing. Correlative mapping of PDF and strain is used to characterize the core structure of shear bands and their surrounding residual strain field. The high strain sensitivity of the analysis approach enabled an experimental visualization of Eshelby inclusions surrounded by quadrupolar strain fields aligned along the shear bands. The examination of two distinct metallic glasses yielded similar basic structures suggesting the universality of this observation. The observations are

qualitatively in line with the concrete scenario for the initiation of a shear band proposed by atomistic modeling^[120, 211]: dilated Eshelby inclusions, resulting from local plastic atomic displacements within the glassy matrix, concentrate a stress field exhibiting quadrupolar symmetry. This quadrupolar stress field disrupts the surrounding material in a vortex-like manner and percolates the inclusions eventually leading to the formation of a shear band. Within the same sample, shear bands with different structures have been observed. A possible explanation for this observation is the presence of both early-stage and mature shear bands as proposed from atomistic modeling.^[249] If a shear band has suffered limited shear displacement the Eshelby-like features are preserved whereas in a more mature shear band with extensive shear displacements, these features are smeared out and become weaker and indistinguishable. However, with the current postmortem characterization, the analysis cannot directly reveal such time-dependent information about shear band formation. Alternatively, different projections of the 3D structure of shear bands may give rise to distinct projected structures. One critical point in the current analysis is to recognize that the strain signal is averaged over the thickness of the TEM sample. This averaging can result in a loss of information concerning the complete 3D strain field. As a consequence, analyzing only the projected 2D strain offers a simplified representation of the strain states present in materials. In the thickness study in chapter 4.4, the core of the Eshelby inclusions remained at nearly identical locations of the shear band for the sample at different thicknesses. This suggests that a similar deformation state is present at least for a couple of 100 nm in the thickness direction indicating that the inclusions might not be point-like objects, but could be more extended. Moreover, there are large strain variations, *e.g.* deviatoric strain up to 0.5 % and volumetric strain up to 1 %, observed at a projected core of inclusion with a diameter of a few tens of nanometers. Considering the projection averaging across the sample thickness, the observed large strain could hardly be physically reasonable for a 200 nm thick sample if the inclusion core is a point-like 0D structure. This led to the speculation if the inclusions are anisotropic extending in and out of the imaging plane. In this case, shear bands would appear differently depending on the misorientation from the projection axis. Both interpretations are also in line with the experimental observation of different shear band structures in the previous works, *e.g.* Rösner et al. observed shear bands displaying alternating STEM-ADF contrast^[204, 210], whereas Maaß et al. observed shear bands exhibiting a simple reduction in intensity^[30].

The sharp concentration of strain suggests that plastic deformation has taken place at the core of the observed inclusions. The experimental structural features and symmetry fit well with Eshelby inclusions resulting from STZs in atomistic modeling^[207, 211] and the inclusions reported in condensed granular colloids^[109, 250] originating from the interaction between STZs through the

stress mediated by the rigid surrounding material. However, a STZ event is considered a transient phenomenon, while the current observation captures a static measurement of the residual stress and structural changes after plastic deformation. Furthermore, the size of the inclusion cores in this study is approximately 15 nm, which is ten times larger than the typical length scale of an STZ observed in atomic modeling.^[251] Therefore, the observed inclusions are probably not related to individual STZ events. This raises the question of what the observed Eshelby-like inclusions are if they are not due to individual STZs. A concentrated strain field with quadrupolar symmetry has also been observed at ~10 nm voids in MD simulations^[252] and at an artificially built micro pole using X-ray diffraction mapping in metallic glasses under load^[184]. One can expect that the continuous creation of STZ events followed by their agglomeration can form such kinds of plastic zones. Note that similar features were also observed at shear band branching points exhibiting dilatation and a strong concentration of tensile stresses. This indicates that Eshelby inclusions can be naturally formed in metallic glasses on a length scale larger than the typical size of STZs seen in atomistic simulations. In this case, the relationship between the size of the plastic segments and the size of individual STZs remains an open question.

Chapter 7 provided a detailed structural analysis of shear band networks and SBAZs in glasses at different annealing states, including the long-range strain field and strain inhomogeneity. Annealing induces more uniform short-range order and increased densification, leading to increased hardness and increased flow barrier in metallic glasses, improving their wear resistance. When the as-prepared metallic glass is deformed, this results in a heterogeneous strain distribution in the SBAZs, suggesting fairly delocalized plastic deformation in the sample. This indicates that shear bands interact via strain fields in the as-prepared glass, which facilitates the formation of secondary shear bands through the overlap of their deformation zones, thus avoiding strain localization and leading to a globally more homogeneous deformation. In contrast, in the well-relaxed glasses, the strain-induced local heterogeneity is weaker, resulting in a limited formation of secondary shear bands and fewer variations in the SBAZs. This leads to stronger strain localization in the matrix, restricting the uniform deformability of the metallic glass. This fits the improved ductility observed for mechanically rejuvenated metallic glasses^[15] and the increased hardness in well-relaxed metallic glasses^[222].

Furthermore, structural variations were observed after deformation in a region far wider than the estimated size of the shear band core. This indicated that the SBAZs alter the local material properties through long-range stress fields and thus influence subsequent deformation processes. Moreover, strain/density inhomogeneities were observed away from individual shear bands without an obvious connection to a shear band. This indicates the occurrence of large-scale shear

transformations occurring not only within the shear plane but also in distant regions of the matrix far from shear bands. The widespread shear transformations likely arise from the ubiquitous formation of local plastic deformation at intrinsic soft spots within the glass matrix and their subsequent agglomeration. As a result, the as-prepared samples, which have more intrinsic soft spots, exhibit a more heterogeneous strain concentration compared to the annealed samples after deformation. These observations suggest that shear bands interact with these local strain concentrations, which reduces strain localization in metallic glasses.

Finally, in chapter 8 a novel analytical technique called Ltz-4D-STEM is developed, which enables correlative mapping of magnetic and strain fields, as well as relative density at the nanoscale. This method is based on the momentum transfer of the electron beam by local magnetic fields, the elliptic distortion of the amorphous diffraction ring resulting from strain, and the area covered by the ring to quantify the relative atomic density. As a proof-of-principle, a soft magnetic metallic glass ribbon after plastic deformation has been imaged in a field-free environment to visualize the magnetoelastic energy distribution in the material. This new technique may shed light on the interplay between material properties, plastic deformation, strain, and the development of complex magnetic structures to stabilize magnetoelastic energy.

Overall, the development of improved correlative approaches to map the strain field and atomic PDF in annealed and deformed metallic glasses opens the path to obtaining crucial information for studying deformation mechanisms in metallic glasses. The method offers very high sensitivity for measuring residual stresses and for determining local S/MRO packing variations in metallic glasses. This allowed to further develop the scenarios for the formation of shear bands. Moreover, the detailed structure of shear band networks and SBAZs, including the long-range strain fields and strain inhomogeneity, were analyzed by this method. This direct experimental observation provides a new understanding of how the atomic structure affects residual strain fields and the deformation of metallic glasses. This new method has the potential to initiate broader research for solving questions in structure-property correlations in glasses.

9.2. Outlook

The present work has made significant progress in understanding the atomic structure and deformation process of metallic glasses. However, several crucial questions remain unanswered

as briefly discussed in the conclusion above. For a comprehensive understanding of the deformation behavior and properties of metallic glasses, these need to be answered.

- The time-dependent process from STZ formation to shear band propagation requires further investigation. Understanding the temporal evolution of deformation events would contribute to a more detailed understanding of the deformation mechanisms and kinetics in metallic glasses.
- Chemical variations within shear bands are important for understanding the role of chemical heterogeneity in deformation behavior. Investigating the elemental distribution and fluctuations within shear bands would provide insights into the correlation between local chemical composition and mechanical properties in metallic glasses.
- How do residual strain fields develop during shear banding and how does this process store/distribute deformation energy during subsequent deformation?
- How do SBAZs and local heterogeneity contribute to the formation of secondary or multiple shear bands?

It is crucial to explore how the factors above influence the overall deformation behavior and properties of metallic glasses. Establishing these connections would help develop a comprehensive understanding of the deformation mechanisms and guide the design of metallic glasses with tailored properties. In principle, *in-situ* studies to follow mechanical deformation processes as well as during thermal annealing are well established in TEM. However, considering surface damage and in particular surface relaxation in the required thin films, the interpretation of the results in terms of bulk properties is difficult. Nevertheless, if the properties of thin film metallic glasses are of interest, *in-situ* TEM could provide details about thermal properties and deformation processes. Furthermore, one possibility to extend the current studies to incorporate more information on chemical variations and the local coordination of the different elements would be to use a STEM-EELS-based element-specific PDF analysis, e.g., Extended energy loss fine structure (EXELFS). The STEM-EXELFS analysis would allow to determine the local chemical state of the different elements and their coordination and could thus provide more details on the chemical variations in SBs and SBAZs. To further study the complex heterogeneous structure in metallic glasses, the projection problem is one of the main challenges for the required sufficiently thick samples. The combination of 4D-STEM with tomography could provide a solution, both for 3D imaging of density differences as well as for 3D strain mapping. This could potentially be employed to analyze the heterogeneity in bulk glasses as well as in shear bands including the 3D shape of the Eshelby inclusions.

Directly connected to the core of this thesis, it is important to acknowledge that the traditional concept of STZs from atomistic simulations does not fully align with the experimentally observed Eshelby inclusions. These inclusions exhibit frozen quadrupole features after plastic deformation, which share similarities to STZs except for their size. Currently, there are no existing theories or atomistic models that can explain this difference. Further studies are necessary to understand shear band dynamics with this kind of inclusion.

The Ltz-4D-STEM development introduced as proof-of-principle opens a new path for investigating magnetic metallic glasses. The correlation between residual strain field and magnetic structure was only partially studied in chapter 8. This investigation raises important questions such as:

- How does the magnetic domain structure change due to the presence of shear bands and SBAZs and what is the reason for the different observations in as-cast and annealed metallic glasses?
- How does the residual strain field influence the local magnetic structure?
- Can the nanoscale magnetic properties of metallic glasses be intentionally tuned through designed thermo-mechanical treatments?

This extension of the metallic glass research has the potential to go beyond insights into the deformation mechanisms of metallic glasses but could provide valuable information on functional structure-property correlations and tuning electric/magnetic properties through structural modification. Finally, the methodology developed in this thesis for metallic glasses can also be extended to other materials classes such as semi-crystalline or amorphous polymers as well as other types of inorganic glasses, e.g. oxidic glasses. While structural modifications by the electron beam are much more of an issue for those materials, an optimized microscopy setting, e.g. enlarged defocus of electron probe to reduce the electron dose, using high DQE pixelated detectors and cryo-TEM, can extend the application of 4D-STEM techniques. Nevertheless, the dose used for the structural analysis needs to be carefully evaluated to quantify radiation damage induced in the sample. In this case, the analysis can offer quantitative information on the local structure to image the phase distribution in beam-sensitive samples that possess complex local structures. The method can be used to discover the structure of the inter-phase boundary of heterojunction materials and the structural variation of the local atomic environment in soft bulk materials.

Curriculum Vitae



SANGJUN KANG

Technische Universität Darmstadt (TUD), Institute of Materials Science
Peter-Grünberg-Straße 2, 64287 Darmstadt, Germany
▫ +49 160 5041754 ▫ sangjun.kang@tu-darmstadt.de

EDUCATION

KIT- Karlsruhe Institute of Technology, Germany

TUD- Technische Universität Darmstadt, Germany

*Ph. D. research at KIT and degree grant from TUD

Degree Type: Ph. D.

Major: Transmission Electron Microscopy, Material Science

Zhejiang University, China

Degree Type: M. Sc.

Jun 2019

Major: Material Science and Engineering

Korea University of Technology and Education, South Korea

Degree Type: B. Sc.

Aug 2015

Major: Material Science and Engineering

WORKING EXPERIENCE

TUD- Technische Universität Darmstadt, Germany

April 2023 – Present

Post-doc researcher

Project: Fermi Level Engineering applied to oxide electroceramics

- Characterization for oxide electroceramics using HR-STEM, HR-EELS/EDX, STEM-DPC
- Setting up for 4D-STEM and in-situ TEM

KIST- Korea Institute of Science and Technology, Seoul, South Korea

September 2022 – March 2023

Post-doc researcher

Project: (1) TEM methodology development for energy materials

(2) Development for big data analysis & establishment of the platform

- Characterization for complex electrode and solid electrolyte interphase (SEI) of solid-state battery using HR-STEM, HR-EELS/EDX, STEM-DPC
- Deep learning (DL) application on TEM dataset
- Setting up for 4D-STEM and in-situ TEM

KIT- Karlsruhe Institute of Technology, Karlsruhe, Germany

August 2019 – August 2022

Research associate for a doctorate

Project: Understanding the atomic structure of shear bands in metallic glass using 4D-STEM

-
- Methodology development for 4D-STEM (correlative imaging, RDF mapping, strain mapping, electric & magnetic property mapping, and Ltz-4D-STEM).
 - Characterization for metallic glasses, polymers, magnets, and battery samples using 4D-STEM, STEM-EELS/EDX, and HR-STEM.
 - Machine learning (ML) application on 4D-STEM dataset
 - Collaborations with TEM/FIB-SEM operation

Korea University of Technology and Education, Cheonan, South Korea

September 2015 - Jun 2016

Assistant researcher

Project: Understanding the wear behavior of metallic glasses

- Experiments and measurements using a scratch tester, AFM, XPS, SEM-FIB
- Performing service measurements for collaborations

INM-Leibniz Institut für Neue Materialien, Saarbrücken, Germany

September 2014 - July 2015

Assistant researcher

Project: Understanding nanotribology and surface properties of metallic glasses

- Investigating the surface oxide layer of metallic glasses using AFM
- Contributing to collaborative projects on nanotribology and nanomechanics by performing AFM service measurements

ACTIVITY / SCHOLARSHIP / AWARD

Best poster presentation award – EKC2022, Korea Institute of Science and Technology Information (KISTI)

July 2022

Academic award - Verein Koreanischer Naturwissenschaftler und Ingenieure (VeKNI)

October 2021

Conference presentation award

“STEM-PDF: Open Source Software for STEM Pair Distribution Function Mapping”,
Microscopy conference (MC2021)

August 2021

Young Scientist Scholarship - European Microscopy Society (EMS)

June 2021

KIT Center Mathematics in Sciences, Engineering, and Economics (MathSEE)

Karlsruhe, Germany

June 2020 – October 2021

Representative of young scientists

List of publications/Patents/Conference papers

S. J. Kang, X. Mu, D. Wang, C. Kübel

Importance of TEM sample thickness for measuring strain fields, Accepted, *Ultramicroscopy*. (2023)

S. J. Kang, X. Mu, D. Wang, A. Caron, C. Minnert, K. Durst, C. Kübel

Direct observation of quadrupolar strain fields forming a shear band in metallic glasses, *Advanced Materials* 2212086 (2023)

S. J. Kang, Q. P. Cao, J. Liu, Y. Tang, X. D. Wang, D. X. Zhang, I. S. Ahn, A. Caron, J. Z. Jiang

Intermediate structural state for maximizing the rejuvenation effect in metallic glass via thermo-cycling treatment. *Journal of Alloys and Compounds* 795 493-500 (2019)

S. J. Kang, K. T. Rittgen, A. Caron, S.G. Kwan, R. Bennewitz.

Importance of surface oxide for the tribology of a Zr-based metallic glass. *Journal of Friction* 5(1) 115-122 (2017)

S. J. Kang, C. Minnert, K. Durst, H. S. Kim, C. Kübel, X. Mu,

Mapping local atomic structure of metallic glasses using machine learning aided STEM-PDF, Under review, *Acta Materialia*.

H.Y Jo, **S. J. Kang**, K.Y. Tag H. K Kim, and J. P Ahn

Degradation mechanism of Si-C composite anode revealed by the role of nanopores, *In preparation*

K. Y. Tag, H.Y Jo, **S. J. Kang**, K.Y. Tag H. K Kim, and J. P Ahn

Degradation mechanism of complex cathode of solid-state battery during cycling, *In preparation*.

S. J. Kang, D. Wang, C. Minnert, K. Durst, RE. Dunin-Borkowski, C. Kübel, and X. Mu,

Directly proving magnetoelastic coupling in a soft ferromagnet using Lorentz 4D-STEM, *In preparation*

PATENTS

S. J. Kang, S. H. Lee, H. C. Cha, U. C. Nha

A new method for manufacturing high efficient TiO₂ Photoelectrode for dye-sensitized solar cells. *Patent* 1020140143238 (2015)

S. J. Park, **S. J. Kang**, K. H. Lee, S. G. Jeong

Controlling apparatus for car seats. *Patent* 1015486140000 (2015)

S. J. Park, **S. J. Kang**, K. H. Lee, S. G. Jeong

Information processing apparatus for vehicles. *Patent* 1020130139619 (2013)

CONFERENCES

S. J. Kang, D. Wang, C. Minnert, K. Durst, C. Kübel, X. Mu

(Invited) Direct measurement of magnetoelastic coupling in soft ferromagnets using Lorentz 4D-STEM, *Annual meeting of Korean physical society* (2023)

H. Y. Cho, **S. J. Kang**, K. R. Tag, H. W. Gong, H. K. Kim, H. R. Kim, J. P. Ahn

Degradation Mechanism of Si Anode in Sulfide-based All-Solid-State Batteries revealed by observation of SEI layer using 4D-STEM/Super-EDS, *Microscopy and Microanalysis* (2023)

S. J. Kang, D. Wang, C. Minnert, K. Durst, C. Kübel, X. Mu

Simultaneous mapping of magnetic and atomic structure of ferromagnetic metallic glass using Ltz-4D-STEM, *Annual meeting & exhibition of Korean microscopy society* (2022)

C. Kübel, **S. J. Kang**, X. Mu, D. Wang, A. Caron, C. Minnert, K. Durst,

Observation of deformation features in metallic glasses, *The Minerals, Metals & Materials Society Annual Meeting & Exhibition* (2023)

S. J. Kang, A. Caron, Y. Ivanisenko, S. H. Nandam, H. Gleiter, C. Kübel, X. Mu
Homogeneous plastic deformation of Pd-Si nanoglass under tribological deformation, *Advanced materials congress* (2022)

S. J. Kang, X. Mu, D. Wang, A. Caron, C. Minnert, K. Durst, C. Kübel
STEM-PDF: Observation of shear transformation zone in metallic glasses, *Inter. Conf. Strength of Materials* (2022)

S. J. Kang, L.Y. Chen, X. Mu, D. Wang, C. Kübel
STEM-PDF: Open Source Software for STEM Pair Distribution Function Mapping, *Microscopy Conference 2021* (2021)

S. J. Kang, X. Mu, D. Wang, A. Caron, C. Kübel
Shear band propagation and networking as a response of tribological deformation of a metallic glass. *Material Science and Engineering (MSE) conference, Deutsche Gesellschaft für Materialkunde* (2020)

S. J. Kang, X. Mu, D. Wang, C. Kübel
Structural understanding of metallic glasses with STEM-PDF analysis. *Verein Koreanischer Naturwissenschaftler und Ingenieure (VeKNI), fall annual meeting/conference* (2019)

References

- [1] M. Telford, *Materials Today* **2004**, 7, 36.
- [2] C. A. Schuh, T. C. Hufnagel, U. Ramamurty, *Acta Materialia* **2007**, 55, 4067.
- [3] W. Klement, R. Willens, P. Duwez, *Nature* **1960**, 187.
- [4] H. S. Chen, T. T. Wang, *Journal of Applied Physics* **1970**, 41, 5338.
- [5] A. L. Greer, *Science* **1995**, 267, 1947.
- [6] T. C. Hufnagel, C. A. Schuh, M. L. Falk, *Acta Materialia* **2016**, 109, 375.
- [7] K. Havner, *FINITE PLASTIC DEFORMATION OF CRYSTALLINE SOLIDS*, Cambridge University Press, **1992**.
- [8] A. L. Greer, Y. Q. Cheng, E. Ma, *Materials Science and Engineering* **2013**, 74, 71.
- [9] Z. Zhang, J. Eckert, L. Schultz, *Acta Materialia* **2003**, 51, 1167.
- [10] Y. Q. Cheng, A. J. Cao, H. W. Sheng, E. Ma, *Acta Materialia* **2008**, 56, 5263.
- [11] J. Eckert, J. Das, S. Pauly, C. Duhamel, *Journal of Materials Research* **2007**, 22, 285.
- [12] C. A. Schuh, A. C. Lund, T. Nieh, *Acta Materialia* **2004**, 52, 5879.
- [13] D. Şopu, S. Scudino, X. Bian, C. Gammer, Eckert, *Scripta Materialia* **2020**, 178, 57.
- [14] A. R. Yavari, A. Le Moulec, A. Inoue, N. Nishiyama, N. Lupu, E. Matsubara, W. J. Botta, G. Vaughan, M. Di Michiel, A. Kvik, *Acta Materialia* **2005**, 53, 1611.
- [15] W. Dmowski, Y. Yokoyama, A. Chuang, Y. Ren, M. Umemoto, K. Tsuchiya, A. Inoue, T. Egami, *Acta Materialia* **2010**, 58, 429.
- [16] B. P. Kanungo, S. C. Glade, P. Asoka-Kumar, K. M. Flores, *Intermetallics* **2004**, 12, 1073.
- [17] K. Flores, E. Sherer, A. Bharathula, H. Chen, Y. Jean, *Acta Materialia* **2007**, 55, 3403.
- [18] Y. Zhang, A. Greer, *Applied Physics Letters* **2006**, 89, 071907.
- [19] Y. F. Shi, M. L. Falk, *Physical Review B* **2006**, 73, 214201.
- [20] F. Shimizu, S. Ogata, J. Li, *Acta Materialia* **2006**, 54, 4293.
- [21] A. J. Cao, Y. Q. Cheng, E. Ma, *Acta Materialia* **2009**, 57, 5146.
- [22] C. E. Lekka, A. Ibenskas, A. R. Yavari, G. A. Evangelakis, *Applied Physics Letters* **2007**, 91, 214103.
- [23] Y. F. Shi, M. L. Falk, *Acta Materialia* **2007**, 55, 4317.
- [24] Y. Ritter, K. Albe, *Acta Materialia* **2011**, 59, 7082.
- [25] Y. Q. Cheng, E. Ma, *Progress in Materials Science* **2011**, 56, 379.
- [26] X. H. Du, J. C. Huang, H. M. Chen, H. S. Chou, Y. H. Lai, K. C. Hsieh, J. S. C. Jang, P. K. Liaw, *Intermetallics* **2009**, 17, 607.
- [27] E. S. Park, *Applied Microscopy* **2015**, 45, 63.
- [28] G. Kumar, T. Ohkubo, T. Mukai, K. Hono, *Scripta Materialia* **2007**, 57, 173.
- [29] V. Hieronymus-Schmidt, H. Rösner, G. Wilde, A. Zacccone, *Physical Review B* **2017**, 95, 134111.
- [30] C. Liu, V. Roddatis, P. Kenesei, R. Maass, *Acta Materialia* **2017**, 140, 206.
- [31] J. Li, Z. L. Wang, T. C. Hufnagel, *Physical Review B* **2002**, 65, 144201.
- [32] D. Alloyeau, C. Ricolleau, T. Oikawa, C. Langlois, Y. Le Bouar, A. Loiseau, *Ultramicroscopy* **2008**, 108, 656.
- [33] M. Treacy, J. Gibson, L. Fan, D. Paterson, I. McNulty, *Reports on Progress in Physics* **2005**, 68, 2899.
- [34] A. Hirata, L. J. Kang, T. Fujita, B. Klumov, K. Matsue, M. Kotani, A. R. Yavari, M. W. Chen, *Science* **2013**, 341, 376.
- [35] S. N. Bogle, P. M. Voyles, S. V. Khare, J. R. Abelson, *Journal of Physics: Condensed Matter* **2007**, 19, 455204.
- [36] J. Hwang, Z. H. Melgarejo, Y. E. Kalay, I. Kalay, M. J. Kramer, D. S. Stone, P. M. Voyles, *Physical Review Letters* **2012**, 108, 195505.
- [37] J. J. Maldonis, J. Hwang, P. M. Voyles, *Computer Physics Communications* **2017**, 213, 217.
- [38] J. Wen, Y. Cheng, J. Wang, E. Ma, *Journal of Applied Physics* **2009**, 105, 043519.
- [39] X. Mu, A. Mazilkin, C. Sprau, A. Colsmann, C. Kubel, *Microscopy* **2019**, 68, 301.
- [40] X. Mu, S. Neelamraju, W. Sigle, C. T. Koch, N. Toto, J. C. Schön, A. Bach, D. Fischer, M. Jansen, P. A. van Aken, *Journal of Applied Crystallography* **2013**, 46, 1105.
- [41] X. Mu, D. Wang, T. Feng, C. Kübel, presented at *European Microscopy Congress 2016: Proceedings*, **2016**.

- [42] B. Toby, T. Egami, *Acta Crystallographica Section A: Foundations of Crystallography* **1992**, 48, 336.
- [43] J. D. Bernal, *Nature* **1960**, 185, 68.
- [44] J. D. Bernal, *Proceedings of the Royal Society of London. Series A, Mathematical and Physical Sciences* **1964**, 280, 299.
- [45] D. R. Nelson, F. Spaepen, *SOLID STATE PHYSICS*, Vol. 42, Academic Press, 1989.
- [46] P. M. Morse, *Physical Review* **1929**, 34, 57.
- [47] M. Dzugutov, *Physical Review A* **1992**, 46, R2984.
- [48] P. H. Gaskell, *Nature* **1978**, 276, 484.
- [49] P. H. Gaskell, *Journal of Non-Crystalline Solids* **1979**, 32, 207.
- [50] P. Ganesh, M. Widom, *Physical Review B* **2008**, 77, 014205.
- [51] N. Jakse, A. Pasturel, *Physical Review Letters* **2003**, 91, 195501.
- [52] N. Jakse, O. Le Bacq, A. Pasturel, *Physical Review B* **2004**, 70, 174203.
- [53] P. Panissod, D. A. Guerra, A. Amamou, J. Durand, W. L. Johnson, W. L. Carter, S. J. Poon, *Physical Review Letters* **1980**, 44, 1465.
- [54] J. W. Allen, A. C. Wright, G. A. N. Connell, *Journal of Non-Crystalline Solids* **1980**, 42, 509.
- [55] F. M. Alamgir, H. Jain, D. B. Williams, R. B. Schwarz, *Micron* **2003**, 34, 433.
- [56] J. Durand, P. Panissod, *Journal of Magnetism and Magnetic Materials* **1983**, 31-4, 1567.
- [57] L. Battezzati, G. Riontino, M. Baricco, A. Lucci, F. Marino, *Journal of Non-Crystalline Solids* **1984**, 61-2, 877.
- [58] G. W. Lee, A. K. Gangopadhyay, K. F. Kelton, R. W. Hyers, T. J. Rathz, J. R. Rogers, D. S. Robinson, *Physical Review Letters* **2004**, 93, 037802.
- [59] G. Voronoi, *J. Reine Angew. Math* **1908**, 134, 198.
- [60] F. t. Frank, J. Kasper, *Acta Crystallographica* **1958**, 11, 184.
- [61] V. A. Borodin, *Philosophical Magazine a-Physics of Condensed Matter Structure Defects and Mechanical Properties* **1999**, 79, 1887.
- [62] H. W. Sheng, W. K. Luo, F. M. Alamgir, J. M. Bai, E. Ma, *Nature* **2006**, 439, 419.
- [63] V. A. Borodin, *Philosophical Magazine a-Physics of Condensed Matter Structure Defects and Mechanical Properties* **2001**, 81, 2427.
- [64] H. Sheng, W. Luo, F. Alamgir, J. Bai, E. Ma, *Nature* **2006**, 439, 419.
- [65] Z. Li, Z. Huang, F. Sun, X. Li, J. Ma, *Materials Today Advances* **2020**, 7, 100077.
- [66] T. Egami, C. W. Ryu, *Journal of Physics: Condensed Matter* **2023**, 35, 174002.
- [67] Y. Cheng, E. Ma, H. Sheng, *Physical Review Letters* **2009**, 102, 245501.
- [68] D. B. Miracle, T. Egami, K. M. Flores, K. F. Kelton, *MRS Bulletin* **2007**, 32, 629.
- [69] K. Laws, D. Miracle, M. Ferry, *Nature Communications* **2015**, 6, 8123.
- [70] E. Ma, *Nature Materials* **2015**, 14, 547.
- [71] T. Egami, V. Vitek, *Journal of Non-crystalline Solids* **1984**, 61, 499.
- [72] L. Huang, X. Fang, C. Wang, M. Kramer, Z. Ding, K. Ho, *Applied Physics Letters* **2011**, 98, 231906.
- [73] D. S. Wilkinson, W. Pompe, M. Oeschner, *Progress in Materials Science* **2001**, 46, 379.
- [74] C. Liu, R. Maaß, *Advanced Functional Materials* **2018**, 28, 1800388.
- [75] E. Ma, J. Ding, *Materials Today* **2016**, 19, 568.
- [76] Y. Waseda, T. Egami, *Journal of Materials Science* **1979**, 14, 1249.
- [77] T. Egami, *JOM* **2010**, 62, 70.
- [78] F. Zhu, S. Song, K. M. Reddy, A. Hirata, M. Chen, *Nature Communications* **2018**, 9, 3965.
- [79] U. R. P. Murali, *Acta Materialia* **2005**, 53.
- [80] A. Inoue, *Acta Materialia* **2000**, 48, 279.
- [81] S. G. Hao, C. Z. Wang, M. Z. Li, R. E. Napolitano, M. I. Mendeleev, K. M. Ho, *Computational Materials Science* **2010**, 49, 615.
- [82] J. D. Ju, D. Jang, A. Nwankpa, M. Atzmon, *Journal of Applied Physics* **2011**, 109, 053522.
- [83] J. Ju, M. Atzmon, *MRS Communications* **2014**, 4, 63.
- [84] J. Qiao, Q. Wang, D. Crespo, Y. Yang, J.-M. Pelletier, *Chinese Physics B* **2017**, 26, 016402.
- [85] W.-H. W. Hai-Bin Yu, Konrad Samwer, *Materials Today* **2013**, 16.
- [86] Q. Wang, S. T. Zhang, Y. Yang, Y. D. Dong, C. T. Liu, J. Lu, *Nature Communications* **2015**, 6, 7876.
- [87] Y. H. Liu, T. Fujita, D. P. B. Aji, M. Matsuura, M. W. Chen, *Nature Communications* **2014**, 5, 3238.

- [88] P. Zhang, J. J. Maldonis, Z. Liu, J. Schroers, P. M. Voyles, *Nature Communications* **2018**, 9, 1129.
- [89] M. D. Ediger, M. Gruebele, V. Lubchenko, P. G. Wolynes, *The Journal of Physical Chemistry B* **2021**, 125, 9052.
- [90] M. Meyers, K. Chawla, *MECHANICAL BEHAVIOR OF MATERIALS*, Cambridge bridge University Press, 2009.
- [91] F. Gao, Z. Gao, X. Shi, Z. Yang, X. Lin, H. Xu, J. D. Joannopoulos, M. Soljačić, H. Chen, L. Lu, *Nature Communications* **2016**, 7, 1.
- [92] Q. K. Jiang, P. Liu, Y. Ma, Q. P. Cao, X. D. Wang, D. X. Zhang, X. D. Han, Z. Zhang, J. Z. Jiang, *Scientific Reports* **2012**, 2, 852.
- [93] X. D. Wang, S. Aryal, C. Zhong, W. Y. Ching, H. W. Sheng, H. Zhang, D. X. Zhang, Q. P. Cao, J. Z. Jiang, *Scientific Reports* **2015**, 5, 9184.
- [94] A. S. Argon, *Acta Metallurgica* **1979**, 27, 47.
- [95] J. Li, F. Spaepen, T. C. Hufnagel, *Philosophical Magazine a-Physics of Condensed Matter Structure Defects and Mechanical Properties* **2002**, 82, 2623.
- [96] A. S. Argon, H. Y. Kuo, *Materials Science and Engineering: R* **1979**, 39, 101.
- [97] A. S. Argon, L. T. Shi, *Philosophical Magazine a-Physics of Condensed Matter Structure Defects and Mechanical Properties* **1982**, 46, 275.
- [98] K. Jensen, D. A. Weitz, F. Spaepen, *Physical Review E* **2014**, 90, 042305.
- [99] C. E. Maloney, A. Lemaitre, *Physical Review E* **2006**, 74, 016118.
- [100] M. J. Demkowicz, A. S. Argon, *Physical Review B* **2005**, 72, 245206.
- [101] M. Zink, K. Samwer, W. L. Johnson, S. G. Mayr, *Physical Review B* **2006**, 73, 172203.
- [102] F. Delogu, *Intermetallics* **2008**, 16, 658.
- [103] F. Delogu, *Physical Review Letters* **2008**, 100, 255901.
- [104] A. Tanguy, F. Leonforte, J. L. Barrat, *European Physical Journal E* **2006**, 20, 355.
- [105] P. Cao, H. S. Park, X. Lin, *Physical Review E* **2013**, 88, 042404.
- [106] E. R. Homer, D. Rodney, C. A. Schuh, *Physical Review B* **2010**, 81, 064204.
- [107] S. Takeuchi, K. Edagawa, *Progress in Materials Science* **2011**, 56, 785.
- [108] D. Rodney, C. Schuh, *Physical Review Letters* **2009**, 102, 235503.
- [109] P. Schall, D. A. Weitz, F. Spaepen, *Science* **2007**, 318, 1895.
- [110] Y. H. Sun, A. Concustell, A. L. Greer, *Nature Reviews Materials* **2016**, 1, 1.
- [111] J. D. Ju, M. Atzmon, *Acta Materialia* **2014**, 74, 183.
- [112] J. C. Qiao, J. M. Pelletier, C. Esnouf, Y. Liu, H. Kato, *Journal of Alloys and Compounds* **2014**, 607, 139.
- [113] D. Pan, Y. Yokoyama, T. Fujita, Y. H. Liu, S. Kohara, A. Inoue, M. W. Chen, *Applied Physics Letters* **2009**, 95, 141909.
- [114] J. J. Lewandowski, A. L. Greer, *Nature Materials* **2006**, 5, 15.
- [115] N. Hu, J. F. Molinari, *Journal of the Mechanics and Physics of Solids* **2004**, 52, 499.
- [116] S. Ogata, F. Shimizu, J. Li, M. Wakeda, Y. Shibutani, *Intermetallics* **2006**, 14, 1033.
- [117] G. P. Shrivastav, P. Chaudhuri, J. Horbach, *Physical Review E* **2016**, 94, 042605.
- [118] S. Ogata, F. Shimizu, J. Li, M. Wakeda, Y. Shibutani, *Intermetallics* **2006**, 14, 1033.
- [119] D. Klaumünzer, R. Maaß, J. F. Löffler, *Journal of Materials Research* **2011**, 26, 1453.
- [120] D. Soper, A. Stukowski, M. Stoica, S. Scudino, *Physical Review Letters* **2017**, 119, 195503.
- [121] Y. Shi, M. B. Katz, H. Li, M. L. Falk, *Physical Review Letters* **2007**, 98, 185505.
- [122] J. C. Lee, K. W. Park, K. H. Kim, E. Fleury, B. J. Lee, M. Wakeda, Y. Shibutani, *Journal of Materials Research* **2007**, 22, 3087.
- [123] K. W. Park, J. I. Jang, M. Wakeda, Y. Shibutani, J. C. Lee, *Scripta Materialia* **2007**, 57, 805.
- [124] Y. Ritter, K. Albe, *Journal of Applied Physics* **2012**, 111, 103527.
- [125] Y. Shi, M. L. Falk, *Physical Review Letters* **2005**, 95, 095502.
- [126] Q. K. Li, M. Li, *Applied Physics Letters* **2006**, 88, 241903.
- [127] S. G. Hao, C. Z. Wang, M. Li, R. E. Napolitano, M. I. Mendeleev, K. M. Ho, *Computational Materials Science* **2010**, 49, 615.
- [128] P. J. Tao, Y. Z. Yang, X. J. Bai, Z. X. Mu, G. Q. Li, Z. W. Xie, X. C. Chen, *Surface and Coatings Technology* **2009**, 203, 1656.

- [129] S. J. Kang, Q. P. Cao, J. Liu, Y. Tang, X. D. Wang, D. X. Zhang, I. S. Ahn, A. Caron, J. Z. Jiang, *Journal of Alloys and Compounds* **2019**, 795, 493.
- [130] J. W. Liu, Q. P. Cao, L. Y. Chen, X. D. Wang, J. Z. Jiang, *Acta Materialia* **2010**, 58, 4827.
- [131] Y. H. Liu, G. Wang, R. J. Wang, D. Q. Zhao, M. X. Pan, W. H. Wang, *Science* **2007**, 315, 1385.
- [132] J. Schroers, W. L. Johnson, *Phys Rev Lett* **2004**, 93, 255506.
- [133] B. A. Sun, W. H. Wang, *Applied Physics Letters* **2011**, 98.
- [134] B. A. Sun, H. B. Yu, W. Jiao, H. Y. Bai, D. Q. Zhao, W. H. Wang, *Physics Review Letters* **2010**, 105, 035501.
- [135] G. W. Yan Hui Liu, Ru Ju Wang, De Qian Zhao, Ming Xiang Pan, Wei Hua Wang, *Science* **2007**, 315.
- [136] S. S. Jiang, Y. J. Huang, F. F. Wu, P. Xue, J. F. Sun, *Journal of Non-Crystalline Solids* **2018**, 483, 94.
- [137] S. X. Liang, X. Q. Wang, W. C. Zhang, Y. J. Liu, W. M. Wang, L. C. Zhang, *Applied Materials Today* **2020**, 19, 100543.
- [138] Z. Han, Y. Li, *Journal of Materials Research* **2009**, 24, 3620.
- [139] P. Thurnheer, F. Haag, J. F. Löffler, *Acta Materialia* **2016**, 115, 468.
- [140] B. Yang, P. K. Liaw, G. Wang, M. Morrison, C. T. Liu, R. A. Buchanan, Y. Yokoyama, *Intermetallics* **2004**, 12, 1265.
- [141] F. Spaepen, *Nature Materials* **2006**, 5, 7.
- [142] O. Haruyama, K. Kisara, A. Yamashita, K. Kogure, Y. Yokoyama, K. Sugiyama, *Acta Materialia* **2013**, 61, 3224.
- [143] H. S. Chen, S. Y. Chuang, *Journal of Electronic Materials* **1975**, 4, 783.
- [144] A. R. Yavari, J. Lewandowski, J. Eckert, *MRS Bulletin* **2007**, 32, 635.
- [145] G. R. Garrett, M. D. Demetriou, M. E. Launey, W. L. Johnson, *Proceedings of the National Academy of Sciences* **2016**, 113, 10257.
- [146] F. Zhu, A. Hirata, P. Liu, S. Song, Y. Tian, J. Han, T. Fujita, M. Chen, *Physical Review Letters* **2017**, 119, 215501.
- [147] F. Zhu, S. X. Song, K. M. Reddy, A. Hirata, M. W. Chen, *Nature Communications* **2018**, 9, 1.
- [148] J. Hwang, P. Voyles, *Microscopy and Microanalysis* **2011**, 17, 67.
- [149] S. Hilke, H. Rosner, D. Geissler, A. Gebert, M. Peterlechner, G. Wilde, *Acta Materialia* **2019**, 171, 275.
- [150] M. Treacy, K. Borisenko, *Science* **2012**, 335, 950.
- [151] X. Mu, M. R. Chellali, E. Boltynjuk, D. Gunderov, R. Z. Valiev, H. Hahn, C. Kubel, Y. Ivanisenko, L. Velasco, *Advanced Materials* **2021**, 33, e2007267.
- [152] H. S. Chen, *Applied Physics Letters* **1976**, 29, 328.
- [153] R. Maaß, P. Birckigt, C. Borchers, K. Samwer, C. Volkert, *Acta Materialia* **2015**, 98, 94.
- [154] S. Scudino, D. Soppa, *Nano Letter* **2018**, 18, 1221.
- [155] H. S. Shahabi, S. Scudino, I. Kaban, M. Stoica, B. Escher, S. Menzel, G. B. M. Vaughan, U. Kuhn, J. Eckert, *Acta Materialia* **2016**, 111, 187.
- [156] L. Shen, P. Luo, Y. Hu, H. Bai, Y. Sun, B. Sun, Y. Liu, W. Wang, *Nature Communications* **2018**, 9, 1.
- [157] L. Q. Shen, P. Luo, Y. C. Hu, H. Y. Bai, Y. H. Sun, B. A. Sun, Y. H. Liu, W. H. Wang, *Nature Communications* **2018**, 9, 4414.
- [158] W. Klement, R. H. Willens, P. Duwez, *Nature* **1960**, 187, 869.
- [159] C. Suryanarayana, A. Inoue, *BULK METALLIC GLASSES*, CRC Press, **1999**.
- [160] A. Inoue, *Science Reports-Research Institutes Tohoku University Series A* **1996**, 42, 1.
- [161] C. B. Rong, B. G. Shen, *Chinese Physics B* **2018**, 27, 117502.
- [162] N. Nishiyama, K. Takenaka, H. Miura, N. Saidoh, Y. Q. Zeng, A. Inoue, *Intermetallics* **2012**, 30, 19.
- [163] Z. O. Yazici, A. Hitit, Y. Yalcin, M. Ozgul, *Metals and Materials International* **2016**, 22, 50.
- [164] J. P. Chu, J. S. C. Jang, J. C. Huang, H. S. Chou, Y. Yang, J. C. Ye, Y. C. Wang, J. W. Lee, F. X. Liu, P. K. Liaw, Y. C. Chen, C. M. Lee, C. L. Li, C. Rullyani, *Thin Solid Films* **2012**, 520, 5097.
- [165] F. P. Bowden, F. P. Bowden, D. Tabor, *THE FRICTION AND LUBRICATION OF SOLIDS*, Vol. 1, Oxford University Press, **2001**.
- [166] D. B. Williams, C. B. Carter, *TRANSMISSION ELECTRON MICROSCOPY*, Springer, 1996.
- [167] A. Wolff.
- [168] L. W. Swanson, *Nuclear Instruments & Methods in Physics Research* **1983**, 218, 347.

- [169] C. Berger, M. Dumoux, T. Glen, N. B.-y. Yee, J. M. Mitchels, Z. Patáková, M. C. Darrow, J. H. Naismith, M. Grange, *Nature Communications* **2023**, 14, 629.
- [170] D. B. Williams, C. B. Carter, D. B. Williams, C. B. Carter, *THE TRANSMISSION ELECTRON MICROSCOPE*, Springer, **1996**.
- [171] L. Reimer, *TRANSMISSION ELECTRON MICROSCOPY: PHYSICS OF IMAGE FORMATION AND MICROANALYSIS*, Vol. 36, Springer, **2013**.
- [172] E. J. Kirkland, *ADVANCED COMPUTING IN ELECTRON MICROSCOPY*, Springer, **2010**.
- [173] G. R. Anstis, Z. Liu, M. Lake, *Ultramicroscopy* **1988**, 26, 65.
- [174] X. K. Mu, L. Y. Chen, R. Mikut, H. Hahn, C. Kubel, *Acta Materialia* **2021**, 212, 116932.
- [175] J. Ankele, J. Mayer, P. Lamparter, S. Steeb, *Zeitschrift für Naturforschung A* **2005**, 60, 459.
- [176] X. Mu, D. Wang, T. Feng, C. Kubel, *Ultramicroscopy* **2016**, 168, 1.
- [177] M. J. Hÿch, E. Snoeck, R. Kilaas, *Ultramicroscopy* **1998**, 74, 131.
- [178] C. Ophus, *Microscopy and Microanalysis* **2019**, 25, 563.
- [179] A. Kobler, A. Kashiwar, H. Hahn, C. Kubel, *Ultramicroscopy* **2013**, 128, 68.
- [180] C. Gammer, J. Kacher, C. Czarnik, O. L. Warren, J. Ciston, A. M. Minor, *Applied Physics Letters* **2016**, 109.
- [181] P. Voyles, J. Hwang, *Characterization of Materials* **2002**, 1.
- [182] H. Yang, L. Jones, H. Ryll, M. Simson, H. Soltau, Y. Kondo, R. Sagawa, H. Banba, I. MacLaren, P. Nellist, presented at *Journal of Physics*, **2015**.
- [183] N. Shibata, S. D. Findlay, T. Matsumoto, Y. Kohno, T. Seki, G. Sanchez-Santolino, Y. Ikuhara, *Accounts of chemical research* **2017**, 50, 1502.
- [184] H. F. Poulsen, J. A. Wert, J. Neuefeind, V. Honkimaki, M. Daymond, *Nature Materials* **2005**, 4, 33.
- [185] A. Fitzgibbon, M. Pilu, R. B. Fisher, *IEEE Transactions on Pattern Analysis and Machine Intelligence* **1999**, 21, 476.
- [186] H. Sheng, D. Soppu, S. Fellner, J. Eckert, C. Gammer, *Physical Review Letters* **2022**, 128, 245501.
- [187] C. Minnert, M. Kuhnt, S. Bruns, A. Marshal, K. G. Pradeep, M. Marsilius, E. Bruder, K. Durst, *Materials & Design* **2018**, 156, 252.
- [188] H. K. Kim, H. Y. Ha, J. H. Bae, M. K. Cho, J. Kim, J. Han, J. Y. Suh, G. H. Kim, T. H. Lee, J. H. Jang, *Scientific Reports* **2020**, 10, 1.
- [189] I. T. Jolliffe, J. Cadima, *Philosophical Transactions of the Royal Society A: Mathematical, Physical and Engineering Sciences* **2016**, 374, 20150202.
- [190] D. D. Lee, H. S. Seung, *Nature* **1999**, 401, 788.
- [191] T. Malis, S. Cheng, R. Egerton, *Journal of Electron Microscopy Technique* **1988**, 8, 193.
- [192] B. Ruta, E. Pineda, Z. Evenson, *Journal of Physics: Condensed Matter* **2017**, 29, 503002.
- [193] M. W. Berry, M. Browne, A. N. Langville, V. P. Pauca, R. J. Plemmons, *Computational Statistics & Data Analysis* **2007**, 52, 155.
- [194] X. Mu, L. Chen, R. Mikut, H. Hahn, C. Kübel, *Acta Materialia* **2021**, 212.
- [195] Y. C. Liang, R. S. Liu, Y. F. Mo, H. R. Liu, Z. A. Tian, Q. y. Zhou, H. T. Zhang, L. L. Zhou, Z. Y. Hou, P. Peng, *Journal of Alloys and Compounds* **2014**, 597, 269.
- [196] S. Pan, J. Qin, W. Wang, T. Gu, *Physical Review B* **2011**, 84, 092201.
- [197] J. Ding, E. Ma, M. Asta, R. O. Ritchie, *Scientific Reports* **2015**, 5, 1.
- [198] Y. Cheng, E. Ma, *Progress in Materials Science* **2011**, 56, 379.
- [199] J. Ding, S. Patinet, M. L. Falk, Y. Q. Cheng, E. Ma, *Proceedings of the National Academy of Sciences of the United States of America* **2014**, 111, 14052.
- [200] S. Kang, D. Wang, A. Caron, C. Minnert, K. Durst, C. Kübel, X. Mu, *Advanced Materials* **2023**, 35, 2212086.
- [201] Y. H. Sun, A. Concustell, A. L. Greer, *Nature Reviews Materials* **2016**, 1.
- [202] J. C. Qiao, J. M. Pelletier, C. Esnouf, Y. Liu, H. Kato, *Journal of Alloys and Compounds* **2014**, 607, 139.
- [203] D. Pan, Y. Yokoyama, T. Fujita, Y. H. Liu, S. Kohara, A. Inoue, M. W. Chen, *Applied Physics Letters* **2009**, 95.
- [204] H. Rosner, M. Peterlechner, C. Kubel, V. Schmidt, G. Wilde, *Ultramicroscopy* **2014**, 142, 1.
- [205] S. Scudino, D. Soppu, *Nano Letters* **2018**, 18, 1221.

- [206] H. Shakur Shahabi, S. Scudino, I. Kaban, M. Stoica, B. Escher, S. Menzel, G. B.M. Vaughan, U. Kühn, J. Eckert, *Acta Materialia* **2016**, 111, 187.
- [207] D. Söpu, X. Yuan, F. Moitzi, F. Spieckermann, X. Bian, J. Eckert, *Applied Materials Today* **2021**, 22, 100958.
- [208] P. Wen, B. Demaske, S. R. Phillpot, D. E. Spearot, G. Tao, S. Q. Yuan, *Journal of Applied Physics* **2019**, 125.
- [209] V. Hieronymus-Schmidt, H. Rosner, G. Wilde, A. Zaccone, *Physical Review B* **2017**, 95, 134111.
- [210] V. Schmidt, H. Rösner, M. Peterlechner, G. Wilde, P. M. Voyles, *Physical Review Letters* **2015**, 115, 035501.
- [211] R. Dasgupta, H. G. Hentschel, I. Procaccia, *Physics Review E* **2013**, 87, 022810.
- [212] X. Mu, M. R. Chellali, E. Boltynjuk, D. Gunderov, R. Z. Valiev, H. Hahn, C. Kübel, Y. Ivanisenko, L. Velasco, *Advanced Materials* **2021**, 33, 2007267.
- [213] B. A. Sun, W. H. Wang, *Applied Physics Letters* **2011**, 98, 201902.
- [214] X. X. Liu, A. Papon, H. Muhlhaus, *Philosophical Magazine* **2012**, 92, 3501.
- [215] J. Liu, Q. Cao, L. Chen, X. Wang, J. Jiang, *Acta Materialia* **2010**, 58, 4827.
- [216] H.-B. Yu, W.-H. Wang, K. Samwer, *Materials Today* **2013**, 16, 183.
- [217] F. Zhu, H. Nguyen, S. Song, D. P. Aji, A. Hirata, H. Wang, K. Nakajima, M. Chen, *Nature Communications* **2016**, 7, 11516.
- [218] J. Carter, E. Fu, M. Martin, G. Xie, X. Zhang, Y. Wang, D. Wijesundera, X. Wang, W.-K. Chu, L. Shao, *Scripta Materialia* **2009**, 61, 265.
- [219] X. Huang, Z. Ling, Y. Wang, L. Dai, *Intermetallics* **2016**, 75, 36.
- [220] J. Pan, Y. Wang, Q. Guo, D. Zhang, A. Greer, Y. Li, *Nature Communications* **2018**, 9, 560.
- [221] F. Wu, Z. Zhang, F. Jiang, J. Sun, J. Shen, S. Mao, *Applied Physics Letters* **2007**, 90, 191909.
- [222] G. Kumar, D. Rector, R. D. Conner, J. Schroers, *Acta Materialia* **2009**, 57, 3572.
- [223] R. Maass, P. Birckigt, C. Borchers, K. Samwer, C. A. Volkert, *Acta Materialia* **2015**, 98, 94.
- [224] S. J. Kang, D. Wang, A. Caron, C. Minnert, K. Durst, C. Kubel, X. Mu, *Advanced Materials* **2023**, e2212086.
- [225] C. Minnert, M. Kuhnt, S. Bruns, A. Marshal, K. G. Pradeep, M. Marsilius, E. Bruder, K. Durst, *Materials & Design* **2018**, 156, 252.
- [226] A. Hammersley, S. Svensson, M. Hanfland, A. Fitch, D. Hausermann, *International Journal of High-Pressure Research* **1996**, 14, 235.
- [227] X. Qiu, J. W. Thompson, S. J. Billinge, *Journal of Applied Crystallography* **2004**, 37, 678.
- [228] C. A. Schuh, T. G. Nieh, *Acta Materialia* **2003**, 51, 87.
- [229] F. P. Bowden, D. Tabor, *THE FRICTION AND LUBRICATION OF SOLIDS*, Vol. 1, Oxford University Press, **2001**.
- [230] J. Schroers, W. L. Johnson, *Physical Review Letters* **2004**, 93, 255506.
- [231] P. Murali, U. Ramamurty, *Acta Materialia* **2005**, 53, 1467.
- [232] J. M. Silveyra, E. Ferrara, D. L. Huber, T. C. Monson, *Science* **2018**, 362, eaao0195.
- [233] J. F. Wang, R. Li, N. B. Hua, L. Huang, T. Zhang, *Scripta Materialia* **2011**, 65, 536.
- [234] Q. Wang, J. Zhou, Q. Zeng, G. Zhang, K. Yin, T. Liang, W. Yang, M. Stoica, L. Sun, B. Shen, *Materialia* **2020**, 9, 100561.
- [235] T. Zhang, F. Liu, S. Pang, R. Li, *Materials transactions* **2007**, 48, 1157.
- [236] D. Jiles, *Introduction to magnetism and magnetic materials*, CRC Press, **2015**.
- [237] M. R. Gibbs, *Modern trends in magnetostriction study and application*, Springer Science & Business Media **2001**.
- [238] S. Pascarelli, M. Ruffoni, A. Trapananti, O. Mathon, G. Aquilanti, S. Ostanin, J. Staunton, R. Pettifer, *Physical Review Letters* **2007**, 99, 237204.
- [239] A. Hubert, R. Schäfer, *Magnetic domains: the analysis of magnetic microstructures*, Springer Science & Business Media, **2008**.
- [240] J. Gutierrez, J. Barandiaran, O. Nielsen, *Physica Status Solidi (a)* **1989**, 111, 279.
- [241] B. Lippmann, *Physical Review Letters* **1965**, 15, 11.
- [242] S. Pascarelli, M. Ruffoni, A. Trapananti, O. Mathon, C. Detlefs, M. Pasquale, A. Magni, C. P. Sasso, F. Celegato, E. Olivetti, *Physical Review B* **2010**, 81, 020406.

-
- [243] P. S. Salmon, R. A. Martin, P. E. Mason, G. J. Cuello, *Nature* **2005**, 435, 75.
- [244] J. D. Livingston, *Physica Status Solidi a-Applied Research* **1979**, 56, 637.
- [245] V. Lakshmanan, J. Li, C. Tsai, *Acta Metallurgica et Materialia* **1990**, 38, 625.
- [246] J. M. Gibson, M. M. J. Treacy, P. M. Voyles, *Ultramicroscopy* **2000**, 83, 169.
- [247] P. M. Voyles, J. R. Abelson, *Solar Energy Materials and Solar Cells* **2003**, 78, 85.
- [248] F. Yi, P. M. Voyles, *Ultramicroscopy* **2011**, 111, 1375.
- [249] D. Şopu, *Journal of Alloys and Compounds* **2023**, 170585.
- [250] J. M. Padbidri, C. M. Hansen, S. D. Mesarovic, B. Muhunthan, *Journal of Applied Mechanics-Transactions of the Asme* **2012**, 79.
- [251] H. Peng, M. Li, W. Wang, *Physical Review Letters* **2011**, 106, 135503.
- [252] P. Wen, B. Demaske, S. R. Phillpot, D. E. Spearot, G. Tao, S. Yuan, *Journal of Applied Physics* **2019**, 125, 215903.